

AN ABSTRACT OF THE THESIS OF

Eve D. Lathrop for the degree of Master of Science in Civil Engineering presented on September 3, 2021.

Title: Regional and Site-Specific Vulnerabilities of the Western Power Grid from a M9.3 Cascadia Subduction Zone Earthquake

Abstract approved:

Michael J. Olsen

Armin W. Stuedlein

The likelihood of a Cascadia Subduction Zone (CSZ) earthquake is estimated between 37 to 42% in the next 50 years, leading to strong shaking, liquefaction, landsliding, and other seismic ground failure resulting in major impacts to critical lifelines such as the western power grid. Electrical power is essential for continued functionality of emergency services, economic recovery, and other basic, essential needs such as water and fuel supply, wastewater treatment, and communications. Hence, understanding the extent of damage to the power grid from a CSZ event is critical. The objective of this research, part of a broader study identifying the seismic resilience of the western power grid, is to assess the vulnerabilities of the synthetic western power grid by quantifying the likelihood and magnitude of seismically induced landslide occurrence to determine the effects of those displacements on electrical transmission poles and towers at a regional scale.

To this end, this thesis presents a probabilistic method for a regional seismic landslide hazard analysis and map for the Western United States based on the USGS M9.3 Megathrust CSZ scenario earthquake with consideration of topographic, geologic, and other geospatial information. The landslide triggering analysis completed uses several empirical seismic displacement prediction models based on the Newmark sliding block method, which are calibrated using strength parameters for each geological unit based on the terrain slope at locations of previously mapped landslides within the unit. A predictive displacement regression model, LOS21 was developed using a logic tree scheme that weights the individual models based on the suitability of the model to this regional assessment. The LOS21 model was used to calculate the probability of exceedance of specific thresholds (e.g., 5%, 15% and 50%) to evaluate potential impacts to the power grid. Electrical infrastructure located west of the Cascades in Washington, Oregon, and Northern California were determined to be subjected to the highest risk of landslide-induced damage.

To provide context to the broader study focusing on non-landslide-induced impacts to the western power grid (e.g., ground shaking and inertial equipment loading), an evaluation site was characterized for a detailed site-specific site response analyses to evaluate the differences in amplification between equivalent linear and nonlinear, total stress analyses using ten ground motions pairs scaled and matched to the USGS seismic scenario hazard. The results of the site-specific site response analysis are used to evaluate the potential impact to the electrical components for the substation at the evaluation site for comparison to the seismic hazard developed using the regional map. The equivalent linear and the nonlinear approach produced PGA amplification results that were lower from the USGS seismic scenario hazard by 6% and 32%, respectively. The maps created are suitable for regional resilience and planning and to guide geotechnical investigations but should not be used in place of site-specific analysis for engineering design purposes.

©Copyright by Eve D. Lathrop

September 3, 2021

All Rights Reserved

Regional and Site-Specific Vulnerabilities of the Western Power Grid from a M9.3
Cascadia Subduction Zone Earthquake

by
Eve D. Lathrop

A THESIS

submitted to

Oregon State University

in partial fulfillment of
the requirements for the
degree of

Master of Science

Presented September 3, 2021
Commencement June 2022

Master of Science thesis of Eve D. Lathrop presented on September 3, 2021.

APPROVED:

Co-Major Professor, representing Civil Engineering

Co-Major Professor, representing Civil Engineering

Head of the School of Civil and Construction Engineering

Dean of the Graduate School

I understand that my thesis will become part of the permanent collection of Oregon State University libraries. My signature below authorizes release of my thesis to any reader upon request.

Eve D. Lathrop, Author

ACKNOWLEDGEMENTS

This research would not be possible without the support of specific individuals and organizations. I would like to first and foremost thank my graduate advisors, Professor Dr. Michael Olsen and Professor Dr. Armin Stuedlein for their endless guidance, support and patience throughout this whole process. Thank you Michael Olsen for your continued support for the past five years in my undergraduate and masters studies and for giving me the opportunity to work on this project. Thank you Armin Stuedlein for always challenging me and pushing me to learn. Your introduction to geotechnical engineering course stemmed my interest in the geotechnical field.

I would also like to thank Professor Dr. Ted Brekken and Professor Dr. Ben Leshchinsky for taking the time to be on my committee. Thank you Ted Brekken for leading the Earthquake Resiliency of the Western Interconnection project. Thank you Ben Leshchinsky for your guidance and helping me decide to pursue a master's degree.

Thank you to Dr. Eduardo Cotilla-Sanchez, Leon Kempner, James Landstrom and everyone else who has been a part of Earthquake Resiliency of the Western Interconnection project. Thank you David Glennon and William Stark for working alongside me and providing insight on a field I have no experience in. I would also like to extend my sincere thanks to the CEI hub at Portland State for providing data for this project. Thank you to the National Science Foundation for funding the project.

Last but certainly not least, I would like to thank my amazing friends and family for their endless support throughout this whole process. I would not be the person I am today without the love and support of my parents. Thank you for always pushing me to learn new things and to never give up on my dreams.

TABLE OF CONTENTS

	<u>Page</u>
Chapter 1: Introduction	1
1.1 Background	1
1.1.1 Western Power Grid	1
1.1.2 Cascadia Subduction Zone Earthquake	2
1.2 Project Description & Research Objectives	3
1.3 Thesis Organization	4
Chapter 2: Literature Review	6
2.1 Relevance of CSZ to Western Power Grid System	6
2.2 Seismic Hazards	7
2.2.1 Types of Seismic Waves	8
2.2.2 Ground Motions	9
2.2.3 Site Response Analysis	11
2.2.4 Seismically induced landslides	13
2.2.4.1 Landslide Types	14
2.2.4.2 Slope Stability Basics	17
2.2.4.3 Empirical displacement prediction equations	18
2.2.5 Liquefaction	23
2.2.5.1 Liquefaction Susceptibility	24
2.2.5.2 Liquefaction Evaluation Methods	26
2.2.6 Liquefaction Triggering	28
2.2.7 Consequences of Liquefaction	33
2.3 Hazard Mapping	34
2.3.1 Overview of Available Seismic Hazard Mapping Methods	34
2.3.2 Deterministic and Probabilistic Methodologies	34
2.3.3 Landslides	35
2.3.4 Liquefaction & Lateral Spreading	39
2.4 Infrastructure and Vulnerabilities of Western Power Grid System	40
2.5 Fragility Curves	44
2.5.1 SEFT	45

TABLE OF CONTENTS (CONTINUED)

2.5.2 CLiP database	45
2.5.2.1 HAZUS	46
2.5.2.2 IN-CORE database.....	48
2.5.2.3 SYNER-G database	49
2.6 Summary	50
Chapter 3: Landslide Hazard Map	51
3.1 Study Area	51
3.2 Data Sources	54
3.2.1 Digital Elevation Model (DEM)	55
3.2.2 Lithological Unit Map.....	58
3.2.3 Landslide Inventory Map.....	60
3.2.4 M9.3 Earthquake Simulation	62
3.2.5 ACTIVS Power Grid datasets	66
3.3 Methodology Overview	69
3.3.1 Methodology for Probabilistic Seismic Landslide Hazard Analysis	71
3.3.2 Distribution of Mobilized Strength (DOMS) Curves per Lithological Unit.....	76
3.3.2.1 Data Collection and Processing	77
3.3.2.2 Workflow	77
3.3.3 Logic Tree	84
3.3.3.1 Models and Processing	84
3.3.3.2 Representative Displacement Model: LOS21	90
3.4 Summary	93
Chapter 4: Landslide Hazard Analysis Results.....	95
4.1 Landslide Hazard Mapping Results	95
4.2 Validation.....	100
4.3 Power Grid Impacts	106
4.3.1 Damage State Probability of Power Poles of according to developed fragility curves	108
4.4 Summary	114

TABLE OF CONTENTS (CONTINUED)

Chapter 5: Site Response Analysis	115
5.1 Introduction.....	115
5.2 Evaluation Site.....	116
5.3 Seismic Hazard for the M9.3 CSZ Scenario Earthquake.....	118
5.3.1 Interpolation of Mapped Bedrock Scenario Intensities.....	118
5.3.2 Ground Motion Selection.....	121
5.4 Development of Representative Soil Profiles at each Exploration Location.....	124
5.4.1 SRA Profiles based on Borings.....	125
5.4.2 SRA Profiles based on CPTs	127
5.4.3 Soil Profiles used for Site Response Analysis	134
5.5 Total Stress Site Response Analysis.....	136
5.4.1 Soil Models and Model Parameters	137
5.4.2 Results of the Site Response Analyses and Discussion	146
5.4.2.1 Computed Peak Horizontal and Ground Accelerations	146
5.4.2.2 Computed Maximum Soil Shear Strain	152
5.4.2.3 Acceleration Response Spectra.....	156
5.4.3 Spatial Distribution of PGA at the Evaluation Site	161
5.5 Impact to Electrical Utility Equipment.....	163
5.6 Summary	169
Chapter 6: Summary	171
6.1 Summary	171
6.2 Conclusion	172
6.3 Suggestions for Future Research	175
References.....	176
Appendix A.....	189
Appendix B	209
Site Profiles.....	209
Peak Horizontal Acceleration Plots	219

TABLE OF CONTENTS (CONTINUED)

Maximum Shear Strain Plots	229
Spectra Acceleration Plots	239

LIST OF FIGURES

<u>Figure</u>	<u>Page</u>
Figure 2-1. Illustration of various landslide types (Highland and Bobrowsky 2008)	15
Figure 2-2. Illustration of the Newmark’s sliding block analysis (a) diagram, (b) acceleration– time history double integrated to determine displacement, (c) considered variables and equation used in analysis (Li et al. 2018).	19
Figure 2-3. Criteria for susceptibility of fine-grained soils (From Armstrong and Malvick 2016)	28
Figure 2-4. Fragility Curves for a 57kV Substation (Obtained from SEFT Report (SEFT 2018))	44
Figure 3-1. Extent of the area of interest (i.e., extent of the Western Power Grid) with a box outlining the extents of the data provided by the USGS for a CSZ M9.3 earthquake dataset (ground motion intensity data).....	53
Figure 3-2. Slope map from the developed DEM of the study region focused on the extent of the M9.3 CSZ earthquake dataset (ground motion intensity data) with five inserts to indicate detail.	57
Figure 3-3. Lithological map of the Western Power Grid.	60
Figure 3-4. Landslide inventory map including landslide deposits and points obtained from COOLR ad USGS. The figure depicts three sites in more detail that have a high number of landslides.....	62
Figure 3-5. Summary of the fault boundaries and location of the epicenter used in the M 9.3 Scenario Earthquake ShakeMap.	64
Figure 3-6. (a) Extent of the CSZ M9.3 event data, (b) Peak ground acceleration (PGA) map for a CSZ M9.3 event in g, (c) Peak ground velocity (PGV) map for a CSZ M9.3 event in cm/s ² ...	65
Figure 3-7. Extent of the ACTIVSg 10k model with bus/substation, transmission power lines and poles projected in the study region with insets of five cities along the west coast.	68

LIST OF FIGURES (CONTINUED)

<u>Figure</u>	<u>Page</u>
Figure 3- 8. The simplified methodology for each pixel in the study region prior to the seismic stability evaluation	72
Figure 3-9. Methodology with simplified pseudo-code for stability evaluation and development of the hazard map (modified from Sharifi-Mood et al (2017)	73
Figure 3-10. Methodology used to develop Distribution of Mobilized Strength (DOMS) curves based on lithological unit type and selecting best fit distribution.....	78
Figure 3-11: Cumulative Distribution Functions (CDF) for Igneous Intrusive lithology type with shape parameters and statistic information regarding the determined bias values: (a) Lognormal, (b) Normal, (c) Gamma, (d)Weibull. The Gamma distribution (c) provided was selected as the best fit for this Igneous Intrusive lithology type.....	81
Figure 3-12: Example CDF of best fit distribution of mobilized strength (DOMS) curves. (i.e., proxy for the distribution of strength parameters) for various lithological units: weaker soils (Unconsolidated and Sedimentary, Undifferentiated* & Igneous Sedimentary Undifferentiated), stronger soils (Sedimentary, Undifferentiated & Metamorphic, Undifferentiated*). Reference Horton et al. (2017) for lithological unit descriptions.	82
Figure 3-13. Example probability of exceedance curves for a single test site where all relevant regression models considered for the logic tree evaluation. (assuming 50% soil strength).	89
Figure 3-14. Example probability of exceedance curves for a single test site for the regression models used in the logic tree model, <i>LOS21</i> . (assuming 50% soil strength).....	92
Figure 4-1. Estimated displacement maps developed using the representative displacement model <i>LOS21</i> assuming a 5% probability of exceedance (POE).....	97
Figure 4-2. Estimated displacement maps developed using the representative displacement model <i>LOS21</i> assuming a 15% probability of exceedance (POE).....	98
Figure 4-3. Estimated displacement maps developed using the representative displacement model <i>LOS21</i> assuming a 50% probability of exceedance (POE).....	99

LIST OF FIGURES (CONTINUED)

<u>Figure</u>	<u>Page</u>
Figure 4 - 4. Seismic landslide hazard map using the <i>LOS2I</i> displacement model assuming a 5% POE overlain with the SLIDO landslide hazard map and electrical transmission lines. The figure depicts 5 regions in Oregon in detail for comparison.	103
Figure 4 - 5. Seismic landslide hazard map using the <i>LOS2I</i> displacement model assuming a 15% POE overlain with the SLIDO landslide hazard map and electrical transmission lines. The figure depicts 5 regions in Oregon in detail for comparison.	104
Figure 4 - 6. Seismic landslide hazard map using the <i>LOS2I</i> displacement model assuming a 50% POE overlain with the SLIDO landslide hazard map and electrical transmission lines. The figure depicts 5 regions in Oregon in detail for comparison.	105
Figure 4 - 7. Cumulative distribution of transmission pole displacement greater than 0.01 m assuming per bin for a 5, 15 and 50% probability of exceedance.	107
Figure 4 - 8. Developed fragility curves for the transmission lines for three voltage levels and each damage state: (a) small voltage (< 69kV), (b) medium voltage levels (69 < x < 230kV), and (c) large voltage levels (≥ 230kV).	110
Figure 4 - 9. Percentage of poles reaching a damage state assuming various threshold values (i.e., 5%, 15%, 25% and 50%) for poles in the study area would be expected to experience some landsliding.	112
Figure 4 - 10. Dot map showing the distribution of damaged poles for a threshold value of 25% denoted by their reached damages state underlayed with the representative <i>LOS2I</i> displacement map assuming a 5% probability of exceedance (POE).	113
Figure 5 - 1. Site map and exploration plan of the evaluation site indicating where the CPTs and borings were completed and the corresponding estimated contours indicating the depth of basalt rock.	117
Figure 5 - 2. The intensity/ground motion (PSA and PGA) data for the rock layer near the evaluation site: (a) PSA at 0.3 sec, (b) PSA at 1.0 sec (c) PSA at 3.0 sec, and (d) PGA, in %g. The red star indicates the evaluation site location with respect to the data.	120

LIST OF FIGURES (CONTINUED)

<u>Figure</u>	<u>Page</u>
Figure 5 - 3. Comparison of the scaled response spectra and average scaled response spectrum to the target input response spectrum.....	123
Figure 5 - 4. Variation of corrected cone tip resistance and I_c with depth for CPT-1 (refer to Figure B-5 in Appendix B).	129
Figure 5 - 5. A comparison of the measured shear wave velocity and the three considered shear wave velocity correlations develop by Andrus et. al. (2007) for CPT-2.	132
Figure 5 - 6. A comparison of the measured shear wave velocity and the combined Holocene and Pleistocene combined methods (average) correlation used for site applied to CPT-2.	133
Figure 5 - 7. Diagram of the soil profile for use in site response analysis developed for Boring 1 (B1) and the associated soil properties.	135
Figure 5 - 8. Hysteretic loop for one cycle of loading showing the G_{max} , G and D (From Zhang et al. 2005).	137
Figure 5 - 9. The Darendeli (2001) (a) G/G_{max} and (2) damping curves assuming $PI = 0$, $OCR=1$, and $f = 1$	140
Figure 5 - 10. The develop (a) G/G_{max} and (b) damping curves for the Vucetic and Dobry (1991) model.	142
Figure 5 - 11. Comparison of peak horizontal acceleration (PHA) with depth for equivalent linear (EL) and nonlinear (NL) site response analyses conducted for the Boring 1 (B1) soil profile. 10 Motions (both NS and EW direction, total 20 motions) were evaluated obtained from the PEER NGA earthquake database: (a) Motion 4000016, (b) Motion 4000521, (c) Motion 4001060, (d) Motion 4022909, (e) Motion 4022989, (f) Motion 4022913, (g) Motion 4032577, (h) Motion 6001373, (i) Motion 4028564, (j) Motion 4032552.	150
Figure 5 - 12. Comparison of average peak horizontal acceleration (PHA) with depth for equivalent linear (EL) and nonlinear (NL) site response analyses conducted for all the profiles developed for the evaluation site. Profile: (a) Boring 1 (B1), (b) Boring 2 (B2), (c) Boring 3 (B3), (d) Boring 4 (B4), (e) CPT-1 (C1), (f) CPT-2 (C2), (g) CPT-3 (C3), (h) CPT-4 (C4), (i) CPT-5 (C5), (j) CPT-6 (C6) and (k) CPT-7 (C7).	151

LIST OF FIGURES (CONTINUED)

<u>Figure</u>	<u>Page</u>
Figure 5 - 13. Comparison of maximum shear strain, γ_{max} (%) with depth for equivalent linear (EL) and nonlinear (NL) site response analyses conducted for the Boring 1 (B1) soil profile. 10 Motions (both NS and EW direction, total 20 motions) were evaluated obtained from the PEER NGA earthquake database: (a) Motion 4000016, (b) Motion 4000521, (c) Motion 4001060, (d) Motion 4022909, (e) Motion 4022989, (f) Motion 4022913, (g) Motion 4032577, (h) Motion 6001373, (i) Motion 4028564, (j) Motion 4032552.	154
Figure 5 - 14. Comparison of average maximum shear strain, γ_{max} (%) with depth for equivalent linear (EL) and nonlinear (NL) site response analyses conducted for all the profiles developed for the evaluation site. Profile: (a) Boring 1 (B1), (b) Boring 2 (B2), (c) Boring 3 (B3), (d) Boring 4 (B4), (e) CPT-1 (C1), (f) CPT-2 (C2), (g) CPT-3 (C3), (h) CPT-4 (C4), (i) CPT-5 (C5), (j) CPT-6 (C6) and (k) CPT-7 (C7).....	155
Figure 5 - 15. Comparison of spectral acceleration (SA) with depth for equivalent linear (EL) and nonlinear (NL) site response analyses conducted for the Boring 1 (B1) soil profile. 10 Motions (both NS and EW direction, total 20 motions) were evaluated obtained from the PEER NGA earthquake database: (a) Motion 4000016, (b) Motion 4000521, (c) Motion 4001060, (d) Motion 4022909, (e) Motion 4022989, (f) Motion 4022913, (g) Motion 4032577, (h) Motion 6001373, (i) Motion 4028564, (j) Motion 4032552.	159
Figure 5 - 16. Comparison of average spectral acceleration (SA) with depth for equivalent linear (EL) and nonlinear (NL) site response analyses conducted for all the profiles developed for the evaluation site. Profile: (a) Boring 1 (B1), (b) Boring 2 (B2), (c) Boring 3 (B3), (d) Boring 4 (B4), (e) CPT-1 (C1), (f) CPT-2 (C2), (g) CPT-3 (C3), (h) CPT-4 (C4), (i) CPT-5 (C5), (j) CPT-6 (C6) and (k) CPT-7 (C7).....	160
Figure 5 - 17. PGA and amplification contour map using EL and NL approach developed values: (a) EL-PGA contour, (b) EL-PGA amplification ratio, (c) NL-PGA contour, and (d) NL-PGA amplification ratio.	162
Figure 5 - 18. Response spectra Group B fragility curves at two voltage levels: (a) 115kV and (b) 270 kV, for the various electrical components with their corresponding failure mode.....	164

LIST OF TABLES

<u>Table</u>	<u>Page</u>
Table 2-1. Description of ground motion spectra used in earthquake engineering practice and the associated capabilities.	11
Table 2-2. Summary of Landslide Movement Types (modified from Cruden and Varnes 1996)	16
Table 2-3. Summary of Seismically Triggered Landslide Movement Types (Kramer 1996)	16
Table 2-4. Examples of empirical predictive models for earthquake-induced sliding displacement of slopes with necessary input parameters and limitations for use in a regional analysis in a CSZ event (modified from Sharifi-Mood et al. 2017) (Note: □ - optional variance of models).....	21
Table 2-5. Liquefaction susceptibility based on several criteria and the applications.....	25
Table 2-6. List of liquefaction susceptibility models and the associated criterion parameters	27
Table 2-7. Summary of deterministic and probabilistic co-seismic landslide mapping models in a GIS framework and the associated limitations	38
Table 2-8. Summary of Liquefaction/Lateral Spreading Mapping Models categorized in various frameworks	40
Table 2-9. Vulnerabilities of the different components within a substation (visuals, unit description and vulnerabilities).....	42
Table 2-10. List of the components with fragility curves available for different voltage levels in SEFT (2018).....	45
Table 2-11. HAZUS: Electrical power generation plants and substation fragility function attributes.....	46
Table 2-12. IN-CORE: Fragility function for different components of the electric power grid system	48
Table 2-13. SYNER-G: Electric power systems fragility function attributes	49
Table 3-1. Datasets used for the landslide analysis and their source, provider and resolution. ...	55

LIST OF TABLES (CONTINUED)

<u>Table</u>	<u>Page</u>
Table 3-2. Relative percentage of space that each lithological unit occupies within the study Region (~3,075,000 km ²).....	59
Table 3-3. Assumed Spacing of poles based on transmission line voltage	67
Table 3-4. Topographical amplification factors applied to the ground intensity data (<i>PGA_i</i> , <i>PGV_i</i>) based on slope angle	71
Table 3-5. Cumulative distribution functions of slope angle at failure by lithological type with corresponding best-fit distribution and shape parameters (α /Mean & β /SD), # of landslides sampled in developing distribution and soil number.	83
Table 3-6. Summary of considered sliding block (Regression) co-seismic landslide displacement models. * = models used in the logic tree model, <i>LOS21</i>	87
Table 3-7. Logic tree weights (percentages) of the relevant regression models for the <i>LOS21</i> displacement model	90
Table 4 - 1. Fragility curves curve parameters (mean and STD) of each damage states per voltage level.....	111
Table 5 - 1. Identified “fitting parameters” for the evaluation site to determine PSA at 0.3, 1.0 and 3.0 s, and PGA.	119
Table 5 - 2. Target peak spectral acceleration (PSA) and PGA representing the bedrock motion for the M9.3 CSZ scenario earthquake determined for the evaluation site.	119
Table 5 - 3. Summary of the selected ground motions, scale factor, and goodness of fit metrics.	123
Table 5 - 4. Scaled and average response spectra for the ten selected ground motions.	124
Table 5 - 5. Summary of SPT correlations and assumptions used to develop the boring profiles soil properties.....	126
Table 5 - 6. Summary of CPT correlations and assumptions used to develop the CPT profiles soil properties.....	128

LIST OF TABLES (CONTINUED)

<u>Table</u>	<u>Page</u>
Table 5 - 7. Shear wave velocity correlations proposed by Andrus et. al. (2007).....	131
Table 5 - 8. Summary of the step-by-step work flow and modeling parameters for DEEPSOIL used in this evaluation.....	145
Table 5 - 9. Summary of the PGA computed using the EL and NL site response analyses at the evaluation site.	149
Table 5 - 10. Summary of the estimated natural periods for each soil profile.....	156
Table 5 - 11. Electrical equipment and associated failure methods evaluated for the site	165
Table 5 - 12. Probability of failure of electrical equipment at 115 kV based on PGA values developed from the EL and NL approach and the hazard map.....	167
Table 5 - 13. Probability of failure of electrical equipment at 230 kV based on PGA values developed from the EL and NL approach and the hazard map.....	168

LIST OF APPENDICES

<u>Appendix</u>	<u>Page</u>
Appendix A.....	189
Appendix B.....	209
Site Profiles.....	209
Peak Horizontal Acceleration Plots	219
Maximum Shear Strain Plots	229
Spectra Acceleration Plots	239

LIST OF APPENDIX FIGURES

<u>Figure</u>	<u>Page</u>
Figure A - 1. Cumulative Distribution Functions (CDF) for Metamorphic and Sedimentary, undifferentiated lithology type with shape parameters and statistic information regarding the determined bias values: (a) Lognormal, (b) Normal, (c) Gamma, (d)Weibull. The Gamma distribution (c) provided was selected as the best fit for this Metamorphic and Sedimentary, undifferentiated lithology type.....	190
Figure A - 2. Cumulative Distribution Functions (CDF) for Metamorphic, gneiss lithology type with shape parameters and statistic information regarding the determined bias values: (a) Lognormal, (b) Normal, (c) Gamma, (d)Weibull. The Gamma distribution (c) provided was selected as the best fit for this Metamorphic, gneiss lithology type.	191
Figure A - 3. Cumulative Distribution Functions (CDF) for Metamorphic, schist lithology type with shape parameters and statistic information regarding the determined bias values: (a) Lognormal, (b) Normal, (c) Gamma, (d) Weibull. The Gamma distribution (c) provided was selected as the best fit for this Metamorphic, schist lithology type.	192
Figure A - 4. Cumulative Distribution Functions (CDF) for Metamorphic, sedimentary lithology type with shape parameters and statistic information regarding the determined bias values: (a) Lognormal, (b) Normal, (c) Gamma, (d) Weibull. The Gamma distribution (c) provided was selected as the best fit for this Metamorphic, sedimentary lithology type.....	193
Figure A - 5. Cumulative Distribution Functions (CDF) for Metamorphic, serpentinite lithology `type with shape parameters and statistic information regarding the determined bias values: (a) Lognormal, (b) Normal, (c) Gamma, (d) Weibull. The Gamma distribution (c) provided was selected as the best fit for this Metamorphic, serpentinite lithology type.	194
Figure A - 6. Cumulative Distribution Functions (CDF) for Metamorphic, undifferentiated lithology type with shape parameters and statistic information regarding the determined bias values: (a) Lognormal, (b) Normal, (c) Gamma, (d) Weibull. The Weibull distribution (d) provided was selected as the best fit for this Metamorphic, undifferentiated lithology type.	195

LIST OF APPENDIX FIGURES (CONTINUED)

<u>Figure</u>	<u>Page</u>
Figure A - 7. Cumulative Distribution Functions (CDF) for Metamorphic, volcanic lithology type with shape parameters and statistic information regarding the determined bias values: (a) Lognormal, (b) Normal, (c) Gamma, (d) Weibull. The Weibull distribution (d) provided was selected as the best fit for this Metamorphic, volcanic lithology type.....	196
Figure A - 8. Cumulative Distribution Functions (CDF) for Metamorphic, sedimentary clastic lithology type with shape parameters and statistic information regarding the determined bias values: (a) Lognormal, (b) Normal, (c) Gamma, (d)Weibull. The Gamma distribution (c) provided was selected as the best fit for this Metamorphic, sedimentary clastic lithology type.	197
Figure A - 9. Cumulative Distribution Functions (CDF) for Igneous and Sedimentary, undifferentiated lithology type with shape parameters and statistic information regarding the determined bias values: (a) Lognormal, (b) Normal, (c) Gamma, (d)Weibull. The Weibull distribution (d) provided was selected as the best fit for this Igneous and Sedimentary, undifferentiated lithology type.....	198
Figure A - 10. Cumulative Distribution Functions (CDF) for Igneous Metamorphic, undifferentiated lithology type with shape parameters and statistic information regarding the determined bias values: (a) Lognormal, (b) Normal, (c) Gamma, (d)Weibull. The Weibull distribution (d) provided was selected as the best fit for this Igneous Metamorphic, undifferentiated lithology type.....	199
Figure A - 11. Cumulative Distribution Functions (CDF) for Igneous, undifferentiated lithology type with shape parameters and statistic information regarding the determined bias values: (a) Lognormal, (b) Normal, (c) Gamma, (d)Weibull. The Gamma distribution (c) provided was selected as the best fit for this Igneous, undifferentiated lithology type.	200
Figure A - 12. Cumulative Distribution Functions (CDF) for Igneous, volcanic lithology type with shape parameters and statistic information regarding the determined bias values: (a) Lognormal, (b) Normal, (c) Gamma, (d)Weibull. The Gamma distribution (c) provided was selected as the best fit for this Igneous, volcanic lithology type.	201

LIST OF APPENDIX FIGURES (CONTINUED)

<u>Figure</u>	<u>Page</u>
Figure A - 13. Cumulative Distribution Functions (CDF) for Melange lithology type with shape parameters and statistic information regarding the determined bias values: (a) Lognormal, (b) Normal, (c) Gamma, (d)Weibull. The Normal distribution (b) provided was selected as the best fit for this Melange lithology type.	202
Figure A - 14. Cumulative Distribution Functions (CDF) for Sedimentary, carbonate lithology type with shape parameters and statistic information regarding the determined bias values: (a) Lognormal, (b) Normal, (c) Gamma, (d)Weibull. The Gamma distribution (c) provided was selected as the best fit for this Sedimentary, carbonate lithology type.	203
Figure A - 15. Cumulative Distribution Functions (CDF) for Sedimentary, clastic lithology type with shape parameters and statistic information regarding the determined bias values: (a) Lognormal, (b) Normal, (c) Gamma, (d)Weibull. The Weibull distribution (d) provided was selected as the best fit for this Sedimentary, clastic lithology type.	204
Figure A - 16. Cumulative Distribution Functions (CDF) for Sedimentary, undifferentiated lithology type with shape parameters and statistic information regarding the determined bias values: (a) Lognormal, (b) Normal, (c) Gamma, (d)Weibull. The Weibull distribution (c) provided was selected as the best fit for this Sedimentary, undifferentiated lithology type.	205
Figure A - 17. Cumulative Distribution Functions (CDF) for Unconsolidated, undifferentiated lithology type with shape parameters and statistic information regarding the determined bias values: (a) Lognormal, (b) Normal, (c) Gamma, (d)Weibull. The Weibull distribution (d) provided was selected as the best fit for this Unconsolidated, undifferentiated lithology type..	206
Figure A - 18. Cumulative Distribution Functions (CDF) for Unconsolidated and Sedimentary, undifferentiated lithology type with shape parameters and statistic information regarding the determined bias values: (a) Lognormal, (b) Normal, (c) Gamma, (d)Weibull. The Normal distribution (b) provided was selected as the best fit for this Unconsolidated and Sedimentary, undifferentiated lithology type.....	207

LIST OF APPENDIX FIGURES (CONTINUED)

<u>Figure</u>	<u>Page</u>
Figure A - 19. Cumulative Distribution Functions (CDF) for General lithology type with shape parameters and statistic information regarding the determined bias values: (a) Lognormal, (b) Normal, (c) Gamma, (d)Weibull. The Normal distribution (b) provided was selected as the best fit for this General lithology type.....	208

LIST OF APPENDIX TABLES

<u>Table</u>	<u>Page</u>
Table A - 1. Site information for the twenty-four sites used in developing the regression model, <i>LOS21</i>	189

To my Mom

Who has always been my rock and encouraged me to attend OSU over 6 years ago. I
would not be who I am without your love, support, and guidance

Chapter 1: Introduction

1.1 Background

In the next 50 years, there is a 7 to 15% chance that a great (i.e., Magnitude 8.7 to 9.3) Cascadia Subduction Zone earthquake will occur along the entire segment of the fault (reference *Section 1.1.2*) (Goldfinger et al. 2003). Such a powerful earthquake is likely to cause significant disruptions to the electrical system (i.e., the Western Power Grid) along the west coast of the continental United States. Electrical power is essential for the continued functionality of emergency services, economic recovery, and other basic essential needs such as water and fuel supply, wastewater treatment, and communications. Understanding the extent of damage to the electrical system following a CSZ or other event is critical for system resilience. Hazard maps provide a well-suited tool to model the regional impacts from seismic hazards and evaluate corresponding and cascading failures anticipated for civil infrastructure. Hazard maps can be implemented with fragility curves specific to particular infrastructure components to model the probability of the component to reaching or exceed a specific damage state. Nevertheless, the estimation of the performance of the entire western power grid following a CSZ event is extremely challenging due in part to its vast size and the variation in topography and geology. No one method or tool has been previously developed to tackle this problem due to the interdisciplinary knowledge required to tackle the problem and the scale of the challenge.

1.1.1 Western Power Grid

The western power grid (i.e., the Western Interconnected System) is one of three transmission systems in the United States (WECC 2019). The system consists of much of North America west of the Rocky Mountains, spanning all or a portion of 14 states, the Canadian

provinces of British Columbia and Alberta, and the northern portion of Baja California in Mexico (WECC 2019). It spans more than 1.8 million square miles and serves over 80 million people (WECC 2019). The reliability and security of the Western Power Grid is overseen by the Western Electricity Coordinating Council (WECC) who performs compliance monitoring, enforcement, planning, and performance assessments. Their mission is to mitigate risks effectively and efficiently to ensure the reliability and security of the power system, including the systems' seismic resilience. The assessment of the regional seismic hazards and potential impacts to the grid forms the focus of this work and can inform decisions to make certain investments to the Western Power Grid to improve its resilience.

1.1.2 Cascadia Subduction Zone Earthquake

The Cascadia Subduction Zone (CSZ) is a 600-mile-long fault initiating 121 km off the west coast. The CSZ runs from Northern Vancouver Island in British Columbia to Cape Mendocino in California (Cascadia, 2013). The CSZ is formed by the subduction of the oceanic Juan de Fuca and Gorda Plates beneath the North American Plate (Goldfinger et al. 2012). These plates is located along the “ring of fire” (or Circum-Pacific Seismic Belt), the world’s greatest earthquake belt where 90% of earthquakes occur (OSSPAC 2013). Due to geophysical characteristics at the interface of these subducting plates along the North American Plate, the CSZ is categorized with one of the highest probabilities for a high-intensity megathrust (i.e., M 8.0 or greater) earthquake (OSSPAC 2013). The CSZ shares many common characteristics with subduction zones in southern Chile, southwestern Japan, and Colombia where comparable oceanic plates are also subducting (Heaton and Hartzell 1987).

The CSZ has produced powerful (magnitude 8 to 9⁺) earthquakes at least 40 times over the last 10,000 years (Goldfinger et al. 2012) and therefore presents a regularly occurring hazard

to the Pacific Northwest. Although it is difficult to predict the intensity of an earthquake, the region is known for having seismic events that are comparable to the M9.1 2011 Tohoku Earthquake or the M9.1 2004 Indonesian Earthquake. Paleoseismic records suggest that there is a strong likelihood that the rupture of the northern (7 to 12% chance) or southern (37 to 42%) margins of the Cascadia Subduction Zone will occur in the next 50 years (Goldfinger et al. 2003). This mix of topography, climate, geology, and seismicity make Pacific Northwest (PNW) a zone of great instability with significant potential to threaten civil infrastructure and those who depend on that infrastructure.

1.2 Project Description & Research Objectives

This research is a part of a boarder National Science Foundation (NSF) project, titled: *Earthquake Resilience of the Western Power Grid*, with the primary goal of estimating the expected initial load losses and load recovery times caused by a major CSZ event through the development of a framework to identify the extent, distribution, and duration of the western electrical grid damage. The extent of damage should correspond to the earthquakes ground motion intensity and associated seismic hazards (e.g., co-seismic landslide-induced damage). The main purpose of this thesis is to quantify of the likelihood of seismically-induced landslides and the corresponding probability of exceeding certain thresholds of ground displacement on electrical transmission poles and towers at a regional scale. This work will help inform the understanding of the vulnerabilities of a synthetic model of the western power grid to seismic shaking and landslides towards supporting the larger study.

This thesis develops a probabilistic method for a regional seismic landslide hazard analysis and a corresponding map for the Western United States based on the USGS M9.3 Megathrust CSZ scenario earthquake (USGS 2017) in consideration of topographic, geologic,

and other geospatial information. The landslide triggering analysis completed uses several empirical seismic displacement prediction models based on the Newmark sliding block method, which are calibrated using strength parameters for each geological unit based on the terrain slope at locations of previously mapped landslides within the unit. A predictive displacement regression model, *LOS21* was developed using a logic tree scheme that weights the individual models based on the suitability of the model to this regional assessment. The *LOS21* model was used to calculate the probability of exceedance of specific thresholds (e.g., 5%, 15% and 50%) to evaluate potential impacts to the power grid.

To provide context to the broader study focusing on non-landslide-induced impacts to the western power grid (e.g., ground shaking and inertial equipment loading), an evaluation site was characterized for a detailed site-specific site response analysis to evaluate the differences in amplification between equivalent linear and nonlinear, total stress analyses using ten ground motions pairs scaled and matched to the USGS seismic scenario hazard. The results of the site-specific site response analysis are then used to evaluate the potential impact to the electrical components for the substation at the evaluation site for comparison to the seismic hazard developed using the regional map.

1.3 Thesis Organization

This thesis is comprised of six chapters and two appendices, which describe the problem statement in more detail. The thesis is organized in the following manner:

- Chapter 2 presents a literature review providing necessary background information on the main overarching topics: seismic hazards, hazard mapping, fragility curves, and site response analysis;

- Chapter 3 presents a methodology for developing a probabilistic regional seismic landslide hazard analysis and map;
- Chapter 4 presents the results for the developed probabilistic regional seismic landslide hazard map in Chapter 3 and results from using the map to assess the vulnerabilities of the electrical network;
- Chapter 5 presents the methodology and results of site response analyses conducted for an evaluation site home to an electrical substation, which are used for comparison to the mapped seismic hazard for the CSZ scenario earthquake and corresponding differences in the vulnerabilities of selected electrical equipment at the site; and,
- Chapter 6 provides a summary of the work completed in this thesis, conclusions drawn from Chapters 3 to 5, and suggestions for future work.

This thesis concludes with a list of references cited and several appendices containing supplemental tables and figures supporting the findings made in each chapter.

Chapter 2: Literature Review

The literature review focuses on landslides and liquefaction. It is laid out in the following manner initially focusing on relevant background information: (1) relevance of the Cascadia Subduction Zone event to the Western Power Grid (WPG) system (Section 2.1) and (2) background information regarding seismic hazards (Section 2.2) (e.g., seismic wave types, important ground motions parameters and importance of site response analysis). It then focuses on basic information regarding co-seismically induced landslides (Section 2.2.4) and liquefaction (Section 2.2.5) (e.g., sub-hazard types, failure mechanics, common evaluation methods and consequences of the hazard). The development of co-seismic hazard maps (Section 2.3) (i.e., landslide and liquefaction maps) is then discussed in detail, followed by a discussion of the infrastructure and vulnerabilities of WPG system (Section 2.4) and fragility curves used to evaluate electrical systems (Section 2.5).

2.1 Relevance of CSZ to Western Power Grid System

Large earthquakes resulting from the Cascadia Subduction Zone (CSZ) will have a major impact on critical lifelines such as the WPG affecting service in the Pacific Northwest and beyond. In addition to damages from intense seismic shaking, widespread liquefaction and landsliding will likely occur throughout the coast range and as well as inland throughout the Willamette Valley and Cascades. Given these anticipated impacts, the Oregon Resilience Plan estimates that the recovery of the electrical system could take anywhere from 1 to 6 months depending on the distance to the fault rupture zone (OSSPAC 2013).

Damages and losses extend well beyond the direct impact to the utility providers but also adversely affect communities. Electrical power is essential for the continued functionality of

emergency services, economy, and other essential lifelines (e.g., water and fuel supply, wastewater treatment, communications). Thus, the rapid restoration of electric power is vital to the recovery and continued health of an earthquake-stricken region (FEMA 2012). Electric utilities have investigated how to improve their system reliability to seismic events to limit damages to proactively address these impending hazards. In order to effectively use the limited resources available, regional modeling of the hazards and impacts on infrastructure are needed to determine priorities for mitigations. Prior assessments of the electrical systems have been primarily based on expert opinion combined with simplified models (i.e., synthetic electric grids models) for the seismic hazard (Birchfield et al. 2017). Through the development of more rigorous seismic hazard maps and power models that incorporate damage and failure information (e.g., failure rates), a more complete and more reliable picture of damages and their impacts can help identify the most vulnerable and critical infrastructure. To this end, this literature review documents the state of the practice and/or art in seismic hazard assessment, hazard mapping, infrastructure vulnerability assessment, and fragility curves.

2.2 Seismic Hazards

Earthquakes are complicated events that can result in multiple hazards beyond strong ground shaking and surface rupture. For example, they can trigger additional hazards such as landslides, liquefaction, tsunami, flooding, and fires. The degree of damage caused by an earthquake is strongly influenced by the dynamic response and characteristics of the soil deposits on which structures reside (Kramer 1996). The first step in understanding how to analyze these seismic hazards is through understanding seismic waves and how to interpret ground motions for a specific site.

2.2.1 Types of Seismic Waves

Earthquakes produce two main basic types of waves: body and surface waves. Each of which move through materials differently. Body waves, such as P- and S-waves, move through the interior of the earth and arrive at sites before the more erratic surface waves. P-waves can pass through all types of media (i.e., solids, liquids, and gases) and are the first to reach a site after an earthquake because they travel the fastest. Unlike P-waves, S-waves travel slower and can only travel through a solid medium (e.g., rock, soil) (Wilson 1942). Topography can also influence the magnitude of seismic waves. The amplification of body waves on mountain tops is systematically greater for incident S-waves than for P-waves, which generally tends to decrease as the average slope decreases or as the angle of incidence increases (Bard 1982).

Surface waves are lower in frequency and larger in amplitude than body waves. They consist of two types: Love and Rayleigh waves. Love waves are the fastest surface wave and moves the ground from side -to-side (horizontal motions). In contrast, Rayleigh waves roll along the ground and moves the ground up and down and side-to-side in the same direction that the wave propagates. Most of the waves one feels during an earthquake is from surface waves. Surface waves travel along the earth's surface and cause the more ground movements since they travel slower (i.e., longer to pass), therefore the potentially for the most damage (Kramer 1996).

The propagation of the seismic waves depends substantially on geological conditions (e.g., soil layering, water table level). Shallow sediments or soils can increase the amplification and resonance as seismic waves propagate from the rock base to the surface (Bard and Bouchon 1985). Seismic waves travel faster through hard rock than softer rock or sediment. When waves pass through shallow and softer deposits, they slowdown, which causes them to amplify as the energy from the waves build up (Borcherdt 1970).

2.2.2 Ground Motions

Ground motions are commonly presented as a time history (i.e., acceleration-time history) of seismic activity. When earthquakes occur, seismic waves radiate away from the source and travel through the earth's crust. When the waves reach the ground surface, shaking can last anywhere from seconds to minutes (Keefer 1984). The intensity and duration of the shaking depends on the size and location of the earthquake as well as local site characteristics such as the geologic soil profile and topography which can amplify or dampen the waves. In some analyses, it can be an advantage to work with simplified measures from the time history rather than the detailed time history. Quantitative parameters typically used to quantify the strength of the ground shaking include measurements of acceleration, frequency content, velocity, and duration. Examples of common measures include:

- *Peak Ground Acceleration (PGA)*: the largest absolute (peak) acceleration recorded/measured in a ground motion time history,
- *Peak Ground Velocity (PGV)*: the largest velocity recorded/measured in a ground motion time history,
- *Spectral Acceleration (Sa)*: the maximum acceleration measured on an object with given period during shaking,
- *Equivalent number of cycles (N_{eq})*: the number of stress cycles of ground shaking estimated for an earthquake scenario,
- *Earthquake Magnitude (M)*: a measure of energy released from the earthquake event, the maximum trace amplitude recorded on seismometers (Different scales can be used for magnitude. Moment magnitude is more commonly used nowadays as the Richter scale is not as reliable as it saturates for larger earthquakes ($M < 5$)(Bath 1981).
- *Arias Intensity (I_a)*: a parameter that represents the amplitude, frequency content and duration characteristics of the ground motion, strength of the ground shaking. Value can be using the following equation:

$$I_a = \frac{\pi}{2g} \int_0^{t_f} a(t) dt$$

(Eq. 2-1)

where $a(t)$ is the corresponding acceleration time history, g is gravity and t_f is the total duration of the ground motion.

Another important ground motion measure to understand is the *frequency content* of the seismic wave. Fourier transforms are used to show the frequency content in a time history and identify which frequencies dominate the wave. The frequency content is displayed using spectra.

A spectrum is a curve showing the amplitude and phase as a function of frequency or period for a given earthquake. There are three main ground motion spectra that can be used to characterize strong ground motions: Fourier Amplitude, Power, and Response Spectra. Table 2-1 discusses the three ground spectra extensively used in earthquake engineering practice and the capabilities of the spectra.

Table 2-1. Description of ground motion spectra used in earthquake engineering practice and the associated capabilities.

Spectrum Type	Description	Capabilities	References
<i>Fourier</i>	A plot of Fourier amplitude verse frequency that shows how the amplitude of the motion is distributed with respect to frequency (or period). Spectra may be narrow or broad.	When spectra of actual earthquake motions are smoothed and plotted on logarithmic scales, used to see characteristic shapes more easily. A broad spectrum corresponds to a motion that contains a variety of frequencies that produce a more jagged, irregular time history. A narrow spectrum implies that the motion has a dominant frequency, produce a smooth, almost sinusoidal time history.	(Kramer 1996; Scanlan and Sachs 1974)
<i>Power</i>	Describes the distribution of power into frequency components composing that signal. Obtained from the autocorrelation function of the Fast Fourier transform (FFT).	Used to estimate the statistical properties of a ground motion and to compute stochastic response using random vibration techniques, useful in characterizing the earthquake as a random process	(Clough and Penzien 1975; Vanmarcke 1976; Yang 1986)
<i>Response</i>	Describes the maximum response of a single-degree-of-freedom (SDOF) system to a particular input motion as a function of frequency content (i.e., natural period) and damping ratio of the SDOF system. The spectrum does not describe the actual ground motion but provides valuable additional information on its potential effects on structures based on existing conditions.	Used to indicate the peak spectral acceleration, velocity, and displacement values are associated with different frequencies (or periods).	(Kramer 1996; Scanlan and Sachs 1974)

2.2.3 Site Response Analysis

Site response analyses are conducted to estimate how seismic shear waves propagate to the ground through the subsurface from the bedrock, particularly to identify changes in amplitude or frequency content as a result of its transmission through layers in the soil profile (Seed and Idriss 1982). A key product of the analysis is a response spectrum, which can be used to determine the earthquake-induced forces transmitted from the soil (i.e., bedrock) to a structure.

A key part of a site response analysis is having realistic ground motions responses. Empirical methods based on the characteristics of recorded earthquakes (i.e. amplitude, frequency content, duration, magnitude) have been used to develop predictive relationships of expected bedrock motions characteristics at a site (Kramer 1996). The attenuation relationship for estimating the expected site PGA is a function of the moment magnitude and the hypo-central distance. The accuracy of the predictive relationship is dependent on the range in characteristics (e.g., tectonic regime type, hypo-central distance, magnitude) used in a probabilistic seismic hazard assessment (PSHA) (Cornell 1968; Algermissen et al. 1982).

Once realistic ground motions have been determined, a site response analysis method must be selected. One-dimensional site response analysis methods are widely used to assess the effects of soil conditions due to ground shaking. These methods can be divided into two main categories: (1) frequency-domain analyses (e.g., equivalent linear method), and (2) time-domain analyses (e.g., nonlinear analyses) (Phillips and Hashash 2009).

Equivalent linear (EL) analysis is one of the first widely used approaches used to model soil nonlinearity. Common software used to conduct this form of analysis include SHAKE and DEEPSOIL (Hashash et al. 2020a; Schnabel et al. 1972). In the equivalent linear approach, linear analyses are performed with soil properties (e.g., shear modulus) that is iteratively adjusted to coincide with the effective level of shear strain induced in the soil.

A Non-linear (NL) analysis is not as commonly used in practice because it requires significant effort and care in the development of needed input parameters (e.g., model parameters, viscous damping, and profile discretization). This method considers the changes in the soil properties at each time step and thus can better capture the soil behavior under large strains that a site with soft soil and strong ground motions might experience (Kim et al. 2016).

Stewart et al. (2008) compared the results of EL and NL analyses performed by Silva et al. (2000), and noted that there is good agreement between the two approaches over most of the frequency range from 0.1 Hz to 100 Hz for stiff soils subject to weak motions with $PGA < 0.4 g$. However, for larger shaking levels ($PGA \geq 0.4 g$), NL responses were larger than EL responses for frequencies higher than 10 Hz. Differences between EL and NL become more pronounced for soft soils.

2.2.4 Seismically induced landslides

A landslide is defined as the downward and outward movement of slope-forming materials composed of natural rocks, soils, artificial fills, and combination of these materials (Varnes 1958). Landslides are complex and can be caused by many different triggers such as earthquakes, intense rainfall or rapid erosion from a water source (e.g., streams, rivers). These triggers generate landsliding by increasing the loading or pore pressures within the soil mass, by removing stabilizing support at the toe, or by reducing the strength of the soil material. Studies suggest the lithology, topographic slope, seismic intensity, topographic amplification of ground motion, fracture systems in the underlying bedrock, groundwater conditions all play a role in inducing landslides (Nowicki et al. 2014). The distribution of pre-existing landslides also have some impact on the landslide distribution (Keefer 2002).

Earthquake-induced landslides have proven to be a damaging and costly hazard through loss of life and damage to transportation infrastructure or utility lifelines. Bird and Bommer found that 46% of the 50 earthquakes occurring between 1989-2003 resulting in co-seismic landslides causing major damage directing or indirectly to communities (Bird and Bommer 2004). As an example, during the 1994 Northridge earthquakes in Los Angeles, the loss of the Santa Monica

freeway from a major landslide resulted in an estimated direct and indirect loss of \$20 billion US dollars (Bird and Bommer 2004).

2.2.4.1 Landslide Types

Earth slides, debris flows, rockfalls, and mudflows are all types of landslides (The National Research Council, 1996). More formally, landslides are generally categorized into five main types (Cruden and Varnes 1996): Falls, topples, slides, spreads and flows. Any combination of the landslide types is referred to as a complex slide (Cruden and Varnes 1996). These classifications are based on characteristics of the material, water content, and movement rate. Table 2-2 provides general information regarding the five main landslide types including material type, water content and Figure 2-1 provides an illustration of the different types of landslides discussed in Table 2-2.

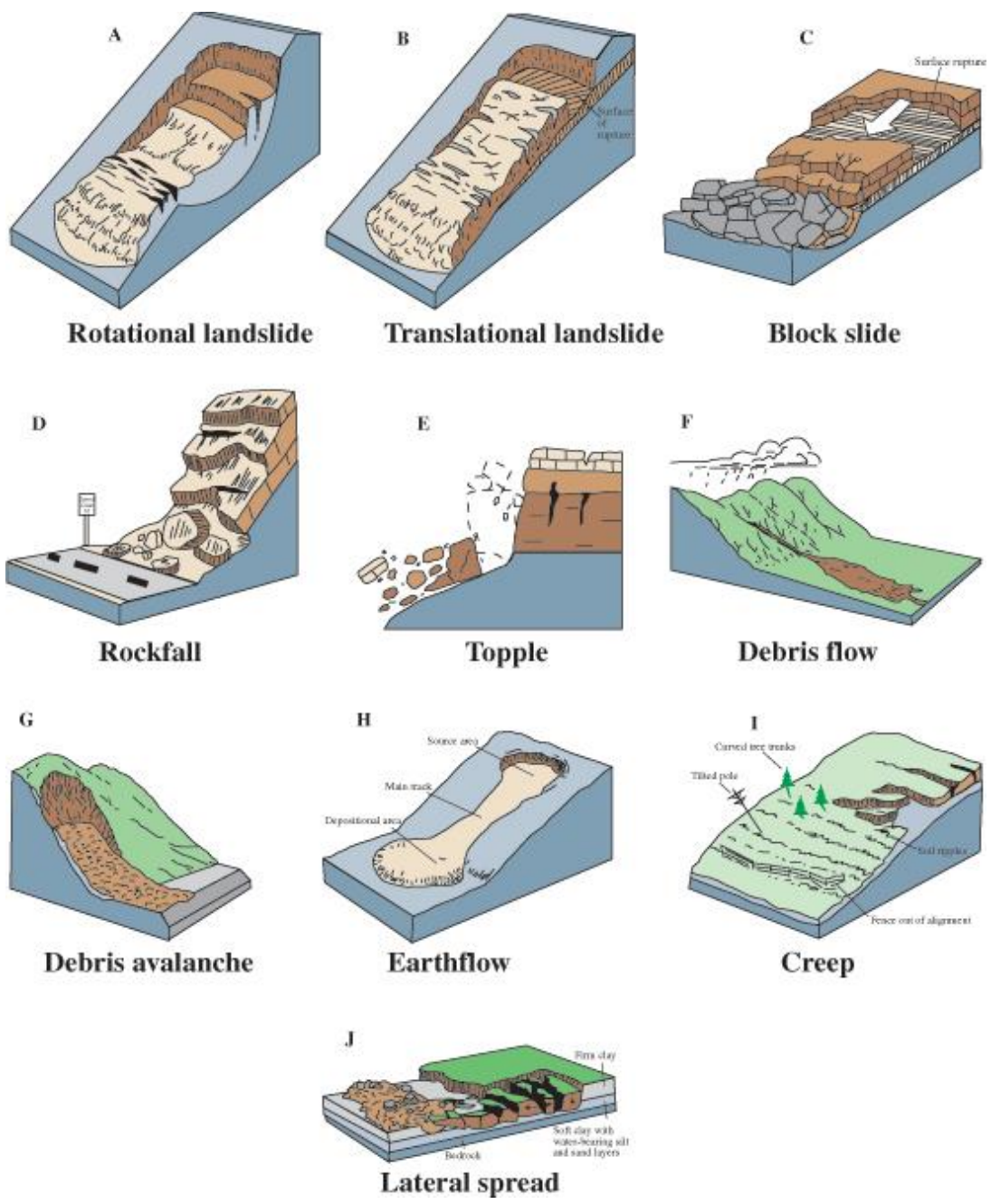


Figure 2-1. Illustration of various landslide types (Highland and Bobrowsky 2008)

Table 2-2. Summary of Landslide Movement Types (modified from Cruden and Varnes 1996)

<u>Movement Type</u>	<u>Material</u>	<u>Water Content</u>	<u>Rate</u>	<u>Examples:</u> <i>*Reference Figure 2-1</i>
Fall	Soil or Rock	Dry or Moist	Extremely Rapid	Rock & Debris fall, Avalanches
Topple	Soil or Rock	Moist	Extremely slow to Extremely Rapid	Flexural, Block, Chevron & Block-flexure topple
Slides	Soil (Earth)	Wet	Rapid	Rotational, Translational, Block, Compound slides
Spreads	Soil (Debris)	Very Wet	Moderate	Lateral, Block, Liquefaction, spread
Flow	---	---	Slow to Moderate	Debris, Earth, Slump-earth, Creep
Complex Slides	---	---	Extremely slow to Extremely Rapid	Combination of landslides

Co-seismic landslides can be categorized as: disrupted slides and falls, coherent slides, and lateral spreads and flows (Keefer 1984). Table 2-3 summarizes the various earthquake-induced landslide movement types and other parameters regarding the type of movement: material type, failure mode, rate of movement, and damage level. Earthquake-induced landslides occur at various magnitudes, historical evidence shows that predominant threats to life are from rock avalanches, rapid soil flows, and rock falls (Keefer 1984).

Table 2-3. Summary of Seismically Triggered Landslide Movement Types (Kramer 1996)

<u>Movement Type</u>	<u>Material</u>	<u>Failure Mode</u>	<u>Rate/Damage</u>	<u>Example:</u>
Disrupted Slides & Falls	Sheared, broken and disturb particles (Rock & soils)	Steep terrains	Extremely Rapid/Devastating damage	Rock falls, rockslides, rock avalanches, soil falls, soil slides, and soil avalanche
Coherent Slides	Soil or Rock	Moderate to steep sloping terrains	Slow (low velocities)/ Devastating damage	Rock and soil sumps, rock and block slides, and slow earth flows
Lateral Spreads	Liquefiable soils	Remarkably flat slopes	Very Rapid to Extremely Rapid (very high velocities)/ Devastating damage	Soil liquefaction

2.2.4.2 Slope Stability Basics

Slope failures at a specific site are highly complex and difficult to assess because many factors influence the stability of slopes, including: geologic and hydrologic conditions, topography, climate, weathering, and land use (Varnes 1958). In a static slope stability analysis, slides occur when the driving forces exceed resisting forces such that masses of earth displace upon the rupture surfaces or the surfaces experiencing high magnitudes of shear strain.

Slides can be broken into two groups geometrically: rotationally and translationally. Rotational slides have curve failure surfaces and generally reach greater depths. Translational slides displace along the planar surfaces (i.e., over the original ground surface) and are generally shallower in nature. The upper extent of rotational and some translational slides are defined by the steep face of undisturbed soil known as the scarp. The lower portion is generally composed of displaced and disturbed material known as deposit. Under very specific conditions (e.g., saturated fine soils) slide deposits can transition to flow movements (Cruden and Varnes 1996).

These slides are evaluated using slope stability analysis methods such as limit equilibrium analysis. Limit equilibrium analysis considers the force and/or moment equilibrium of the soil mass with respect to a failure surface. It is commonly expressed in terms of an index, factor of safety (FS), given by:

$$FS = \frac{\text{Available Shear Strength}}{\text{Shear stress required to maintain equilibrium}} \quad (\text{Eq. 2-2})$$

Another slope stability analysis method is a pseudo-static approach which represents earthquake forces with constant horizontal and/or vertical accelerations. The pseudo-static Sliding Block analysis developed by Newmark (1965) is commonly used in seismic slope stability analyses. The model assumes that a rigid block is placed on an inclined plane and when the shaking acceleration (a_{max}) of the block is greater than the critical acceleration, a_y (*critical*

yield acceleration) of the block, it will start to slide downward along the shearing surface. The sliding subsides once the relative velocity between the block and ground is zero. The *yield acceleration*, a_y value represents the shearing resistance at the interface of the block and inclined plane and is dependent on the slope characteristics (e.g., cohesion, c , and friction, ϕ , angle), site conditions (e.g., groundwater table level, soil layering) and the failure surface (e.g., ground surface, slide surface, soil layering). a_y is compared to the *PGA* (referred to as a_{max}) to determine if a slope failure is initiated. Similar to limit equilibrium analyses, the Newmark method also uses an index of stability (Factor of Safety) to evaluate the serviceability of the slope.

2.2.4.3 Empirical displacement prediction equations

Since the amount of deformation controls the serviceability of a slope and adjacent infrastructure after an earthquake, landslide displacements provide a better indicator of failure and potential damage than the simple limit equilibrium analysis (i.e. Factor of Safety) (Kramer 1996). Newmark's rigid sliding block analogy (Newmark 1965) was one of the first approaches to predict the displacement of a slope when subjected to shaking. The magnitude of permanent displacement is estimated by integrating twice with respect to time over the parts of an earthquake acceleration-time history above the critical yield point (Figure 2-2b). Figure 2-2 illustrates the Newmark Sliding Block Analysis through (a) a free body diagram of the model, (b) how to use an acceleration time history to determine the magnitude of permanent displacement and (c) the equations and variables associated with the model.

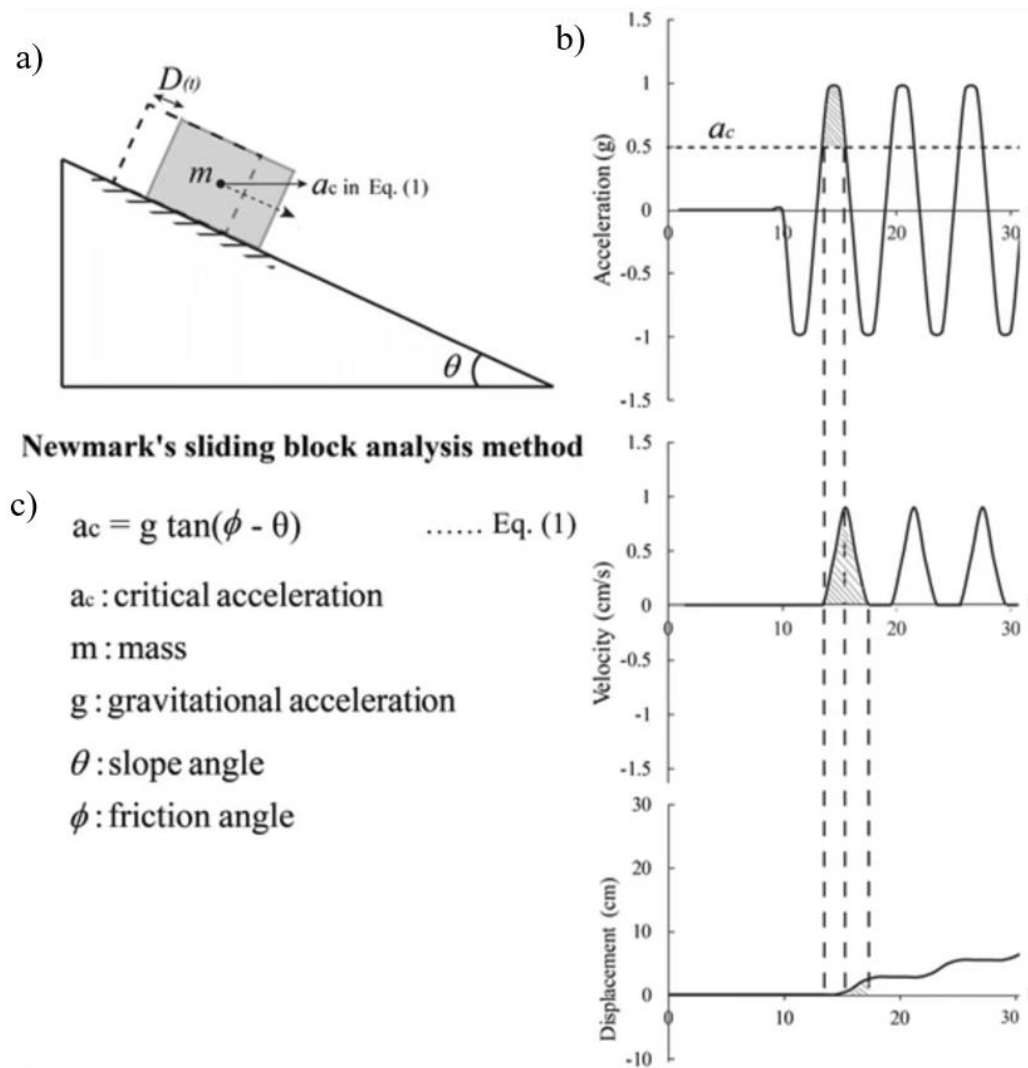


Figure 2-2. Illustration of the Newmark's sliding block analysis (a) diagram, (b) acceleration–time history double integrated to determine displacement, (c) considered variables and equation used in analysis (Li et al. 2018).

Newer methods have been developed to model seismic slope displacement including, a simplified rigid-block, decoupled and coupled methods, as well as more complex models. Many models use empirical equations derived through multivariate regression to empirically estimate the displacement from a co-seismic landslide (Table 2-4) by calibrating the measures described in Section 2.2.2. to case history data. In addition to those measures, additional parameters are used in the regression such as the *predominant period of sliding mass* (T), which is defined as the period associated with the highest Fourier amplitude spectrum. These empirical models can also

be utilized in a probabilistic manner to calculate the likelihood of exceeding a threshold displacement (e.g., Jibson (2007) and Bray and Travasarou (2007)). Table 2-4 summarizes empirical predictive models for earthquake-induced sliding displacement of slopes with necessary input parameters and limitations for use in a regional analysis in a CSZ event.

Table 2-4. Examples of empirical predictive models for earthquake-induced sliding displacement of slopes with necessary input parameters and limitations for use in a regional analysis in a CSZ event (modified from Sharifi-Mood et al. 2017) (Note: □ - optional variance of models).

Method	Year	a_y	PGA	I_a	M	T	S_a	N_{eq}	PGV	Limitations
Makdisi and Seed	(1978)	•	•		•	•				T, challenging to acquire or estimate
Ambraseys and Menu	(1988)	•	•							Derived from 6.6 -7.3 M earthquakes, $a_y/PGA < 0.05$ generates large displacements
Yegian et al.	(1991)	•	•			•		•		T and N_{eq} , challenging to acquire or estimate
Jibson	(1993)	•	•	•						Requires I_a , challenging to acquire or estimate
Jibson (Scalar, Vector A & B)	(2007)	•	•	□	□					Applied for 5.3 -7.6 M earthquakes, extrema of the range of a_y/PGA is equal to 0 or 1. I_a , challenging to acquire or estimate
Bray and Travasarou	(2007)	•	•							Requires T and S_a , challenging to acquire or estimate, Design for earth dams, natural slopes & earthfall, $D_L < 1$ cm equal to 0. Assumes $T \leq 0.05s$ is equal to 0
Saygili and Rathje (Scalar & Vector)	(2008)	•	•	□		□			□	Derived from 5.0 -8.4 M earthquakes. If $a_y/PGA \leq 1$, D_L is 0; underpredicts displacements for larger M earthquakes. designed better for slopes ($a_y \geq 0.1$) when using PGV & PGA
Rathje and Saygili (Scalar)	(2011)	•	•		•					Derived from 5.0 -8.4 M earthquakes, overpredicts displacement when compared to vector model (Saygili & Rathje 2008)
Hsieh and Lee	(2013)	•	•	•						Requires I_a , challenging to acquire or estimate
Rathje et al.	(2014)	•	•		•	•			•	Requires T and mean period of earthquake motion, challenging to acquire or estimate
Du and Wang	(2014)	•	•	•					•	Requires I_a , challenging to acquire or estimate
Lee and Green	(2015)	•	•		•				•	Requires more detailed subsurface information (geotechnical surface characteristics)
Song and Rodrigues-Marek	(2015)	•	•	•		•	•		•	Requires I_a , T and S_a , challenging to acquire or estimate
Fotopoulou and Pitalakis	(2015)	•	•	□	□				□	Limited due to site assumptions (Clay Layer-Elastic Bedrock) and derived from 5.0-7.6 M, I_a , challenging to acquire or estimate

Rodriguez-Marek and Song	(2016)	•			•	•	•		•	Requires T and S _a , challenging to acquire or estimate
Song et al.	(2016)	•	•						•	Derived from Saygili & Rathje 2008, developed for pulse like motions
Song et al.	(2017)	•	•		•				•	Requires detailed directional (degrees) information regarding strike
Du W.	(2018)	•	•	•					•	Requires I _a , challenging to acquire or estimate
Du et al.	(2018)	•	•			•	•			Requires T and S _a , challenging to acquire or estimate
Song et al.	(2018a)	•	•	•	•				•	Requires I _a , challenging to acquire or estimate
Song et al.	(2018b)	•	•	•	•				•	Requires I _a , challenging to acquire or estimate
Bray, Macedo and Travararou	(2018)	•	•		□	□	□			T and S _a , challenging to acquire or estimate, Assumes T = 0, used specifically for Subduction Zone Earthquakes
Bray and Macedo	(2019)	•	•		•	•			•	Uses T, challenging to acquire or estimate
Cho Young	(2020)	□	□	□	□	□	□		□	Derived from Fotopoulou and Pitilakis (2015) assumed clay slopes, compared to shallow crustal motions

2.2.5 Liquefaction

The term liquefaction historically refers to a variety of phenomena that involves “soil deformations caused by a repeated disturbance on saturated cohesionless soils under undrained conditions” (Mogami and Kubo 1953). Soil liquefaction occurs when saturated-to-partially saturated soils lose shear resistance during cyclic loads generated by earthquakes. Cohesionless soils such as sands and silty sands that are saturated, loosely deposited, and poorly cemented are the most susceptible to liquefaction. When large stresses are rapidly or repetitively applied to saturated soils, excess pore pressure builds up because the soil does not have sufficient time to dissipate the pressure. As the loosely deposited soil particles attempt to reach a denser state, additional pore pressure builds up. These undrained conditions result in a decrease of the effective stress of the soil, therefore lowering the overall shear resistance in the soil and causing it to behave like a liquid (Seed and Idriss 1971). The potential for liquefaction increases when the initial shear stresses is higher because less work is needed for the soil to liquefy (Seed and Idriss 1971).

Liquefaction can be classified as flow liquefaction and cyclic mobility:

1. Flow liquefaction occurs when the shear stress required for static equilibrium (static shear stress) is greater than the shear strength of the soil in its liquefied state. The deformations produced by flow liquefaction are driven by static shear stresses. This failure method is characterized by its sudden, speedy and the magnitude in which the liquefied material is displaced (Kramer 1996).
2. Cyclic mobility occurs when the static shear stress is lower than the shear strength of the liquefied soil. The deformations produced by cyclic mobility failures develop

incrementally during earthquake shaking (cyclic loading) and is driven by both cyclic and static shear stresses (Kramer 1996).

The intensity of ground shaking and the duration of the shaking also has an effect on liquefaction triggering. An increase in the duration of ground shaking extends the liquefaction period, therefore possibly resulting in greater deformations. Dense sands will eventually generate enough pore pressure to trigger liquefaction under sufficient ground shaking (i.e., intensity and duration). Under intense shaking, loose sands will liquefy quicker due to their lower shear resistance (Seed and Idriss 1971).

2.2.5.1 Liquefaction Susceptibility

The occurrence of liquefaction is dependent on many factors: earthquake magnitude, duration, peak ground motion, depth of ground water table and liquefaction susceptibility of sediments; therefore, it is hard to predict. Liquefaction susceptibility can be determined by using several criteria types: historical, geologic, compositional, and state (Kramer 1996). Table 2-5 discusses the various liquefaction susceptibility criteria and the applications.

Table 2-5. Liquefaction susceptibility based on several criteria and the applications.

Condition Type	Description	Applications	References
<i>Historical</i>	Observations of the past earthquakes provide a ton of information on liquefaction behavior and has shown that liquefaction often reoccurs at the same location if soil and groundwater conditions remain unchanged between events	Used in identifying sites and general site conditions that may be susceptible to liquefaction in future earthquakes, thus useful in the development of liquefaction susceptibility maps.	(Youd 1984, 1991)
<i>Geological</i>	Process that created the soil deposit influences the liquefaction susceptibility of the soil. Soil deposits that are susceptible to liquefaction fall within a narrow range of geological environments and is dependent on the depositional environment, hydrological environment, and age of the soil deposit	Fluvial, colluvial and aeolian deposits when saturated are the most susceptible to liquefaction. Older soil deposits generally have a lower susceptibility to liquefaction than newer deposits and the susceptibility decreases when the depth of ground water table is greater than a few meters.	(Youd 1991; Youd and Hoose 1977)
<i>Compositional</i>	Characteristics like particle size, shape, and gradation, influences the volume change behavior that make soils susceptible to liquefaction	Well-graded soils are generally less susceptible than poorly graded soils due to the smaller void space between the particles resulting in a smaller volume change potential in drained conditions, therefore lower excess pore pressure under undrained conditions. Rounded particles are known to densify easier than angular soil particles. Field research indicates that most liquefaction failures occur in uniformly graded soils and typically not expected in gravels due to the highly hydraulic conductivity which enables dissipation of pore pressures nearly as quickly as it is generated.	(Kramer 1996; Seed and Idriss 1971; Youd and Perkins 1987)
<i>State "Site Conditions"</i>	Considers the soil type (age, composition), site hydrological conditions (i.e., ground water table, saturation level), intensity of ground shaking and the duration of the shaking	Cohesionless sediments composed of Holocene age or younger located below the ground water table is most susceptible to liquefaction. Also occur in unsaturated soils if the pore pressures (i.e., air and water) reaches its initial effective stress level. The rate at which excess pore pressure is generated through shearing is dependent on the relative density of the soil. When loose sands are sheared, it contracts which generates positive excess pore pressure and effective stresses decreases. Dense sand will initially contract under shearing, but will eventually dilate, therefore generating negative excess pore pressure and increasing the effective stress.	(Bolton 1986; Kramer 1996; Youd and Perkins 1987)

2.2.5.2 Liquefaction Evaluation Methods

Liquefaction evaluation procedures (e.g., semi-empirical liquefaction correlations based on standard penetration test (SPT) or cone penetration test (CPT) data) are recommended for coarse-controlled soils. If a soil is determined to be fines-controlled, then the use of a combination of Boulanger and Idriss (2006) and Bray and Sancio (2006) is suggested. Fines-controlled soils with moderate to high cyclic softening potential should be evaluated using cyclic laboratory tests. If the soil falls within the transition region, the soil may need to be tested using both liquefaction and cyclic softening evaluation techniques (Armstrong and Malvick 2016).

Plastic, insensitive soils (e.g., clays) are not susceptible to liquefaction because in the absence of confining stress, they will not sustain a complete loss of shear strength. Instead these soils are susceptible to cyclic softening which occurs when pore pressures induced by cyclic loading cause strength loss in soils (Chu et al. 2008). Sensitive, plastic soil (Plastic Index (PI) >18) may undergo severe strength loss because of earthquake induced strain. According to Bray and Sancio (2006), all soils can experience large deformations if cyclic stresses exceed the dynamic strength of the soil.

In reality, soils are composed of particles ranging in size and gradation as well gradation (plastic and non-plastic particles). There are a variety of methods that have develop to evaluate the liquefaction susceptibility based on plasticity. Table 2-6 discusses various liquefaction susceptibility models and the associated criterion parameters.

Table 2-6. List of liquefaction susceptibility models and the associated criterion parameters

Reference	Criterion Potential	Criterion Values
"Chinese Criteria" (Wang 1979)	(1) there are less than 15% "clay" fines (based on the Chinese definition of "clay" sizes as less than 0.005 mm), (2) there is a Liquid Limit of $LL \leq 35\%$, and (3) there is a current in-situ water content greater than or equal to 90% of the LL	LL and w_c/LL ratio
Andrews and Martin (2000)	(1) that soils with less than about 10% clay fines (< 0.002 mm), and a Liquid Limit (LL) in the minus #40 sieve fraction of less than 32%, be considered potentially liquefiable, (2) that soils with more than about 10% clay fines and $LL \geq 32\%$ are unlikely to be susceptible to classic cyclically-induced liquefaction, and (3) that soils intermediate between these criteria should be sampled and tested to assess whether or not they are potentially liquefiable	LL
Seed et al. (2003)	Soils in Zone A are considered potentially susceptible to "classic" cyclically induced liquefaction when the $FC \geq 20\%$ if $PI > 12\%$ and if $w_c > 0.8(LL)$. Soils in Zone B may be liquefiable $20\% < FC \leq 35\%$ if $PI > 12\%$ and if $w_c > 0.8(LL)$, however more testing is required to determine if the soil will liquefy. Soils that fall outside of Zone A or B are not susceptible to "classic" cyclic loading but should be checked for potential liquefaction.	FC , PI , and w_c/LL ratio
Boulanger and Idriss (2006)	$PI \geq 7$ can be expected to exhibit clay-like behavior, PI criteria is reduced for soils that fall within the CL-ML range to $PI \geq 5$ to exhibit clay-like behavior.	PI and LL
Bray and Sancio (2006)	Loose soils with $PI < 12$ and $w_c/LL > 0.85$ were susceptible to liquefaction, and loose soils with $12 < PI < 18$ and $w_c/LL > 0.8$ were systematically more resistant to liquefaction. Soils with $PI > 18$ tested at low effective confining stresses were not susceptible to liquefaction	PI and w_c/LL ratio
Armstrong and Malvick (2016)	(1) if $FC \leq 20$ & $PI \leq 7$ or $PI \leq 7$, Liquefaction evaluation, (2) if $20 < FC \leq 50$ & $PI > 7$ Liquefaction and cyclic softening evaluation, (3) if $FC > 50$ and $PI > 7$, Cyclic softening evaluation	FC and PI

One model in Table 2-6 is of particular interest: Armstrong and Malvick. The Armstrong and Malvick model (2016) drew from the criteria discussed in Table 2-6 (i.e., Boulanger and Idriss 2006; Bray and Sancio 2006; Seed et al. 2003) to develop their own procedure for determining the susceptibility of fine-grained soils. This method suggests evaluation methods to determine liquefaction susceptibility rather than stating whether a soil is susceptible or not.

Figure 2-3 displays Armstrong and Malvick criterion in a graphical formation, depending on the PI and FC values, specific evaluation techniques are suggested.

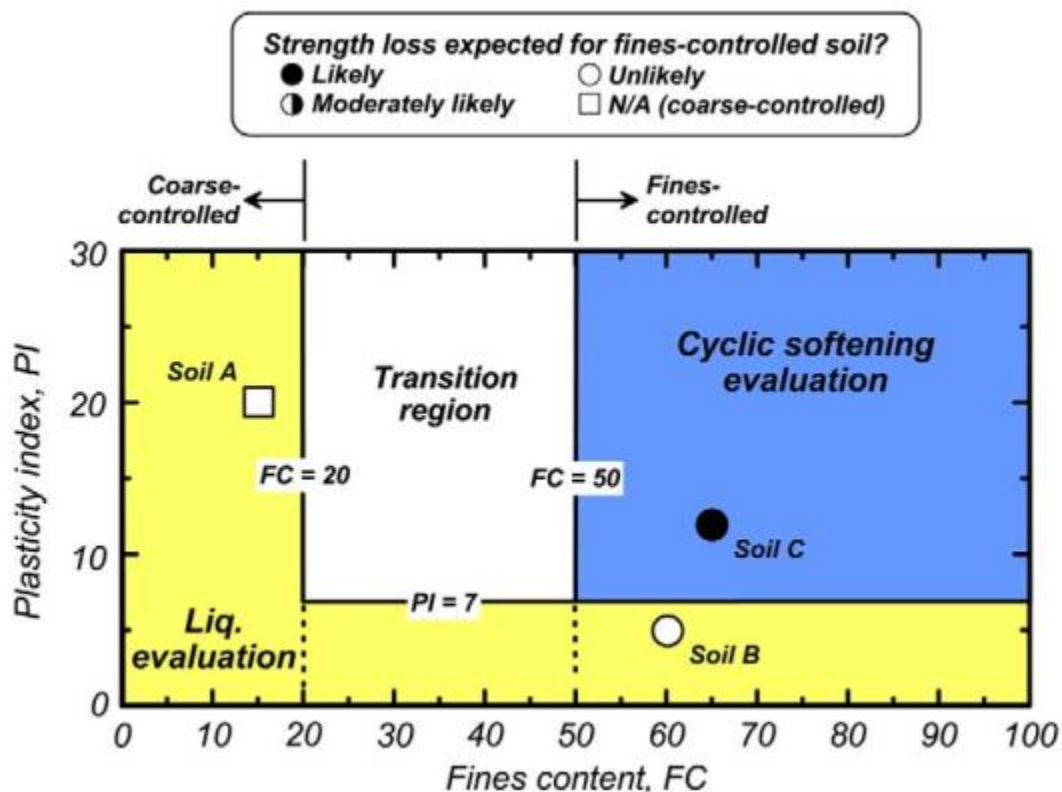


Figure 2-3. Criteria for susceptibility of fine-grained soils (From Armstrong and Malvick 2016)

2.2.6 Liquefaction Triggering

Even if a soil is susceptible to liquefaction, it does not mean it will liquefy or result in surface deformation. A widely common method known as the simplified stress-based procedure

is used in practice to predict liquefaction triggering (Whitman 1971; Seed et al. 1985; Seed and Idriss 1971). The method relies on a comparison of load and capacity of the soil which is expressed in terms of cyclic stress ratio (CSR) and cyclic resistance ratio (CRR). The cyclic stress ratio can be calculated using the following equation (Seed and Idriss 1971), given by:

$$CSR = 0.65 * \frac{\sigma_{vo}}{\sigma'_{vo}} * \frac{a_{max}}{g} * r_d \quad (\text{Eq. 2-3})$$

where σ_{vo} is total vertical stress; σ'_{vo} is vertical effective stress; a_{max} is the peak horizontal ground acceleration; g is gravitational acceleration; and r_d is the shear stress participation factor (accounts for the flexibility of soil under dynamic loading). The equation for r_d was first introduced by Seed and Idriss (1971) and only accounted for shear stress reduction with depth. Therefore, Idriss (1999) developed a single equation for r_d which accounts for the earthquake magnitude in addition to the depth parameter, given by:

$$r_d = \exp[\alpha(z) + \beta(z) * M] \quad (\text{Eq. 2-4})$$

$$*\alpha(z) = -1.012 - 1.126 * \sin\left(\frac{z}{11.73} + 5.133\right) \quad (\text{Eq. 2-5})$$

$$*\beta(z) = 0.106 + 0.118 * \sin\left(\frac{z}{11.73} + 5.142\right) \quad (\text{Eq. 2-6})$$

where z is depth in meters; and M is earthquake magnitude.

CRR depends on the relative density of the soil. Relationships for CRR have been developed which consists using the Standard Penetration Test (SPT) based blow count (N), the Cone Penetration Test (CPT) based cone tip resistance (q_c) and shear wave velocity (V_s) of liquefiable soils (Youd and Idriss 2001). It is assumed that the first two penetration test-based methods used for calculating the CRR is a clean sand equivalent and a corrected penetration resistance (i.e. accounts for procedural and overburden stress effects). These corrections must be applied before the CRR is calculated and is done so through being applied to N through the SPT correction (Idriss and Boulanger 2010), given by:

$$(N_1)_{60} = C_N C_E C_B C_R C_S N \quad (\text{Eq. 2-7})$$

where C_N is an overburden correction factor, $C_E = ER_m/60\%$, ER_m is the measured value of the delivered energy as a percentage of the theoretical free-fall hammer energy, C_R is a rod correction factor to account for energy ratios being smaller with shorter rod lengths, C_B is a correction factor for nonstandard borehole diameters, C_S is a correction factor for using split spoons with room for liners but with the liners absent, and N is the measured SPT blow count.

Procedural and overburden stress corrections for q_c (Boulanger and Idriss 2014) are given by:

$$q_t = qc + (1 - a_r) * u_2 \quad (\text{Eq. 2-8})$$

$$q_{c1N} = C_N \left(\frac{q_t}{P_a} \right) \quad (\text{Eq. 2-9})$$

where q_t is corrected cone tip resistance; a_r is cone tip area ratio (typical values range between 0.65 and 0.85); u_2 is measured pore pressure; q_{c1N} is cone tip resistance corrected for overburden stress; and P_a is atmospheric pressure.

Overburden pressure correction factor and clean sand equivalent penetration resistance are calculated via iteration of the stress exponent, m (Boulanger and Idriss 2014) given by:

$$C_N = \left(\frac{P_a}{\sigma'_v} \right)^m \leq 1.7 \quad (\text{Eq. 2-10})$$

$$m = 0.784 - 0.0768\sqrt{(N_1)_{60cs}} \quad (\text{Eq. 2-11})$$

$$m = 1.338 - 0.249(q_{c1Ncs})^{0.264} \quad (\text{Eq. 2-12})$$

where $(N_1)_{60cs}$ is clean sand equivalent corrected blow count and q_{c1Ncs} is clean sand equivalent corrected cone penetration with q_{c1Ncs} limited to values between 21 and 254 and $(N_1)_{60cs}$ values limited to values ≤ 46 for use in these expressions.

Eq. (10) and Eq. (11) for SPT and CPT respectively are used to calculate the cyclic resistance ratio (Idriss and Boulanger 2008; Boulanger and Idriss 2016), given by:

$$CRR_{M=7.5, \sigma'_v=1atm} = \exp \left(\frac{(N_1)_{60cs}}{14.1} + \left(\frac{(N_1)_{60cs}}{126} \right)^2 - \left(\frac{(N_1)_{60cs}}{23.6} \right)^3 + \left(\frac{(N_1)_{60cs}}{25.4} \right)^4 - 2.8 \right) \quad (\text{Eq. 2-13})$$

$$CRR_{M=7.5, \sigma'_v=1atm} = \exp \left(\frac{q_{C1Ncs}}{113} + \left(\frac{q_{C1Ncs}}{1000} \right)^2 - \left(\frac{q_{C1Ncs}}{140} \right)^3 + \left(\frac{q_{C1Ncs}}{137} \right)^4 - C_o \right) \quad (\text{Eq. 2-14})$$

where $(N_1)_{60cs}$ is the clean and corrected equivalent blow count, q_{C1Ncs} is the clean corrected sand equivalent cone penetration and C_o is a fitting parameter with a mean of 2.6 and the standard deviation of 0.2 (Boulanger and Idriss, 2016). Note that the CRR equations are derived from using case history data that are standardized to a reference overburden stress of 1 atm and earthquake magnitude of 7.5 (Idriss and Boulanger 2008; Boulanger and Idriss 2016).

Because liquefaction resistance increases with increasing confining pressure, an overburden stress correction (K_σ) must be applied to the CRR equation in order for it to be used over a wide range of overburden stresses that may be encountered in the field (Youd et al. 2001). The following equations are used to calculate K_σ (Boulanger and Idriss (2014; 2015, respectively) given by:

$$K_\sigma = 1 - C_\sigma \ln \left(\frac{\sigma'_v}{p_a} \right) \leq 1.1 \quad (\text{Eq. 2-15})$$

$$C_\sigma = \frac{1}{37.3 - 8.27(q_{c1Ncs})^{0.264}} \leq 0.3 \quad (\text{Eq. 2-16})$$

$$C_\sigma = \frac{1}{18.9 - 2.55\sqrt{(N_1)_{60cs}}} \leq 0.3 \quad (\text{Eq. 2-17})$$

Considerations regarding how the earthquake magnitude and its effects on liquefaction resistance are applied through the magnitude scaling factor (MSF). The MSF is used to adjust the CRR equations to earthquake magnitudes that differ from the 7.5 magnitude earthquake used in developing the original CRR equations (Boulanger and Idriss 2014; 2015), given by:

$$MSF = 1 + (MSF_{max} - 1) \left(8.64 \exp \left(\frac{-M}{4} \right) - 1.325 \right) \quad (\text{Eq. 2-18})$$

$$MSF_{max} = 1.09 + \left(\frac{(N_1)_{60cs}}{31.5}\right)^2 \leq 2.2 \quad (\text{Eq. 2-19})$$

$$MSF_{max} = 1.09 + \left(\frac{q_{c1Ncs}}{31.5}\right)^3 \leq 2.2 \quad (\text{Eq. 2-20})$$

The MSF equation (Boulanger and Idriss 2014; 2015) is derived from compilation of laboratory test data and analyses of ground motion recordings. The standardized CRR has the MSF and overburden correction factor applied (Boulanger and Idriss 2014), given by:

$$CRR = CRR_{M=7.5, \sigma'_v=1atm} * MSF * K_\sigma \quad (\text{Eq. 2-21})$$

In addition to the SPT and CPT methods for determining CRR, there are other in-situ tests that may be used. The Becker Penetration Test (BPT) developed by Youd et al. (2001) is suggested for gravelly soils that are not well defined through the SPT and not appropriate for exploration through the CPT. Due to a lack of liquefaction sites investigated using the BPT and standardization of the BPT, a BPT-based method have not been developed. Instead, the BPT data can be correlated to an equivalent SPT N-values (e.g., Sy and Campanella 1994; Ghafghazi et al. 2017). The SPT-based method can then be followed to determine the CRR using the equivalent SPT N-values (Youd et al. 2001).

Another method developed by Kayen et al. (2013) considers using the shear-wave velocity (V_s), which can be obtained through downhole, cross-hole, or non-destructive surface wave techniques. The relationship is based on normalized shear wave velocity (V_{s1}), as follows:

$$V_{s1} = V_s \left(\frac{P_a}{\sigma'_v}\right)^{0.25} \quad (\text{Eq. 2-22})$$

It is suggested the V_s based triggering method be used for soils that have “unusual” characteristics (e.g. aging and/or bonding) (Robertson 2015).

2.2.7 Consequences of Liquefaction

Depending on the surface loads, site geometry and extent (depth, thickness) of the liquefiable layer, liquefaction can lead to several forms of ground failure such as settlement and lateral spreading.

Liquefaction-induced ground settlements are caused by the densification and compaction of granular soils which leads to vertical deformations of the surficial soil layers (Youd 1993). On flat ground, blocks of mostly intact surficial soil above a liquefied layer may collide and jostle during ground shaking, opening cracks at the ground surface or causing settlements. Several methods (e.g., numerical, analytical and empirical.) have been proposed to calculate liquefaction-induced ground settlements.

Lateral spreading occurs when a liquefied soil flows downslope, specifically in proximity to an abrupt change in topography (i.e., “free faces”). It commonly occurs in slopes adjacent to bodies of water and often results in displacements (meter) that encompasses large areas. Lateral spreads tend to move slowly (Youd 1993). It has the potential to inflict the greatest amount of damage during an earthquake (McCulloch and Bonilla 1970). Lateral spreading also occurs on gentle slopes (typically less than 6%) (Youd 1993), the blocks of mostly intact, surficial soil above the liquefied layer of soil may slowly displace down slope or towards a free-face (Rauch 1997). Current methods for determining liquefaction potential and subsequent lateral spreading displacements is highly empirical. These methods are typically derived empirically by studying earthquake case histories. The following models (i.e., Bartlett and Youd 1992; Gillins and Bartlett 2014; Youd et al. 1999, 2002) contain the main procedures used to predict the magnitude of displacement.

2.3 Hazard Mapping

Seismic hazard maps visually and spatially convey the relative hazard across an area, and are of great significance for land-use planning, mitigation, and emergency response (USGS 2016). These maps consider the location of faults, past earthquakes, behavior of seismic waves in various mediums, and near-surface site conditions for regions of interest (e.g., slope, soil type).

2.3.1 Overview of Available Seismic Hazard Mapping Methods

Common types of seismic hazard (e.g., landslide, liquefaction) mapping techniques are available to investigate seismic threats qualitatively or quantitatively across a regional scale, such as:

1. *Inventory Maps* document and report locations where hazards historically have occurred from field evidence or interpretation of digital elevation models (e.g., lidar) or high-resolution photographic imagery
2. *Susceptibility Maps* identify susceptible terrain based on physical characteristics of the soil/site (e.g. slope, shear strength) where slopes or soil are likely to experience ground failure from a trigger (e.g., rainfall or seismic activity)
3. *Potential Maps* considers the likelihood of external impacts and triggering source (e.g. seismic activity such as a CSZ earthquake)

2.3.2 Deterministic and Probabilistic Methodologies

Methodologies for developing susceptibility and potential maps can generally be classified into two categories: deterministic and probabilistic. Deterministic methodologies can produce reliable results but require comprehensive datasets with detailed input information (e.g., geological data, slope stability models,) depending on the intended purpose. Probabilistic hazard

mapping methodologies incorporate the uncertainty associated with geotechnical, geological, and geomorphological data through computing the probability of occurrence of a hazard.

Seismic probabilistic models take numerous variables into consideration such as acceleration, strength parameters, and distance and magnitude values. And the geological maps can be developed and derived from geotechnical parameter determined through laboratory tests. Through determining the impact of ground motion parameters in slope failures and the slope displacement parameters corresponding to existing geometrical and seismic properties, a probabilistic hazard map can be developed.

2.3.3 Landslides

A hazard has been defined as the probability of occurrence within a certain time period, which is a function of both spatial and temporal probabilities influenced by static environmental factors slope and dynamic factors such as ground shaking (Van Westen et al. 2006). In regional mapping, slope values can be produced from a Digital Elevation Model (DEM). For landslide mapping, effects of weathering are less significant on a regional scale due to the variability in subsurface data (Corominas et al. 2014). In a deterministic analysis, information for each point (e.g., failure surface depth, strength parameters, limiting equilibrium slope stability) are essential in the evaluation, however due to the difficulty to obtain that information on large scales, it leads to lower credibility in the spatial variability (Jibson 2007).

In a GIS framework, the use of both a ground shaking attenuation model (i.e., pseudo-static slope stability analysis) and the Newmark's displacement method are common approaches employed in several deterministic models when conducting an earthquake-induced landslide assessment. Although deterministic methodologies are most commonly used in hazard mapping, the method does not incorporate the uncertainty associated with geotechnical, geological, and

geomorphological data. Probabilistic methodologies incorporate all those uncertainties as well as the uncertainty associated with the advanced procedures used in developing the probabilistic hazard map. Rathje et. al. (2014) compared deterministic and probabilistic approaches in landslide hazard analysis and found that the deterministic approach commonly used in practice excessively underestimates the landslide displacement due to the variability in the movement mechanism of the sliding mass. Table 2-7 summarizes deterministic and probabilistic co-seismic landslide mapping models in a GIS framework and the associated model limitations.

Jibson et al. (2000) develop a fully probabilistic model and used DEMs, geological maps, and engineering properties of geological units to analyze seismically-triggered landslides. They introduced a dynamic model based on Newmark's analysis to calculate the landslide displacement of each pixel a similar approach to the approached presented. Saygili and Rathje (2008) developed a similar approach to the approached presented to identify regions with high seismically-induced landslide hazard. But their approach only considers two threshold scenarios: (1) 2% in 50 years and (2) 10% in 50 years and is fully probabilistic, rather than a full performance-based design approach and partially probabilistic approach used in this study. This probabilistic approach accounts for the variability in the displacement prediction but does not account for the epistemic uncertainties associated with various components of the analysis.

Monte Carlo simulations have been used to account for the uncertainties in seismic landslide studies (e.g., Refice and Capolongo 2002), however they require a large number of simulations which is difficult for large regional studies. Logic trees been used to efficiently account for epistemic uncertainties and become a standard in practice for accounting for epistemic uncertainty in probabilistic seismic hazard analyses for ground shaking (e.g., Bommer and Scherbaum 2008; Wang and Rathje 2015). Logic trees identify different values of input

parameters or different alternative models with specific weights assigned to each value /model based on the relative belief in their accuracy. Even though the values and weights assigned to a logic tree are somewhat subjective, they acknowledge and account for the other possible parameter values/models.

A more recent probabilistic landslide hazard analysis was developed by Sharifi-Mood et al. (2017) which this approach was derived from. However, their approach developed histograms as a function of lithology type based on parameters like slope, aspect and vegetation index to determine the landslide probability for a smaller region for all possible earth, rather than directly developing landslide distribution curves based on landslide inventories as presented.

Table 2-7. Examples of deterministic and probabilistic co-seismic landslide mapping models in a GIS framework and the associated limitations

Framework	Model	Description/Developments	Limitations
GIS: Deterministic	Jibson (1993)	On regional scale, suggested that Newmark's method could effectively be applied to capture permanent ground deformation using two different methods: (1) by performing two sequential integrations of the area under the accelerogram record and the block's velocity time period that exceeds the critical acceleration and velocity values respectively, or (2) by deriving a regression equation from the ground motion to determine displacement.	Method 2: displacement at a particular location may not be calculated accurately with a mean displacement curve, therefore local site responses are not accounted for in this analysis
	Khazai and Sitar (2000)	Integrated three factors to analyze seismic slope stability: (1) an attenuation relationship, natural attenuation of ground shaking with respect to the distance from the source; (2) a pseudo-static slope stability analysis, inertial effects of the earthquake represented as horizontal and vertical forces; and (3) Newmark's Displacement Method (Newmark 1965), seismically induced deformation calculations	Does not capture overall performance of any particular slope, ground-shaking attenuation models have to be selected very carefully, since they are specific to the type of earthquake and associated fault movement. Only develops the mean estimate of the potential ground displacement in failing slopes and site-specific response
	Lee et. al (2008)	Introduced a new parameter, Landslide Susceptibility Index (LSI), which develops a LSI value for each pixel using a summation of considered factors weighed linearly.	Requires extensive site parameters, may be applicable only to the small region where the model was trained
GIS: Probabilistic	Refice and Capolongo (2002)	Developed a simplified Newmark's slope stability model that used a Monte Carlo technique to simulate samples to develop probability density functions (PDF). Newmark's equations, PDFs and statical parameters of interested variables were used to generate the probabilistic map	Accounts for the variability in the displacement prediction but does not account for the epistemic uncertainties associated with various components of the analysis
	Del Gaudio et al (2003)	First proposed a fully probabilistic landslide hazard analysis which included developing full seismic hazard curves	Limited for locations of recurrence and diffusion of earthquake-induced landslides

2.3.4 Liquefaction & Lateral Spreading

The horizontal movement in soils above a liquified subsurface layer is called a lateral spread and usually develops on gently sloping grounds or in the vicinity of free-face (e.g., river channels, canals or abrupt topographical depression (Youd et al. 2001). Lateral spreads have historically resulted in excessive damage to communities by rupturing utilities lines and destroying foundations.

Geotechnical engineers typically evaluate liquefaction and lateral spread hazards analytically or empirically using site specific properties and techniques. Early liquefaction hazard mappings techniques were primarily qualitative and largely based on the liquefaction susceptibility correlations with mapped surficial geology, however, lacked sufficient subsurface information (e.g. Youd and Hoose 1977; Youd and Perkins 1987). Later liquefaction potential mapping techniques began considering regional seismic loading levels (e.g. Anderson et al. 1982; Baise et al. 2006). Researchers have also quantified this hazard through using different metrics like liquefaction potential index (LPI) (e.g. Iwasaki et al. 1982; Luna and Frost 1998; Holzer et al. 2007; Cramer et al. 2008) , liquefaction risk index (LRI) (e.g. Lee et al. 2004; Sonmez et al. 2005) or liquefaction severity index (LSI) (e.g. Youd and Perkins 1987).

Liquefaction hazard metrics (e.g., LPI, LSI and LRI) are useful in mapping the liquefaction triggering hazards across large regions but have been shown to correlate poorly with observed seismically induced lateral spreads because it does not consider relevant factors such as topography and continuous spatial data. Other lateral spread displacement hazard maps investigations have used mapped surface geology or empirical displacement prediction models in the mapping procedure. Table 2-8 summarizes Liquefaction/Lateral Spreading Mapping Models in various frameworks.

Table 2-8. Summary of liquefaction/lateral spreading mapping models categorized in various frameworks

Framework	Model
Liquefaction hazard metrics	(Youd and Perkins 1987; Baise et al. 2002; Holzer et al. 2003; Baise et al. 2006; Holzer et al. 2006; Gillins 2014; Maurer et al. 2014; Rashidian and Gillins 2018)
Surface Geology	(Youd and Perkins 1987; Gillins 2014; Zhu et al. 2016)
Empirical	(Mabey and Madin 1993; Olsen et al. 2007; Holzer 2008; Cramer et al. 2008; Oommen et al. 2010; Gillins 2012; Jaimes et al. 2015; Liu et al. 2016; Rashidian and Gillins 2018)

These displacement hazard maps (i.e., Jaimes et al. 2015; Mabey and Madin 1993; Olsen et al. 2007; Rashidian and Gillins 2018) were determined using a single earthquake scenario developed through either a deterministic or probabilistic seismic hazard analysis at a single return period. However, these maps are limited since they do not consider seismic loading from multiple seismic sources or return periods and does not account for variation in ground motion amplification from site response effects (i.e. Bazzurro and Cornell 2004; Stewart et al. 2014). To address some of those limitations, Erickson (2006) developed a procedure to create a fully probabilistic lateral spread hazard prediction map using available seismic, geotechnical, geological and topographical data (e.g., lidar data), which accounted for the uncertainties associated with the datasets. Maps were created to show the displacements associated with two return periods (i.e., 1033 and 2475 years).



2.4 Infrastructure and Vulnerabilities of Western Power Grid System




The electric system consists of three main components: generation, high-voltage transmission, and distribution. Generation refers to the power plant that generates the electricity such as wind, hydroelectric, nuclear or coal. Electricity is transmitted through a grid system of electrical substations and transformers which is then distributed to the consumer through

powerlines. There are several types of substations: transmission, distribution, collector, converter substations.

The substations in the WPG performs various functions such as protection, voltage regulation and switching, power factor correction and relaying and monitoring. A typical electrical substation is composed of transformers, circuit breakers, relaying and monitoring apparatuses, disconnect switches and primary power lines. Each of these components are vital and represent a possible failure point in the event of seismic activity. Table 2-9 provides a description of the various components within a substation and the associated vulnerabilities due to seismic loading.

Table 2-9. Vulnerabilities of the different components within a substation (visuals, unit description and vulnerabilities)

<u>Item</u>	<u>Description</u>	<u>Image of item</u> <i>*images obtained from Kempner Jr. (n.d.)</i>	<u>Vulnerability</u> <i>*obtained from Omidvar et al. (2017)</i>
Circuit Breaker	Interrupts the flows of current when fault conditions occur and usually is connected to the relaying apparatus for monitoring and communication purposes. <i>*Alternative option that performs same function as circuit switcher</i>		Displacement of the porcelain insulator, insufficient conductor slack, (due to limited base isolation and supplemental damping system). Insufficient framing support and anchoring. If out of phase (displaced ajar) with the rest of grid, will cause it to explode.
Disconnect Switch	Physically isolates a line or component for repair or inspection, but not designed to respond to fault conditions.		Damage of the switch, damage to circuit breaker. Insufficient framing support. For limitation of main components, see respective sections.

<p>Relaying and Monitoring Apparatus</p>	<p>A combination of current transformers, potential transformers, sensors, control systems and communication devices that track any abnormalities or fluctuations in substation operation.</p>		<p>Inflexibility of the components being monitored.</p> <p>For limitation of main component, see respective sections.</p>
<p>Transformer</p>	<p>Regulates the voltage going in and out of the system, allowing for a transfer between transmission and distribution lines at different voltage levels.</p>		<p>Inflexibility of bushing support, top plate of tank and bottom of cast aluminum flange.</p> <p>Insufficient framing support.</p> <p>Insufficient anchoring can lead to slippage and overturning of transformer unit.</p>
<p>Control Building/Enclosure</p>	<p>Structure that houses all the complex electrical and computerized components. Isolated from the active substation lines and the interface point for the substation as a whole.</p>		<p>Low structural standards of design</p>

2.5 Fragility Curves

A fragility function is a common analysis tool used to indicate the probability of failure of a component, element, or system (Porter et al. 2012) from a seismic event. A fragility curve is typically represented as a 2-dimensional plot that shows the probability distribution for specific damage states of a component as a function of a seismic energetic input (e.g., PGA). Figure 2.4 shows an example of a fragility curve for a 57kV substation site displaying the probability of failure for select components within the station.

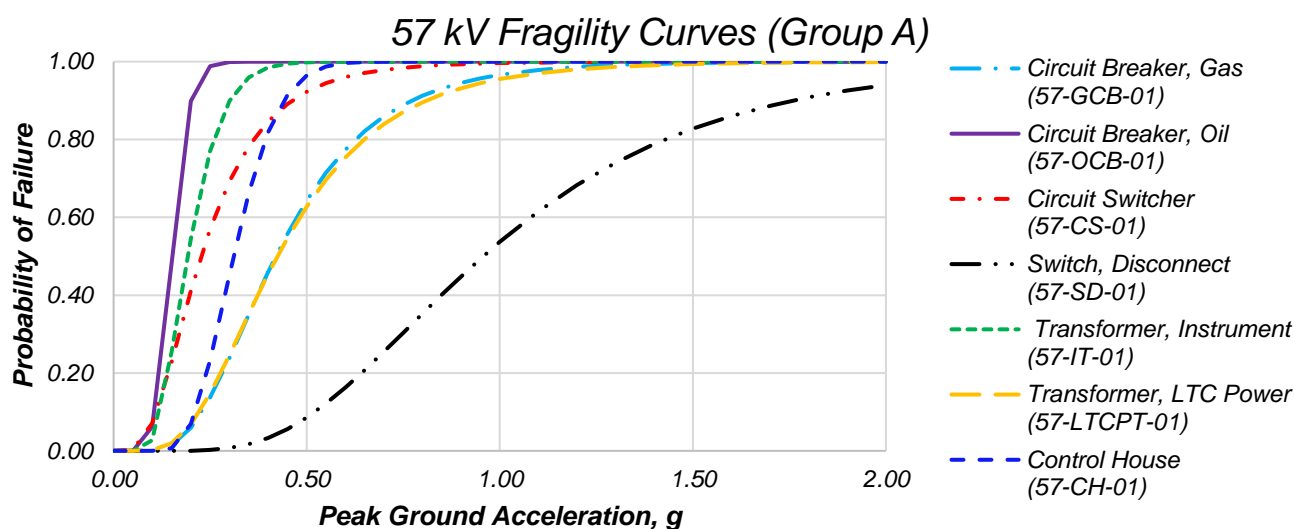


Figure 2-4. Fragility Curves for a 57kV Substation (Obtained from SEFT Report (SEFT 2018))

Fragility curves can be characterized using multiple approaches: (i) empirically by utilizing statistical representations and analyzing large databases of failure; (ii) expertly through judgement; (iii) experimentally by applying forces at different intensity levels on an element; (iv) analytically by extensive simulation of an element's performance under different simulated shocks with different intensity levels; and (v) using a combination of the approaches (Panteli et al. 2017). Several fragility curve databases are available and will be described in this section.

2.5.1 SEFT

Portland General Electric (PGE) commissioned SEFT Consulting to identify crucial failures in PGE owned substations in the greater Portland area (SEFT 2018). SEFT developed fragility curves (Table 2-10) for three transmission voltage levels (57 kV, 115 kV, and 230 kV). These fragility curves do not consider the interaction of adjacent asset/structure combinations connected with rigid bus or conductors without adequate slack. Table 2-10 displays a complete list of the components gathered from the SEFT report based on voltage level.

Table 2-10. List of the components with fragility curves available for different voltage levels in SEFT (2018)

57 kV	115 kV	230kV
Circuit Breaker (gas & oil)	Circuit Breaker (gas & oil)	Circuit Breaker (gas & oil)
Circuit Switchers	Circuit Switchers	-
Switch, Disconnect	Switch, Disconnect	Switch, Disconnect
Transformer, Instrument	Transformer, Instrument	Transformer, Instrument
Transformers, LTC Power	Transformers, LTC Power	Transformers, LTC Power (2 systems)
-	Transformers, Non-LTC Power	-
Control House	Control House	Control House

2.5.2 CLiP database

A recent Cascadia Lifelines Program (CLiP) research project developed a database of fragility functions relevant to Oregon lifelines and hazards (Alam et al. 2020). This database was compiled through summarizing appropriate fragility functions from existing and past efforts, identifying available and missing fragility functions suitable for Oregon lifelines, evaluating the quality of existing fragility functions and their relevance to Oregon's geology and seismic characteristics. The database integrates several public databases such as HAZUS, IN-CORE, and SYNER-G. and other extensive fragility function research studies. The database contains 163 fragility curves that focus on the electrical power system including 85 for substations, 41 for

power generation plants, 9 transformers, 9 for macro-components, and 11 for micro-components. All fragility functions were developed using *PGA*, *PGD* and *Sa* (Spectral Acceleration) as the intensity measurement.

2.5.2.1 HAZUS

HAZUS is a geographic information systems-based natural hazard analysis tool developed by the Federal Emergency Management Agency (FEMA 2012). The HAZUS Earthquake Model Technical Manual provides fragility functions for lifeline infrastructure systems such as electrical power systems. The fragility functions for electrical power system components are modeled with lognormal distributed functions (FEMA 2012). Table 2-11 presents the fragility function attributes for power generation plants, substations, and distribution circuits, respectively.

Table 2-11. HAZUS: Electrical power generation plants and substation fragility function attributes

Infrastructure	Description	Intensity Measurement	Damage States
Generation plant (anchored or unanchored components)	Small (capacity < 200 MW) or medium/large (capacity ≥ 200 MW) subcomponents (anchored or unanchored)	PGA (g)	(5) None, slight, moderate, severe, and complete.
Substation (anchored or unanchored)	Low voltage (34.5 - 150 kV), Medium voltage (150 kV -350 kV), and High voltage (350 kV & up)	PGA (g)	(5) None, slight, moderate, severe, and complete.
Substation Components	Includes disconnect switches, circuit breakers, high voltage switches and lightning arrestors (anchored or unanchored)	PGA (g)	(5) None, slight, moderate, severe, and complete.
Transmission and Distribution Circuits	Includes Poles, wires, above ground and underground conductors and these components (anchored or unanchored)	PGA (g)	(5) None, slight, moderate, severe, and complete.

Their analysis of the electrical grid views each generator, substation and distribution network as a node and designates each node at various states of failure. The damage state is calculated based on a tally of failed components as a percentage of all present components. Switches, circuit breakers and transformers are the three major areas examined in a substation. If 5% of the circuit breakers fail, the entire substation is considered slightly damaged. If the sum of any of the components failure rates is below this threshold rate, it will register identically to an undamaged substation. Threshold damage states for moderate, severe, and complete damage are 40%, 70% and 100% respectively (FEMA 2012).

2.5.2.2 IN-CORE database

The Interdependent Network Community Resilience Modeling Environmental (IN-CORE) is a modeling platform for running scientific analyses to model the impact of natural hazards on the resilience of the community (Gardoni et al. 2018). The IN-CORE platform is currently under development by the National Institute of Standard and Technology (NIST).

Table 2-12 summarizes the IN-CORE fragility curves for electrical power systems and their attributes (i.e., intensity measurement and damage states)(Gardoni et al. 2018).

Table 2-12. IN-CORE: Fragility function for different components of the electric power grid system

Infrastructure	Description	Fragility Curves	Intensity Measurement	Damage States
Power Generation plant	For boilers and pressure vessels, small to medium horizontal vessels, large horizontal vessels, motor-driven pumps, turbine, small generation facility with unanchored and anchored components, and medium/large generation facility with unanchored and anchored components	23	PGA, PGD, Sa	(4) Slight, moderate, extensive, complete, loss of function
Substation (anchored or unanchored)	For Bus structure (flexible/rigid), cable trays, CCVT, control panels, dead tank circuit breaker (standard/seismic), disconnect switch (flexible bus/rigid bus), distribution circuits (standard component/seismic component), HVAC ducting, HVAC equipment, lightning arrester, large hydraulic and air actuated valves, live tank circuit breaker (standard/seismic), switchgear, and wave trap (cantilever/suspended)	79	PGA, PGD, Sa	(4) Slight, moderate, extensive, complete, loss of function
Transformer	For Unanchored and anchored components and gasketed or flanged transformers	11	PGA	(1) Loss of function
Transmission and Distribution	For transmission towers and distribution poles for tornado hazards as a function of wind speed	4	Wind Speed	(1) Loss of function

2.5.2.3 SYNER-G database

SYNER-G was a collaborative research project funded by the European Commission with the objective to develop an integrated methodology for the systematic seismic vulnerability and risk analysis of buildings, transportation systems, utility networks, and critical facilities considering the interactions between different components and systems. The SYNER-G database was developed as a by-product of this effort and contains forty-nine seismic fragility functions for the electric power system. Table 2-13 summarizes the SYNER-G fragility curves for electrical power systems and their attributes (i.e., intensity measurement and damage states).

Table 2-13. SYNER-G: Electric power systems fragility function attributes

Infrastructure	References	Fragility Curves	Intensity Measurement	Damage States
Power Generation plant	(FEMA 2010)	4	PGA	(4) Slight, moderate, extensive, complete
Substation (anchored or unanchored)	(Dueñas-Osorio et al. 2007; FEMA 2010; Hwang and Huo 1998)	11	PGA	(4) Slight, moderate, extensive, complete
Transformer			PGA	(1) Failure
Circuit Breaker	(Straub and Der Kiureghian 2008)	9	PGA	(1) Failure
Power Grid	(Dueñas-Osorio et al. 2007)	1	PGA	20% connectivity, 50% connectivity, 80%
Macro-Components	(Vanzi 1996)	4	PGA	(1) Failure
Mirco-Components	(Vanzi 2000)	11	PGA	(1) Failure

2.6 Summary

Earthquakes are complex natural disasters that can have major impacts on different lifelines such as the electrical system. Seismic hazards maps are common tools to estimate and communicate the damage anticipated from a seismic event. Existing seismic hazard mapping methods can generally be categorized into two groups: broad regional maps develop using simplified assumptions and detailed localized site maps over a small area. Assessments at a localized scale require detailed site-specific evaluations and analyses, which are cost-prohibitive to apply across a regional scale.

The WPG is a complex network spanning multiple states and jurisdictions; therefore, the types, quality, and formatting of readily available datasets vary significantly, presenting challenges in producing consistent hazard maps. Although methods such as those developed in Sharifi-Mood et al (2017) have been applied to a large portion of a state, such landslide mapping procedures have rarely been applied to specifically evaluate the seismic hazard potential of an area the size of the WPG.

In a seismic hazard evaluation, a site response analysis is extremely common. Site specific evaluations requires detailed site information and consists of predicting the expected ground surface motions. There are many geotechnical earthquake engineering models used for conducting site specific analyses. The models consist of using empirical methods based on characteristics of recorded earthquakes in conjunction with seismic hazard analysis are used to predict bedrock motion characteristics. Unfortunately, these methods are limited since existing earthquakes databases have minimal information for large earthquakes (> M9) in this region.

In a seismic event, fragility curves are commonly used to indicate the probability of failure of a component. Unfortunately, the existing models used to evaluate electrical systems

Chapter 3: Landslide Hazard Map

3.1 Study Area

The western US experiences significant tectonic movements and is an area of high seismicity (Figure 3-1). The region encompassing the Western Power Grid (WPG) within the United State comprises the study area, which spans from eastern Colorado west to the Pacific Ocean and south of the Canadian/US border to the Mexico/US border, totaling 3,075,000 km². Figure 3-1 outlines the study area and the extent of the available Cascadia Subduction Zone M9.3 earthquake ground motion intensity data.

A large portion of this region is prone to significant seismic hazards such as the Cascadia Subduction Zone (CSZ) or the Wasatch fault (Utah), whereas other portions of the study region exhibit less seismicity. The mean recurrence interval for those subduction zone earthquakes is about 600 ± 30 years, with intervals perhaps as short as 215 years and as long as 1500 years (Adams 1990; Goldfinger et al. 2003). The CSZ runs largely north-south along the Pacific Northwest (PNW) of the continental US and is capable of producing a great earthquake, corresponding to a magnitude M9⁺, which will likely trigger many new landslides or reactivate existing landslides. The PNW is particularly vulnerable to co-seismic landslides from CSZ earthquakes given the strong ground motions expected (Goldfinger et al. 2003), prevalence of weak soils and weathered rock (Sharifi-Mood et al. 2017), and high precipitation levels throughout the coastal ranges (Burns and Franczyk 2021). According to an implementation of the empirical Green's function technique (Irikura 1986), which is a model used to predict ground motions for large earthquakes (i.e., $M > 8.5$), the CSZ event is estimated to produce strong ground motions about 25% greater at coastal sites (i.e., peak acceleration = 6 m/sec²) and about 67% as great at sites in the Puget Sound (i.e., peak acceleration = 2.5 m/sec²) located about 50

km inland than what would be expected from observed $M < 8.0$ earthquakes (Heaton and Hartzell 1987). Stronger ground motions indicate a greater potential for damage thereby threatening civil and electrical power infrastructure and their users.

For the study region, the existing terrain of the region is of importance. This chapter presents a methodology for evaluating and mapping seismically-induced landslide hazards across a large region utilizing performance-based design strategies. Focusing specifically on developing a methodology for determining probabilities of exceeding displacement thresholds (δ , 0.03, 0.05, 0.07, 0.1, 0.13, 0.15, 0.2, 0.4, 0.6, 1.0, 1.5, 2.0, 3.0, 5.0, 10, and 100 m) through applying a logic tree approach, model *LOS2I*, to develop a regional seismically-induced landslide hazard map. This approach scales site-specific techniques to a regional scale evaluation through combining generally available data: (1) previous landslide inventories, (2) lidar and photogrammetric topographic data, (3) geological (lithological) mapping, (4) seismic ground intensity data to conduct the analysis.



Figure 3-1. Extent of the area of interest (i.e., extent of the Western Power Grid) with a box outlining the extents of the data provided by the USGS for a CSZ M9.3 earthquake dataset (ground motion intensity data).

3.2 Data Sources

Several geospatial geological and geotechnical data sources are necessary to estimate landslide hazards including topographic information such as the inclination of sloping ground, soil and/or rock properties, shaking intensity, and probability of slope instability triggering sources such as earthquakes (Soeters & Van Western, 1996). For this study, the slope gradient, generalized geological information, historical landslide data, and electric bus/substation data were paired with earthquake intensities such as the PGA, PGV and PSA shake map datasets for the USGS M 9.3 Cascadia Subduction Zone Scenario Earthquake to develop a landslide hazard map (USGS 2017). These datasets were projected in the following coordinates systems: *USA Contiguous Albers Equal Area Conic (USGS_version) projection* (horizontal) and *1983 North American Datum* (vertical) to limit the longitudinal and horizontal distortion due to the large extent of the area of interest ($\sim 3,075,000 \text{ km}^2$). For more efficient computations, the raster layers were resampled to 90 m for the analysis. Table 3-1 summarizes the various datasets used in this co-seismic landslide hazard analysis and their associated attributes (source, provider and resolution).

Table 3-1. Datasets used for the landslide analysis and their source, provider and resolution.

Dataset	Source	Provider	Native resolution
Digital Elevation model used to compute the Slope gradients	National Elevation Database	USGS	1/3 arc-sec (~10 m)
M9.3 CSZ Scenario Earthquake data	Earthquake Hazards Program	USGS	0.031564°
Generalized Geology	The State Geologic Map Compilation (SGMC) Geodatabase	USGS	Ranging from 1:50,000 to 1:1,000,000
Global Landslide Catalog	The Cooperative Open Online Landslide Repository	COOLR	N/A
Landslide Incidence (polygon)	Landslide Map of Continuous United States	USGS	1:3,750,000
Landslide Incidence (point)	Landslide Map of Continuous United States	USGS	N/A
ACTIVS Substation & Bus Model	Advanced Research Projects Agency–Energy	--	N/A
ACTIVS branch/power pole Model	Advanced Research Projects Agency–Energy	--	N/A

3.2.1 Digital Elevation Model (DEM)

Detailed topographic information of the study region is necessary to characterize terrain that would be most susceptible to landslides. Regional-scale modeling of soil landslides may be performed using an infinite slope model and characterized based on the existing slope angle and soil characterization (Wyllie and Norrish 1996; Sarkar and Kanungo 2004; Sharifi-Mood et al. 2017). Steeper slopes result in larger driving (i.e., destabilizing) forces. A 90 m resolution digital elevation model (DEM) was compiled for the study region by subsampling and mosaicking data available from the USGS National Elevation Dataset (NED) (USGS 2020). These data represent the “best” available topographic information and range from high resolution airborne lidar data to photogrammetric surveys to digitized contour maps depending on the location. As a result,

data accuracy and resolution can vary substantially throughout the dataset. However, these data tend to be more accurate than satellite-derived rasters (e.g., ASTER, SRTM), which represents the sole alternative for study regions of this scale (i.e., spanning multiple states). A slope raster was computed using ArcGIS Pro (ESRI 2019) and the DEM by computing the gradients between neighboring pixels. Large DEMs tend to have resolution constraints, where higher resolution features from shallow landslides are not necessarily captured but general slope trends in the area conducive to landsliding are. Figure 3-2 displays the slope map produced from the DEM developed for the study region with insets of areas along the west coast.

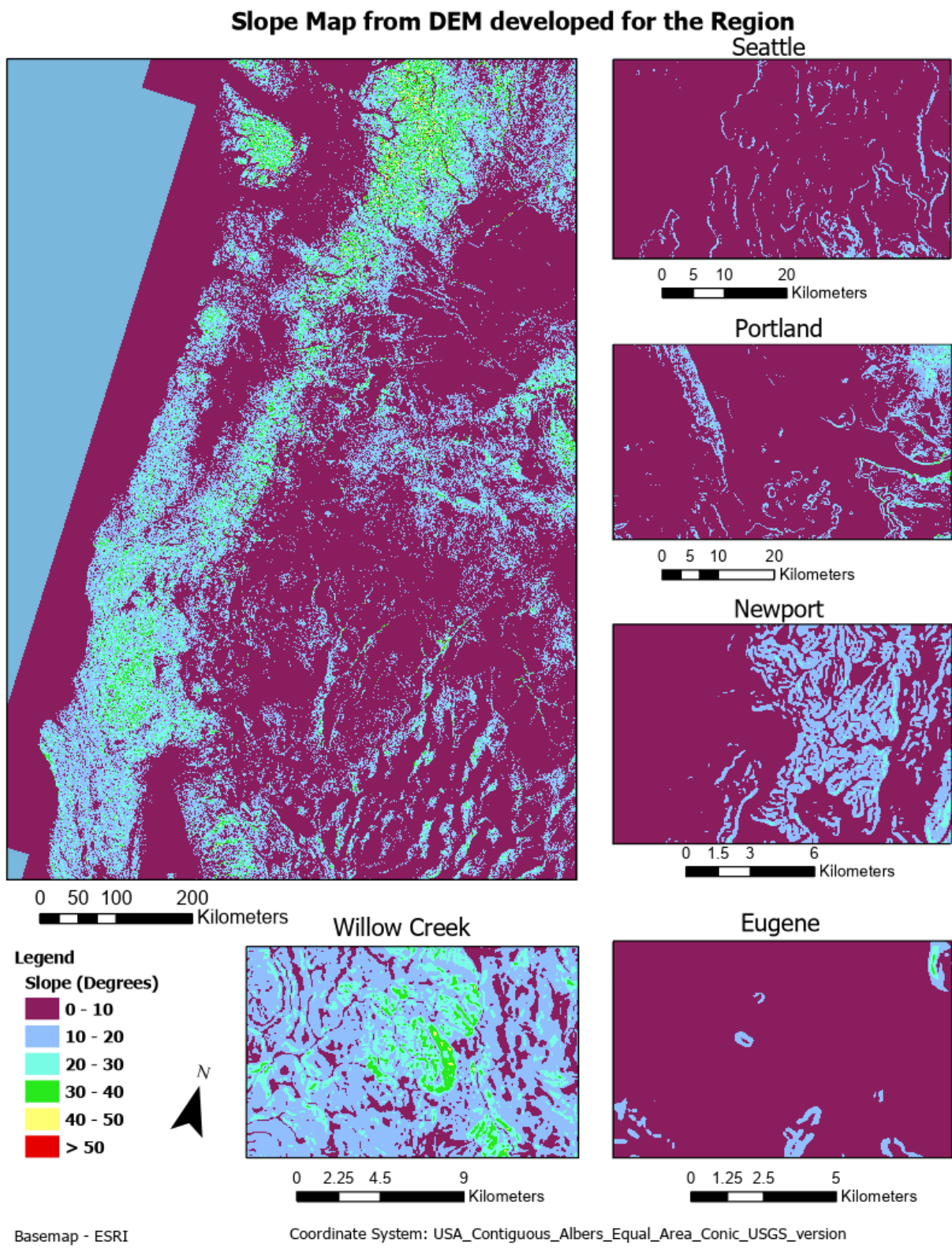


Figure 3-2. Slope map from the developed DEM of the study region focused on the extent of the M9.3 CSZ earthquake dataset (ground motion intensity data) with five inserts to indicate detail.

3.2.2 Lithological Unit Map

To characterize the likely soil and rock properties (i.e., soil strength, friction angle) that can be expected throughout the study region, a generalized geological map was extracted from the State Geologic Map Compilation (SGMC) geodatabase of the conterminous United States (Horton et al. 2017), which provides a seamless, spatial database of 48 state geological maps and represents the most current geological and lithological mapping in the study area. Lithological units were mapped as polygons at scales ranging from 1:50,000 to 1:1,000,000. For efficient computation, the polygons were converted into a raster format with 90 m pixels. Reference Horton et al. (2017) for descriptions of each lithological unit type used in this evaluation (i.e., USGS State geological map compilation (SGMC) database). The following five lithological units occupy rough 88% of the study region: Sedimentary, clastic; Unconsolidated, undifferentiated; Igneous, volcanic; Igneous, intrusive; and Sedimentary, undifferentiated. Table 3-2 summarizes the relative percentage that each lithological unit occupies within the study region.

Table 3-2. Relative percentage of space that each lithological unit occupies within the study Region (~3,075,000 km²)

Lithological Unit Types	Percent of Area
Sedimentary, clastic	29.2%
Unconsolidated, undifferentiated	28.0%
Igneous, volcanic	17.5%
Igneous, intrusive	6.8%
Sedimentary, undifferentiated	6.44%
Metamorphic, sedimentary clastic	2.57%
Igneous and Sedimentary, undifferentiated	1.78%
Sedimentary, carbonate	1.70%
Metamorphic and Sedimentary, undifferentiated	1.17%
Metamorphic, undifferentiated	1.02%
Unconsolidated and Sedimentary, undifferentiated	0.97%
Metamorphic, gneiss	0.96%
Igneous and Metamorphic, undifferentiated	0.50%
Igneous, undifferentiated	0.40%
Melange	0.30%
Metamorphic, schist	0.27%
Metamorphic, volcanic	0.18%
Metamorphic, serpentinite	0.09%
Metamorphic, sedimentary	0.06%
Sedimentary, evaporite	0.03%
Metamorphic, carbonate	0.02%
Tectonite, undifferentiated	0.01%
Metamorphic, intrusive	0.005%
Metamorphic, other	0.004%
Metamorphic, igneous	0.001%
Sedimentary, chemical	0.001%

For efficient computation, the polygons were converted into a raster format with 90 m pixels. Figure 3-3 displays the lithological units for the study region.

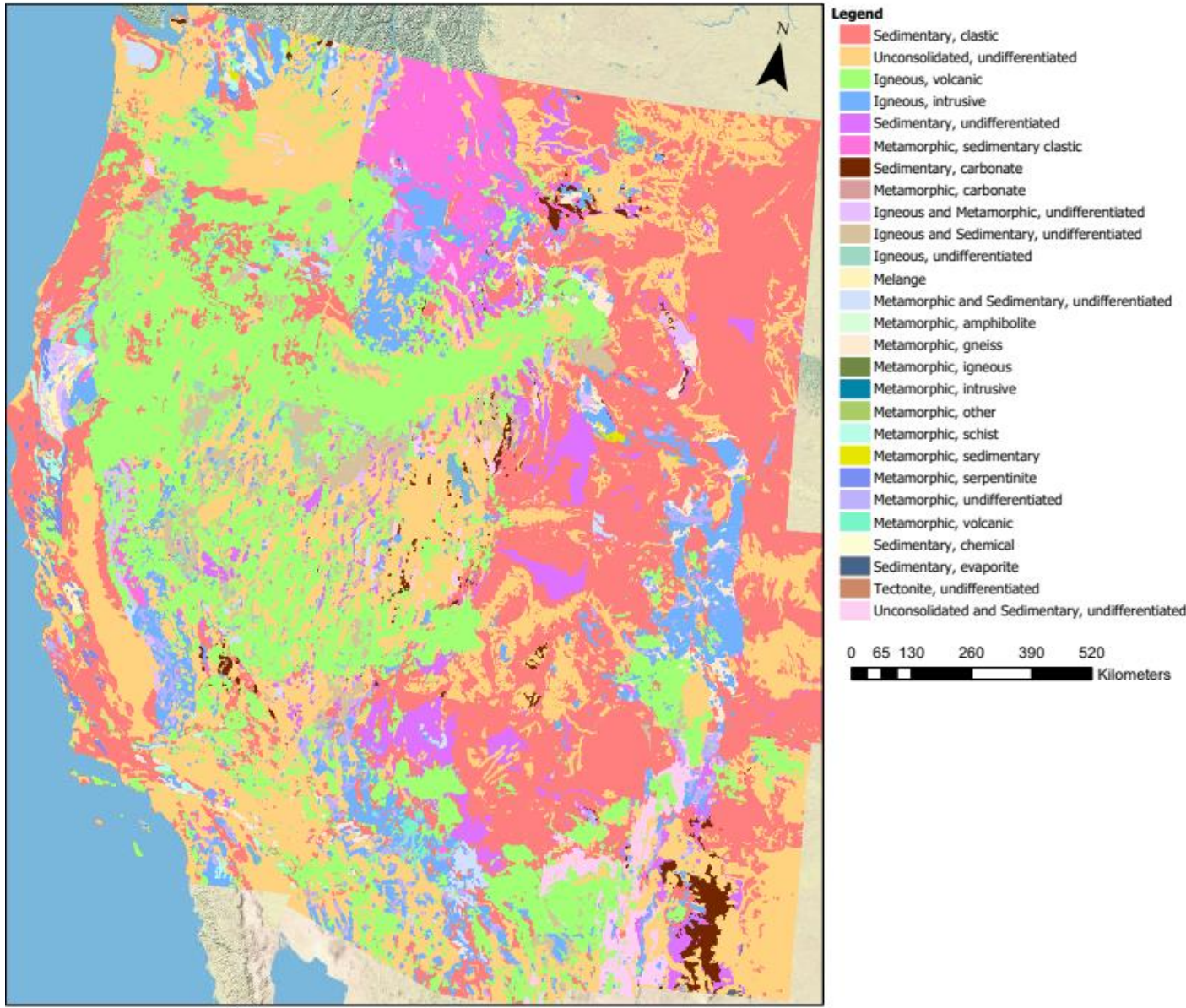


Figure 3-3. Lithological map of the Western Power Grid.

3.2.3 Landslide Inventory Map

To characterize the different soil and rock deposits and their susceptibility to landslides, a landslide inventory consisting of displaced soil deposits mapped as both polygon and point features were obtained from the Cooperative Open Online Landslide Repository (COOLR, Kirschbaum et al. 2015, 2010) database and the USGS Landslide Incidence and Confidence

dataset (USGS 2018). A polygon feature provides more detailed representation mapping for the extents of the landslides from a DEM. A point feature is usually from a reported event, but the extents have not been delineated. The COOLR dataset contains 2,663 landslides that fell within the study area; whereas the USGS Landslide Incidence and Confidence dataset contains approximately 13,493 landslide points and 342,487 landslide polygons that span 44,700 km² in the study region. It is important to note that the landslide inventories are not complete and quality can vary substantially across the area of study. Figure 3-4 displays the landslide inventory map for the study region focusing specifically on extent of the available Cascadia Subduction Zone M9.3 earthquake ground motion intensity data. Note that a large number of landslides have been recorded along the coastline where the ground motion intensity data is the greatest meaning that this region is already prone to landslides. In Oregon, the number of recorded landslides is greater than the other coastline states (i.e., Washington and California) due to the extensive funding allocated for developing a statewide landslide information database (i.e., statewide landslide information database for Oregon (SLIDO)).

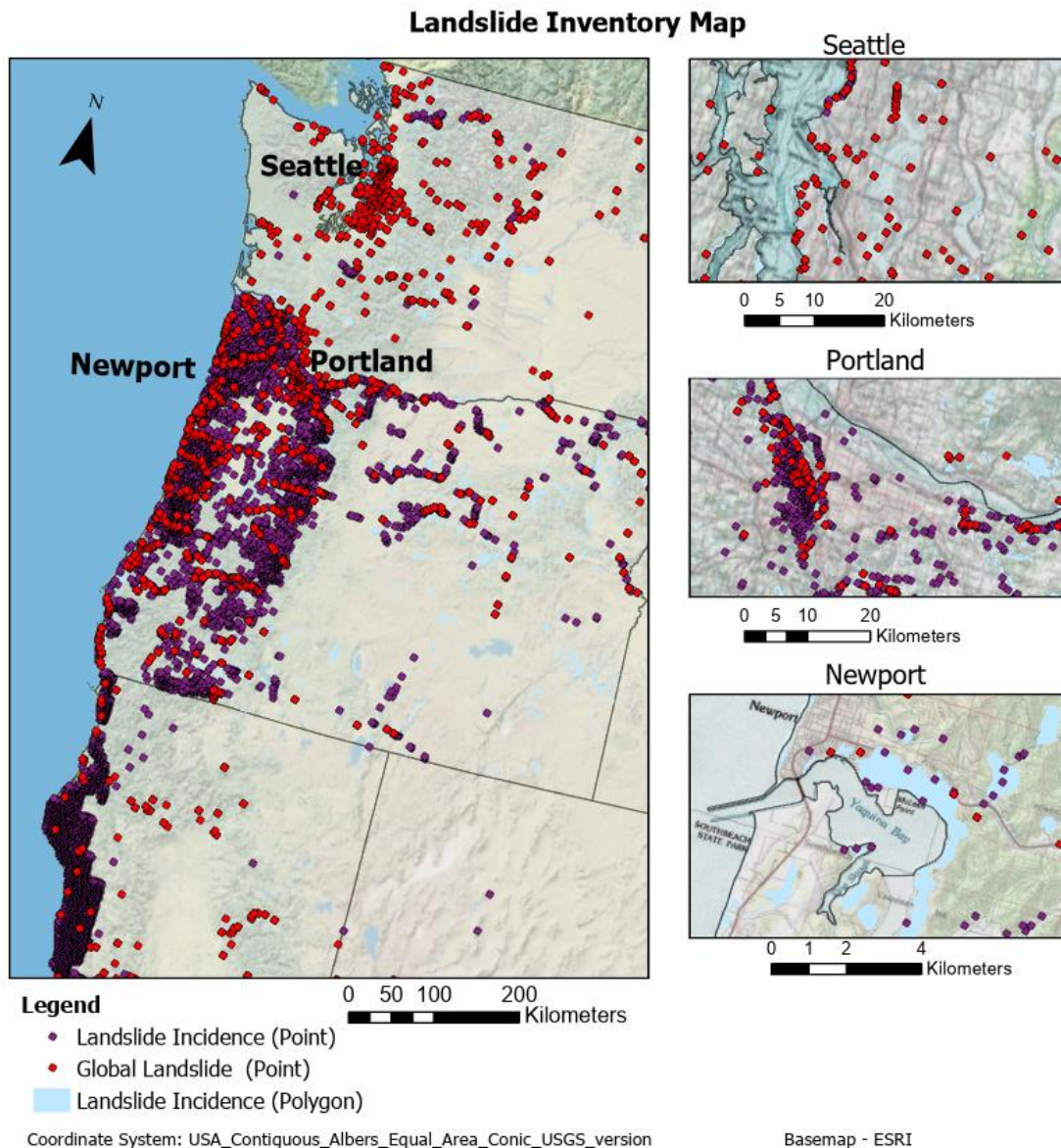


Figure 3-4. Landslide inventory map including landslide deposits and points obtained from COOLR and USGS. The figure depicts three sites in more detail that have a high number of landslides.

3.2.4 M9.3 Earthquake Simulation

To understand the extent of seismic damage that may be expected following a CSZ event, the USGS (USGS 2017) evaluated an M9.3 Scenario Cascadia Megathrust Earthquake to provide a simulated dataset produced using their ShakeMap computational tool that can provide a basis for resilience planning. Ground motions that were simulated as part of this scenario event were estimated by defining an assumed rupture zone and pairing it with ground motion prediction

equations (GMPE's) to estimate likely PGAs and PGVs. Note that while the scenario identifies the intensities anticipated from a M9.3 CSZ earthquake, it does not consider the direction of rupture (i.e., earthquake directivity; Worden et al. 2020), which can significantly affect the size and prevalence of co-seismic landslides (Keefer 1984). The direction of rupture impacts the directional intensity of the released seismic energy and therefore the degree of ground shaking at a given site. For example, when a fault ruptures unidirectionally (with the epicenter at or near one end of the fault), seismic waves radiate more strongly in one direction along the fault than another (USGS 2007). The fault is located off the coast of Oregon (Epicenter coordinates: 45.061°N 124.418°W) at a depth 21.4 km, total area of ~160,000 km². Figure 3-5 displays the extents of the fault and the location of the epicenter for the M9.3 Scenario Earthquake. The GMPE's for this situation was conducted externally estimated. The ground motion intensity data rasters were resampled to 90 m using bilinear interpolation. The PGA and PSA are in units of *g* (%) and *PGV* is in units of cm/s. The PSA datasets were determined assuming a 5% damping ratio. Figure 3-6 displays the extent of the ground motion intensity data (PGA and PSA) for a Cascadia Subduction Zone M9.3 earthquake.

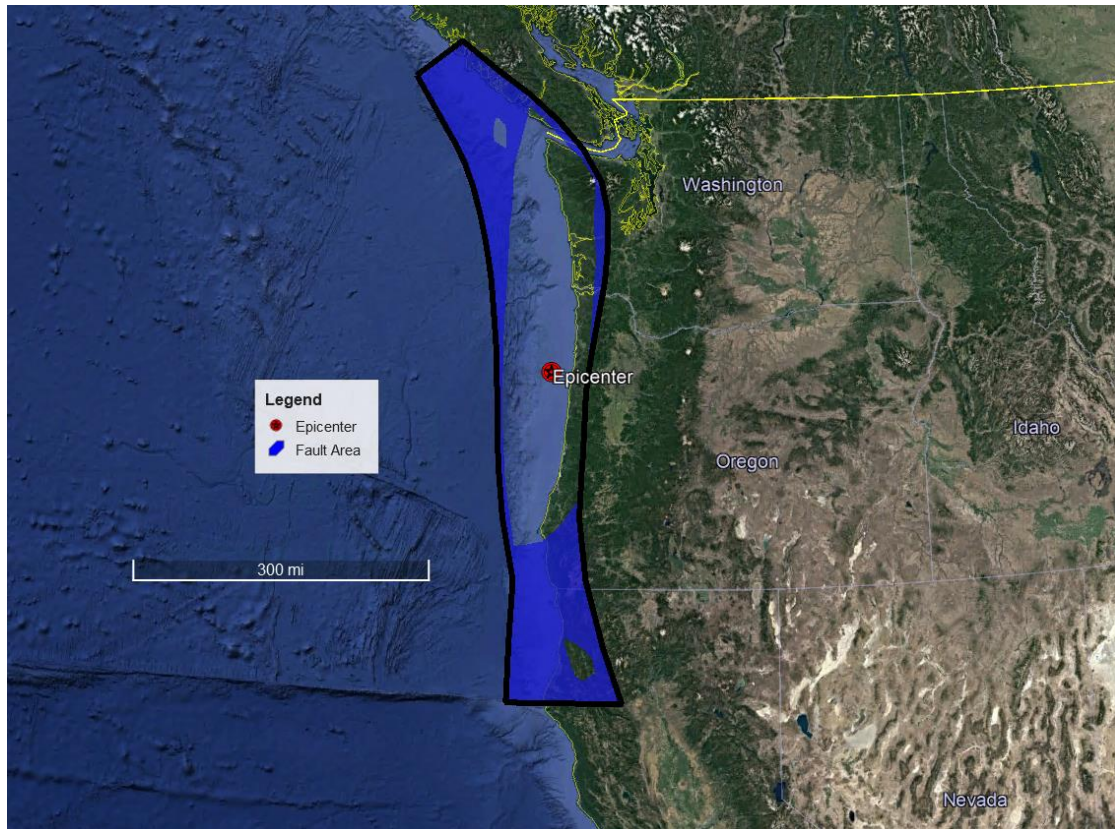


Figure 3-5. Summary of the fault boundaries and location of the epicenter used in the M 9.3 Scenario Earthquake ShakeMap.

USGS Cascadia Subduction Zone M9.3 Earthquake Dataset Map

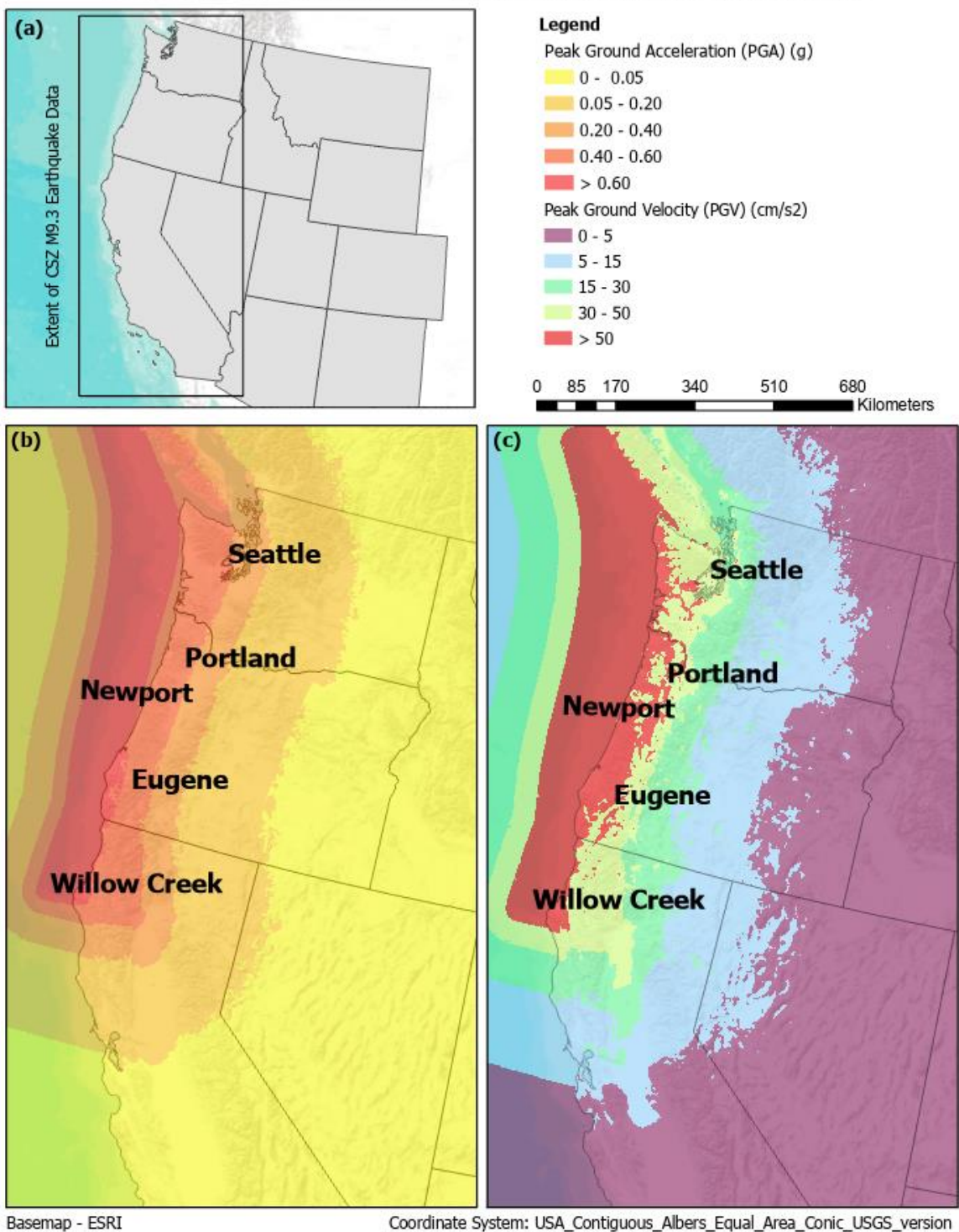


Figure 3-6. (a) Extent of the CSZ M9.3 event data, (b) Peak ground acceleration (PGA) map for a CSZ M9.3 event in g, (c) Peak ground velocity (PGV) map for a CSZ M9.3 event in cm/s².

3.2.5 ACTIVS Power Grid datasets

The synthetic ACTIVS10g (Birchfield et al. 2017) power grid network database was used to evaluate the extent of damage to the WPG caused by a CSZ event. Given the complexity of the actual WPG, the ACTIVS database was developed as a part of the US ARPA-E Grid data research project to develop large-scale, realistic, validated and open access power system network models. The ACTIVSg 10k database consists of a 10,000- bus synthetic power-grid model with branches connecting the buses. The model does not represent the actual grid network but shares similar generation and load profiles of the actual system (Birchfield et al. 2017) with sixteen regions which is divided along state lines, where California, being subdivided into five areas and seven nominal voltage levels (e.g., 765, 500, 345, 230, 161, 138, and 115 kV) which captures the range in power distribution that is representative of the Western Powergrid (Birchfield et al. 2018). The database provides load, generation, and geographical coordinate information for each bus and information including the branch name, location (i.e., longitude and latitude), nominal voltage, and minimum and maximum load for each branch.

Using the branches in the synthetic transmission line model, the locations of transmission power poles were estimated based on the maximum nominal voltage transmitted through the branches to the substations. Table 3-3 summaries the assumed spacing of poles based on transmission line voltage which were determined using expert opinion and existing spacing for the various electric utilities. To produce more realistic results than using the raw data, power poles located within large water bodies (i.e., Pacific Ocean) or were within 60 m of the coastline were relocated 60 m inland. Figure 3-7 presents the ACTIVSg 10k model for the study region displaying the bus/substation, transmission power lines and poles in the model with inserts showing cities located along the west coast of the US.

Table 3-3. Assumed Spacing of poles based on transmission line voltage

Voltage Range (kV)	Spacing (m)
$1 < x \leq 24$	91
$24 < x \leq 161$	152
$161 < x \leq 230$	244
> 230	305

ACTIVs 10k Model: Electric Pole, Electric Branches and Bus & Substation Locations

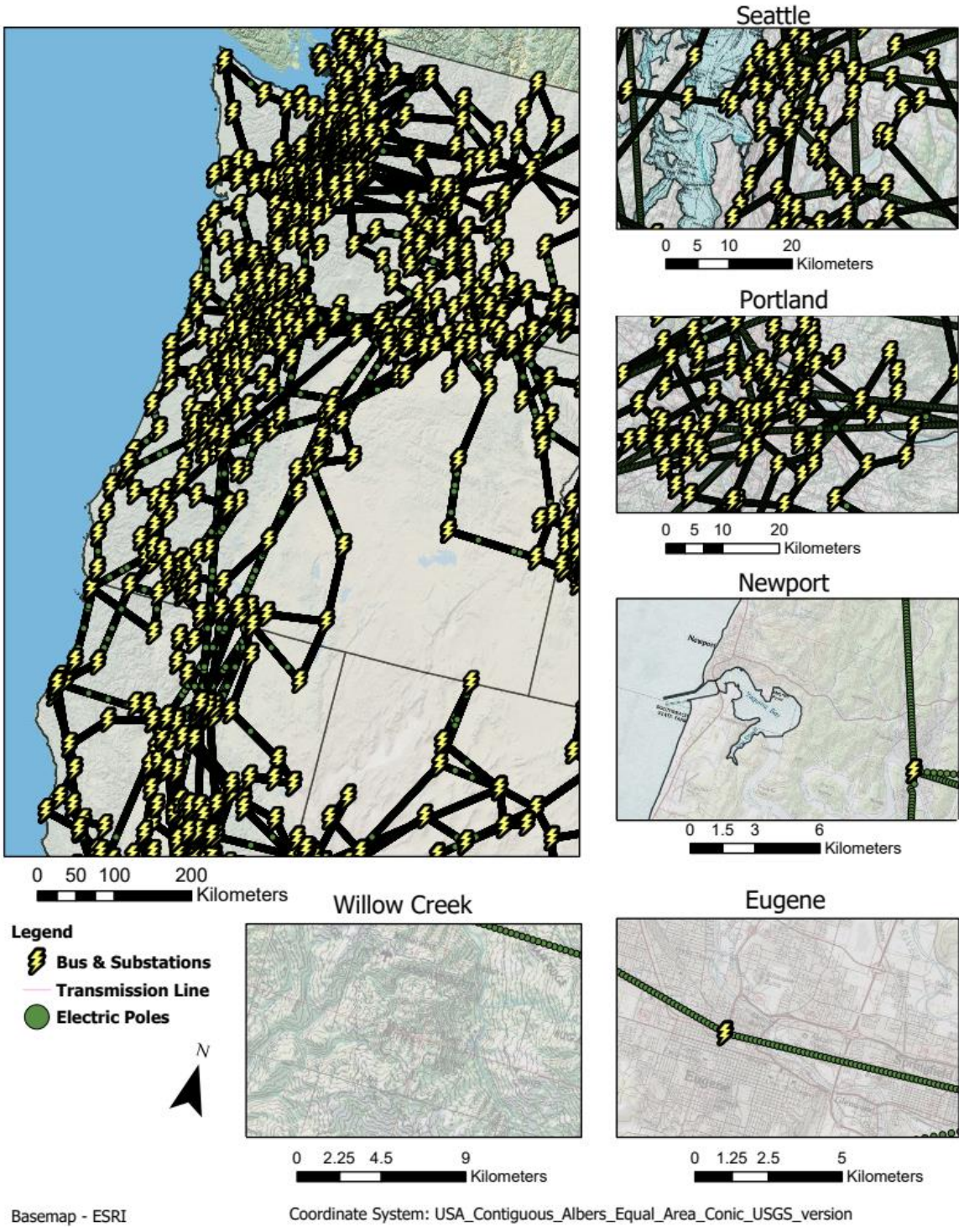


Figure 3-7. Extent of the ACTIVs 10k model with bus/substation, transmission power lines and poles projected in the study region with insets of five cities along the west coast.

3.3 Methodology Overview

The primary goal of this study is to quantify the likelihood of co-seismic landslides for a CSZ event through producing a landslide hazard map to determine vulnerable sections in the WPG. The approach used in this analysis was adapted from a fully-probabilistic regional mapping approach that was developed in C++ by Sharifi-Mood et al. (2017) that estimates the probability of a co-seismic landslide that exceeds a given displacement threshold. Rather than incorporate and aggregate the results from the seismic hazard curves from the USGS National Seismic Hazard Maps (USGS 2008), the maps in this study only considers the M9.3 Cascadia Subduction Zone Earthquake Scenario. Improvements to the methodology of Sharifi-Mood et al. (2017) were adopted, including:

- Inclusion of a more rigorous determination of the statistical distribution of likely soil strength parameters (i.e., friction angle) through fitting the cumulative distribution functions (CDFs) representing soil strengths which was based on the distribution of slopes at landslide inventory locations for each lithological unit,
- Introducing a PGA-based landslide triggering threshold, and
- Incorporating a logic tree analysis method that considers and weighs the various co-seismic landslide displacement models considered, rather than relying solely on a single model to enable the resulting hazard map to account for the uncertainty associated with each model.

The resulting deterministic maps can be imported into a GIS platform for further analysis and visualization to determine vulnerable power grid assets.

The methodology underpinning the selected mapping approach is presented in the following manner:

- Section 3.3.1 describes the calculations implemented to evaluate slope stability;
- Section 3.3.2 focuses on the development of landslide distribution curves (i.e., Distribution of Mobilized Strength (DOMS)) used to estimate a soil strength parameter (i.e., friction angle) for each lithological unit due to limited subsurface data and the regional scale of inquiry;
- Section 3.3.3 describes implementing a logic tree technique to weigh different displacement models based on their degree of complexity and range of applicability.

3.3.1 Methodology for Probabilistic Seismic Landslide Hazard Analysis

Delgado et al. (2011) describes that three factors contribute to seismically-induced landslide hazards are (1) lithological type (i.e., soil strength parameters), (2) slope angle and, (3) ground motion intensity (e.g., PGA). The methodology for the probabilistic seismic landslide hazard analysis was modified from that proposed by Sharifi-Mood et al. (2017) and simplified for use with the specific, deterministic M9.3 Cascadia Subduction Zone earthquake scenario.

Figure 3-8 displays a flowchart of the process that was applied to each pixel within the study region prior to the stability evaluation. For each pixel within the study region, the following information was extracted: lithological unit (L_i), slope angle (θ_i) and ground intensity data (PGA_i, PGV_i). To account for topographical amplification, the ground intensity data, PGA_i, PGV_i , was scaled by a factor dependent on its corresponding slope angle associated with each pixel (x, y). The amplification factors (Table 3-4) were compiled from the findings of Bray and Rathje (1998), Ashford and Sitar (1997, 2002) and Ashford et. al. (1997).

Slope Angle (°)	Amplification Factor
$0 < \theta_i \leq 30$	$(PGA_i, PGV_i) * 1.0$
$30 < \theta_i \leq 60$	$(PGA_i, PGV_i) * 1.3$
$60 < \theta_i$	$(PGA_i, PGV_i) * 1.5$

Table 3-4. Topographical amplification factors applied to the ground intensity data (PGA_i, PGV_i) based on slope angle

Distribution of Mobilized Strength (DOMS) curves were developed for each lithological unit as described in Section 3.3.2. Figure 3-9 displays the methodology of the development of the hazard map (i.e., landslide probability map) through conducting a seismic stability analysis and applying the logic tree approach (i.e., *LOS2I* model) discussed in Section 3.3.3.

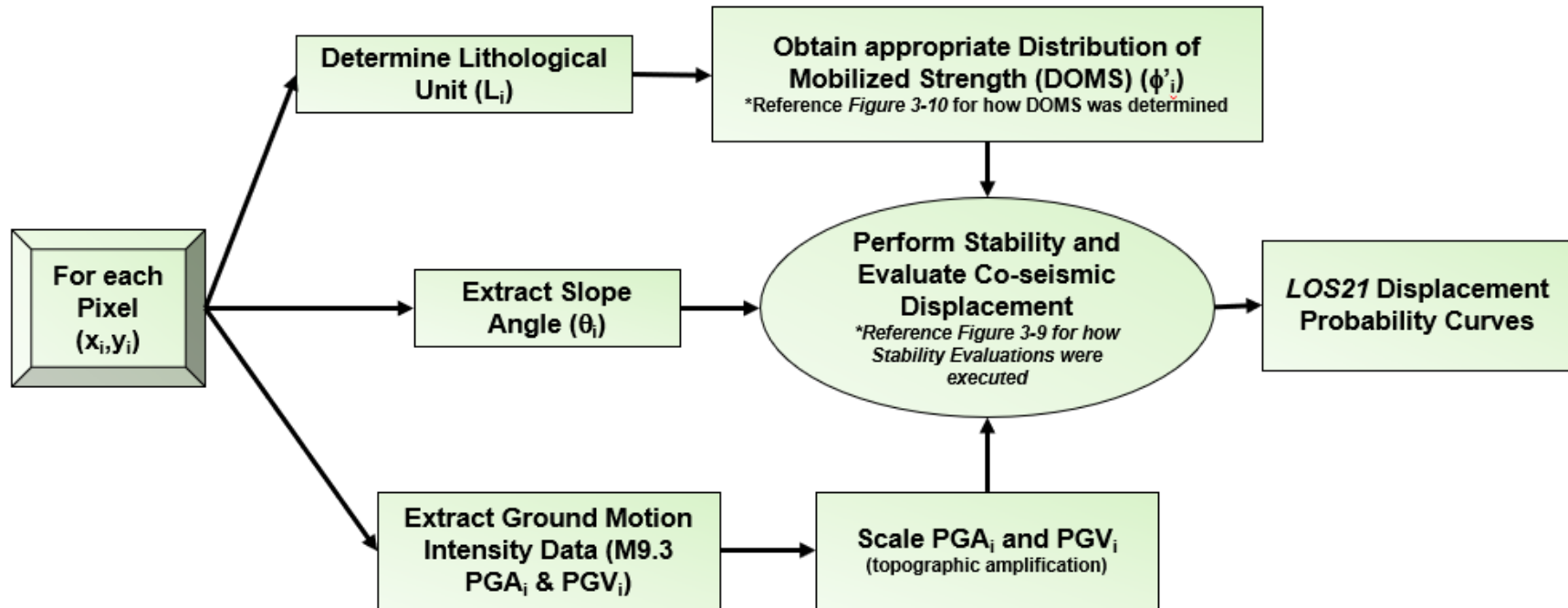


Figure 3- 8. Simplified methodology for extracting information for each pixel in the study region as input into the seismic slope stability evaluation

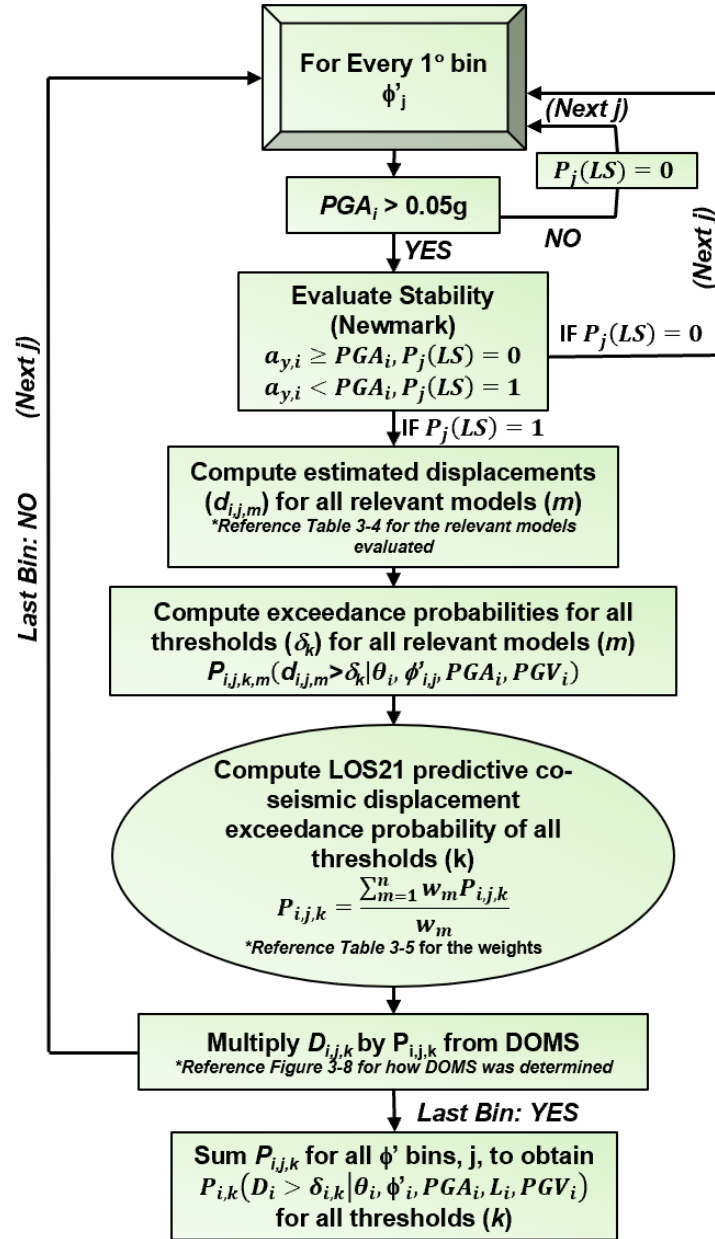


Figure 3-9. Methodology with simplified pseudo-code for stability evaluation and development of the hazard map (modified from Sharifi-Mood et al (2017))

Shaking intensity threshold (i.e., $PGA > 0.05g$) was used with a set of random variables (e.g., slope angle, lithological unit, PGA and PGV) for the fitting of representative displacement probability distributions. Evidence for such a threshold has been discussed in the literature; Jibson and Harp (2016) evaluated six earthquakes and determined that the minimum PGA

associated with triggering seismically-induced landslides ranged from 0.02 g to 0.08 g and 0.05 to 0.11 g when using PGA obtained from ShakeMap models or aerial-photographic interpretations, respectively. Wilson and Keefer (1985) analyzed the worldwide landslide data of Keefer (1984) and proposed that 0.05 g is a reasonable minimum threshold of shaking (i.e., PGA) that would trigger outer boundary landslides. Based on these prior studies, a landslide triggering threshold of $PGA = 0.05g$ was implemented in this study.

The probability of a landslide occurring at a given location for a M9.3 CSZ event can be calculated as:

$$P(LS)_{x,y} = \sum_{i=0}^n \sum_{j=0}^{90^\circ} P(PGA_i > a_{y(\theta_{x,y}, \phi'_j)} | \theta_{x,y}, \phi'_j) * P(\phi'_j) \quad (\text{Eq. 3-1})$$

where i is an increment and n is the number of bins for the probability of distribution function for PGA , $P(LS)_{x,y}$ represents the exceedance probability of a seismically-induced landslide at a location x,y , $\theta_{x,y}$ is the slope angle at location x, y . PGA_i is the peak ground acceleration value obtained from the USGS M9.3 earthquake SHAKE model at location x, y . $a_{y(\theta_{x,y}, \phi'_j)}$ is the minimum pseudo-static acceleration, yield acceleration, required to produce instability in the sliding block. It is calculated using Newmark's Method downhill equation (reference *section 2.2.4.2*), given by:

$$a_y = \tan(\phi'_j - \theta_{x,y}) * g \quad (\text{Eq. 3-2})$$

where g is gravitational acceleration. Should $\phi'_j < \theta_{x,y}$, which is possible due to the probabilistic representation of friction angle but physically inadmissible, a large bin (0 to $\theta_{x,y}$) representing a soil slope at the verge of failure is generated, and $\phi'_j \approx \theta_{x,y}$ is set to limit the degree of seismic displacement and sum those probabilities within the bin.

$P(PGA > a_{y(\theta_{x,y}, \phi'_j)} | \theta_{x,y}, \phi'_j)$ is the probability of the peak ground acceleration exceeding the yield acceleration given the condition that a pixel located at x,y with a slope angle of θ , and estimated friction angle of ϕ'_j sampled from the statistical distribution of the corresponding lithological unit (Figure 3-9). If $PGA > a_y$, then the probability of a landslide occurring for that bin of ϕ' is one, zero otherwise. The probability of the soil having a given friction angle obtained from the lithological determined DOMS is ϕ'_j such as that is shown in Figure 3-9. Calculations were completed for each 90 x 90m pixel in the Western US.

In conjunction with landslide triggering analysis, probabilities of exceeding displacement thresholds, δ , of 0.03, 0.05, 0.07, 0.1, 0.13, 0.15, 0.2, 0.4, 0.6, 1.0, 1.5, 2.0, 3.0, 5.0, 10, and 100 m were determined for each relevant model. Displacements less than or equal to 0.1 m is consider a low hazard with minimal damage that can be easily repaired (Saygili and Rathje 2008). Displacements of 0.3 m represent the potential for significant damage to structures (Olsen et al. 2007). Displacements exceeding 1 m can lead to serious damage to lifelines (e.g., electrical networks; Olsen et al. 2007). Displacements of 10 m or 100 m can lead to severe damage to lifeline corridors (e.g., electrical distribution network; Bird and Bommer 2004). Although large displacements are associated with a low probability of occurring, they are often produced by large magnitude earthquakes such as the CSZ.

Once the probabilities of exceedance thresholds (δ) were determined for the relevant models (Table 3-5), the logic tree approach, representative displacement model *LOS2I*, was applied to probabilities to calculate the final probability of exceedance for each displacement threshold. Equation 3-3 can be used to estimate the probability of exceedance using the weights determined in the representative displacement model: *LOS2I*, given by:

$$P(D_L > t | a_y, PGA_i)_{LOS21} = \sum_{i=1}^n w_i * P(D_L > \delta | a_y, PGA_i, PGV_i)$$

(Eq. 3-3)

Where w_i is the weight applied to the determined probability of exceedance for the various regression models dependent on the ratio of $\frac{a_y}{PGA}$.

To calculate the exceedance rates after the model *LOS21* has been applied, equation 3-1 and 3-3 can be merged, given by:

$$P[D_L > t]_{x,y} = \sum_{i=0}^n \sum_{j=0}^{90^\circ} P(PGA > a_{y(\theta_{x,y}, \phi'_j)} | \theta_{x,y}, \phi'_j) * P(D_L > t | a_y, PGA_i, PGV_i)_{LOS21}$$

(Eq. 3-4)

The probability of D_L exceeding a threshold value can be calculated with equation 3-4, which is a summation of PGA, friction angle and PGV with a given slope and computed yield acceleration in a particular cell. After the aggregation of all the PGA values on the seismic hazard curve, the mean annual rate of exceedance of several displacement thresholds will be produced, resulting in the creation of a series of hazard maps discussed in *Chapter 4*.

3.3.2 Distribution of Mobilized Strength (DOMS) Curves per Lithological Unit

Since the study region is too large to obtain detailed geotechnical information (e.g., soil and/or rock unit weight, friction angle, depth to groundwater table, and other pertinent details), an alternative means for quantifying relevant parameters was necessary. In this seismic slope stability evaluation, an infinite slope failure is assumed and which implies that the soil constituting the sliding mass is relatively uniform and the slope extends for a relatively long distance. Slope stability is ultimately determined by two factors: the angle of the slope and the strength of the materials. The friction angle is the only soil variable considered since other slope

information (i.e., height of slope and ground water table levels/saturation levels) is not readily available. The soil strength (i.e., friction angle) for each lithological unit was estimated by determining the slope failure angle of past landslides and used to develop cumulative distribution functions (CDF). The CDF curves (i.e., Distribution of Mobilized Strength (DOMS) curves) is used as a proxy for the friction angle of the lithological units. The developed DOMS curves display the probability of failure for a lithological unit given a specific angled slope face.

3.3.2.1 Data Collection and Processing

The following datasets (Table 3.1): slope, lithological unit, global landslide catalog, and landslide extents (polygon) or occurrences (points), were analyzed across the study region in ArcGIS Pro 2.5 to develop the Distribution of Mobilized Strength (DOMS) for each lithological unit.

3.3.2.2 Workflow

Figure 3-10 illustrates the geospatial data processing workflow to determine the characteristics (e.g., slope angle and lithological unit) of landslides (i.e., point or polygon). For each landslide that occurred in the region of interest, the slope angle and geological type was extracted using the DEM and generalized geological layer, respectively. Slope angle and lithological unit values corresponding to mapped landslide polygons were extracted from the pixel intersecting the centroid of the polygon. Note that the centroid is unlikely to occur at the steep headscarp, but rather is more likely to occur within the gentler terrain within the deposit material, potentially underestimating the slope angle per the lithological unit. This approach tends to provide a more conservative estimate for the mix of landslides evaluated (e.g., deep-seated, shallow) to account for uncertainty in the resulting maps. Cumulative distribution functions (CDFs) of slope failure were produced for each lithological unit based on the slope

angle values at each landslide. The CDFs was compared to common statistical distributions, such as the normal, lognormal, gamma, and Weibull distributions, to identify a suitable, best-fitting distribution for sampling in the forward analysis of co-seismic hazard mapping. For each lithological unit, a rank distribution was used to determine the associated probability for each slope angle and an ordinary least squares regression was used to determine the fitting parameters for each regression model. The corresponding bias were determined for each distribution type: average (mean) bias, standard deviation bias and coefficient of variation (COV) of the bias. Bias is the difference between the expected value of the results and the true underlying quantitative parameter being estimated. COV shows the dispersion of the distribution and is equal to the ratio between the SD and Mean. The best fitting statistical distribution was determined as that which exhibited the smallest COV in bias and/or average bias (being closest to 1.0) and/or best visual inspection.

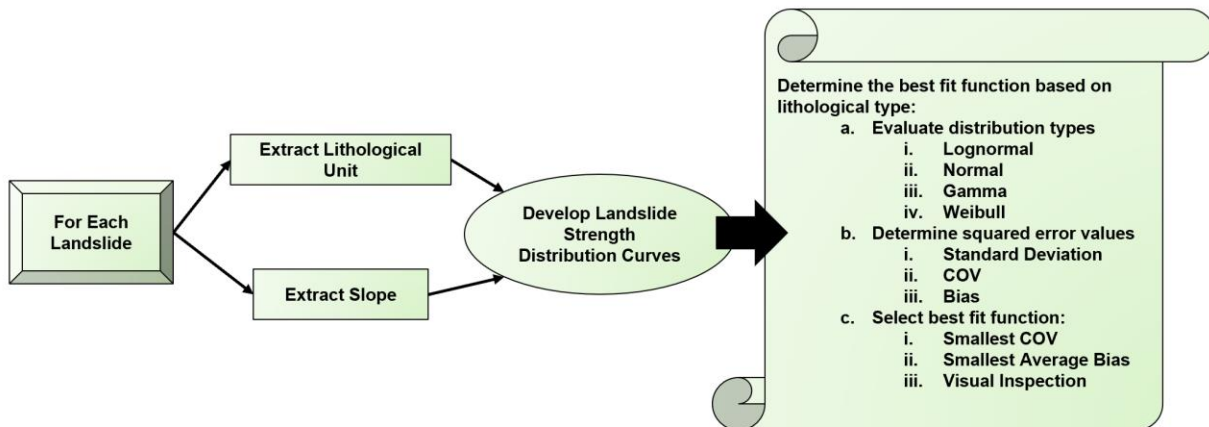


Figure 3-10. Methodology used to develop Distribution of Mobilized Strength (DOMS) curves based on lithological unit type and selecting best fit distribution.

Figure 3-11 presents an example set of CDFs for lithological unit: Igneous Intrusive, which compares the distribution of mobilized strength (DOMS) for the statistical distributions. The figure also shows the corresponding distribution shape parameters and goodness-of-fit statistics described above (i.e., biases). The normal and lognormal distributions over- and under-

predicts the sample distribution with an average bias of 0.968 and 1.09, respectively. The gamma and Weibull distributions appear more accurate than the normal and lognormal distributions with bias values closer to 1. Since the gamma distribution has the smallest COV, average bias (closest to 1.0) and exhibits the best visual fit to the sample distribution, it was selected as the representative distribution. Refer to *Appendix A* for the CDFs for all the lithological units present within the study region (Figure A-1 to Figure A-19). It should be noted that the friction angle sampled from the distribution reflects the incipient failure of the slope face for each lithological unit. Using the friction angle as a proxy for slope failure can lead to a bias in stability for steep slopes when the sampled friction angles are low, and in gentle slopes which are typically stable. Recent models (i.e., Bunn et al. 2020) have been developed to address such a sampling bias, but these are difficult to apply the scale of the current study.

Figure 3-12 highlights the variation of the best fit distribution of mobilized strength (DOMS) curves (i.e., strength distributions) for various lithological unit types. Note that the Unconsolidated and Sedimentary, Undifferentiated (USU) DOMS curve is smaller than the other curves meaning that internal friction angle of the lithological unit is weaker, therefore we would expect regions classified as USU to failure more often than the other lithological units.

Table 3-5 summarizes the best fit distribution of mobilized strength for each lithological unit, the type of statistical distribution, and the corresponding shape parameters. The mean and standard deviation (SD) shape parameters are used for normal and lognormal distribution and the alpha (α) and beta (β) shape parameters are used for Gamma and Weibull distributions, where mean/ α are “shape” parameters and SD/ β are “scale” parameter. Due to insufficient samples for some lithological unit types, the sparse samples were combined with common lithological unit

types (i.e., Metamorphic, undifferentiated; Unconsolidated and Sedimentary, undifferentiated; Unconsolidated, undifferentiated).

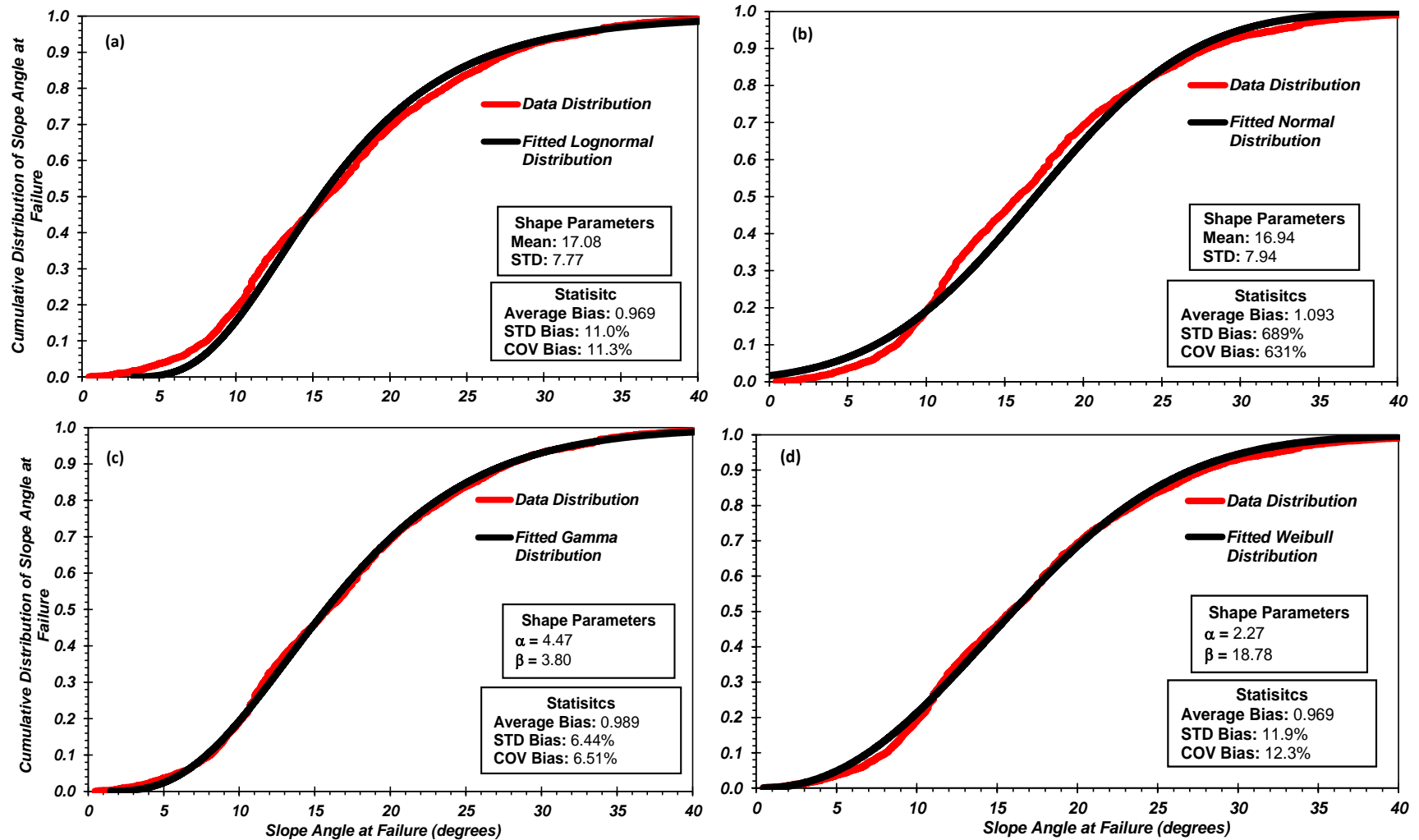


Figure 3-11: Cumulative Distribution Functions (CDF) for Igneous Intrusive lithology type with shape parameters and statistic information regarding the determined bias values: (a) Lognormal, (b) Normal, (c) Gamma, (d) Weibull. The Gamma distribution (c) provided was selected as the best fit for this Igneous Intrusive lithology type.

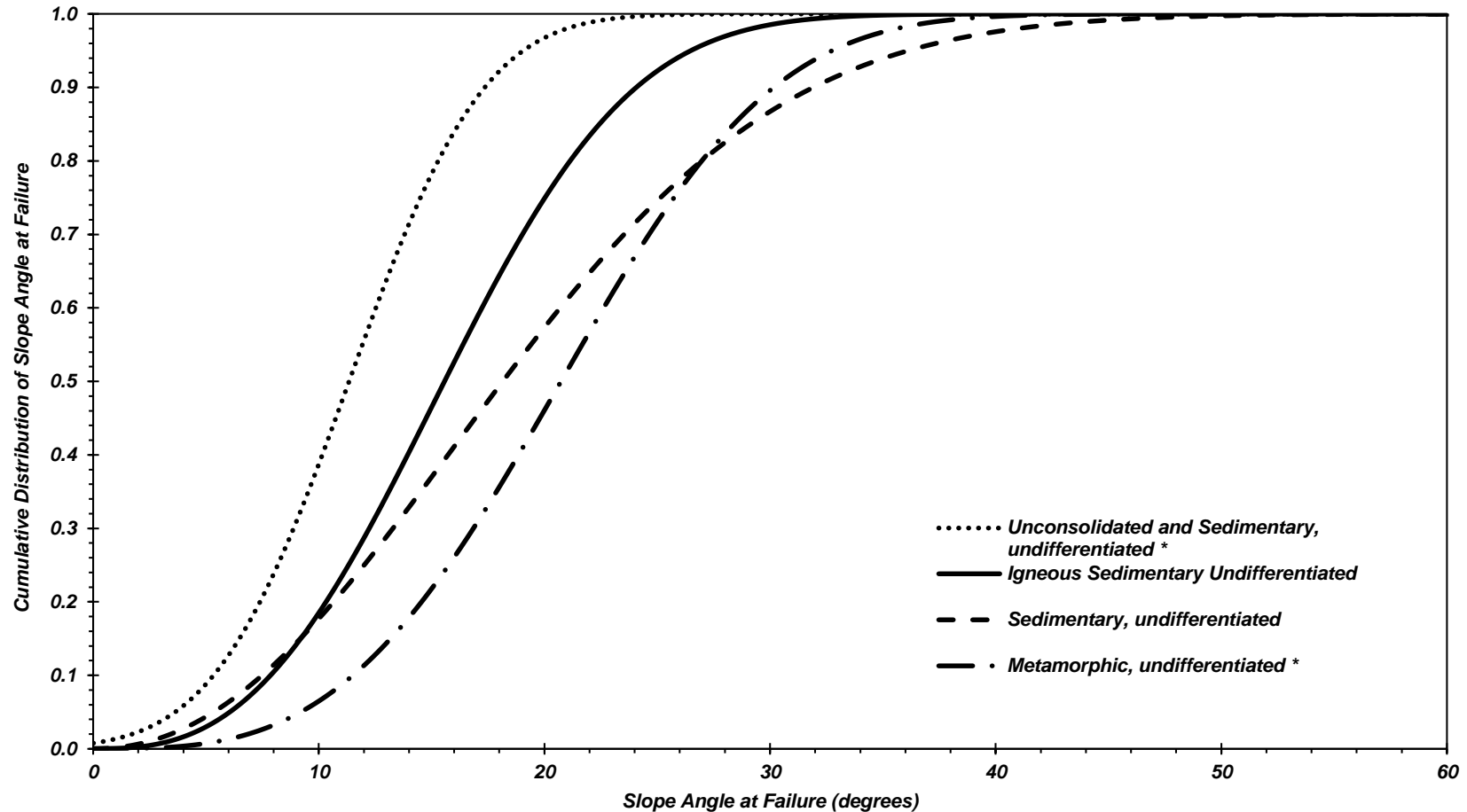


Figure 3-12: Example CDF of best fit distribution of mobilized strength (DOMS) curves. (i.e., proxy for the distribution of strength parameters) for various lithological units: weaker soils (Unconsolidated and Sedimentary, Undifferentiated* & Igneous Sedimentary Undifferentiated), stronger soils (Sedimentary, Undifferentiated & Metamorphic, Undifferentiated*). Reference Horton et al. (2017) for lithological unit descriptions.

Table 3-5. Cumulative distribution functions of slope angle at failure by lithological type with corresponding best-fit distribution and shape parameters (α /Mean & β /SD), # of landslides sampled in developing distribution and soil number.

Soil Type	Soil Number *for coding purposes	# Samples	Statistical Distribution	α /Mean	β /SD
General Soil ¹	20	264,223	Weibull	2.36	17.10
Igneous Sedimentary Undifferentiated	1	7,553	Weibull	2.76	17.78
Igneous Metaphoric Undifferentiated	2	588	Weibull	2.91	17.33
Igneous Intrusive	3	4,803	Gamma	4.47	3.80
Igneous, undifferentiated	4	205	Gamma	5.27	3.43
Igneous, Volcanic	5	57,275	Gamma	4.61	3.20
Metamorphic and Sedimentary, undifferentiated	6	3787	Gamma	5.61	3.67
Metamorphic, gneiss	7	245	Gamma	4.22	4.43
Metamorphic, schist	8	2,913	Gamma	8.05	2.180
Metamorphic, sedimentary	9	223	Gamma	5.98	2.91
Metamorphic, sedimentary clastic	10	1,730	Weibull	3.27	22.56
Metamorphic, serpentinite	11	819	Gamma	8.65	1.89
Metamorphic, undifferentiated ²	12	1,601	Weibull	3.20	23.25
Metamorphic, volcanic	13	1,491	Weibull	2.47	18.64
Melange	14	956	Normal	16.22	5.76
Sedimentary, carbonate	15	2,085	Gamma	5.94	2.72
Sedimentary, Clastic	16	123,387	Weibull	2.53	18.09
Sedimentary, undifferentiated	17	6,939	Weibull	2.13	21.56
Unconsolidated and Sedimentary, undifferentiated ³	18	581	Normal	11.34	4.69
Unconsolidated, undifferentiated ⁴	19	47,042	Weibull	2.20	14.00

1. General Soil incorporates all landslide samples.

2. Metamorphic, undifferentiated incorporates the following lithological types; Metamorphic Intrusive, Metamorphic Other, Metamorphic Igneous, Metamorphic, amphibolite and Metamorphic Carbonate

3. Unconsolidated and Sedimentary, undifferentiated incorporates the following lithological types: Sedimentary Chemical, and Sedimentary Evaporite

4. Unconsolidated, undifferentiated incorporates the following lithological types: Tectonite, Undifferentiated

3.3.3 Logic Tree

Creating a logic tree for a deterministic/probabilistic seismic hazard analysis involves selecting alternative models or model parameters for various inputs and then assigning weights to the different branches at each node to reflect the “relative” confidence in the models (Bommer and Scherbaum 2008). Due to the extent of the study region, accessibility of ground motions data is limited, therefore predictive sliding block models containing the following input parameters to calculate permanent displacement were only considered: a_y , a_{max} (PGA), PGV and Magnitude (M). For the remainder of this paper, a_{max} will be referred to as PGA . Table 2-3 shows models that were initially considered.

3.3.3.1 Models and Processing

The list of selected predictive sliding block models evaluated for the logic tree are presented in Table 3-6, which provides information regarding the model names, ground motion input parameters, the mean equation and standard deviation values. In these equations, the rigid sliding displacement D_L is in units of cm; PGA and a_y are in units of g ; PGV is in cm/s; and magnitude (M) according to the Moment scale. The following models: AM88, JS07, JV07, are calculated using the $\log(D_L)$ but were converted to natural log, $\ln(D_L)$ through multiplying the $\log(D_L)$ expression by 2.303; therefore all models considered were calculated in terms of $\ln(D_L)$. Consistent with the development of models $BT07$ and $JS07$, displacements of $D_L \leq 0.01$ m were considered to be negligible for those models.

The following models were evaluated by comparing the outputs across twenty-four sites with varying PGA and slope values to estimated permanent displacement (see Table A-1 in the Appendix A for information (i.e., Soil Unit, PGA , Slope, PGV) regarding tested sites). Of the twenty-four sites, eight sites had a PGA value of 0.0 – 0.2 g with varying slope conditions, eight

sites had a *PGA* value of 0.2 – 0.4g with varying slope conditions and eight sites had a *PGA* value of $\geq 0.4g$ with varying slope conditions. In this primary analysis, a mean soil strength was assumed (50% soil strength). The goal of the analysis was to understand the extents of the regression models for a M9.3 CZS event.

The equations of the regression models (in Table 3-6) were used to estimate D_L and the exceedance probability was calculated from equation 3-5, given by:

$$P(D_L > t | a_y, PGA_i, PGV_i) = 1 - F(Z) \quad (\text{Eq. 3-5})$$

where t is the threshold value, equal to (0.03, 0.05, 0.07, 0.1, 0.13, 0.15, 0.2, 0.4, 0.6, 1.0, 1.5, 2.0, 3.0, 5.0, 10, 100 m). $F(Z)$ is the cumulative density functions (CDF) for the standard normal distribution where z can be calculated using equation 3-6 for the selected regression models, given by:

$$z = \frac{\overline{\ln(D_L = t)} - \ln(D_L)}{\sigma_{\ln(D_L)}} \quad (\text{Eq. 3-6})$$

where $\ln(D_L)$ is the natural logarithm of the estimated displacement by the regression models in Table 3-6. $\sigma_{\ln(D_L)}$ is the standard error for the regression models in Table 3-6.

Figure 3-13 displays a set of developed probability of exceedance curves for a tested site assuming a mean soil strength (50% soil strength) for all regression model considered for the logic tree model. Models *RS09* and *JV07* produced notably larger displacement curves for all ranges of *PGA*/slope values and exceeded the reasonable range of displacement values. Both models use M as an input parameter and were derived from earthquakes magnitudes smaller than what is expected from a CSZ earthquake event, therefore the models were excluded from this landslide hazard analysis. Model *S16* was developed after and derived from model *SRV08*. To

limit the over-weight of one regression model procedure, model *SRV08* was excluded from this landslide hazard analysis. The *FT15* models were excluded from this landslide hazard analysis because the site conditions assumptions (i.e., clay slopes) were not appropriate for this evaluation.

Table 3-6. Summary of considered sliding block (Regression) co-seismic landslide displacement models. * = models used in the logic tree model, LOS21.

Model (Abbreviation)	Input parameters	Equation of Regression Models	Standard Error
*Ambraseys & Menu '88 (AM88)	a_y , PGA	$\log(D_{LAM88}) = 0.90 + \log\left[\left(1 - \frac{a_y}{PGA}\right)^{2.53} \left(\frac{a_y}{PGA}\right)^{-1.09}\right] + 0.3t$ *assumed probability of exceedance 50%, t=0	$\sigma_{\log D_{LAM88}} = 0.30$
*Jibson '07 Scalar (JS07)	a_y , PGA	$\log(D_{LJS07}) = 0.215 + \log\left[\left(1 - \frac{a_y}{PGA}\right)^{2.341} \left(\frac{a_y}{PGA}\right)^{-1.438}\right]$	$\sigma_{\log D_{LJS07}} = 0.510$
Jibson '07 Vector (JV07)	a_y , PGA, M	$\log(D_{LJV07}) = -2.71 + \log\left[\left(1 - \frac{a_y}{PGA}\right)^{2.335} \left(\frac{a_y}{PGA}\right)^{-1.478}\right] + 0.42M$	$\sigma_{\log D_{LJV07}} = 0.454$
*Bray & Travasarou '07 (BT07)	a_y , PGA, M	$\ln(D_{LBT07}) = -0.22 - 2.83 \ln(a_y) - 0.333(\ln(a_y))^2 + 0.566(\ln(a_y) * \ln(PGA)) + 3.04 \ln(PGA) - 0.244(\ln(PGA))^2 + 0.278(M - 7)$	$\sigma_{\ln D_{LBT07}} = 0.66$
*Saygili & Rathje '08 Scalar (SRS08)	a_y , PGA	$\ln(D_{LSRS08}) = 5.52 - 4.43 \left(\frac{a_y}{PGA}\right) - 20.39 \left(\frac{a_y}{PGA}\right)^2 + 42.61 \left(\frac{a_y}{PGA}\right)^3 - 28.74 \left(\frac{a_y}{PGA}\right)^4 + 0.72 \ln(PGA)$	$\sigma_{\ln D_{LSRS08}} = 1.13$
Saygili & Rathje '08 Vector (SRV08)	a_y , PGA, PGV	$\ln(D_{LSRV08}) = -1.56 - 4.58 \left(\frac{a_y}{PGA}\right) - 20.84 \left(\frac{a_y}{PGA}\right)^2 + 44.75 \left(\frac{a_y}{PGA}\right)^3 - 30.5 \left(\frac{a_y}{PGA}\right)^4 - 0.64 \ln(PGA) + 1.55 \ln(PGV)$	$\sigma_{\ln D_{LSRV08}} = 0.732 + 0.789 \left(\frac{a_y}{PGA}\right) - 0.539 \left(\frac{a_y}{PGA}\right)^2$
Rathje & Saygili '09 Scalar (RSS09)	a_y , PGA, M	$\ln(D_{LRSS09}) = 4.89 - 4.85 \left(\frac{a_y}{PGA}\right) - 19.64 \left(\frac{a_y}{PGA}\right)^2 + 42.49 \left(\frac{a_y}{PGA}\right)^3 - 29.06 \left(\frac{a_y}{PGA}\right)^4 + 0.72 \ln(PGA) + 0.89(M - 6)$	$\sigma_{\ln D_{LRSS09}} = 0.405 + 0.524(PGA)$
Fotopoulou & Pitilakis (FP15)	a_y , PGA, PGV, M	(1) $\ln(D_{LFP15(1)}) = -9.891 + 1.873 * \ln(PGV) - 5.964(a_y) + 0.285 * M$ (2) $\ln(D_{LFP15(2)}) = -2.965 + 2.127 * \ln(PGA) - 6.583(a_y) + 0.535 * M$ (3) $\ln(D_{LFP15(3)}) = -10.246 - 2.165 * \ln\left(\frac{a_y}{PGA}\right) + 7.844(a_y) + 0.654 * M$	(1) $\sigma_{\ln D_{FP15(1)}} = 0.65$ (2) $\sigma_{\ln D_{FP15(2)}} = 0.72$ (3) $\sigma_{\ln D_{FP15(3)}} = 0.75$ (4) $\sigma_{\ln D_{FP15(4)}} = 0.64$

		$(4) \ln(D_{LFP15(4)}) = -8.076 + 1.873 * \ln(PGA) - 0.347 \left(\frac{a_y}{PGA}\right) - 5.964 \ln(a_y)$	
*Song et. al. '16 (S16)	a_y, PGA, PGV	$\ln(D_{LS16}) = -1.56 - 4.58 \left(\frac{a_y}{PGA}\right) - 20.84 \left(\frac{a_y}{PGA}\right)^2 + 44.75 \left(\frac{a_y}{PGA}\right)^3 - 30.5 \left(\frac{a_y}{PGA}\right)^4 - 0.64 \ln(PGA) + 1.55 \ln(PGV) - 0.32$	$\sigma_{\ln D_{LS16}} = 0.408 + 0.27 \left(\frac{a_y}{PGA}\right)$ <p>For $\frac{a_y}{a_{max}} \leq 0.25$</p> $\sigma_{\ln D_{LS16}} = 0.405 + 0.524 \left(\frac{a_y}{PGA}\right)$ <p>For $\frac{a_y}{a_{max}} \leq 0.25$</p>
*Bray, Macedo & Travararou (BMT18)	a_y, PGA, M	$\ln(D_{LBMT18}) = -5.864 - 3.353 \ln\left(\frac{a_y}{PGA}\right) - 0.390 \left(\ln\left(\frac{a_y}{PGA}\right)\right)^2 + 0.538 \ln\left(\frac{a_y}{PGA}\right) * \ln(PGA) + 3.060 \ln(PGA) - 0.225 \ln(PGA)^2 + 0.550M$	$\sigma_{\ln D_{LBMT18}} = 0.73$

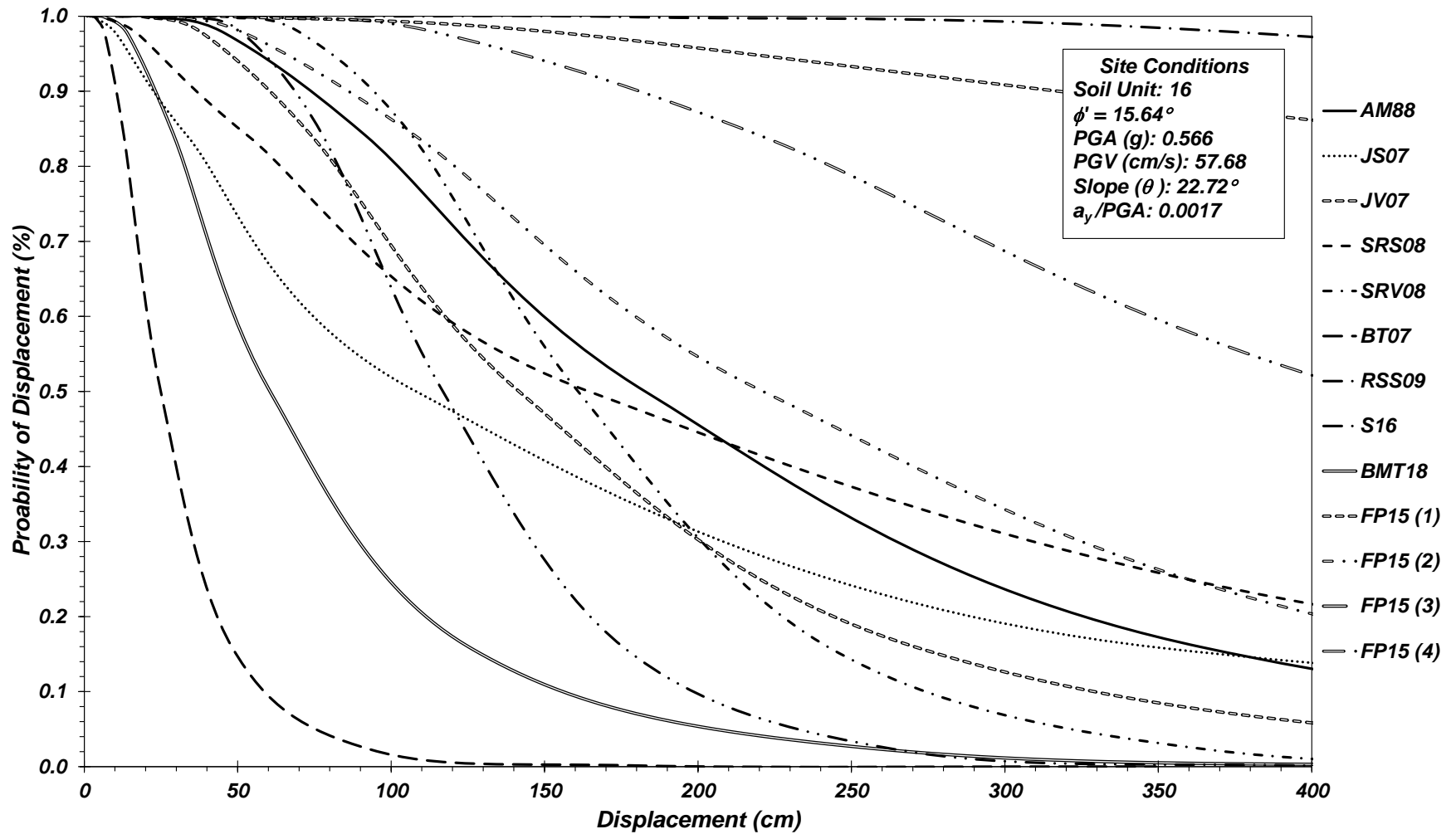


Figure 3-13. Example probability of exceedance curves for a single test site where all relevant regression models considered for the logic tree evaluation. (assuming 50% soil strength).

3.3.3.2 Representative Displacement Model: LOS21

The following models: *AM88*, *JS07*, *BT07*, *SRS08* and *S16*, were incorporated in the development of the representative displacement model: *LOS21*. The models are dependent on the degree of the ratio of $\frac{a_y}{PGA}$. The closer the $\frac{a_y}{PGA}$ ratio is to 0 or 1, the estimated displacements value increases exponentially (negatively or positively). The assigned weights for the relevant regression models were adjusted depending on the ratio of $\frac{a_y}{PGA}$ for the x, y , location. When $\frac{a_y}{PGA} \leq 0.05$, the *AM88*, *JS07*, and *BT07* model-predicted displacements increase rapidly; therefore, when $\frac{a_y}{PGA} \leq 0.05$, Weighting Scheme 1 is used to give lower weight to those models, otherwise Weighting Scheme 2 is used assuming a probability of displacement value of 1 and the exposure $PGA > 0.05g$. The variation in percentages between the methods has to do with how the regression models $\frac{a_y}{PGA} \leq 0.05$.

Table 3-7 displays the logic tree weights for all the relevant regression models used in the *LOS21* representative displacement model.

Table 3-7. Logic tree weights (percentages) of the relevant regression models for the *LOS21* displacement model

Model	Weighting Scheme 1 (%) $(\frac{a_y}{PGA} \leq 0.05)$	Weighting Scheme 2 (%) $(\frac{a_y}{PGA} > 0.05)$
<i>AM88</i>	5.0	7.5
<i>JS07</i>	5.0	7.5
<i>SRS08</i>	17.5	10.0
<i>S16</i>	17.5	20.0
<i>BT07</i>	5.0	15.0
<i>BMT17</i>	50.0	40.0

Equation 3-3 can be used to estimate the probability of exceedance using the weights determined in the representative displacement model: *LOS21*, given by:

$$P(D_L > t | a_y, PGA_i)_{LOS21} = \sum_{i=1}^n w_i * P(D_L > t | a_y, PGA_i, PGV_i) \quad (\text{Eq. 3- 7})$$

where w_i is the weight applied to the determined probability of exceedance for the various regression models dependent on the ratio of $\frac{a_y}{PGA}$.

Figure 3-12 displays a set of developed probability of exceedance curves for the same test site assuming a mean soil strength (50% soil strength) for the models used in the logic tree model: *LOS21*, and the *LOS21* model probability of exceedance curve. Method 1 was used in this site since $\frac{a_y}{PGA} < 0.05$. The *LOS21* model plots in the model of the other regression curves for the sedimentary clastic soil type.

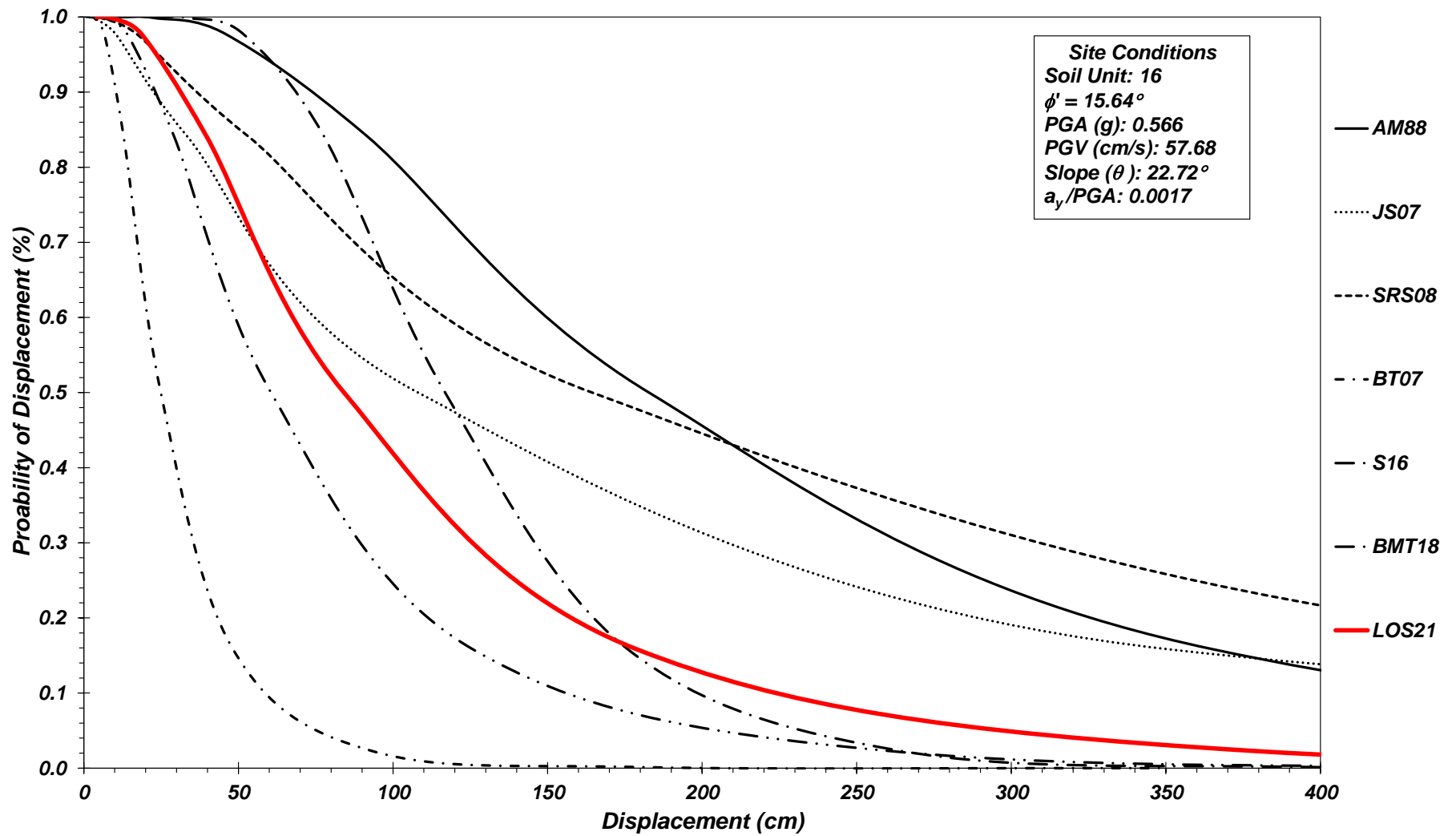


Figure 3-14. Example probability of exceedance curves for a single test site for the regression models used in the logic tree model, *LOS21*. (assuming 50% soil strength).

3.4 Summary

This portion of the study consisted of developing a probabilistic method for a regional seismic landslide hazard analysis and map for the Western United States based on the M9.3 Megathrust CSZ scenario earthquake. This was accomplished by:

- Developing CDFs (i.e., Distribution of Mobilized Strength (DOMS) curves) that can be used as a proxy for the friction angle of the lithological units and display the probability of failure for a lithological unit given a specific angled slope face.
- The soil strength (i.e., friction angle) for each lithological unit was estimated by determining the slope failure angle of past landslides to develop cumulative distribution functions (CDF).
- To calculate the aggregated probability of a landslide, conditional properties (i.e., $PGA > 0.05g$) were used for a set of random variables (e.g., slope angle, lithological unit, PGA and PGV), Newmark's Method downhill equation was used to calculate the yield acceleration of the slope face (*section 3.3.1*). When the peak ground acceleration exceeds the yield acceleration given the condition that a pixel located at x,y with a slope angle of θ , and estimated friction angle of ϕ'_j sampled from the statistical distribution of the corresponding lithological unit (i.e., DOMS curves).
- A logic tree approach was used to develop the *LOS21* model that is dependent on a minimum threshold of shaking (i.e., $PGA = 0.05g$). The following landslide regression models were used: *AM88*, *JS07*, *BT07*, *SRS08* and *S16* (Reference *Table 3-6* for the regression model), with the following weights stated in *Table 3-7*. When the ratio of $\frac{a_y}{PGA} < 0.05$, method 1 is used, otherwise method 2 is applied.

- Probabilities of exceeding displacement thresholds, δ , of 0.03, 0.05, 0.07, 0.1, 0.13, 0.15, 0.2, 0.4, 0.6, 1.0, 1.5, 2.0, 3.0, 5.0, 10, and 100 m were determined for the following models: *AM88*, *JS07*, *BT07*, *SRS08* and *SI6*. The representative displacement model *LOS21*, was applied to the probabilities to calculate the final probability of exceedance for each displacement threshold.

Chapter 4: Landslide Hazard Analysis Results

4.1 Landslide Hazard Mapping Results

Seismic landslide hazard maps incorporating the multiple displacement models within a logic tree as described in Chapter 3 were created for the Western US based on a M 9.3 CSZ earthquake event. The evaluation of landslide hazards were limited to relatively shallow soil slope failures, whereas deep-seated landslides and debris runout and its impact to utility poles were not directly considered. For each x,y pixel, probabilities associated with exceeding displacements of 0.01, 0.03, 0.05, 0.07, 0.1, 0.15, 0.2, 0.4, 0.6, 1, 1.5, 2, 3, 5, 10, and 100 m were computed, resulting in a seismic landslide displacement hazard curve. Visualization of the results is facilitated through three seismic landslide hazard maps (Figure 4-1 to 4-3) developed using the landslide displacement seismic hazard curves assuming three probabilities of exceedance (POE) levels: 5%, 15% and 50%. The seismic landslide hazard maps in conjunction with fragility curves were used to evaluate the impacts to the ACTIVs transmission towers and poles.

To examine the results of the analyses in more detail, six different locations were selected to highlight the differences across the study area based on topography and seismicity. The City of Seattle is the furthest north location in the study area. It is positioned in Puget Sound with topography ranging from steep bluffs to mild slopes. Newport is a coastal city with a very high seismic hazard given its proximity to the CSZ. It is also a location where two critical lifeline corridors, Highway US 101 and US 20, connect. The topography of the City of Portland is generally characterized by milder slopes with several areas of steeper slopes between the river and the Forest Park area, and is located between the Coastal Range and Cascade Range within the Portland basin. Moderate shaking is anticipated from the CSZ. The City of Eugene is located in the southern Willamette Valley, consisting of milder slopes with moderate shaking

anticipated. Grants Pass, located near the border of Oregon and California, has significant topographic variability with numerous steep slopes but only moderate shaking is expected from the CSZ. Lastly, Smith River is located west of the California Coast Range in a high seismic region consisting of mild slopes.

Figures 4-1 to 4-3 present the estimated landslide displacement maps developed using the representative displacement model $LOS2I$, Eq (3-11) and for the different probability of exceedance thresholds (i.e., 5%, 15% and 50%, respectively). Note that the maximum value of the purple (low hazard, small displacement) to red (high hazard, large displacement) legend bar varies between Figures 4-1 to 4-3. The maximum estimated horizontal displacement was approximately 6.0, 3.5, and 1.1 m for 5%, 15%, and 50% probabilities of exceedance, respectively.

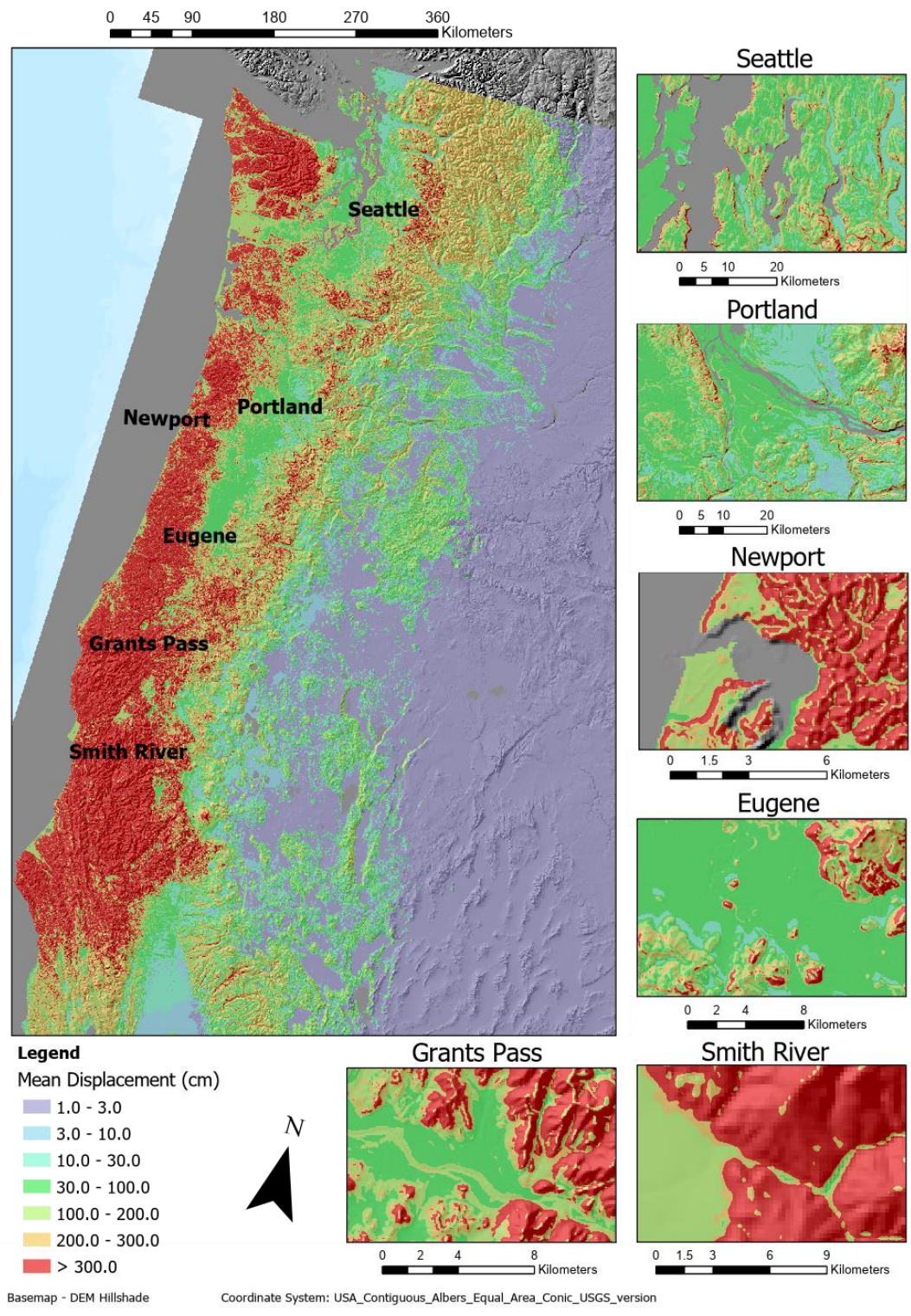


Figure 4-1. Estimated displacement maps developed using the representative displacement model *LOS21* assuming a 5% probability of exceedance (POE).

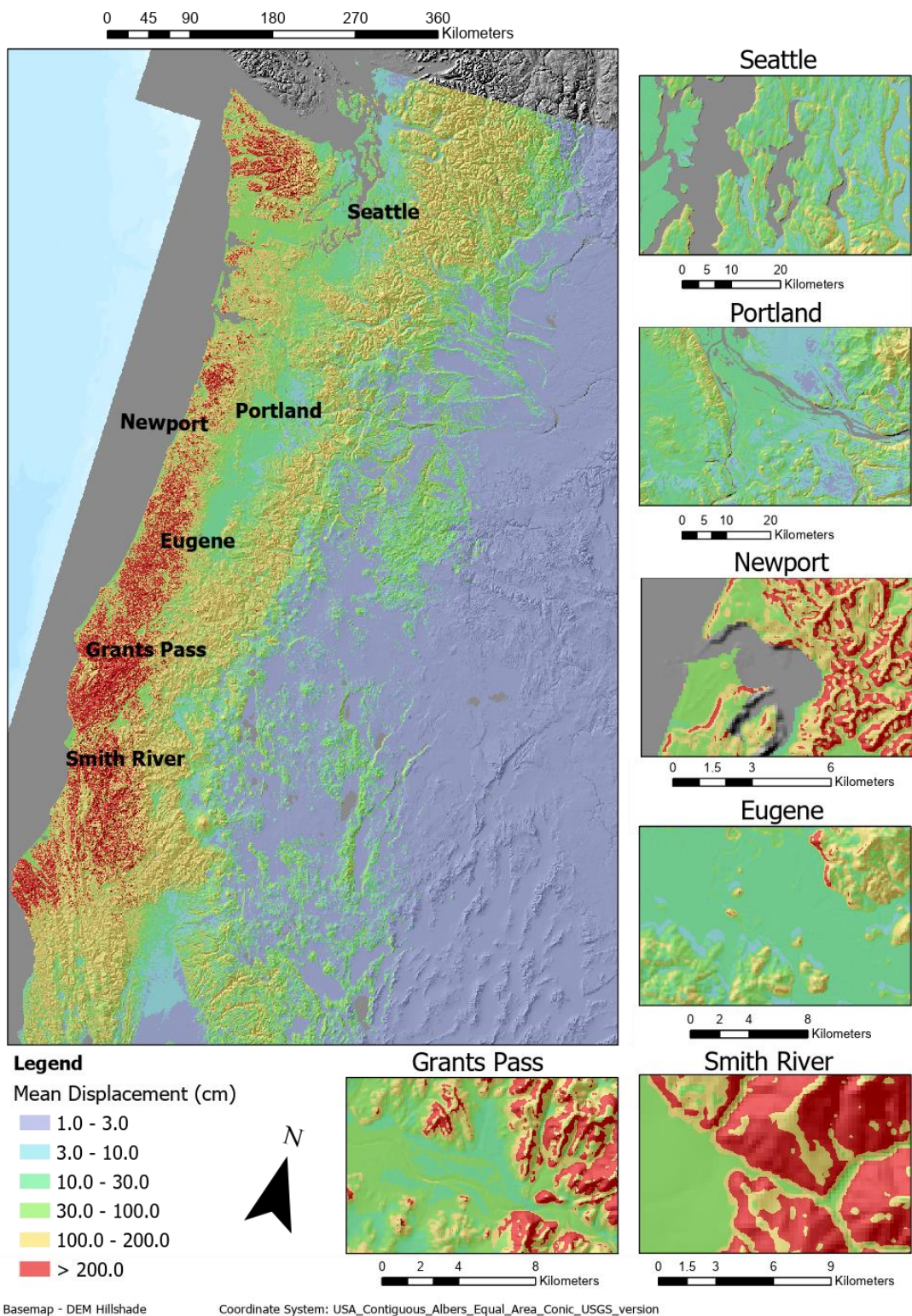


Figure 4-2. Estimated displacement maps developed using the representative displacement model *LOS21* assuming a 15% probability of exceedance (POE).

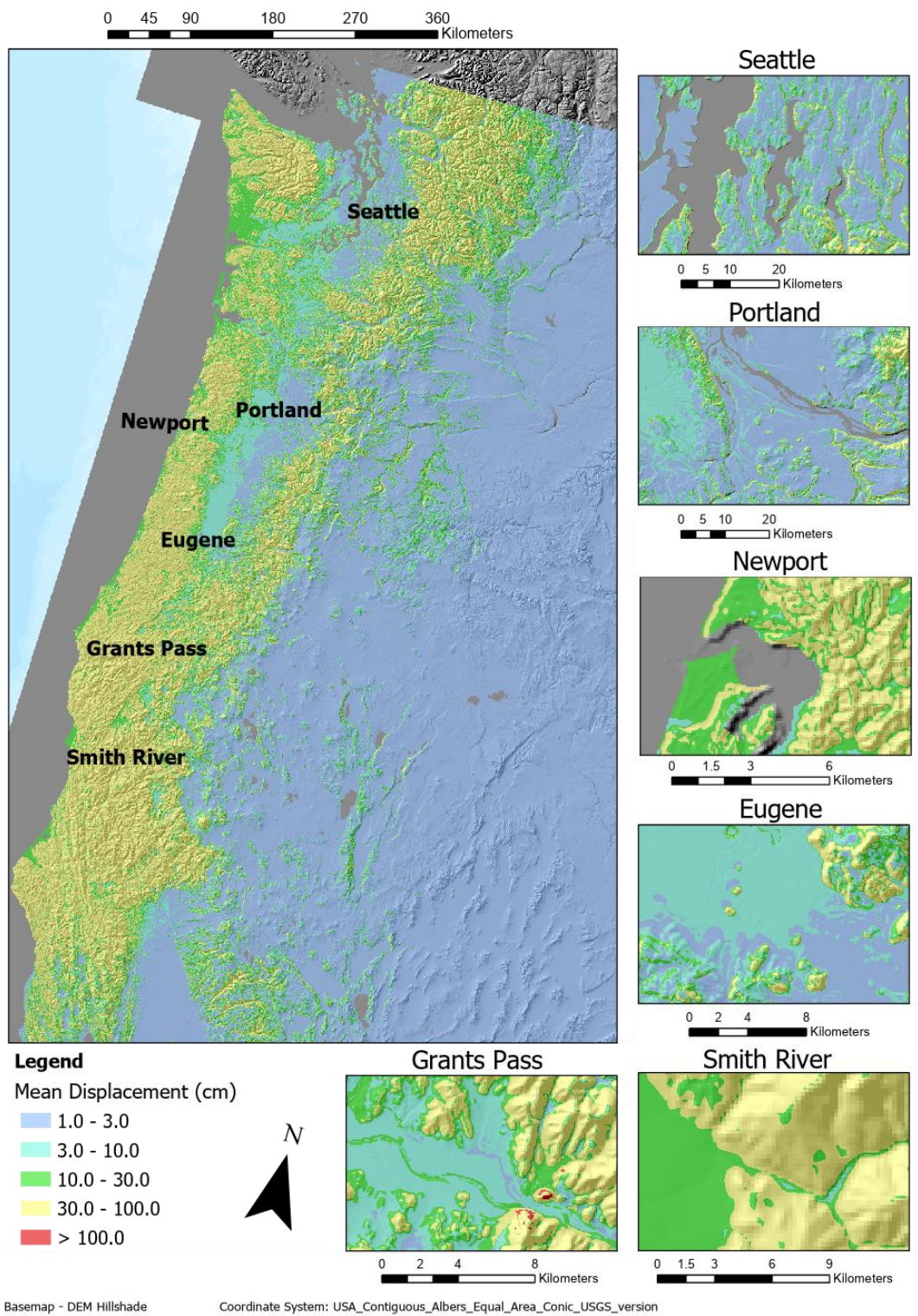


Figure 4-3. Estimated displacement maps developed using the representative displacement model *LOS21* assuming a 50% probability of exceedance (POE).

4.2 Validation

A qualitative analysis of the landslide hazard map assuming POE 5, 15 and 50% were conducted to evaluate the accuracy of the analysis. A post-earthquake landslide inventory does not exist for the study region; however, the Statewide Landslide Information Database for Oregon (SLIDO) V4.2 is one of the most comprehensive and detailed statewide landslide inventories available. Information regarding the location of the head scarp (polyline), deposits (polygon), and scarp flanks (polygon) of landslides were used for reference (Burns and Watzig 2020). Historical landslides are mapped as point features; however, note that the accuracy of the landslide points varies, particularly for those recorded prior to the availability of GIS software. In most regions, SLIDO only contains a subset of landslides that actually exist in the topography given that most were landslides were mapped from field investigations and aerial photographs where many of the landslide features were masked by vegetation. DOGAMI regularly updates portions of this database using lidar topographic information (Burns and Madin 2009), which has dramatically improved the ability to detect and map landslides for inventorying. Unfortunately, these mapping efforts take significant time and updates have only been completed for select locations in Oregon. Although this database does not distinguish the triggering mechanisms (e.g., seismic or precipitation) for each landslide, it does provide an indication of where landsliding has occurred and can be used to infer where landsliding is likely to occur. Some researchers (e.g., O'Banion et al.(2014); Mahalingam et al. (2016)) have investigated the likely triggering mechanisms of the landslides.

The extent of earthquake-induced versus precipitation-induced landsliding is unclear, particularly within the Pacific Northwest (PNW). A recent study (LaHusen et al. 2020) concluded that many of the deep landslides in the PNW were triggered by rain events, rather than

directly from a large earthquake. However, it is worth noting that widespread shallow landsliding can occur during earthquakes but leave no long-term evidence. Deep seated landslides triggered by earthquakes can also be retriggered from rainfall events, overprinting the evidence of the seismically induced landsliding. This have been observed in locations with similar climate and geology as the PNW. For example, from detailed investigations and comprehensive mapping efforts of earthquake-induced landslides from the Kaikoura, New Zealand earthquake (Massey et al. 2020), the depth of many landslides triggered by earthquakes were observed to be relatively shallow; nevertheless (Massey et al. 2020) documented many large, deep seated landslides in close proximity to the fault rupture.

Shallow landslides may also occur as a result of heavy rainfall (Tsai and Chen 2010). The increase in pore water pressure due to a rise in groundwater level is accompanied by the loss of shear strength as soils evolve from partially-saturated to fully saturated provides the mechanism for rainfall-induced slope failure. Accordingly, the occurrence of an earthquake during a wet season is likely to exacerbate slope instability.

Five sites located within the state of Oregon were evaluated to highlight the difference in seismicity across the study region as well as the influence of topography. The selection of the sites was also dependent on the location of existing electric power transmission lines provided by Homeland Infrastructure Foundation-Level Data (HIFLD). The City of Salem site contains milder slopes with a moderate number of transmission lines running through the site. The Estacada site contains shallow slopes with a low number of transmission lines. The West Hills of Portland and the Fox Valley sites are located in steep slopes with a moderate number of transmission lines. Lastly, the city of Springfield, where a large number of transmission lines

exists, contains shallow slopes through much of the city limits but is surrounded by hills with moderate-to-high slopes.

Figure 4-4 to 4-6 presents close-up views of the landslide deposits, scarp, scarp flanks and transmission lines for the five sites underlain with the seismic landslide hazard maps developed using *LOS21* assuming different POE (5%, 15% and 50%). The landslide deposits are identified using a brown overlay displaying the extend of soil displaced. The scarps and scrap flanks are identified using a blue line and outlined in black, respectively.

Most of the regions where significant displacement is anticipated are characterized by widespread landsliding without significant seismic activity. In most cases, the large displacement prediction inside the maps agree well with the existing landslide features from SLIDO including active and dormant steep slopes, which have historically failed. For example, in the West Hills of Portland and Fox Valley sites, the existing scarps and deposits from past landslides match closely to regions that are predicted to experience large displacements. Although the Salmon and Estacada sites have milder slopes than the Portland and Fox Valley sites, the existing scarps and deposits also match closely to the predicted displacement map.

Overall the maps show reasonable displacement results when compared with landslide inventory databases (i.e., SLIDO) and susceptibility maps (i.e., Burns et al. 2016; Sharifi-Mood et al. 2017). An overall trend of high displacement is observed along the west coast on steep slopes (i.e., high seismic region) and in proximity to the Cascadia Subduction Zone. For example, high displacements are limited to west of the Cascadia range due to its proximity to the seismic event. Note that some mapped landslide complexes encompass a large area with varying terrain which explains the variability in displacements estimated within those complexes as the entire area would not be expected to fail.

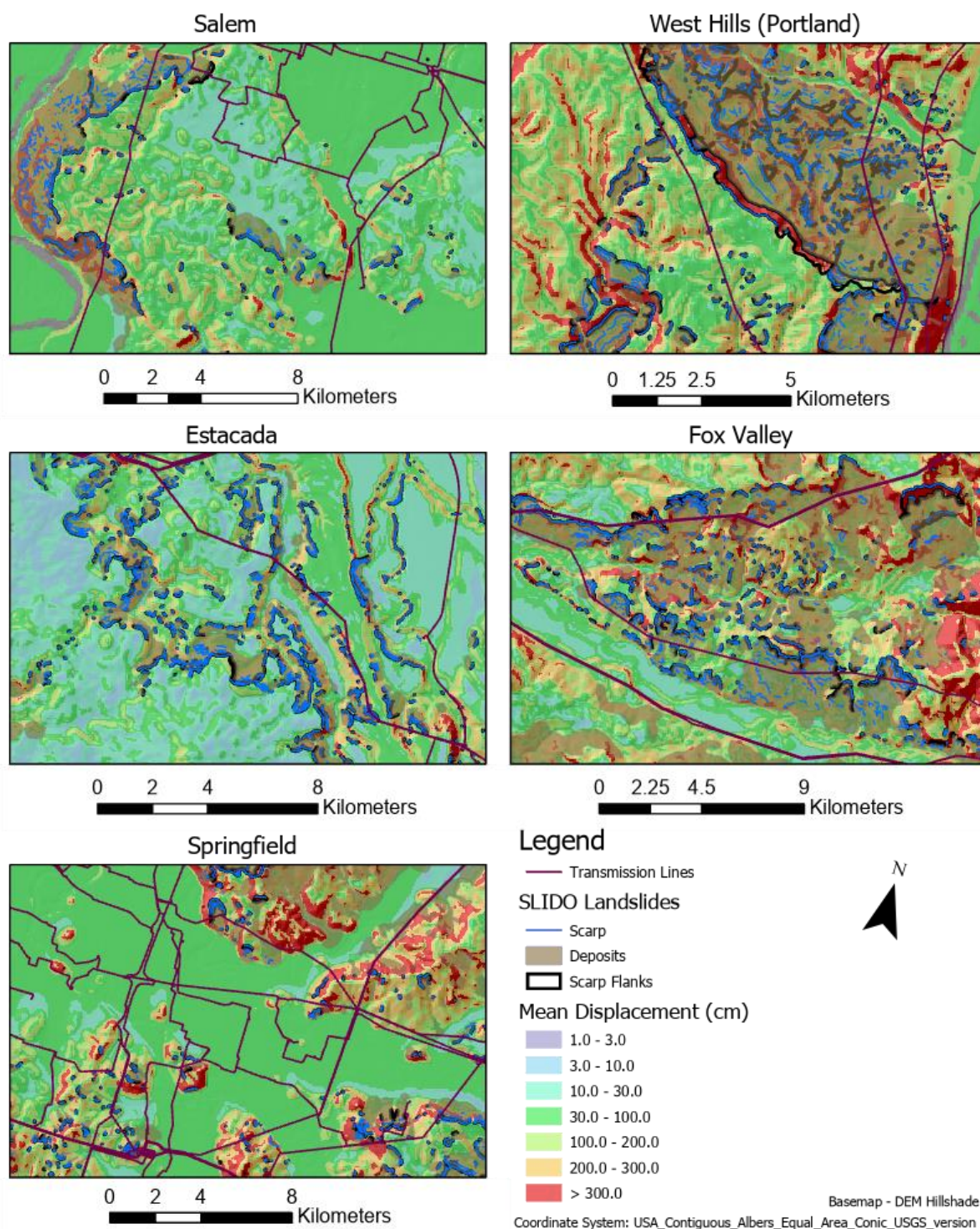


Figure 4 - 4. Seismic landslide hazard map using the *LOS21* displacement model assuming a 5% POE overlain with the SLIDO landslide hazard map and electrical transmission lines. The figure depicts 5 regions in Oregon in detail for comparison.

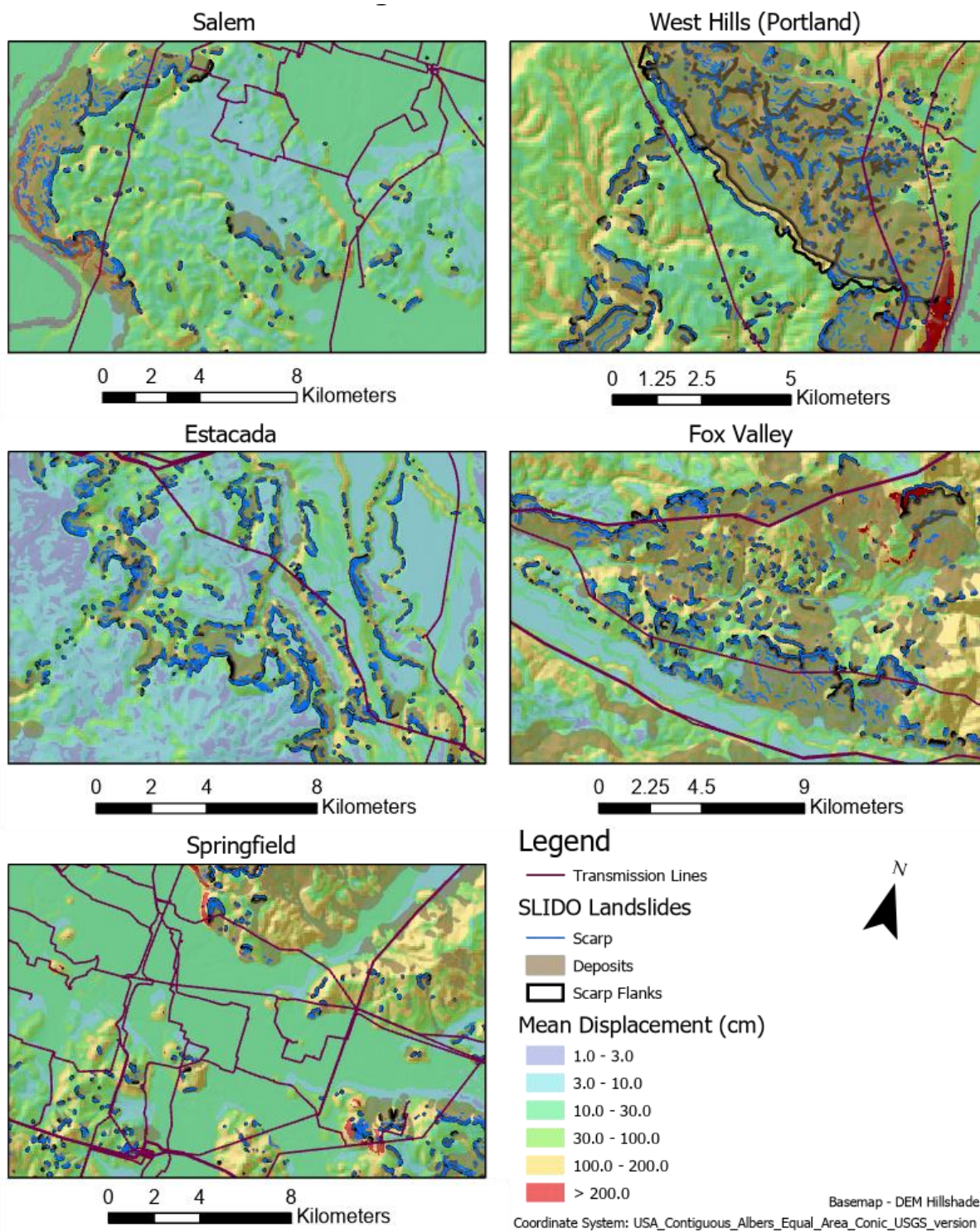


Figure 4 - 5. Seismic landslide hazard map using the *LOS21* displacement model assuming a 15% POE overlain with the SLIDO landslide hazard map and electrical transmission lines. The figure depicts 5 regions in Oregon in detail for comparison.

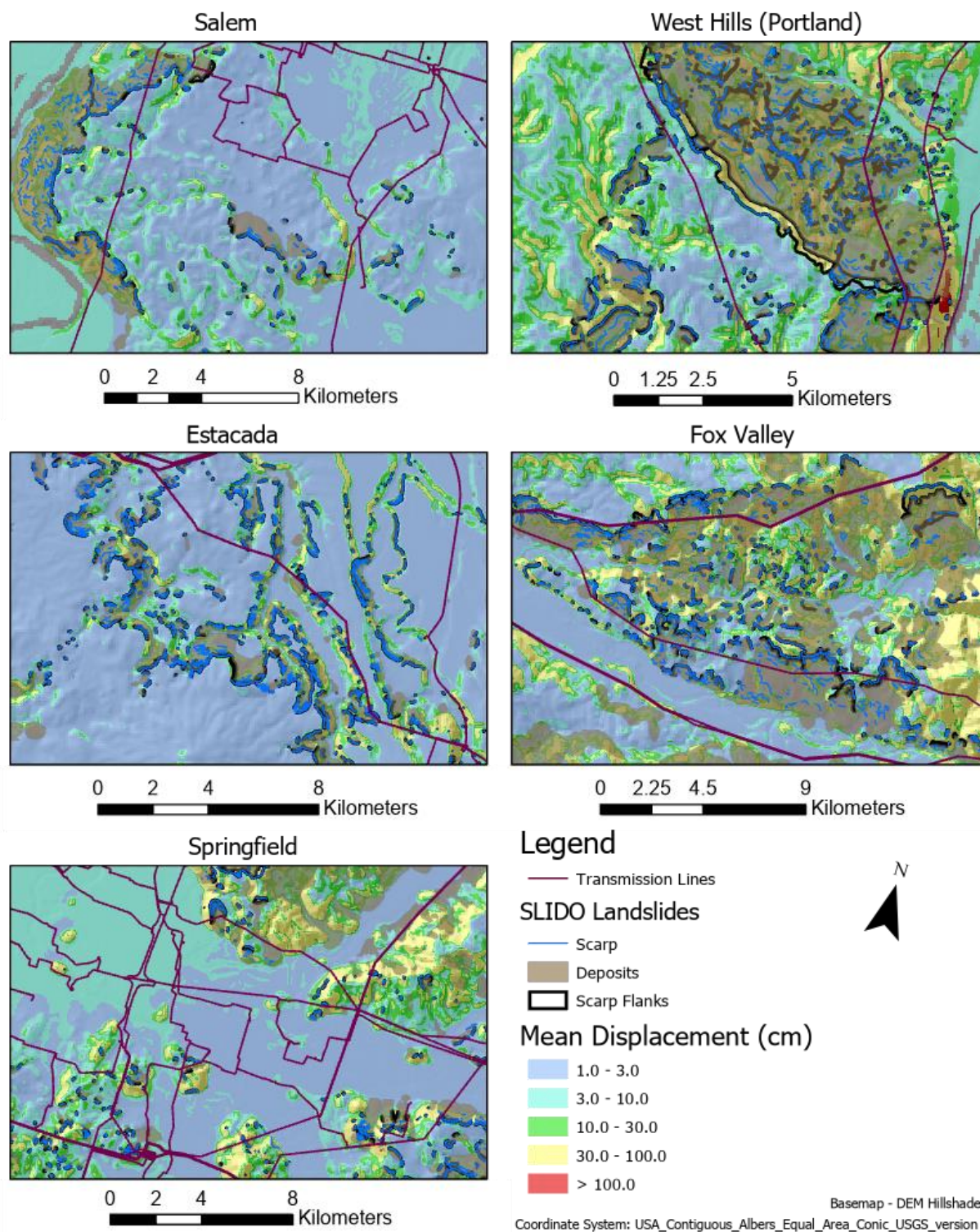


Figure 4 - 6. Seismic landslide hazard map using the *LOS21* displacement model assuming a 50% POE overlain with the SLIDO landslide hazard map and electrical transmission lines. The figure depicts 5 regions in Oregon in detail for comparison.

4.3 Power Grid Impacts

To evaluate the impacts the M9.3 earthquake would have on the western power grid, the amount of displacement for the transmission towers/poles were evaluated. In this analysis, the poles were treated as independent elements, such that cable tension between the poles and towers that could provide some resisting force or dragging force on poles adjacent but not in the slide mass, were not considered in this evaluation. The estimated maximum number of displaced poles were approximately ~156,000, ~132,000, and ~94,500 for 5%, 15%, and 50% probabilities of exceedance, respectively. Figures 4-7 displays the cumulative distribution of displaced transmission towers/poles for the three POE levels (i.e., 5%, 15% and 50%) greater than 0.01 m. For a 5%, 15%, and 50% POE, an estimated ~156,000, ~132,000 and ~94,500 poles are estimated to be displaced, respectively. Assuming a 5% POE, fifty percent of the poles are estimated to displace > 1.0 m and 23% are estimated to displace 0.3 to 1 m. Assuming a 15% POE, thirty five percent of the poles are estimated to displace > 1.0 m and twenty-five percent are estimated to displace 0.3 to 1 m. Assuming a 50% POE, zero-point five percent of the poles are estimated to displace > 1.0 m and forty percent of the poles are estimated to displace 0.3 to 1m. Note that while a single pole or tower itself may be able to handle a relatively large amount of displacement, the connecting powerlines would be damaged from different pole displacements.

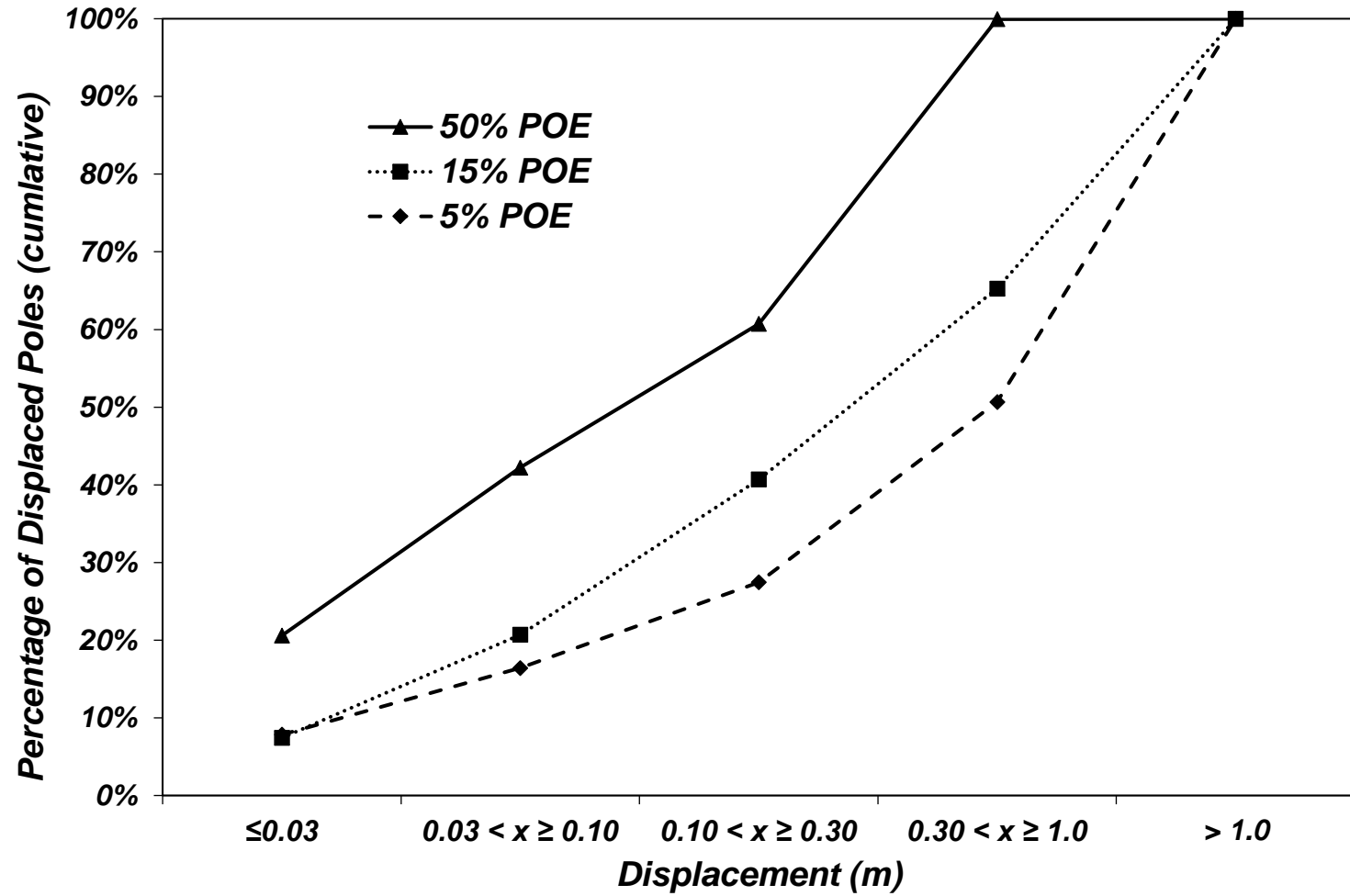


Figure 4 - 7. Cumulative distribution of transmission pole displacement greater than 0.01 m assuming per bin for a 5, 15 and 50% probability of exceedance.

4.3.1 Damage State Probability of Power Poles of according to developed fragility curves

The vulnerability of transmission towers and power poles within the study region were evaluated using displacement-based fragility curves developed from a questionnaire to industry experts in the PNW that was conducted by the larger NSF collaborative team (Brekken et al., Unpublished). The tower/pole fragility curves were generated using the rank-size distribution method to determine the expert consensus of estimated lateral shift values that would result in specific damage states for different types of poles/towers. Experts provided a minimum distance corresponding to temporarily restoration and a maximum distance corresponding to a full replacement including the procurement time for the item.

From these results, three sets of fragility curves were developed considering the voltage level transmitted through the lines, which dictates the material composition and structural design of the pole (i.e., wood (<115 kV), or steel (≥ 115 kV) necessary to support lines with those voltage. Fragility curves were prepared for each of the four damage states (i.e., slight, moderate, extensive, and complete) and for three transmission voltage levels of 69 kV (small, Figure 4-8), $69 \text{ kV} < \text{voltage} < 230 \text{ kV}$ (medium, Figure 4-9), and $\geq 230 \text{ kV}$ (large, Figure 4-10) given that higher voltage lines require more robust supports. Slight damage corresponds to assets that are still functional, but show some signs of cracking, misalignment, displacement, and/or bending, but does not require immediate repair or replacement. Moderate damage corresponds to assets that are still functional, and shows some signs of cracking, misalignment, displacement, and/or bending, and are considered to represent a high-priority for service. An asset is at risk of total failure if it experiences any further damage. Extensive damage corresponds to an asset that is not functional or able to operate safely, and requires de-energizing and removal from the system for repair or replacement. However, this damage state may not represent a total loss, as it may be

repaired more quickly than a new replacement can be ordered, delivered, and installed. The complete damage state indicates that an asset that must be replaced.

The fragility curve parameters (e.g., mean and standard deviation) of each damage state per each voltage level are provided in Table 4-1. The curves show display the probability of a pole reaching one of the four damage states based on the estimated displacement value, dependent on voltage transmitted through the transmission line. For example, if the voltage transmitted through the transmission line is designated as small (reference Figure 4-7(a)) and the estimated displacement is equal to 0.5 m, the probability of reaching a slight, moderate, complete and extensive damage state is 62%, 20%, 10% and 2%, respectively.

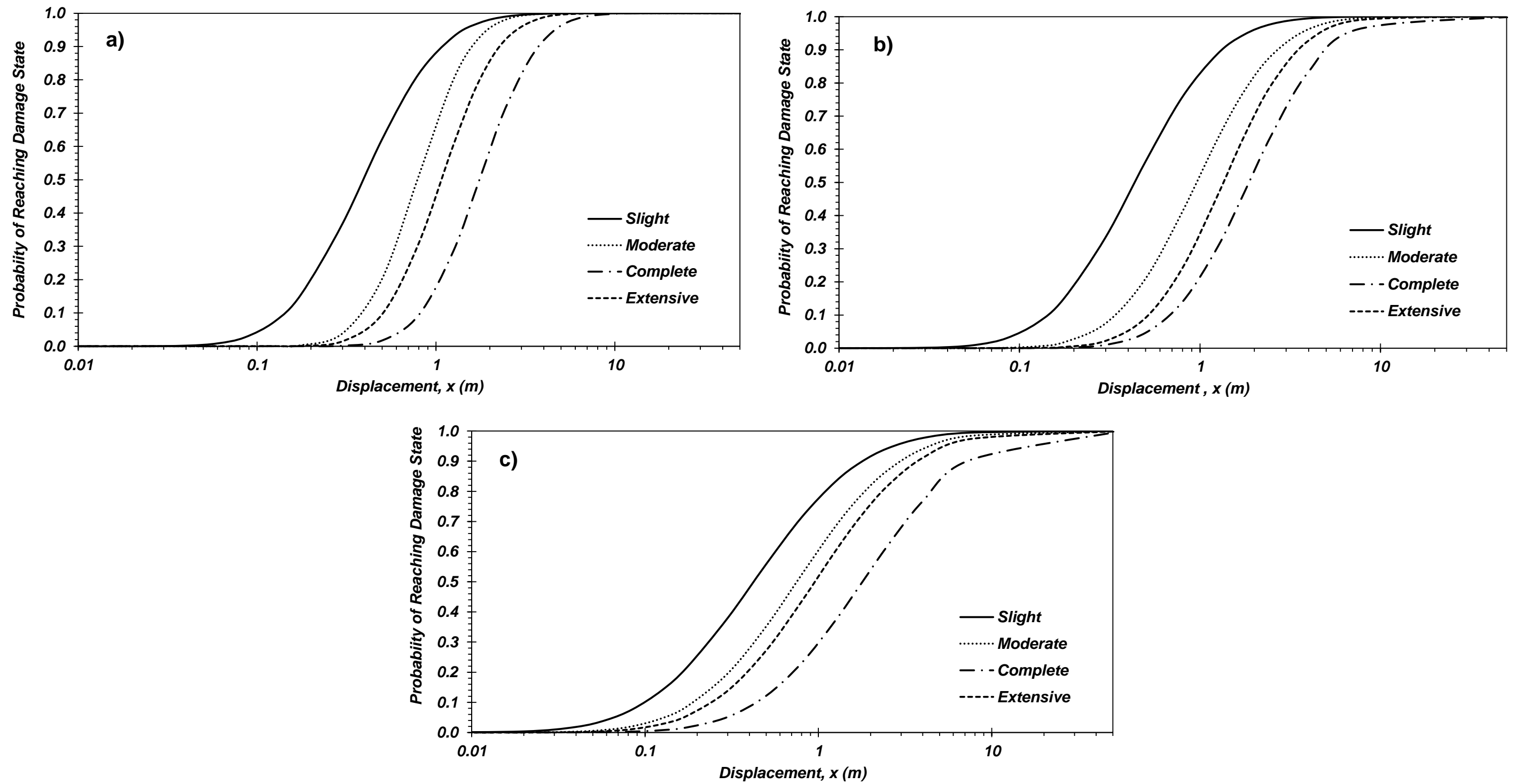


Figure 4 - 8. Developed fragility curves for the transmission lines for three voltage levels and each damage state: (a) small voltage ($< 69\text{kV}$), (b) medium voltage levels ($69 < x < 230\text{kV}$), and (c) large voltage levels ($\geq 230\text{kV}$).

Table 4 - 1. Fragility curves curve parameters (mean and STD) of each damage states per voltage level

<i>Damage State</i>	<i>Voltage Level</i>					
	Small (≤ 69 kV)		Medium (69 kV < voltage < 230 kV)		Large (≥ 230 kV)	
	Log Mean	Log SD	Log Mean	Log SD	Log Mean	Log SD
Slight	0.076	0.240	0.108	0.265	0.100	0.344
Moderate	0.289	0.167	0.348	0.245	0.275	0.327
Extensive	0.383	0.178	0.453	0.227	0.347	0.324
Complete	0.532	0.181	0.553	0.239	0.541	0.334

Using the fragility curve design parameters provided in Table 4-1, Equation 4-1 can be used to determine the probability of exceedance (POE) of a pole reaching a damage state based on the transmission line voltage level and estimated displacement:

$$a_{ij} = \sum P_{jk} d_{kj} \quad (\text{Eq. 4-1})$$

where, a_{ij} is the POE of a pole reaching a damage state based on the transmission line voltage level and estimated displacement. P_{ik} is the probability of displacement i given a threshold bin value k and d_{kj} is the probability of reaching a damage state j given a specific voltage level for a threshold displacement bin value k .

Given that sufficient shaking does not occur throughout much of the study area given its vast size, of all the transmission towers/poles in the western power grid approximately 23% (~192,000 poles) were estimated to experience some displacement. The probability of those poles experiencing a specific damage state were evaluated considering four different threshold values (i.e., 5%, 15%, 25% and 50%) to define the damage states (Figure 4-10).

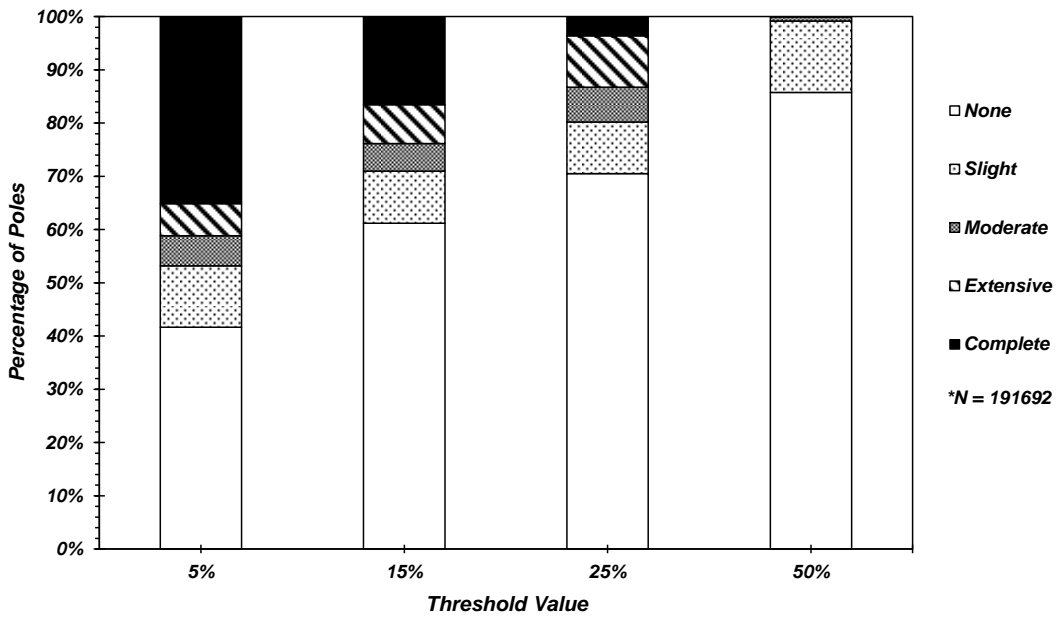


Figure 4 - 9. Percentage of poles reaching a damage state assuming various threshold values (i.e., 5%, 15%, 25% and 50%) for poles in the study area would be expected to experience some landsliding.

To visualize the distribution and impact of the poles being displaced and reaching one of the four damages states, a dot map was produced (Figure 4-10) showing the distribution of damaged poles for a threshold value of 25% denoted by their reached damages state. The map is underlays with the representative *LOS21* displacement map assuming a 50% probability of exceedance (POE). The distribution variance in reaching different damage state is extremely noticeable in the Portland area where there is a mixture of mild to steep slopes. A trend of poles reaching a complete damage state is noticeable along the coastline where the strongest ground motions are likely to occur.

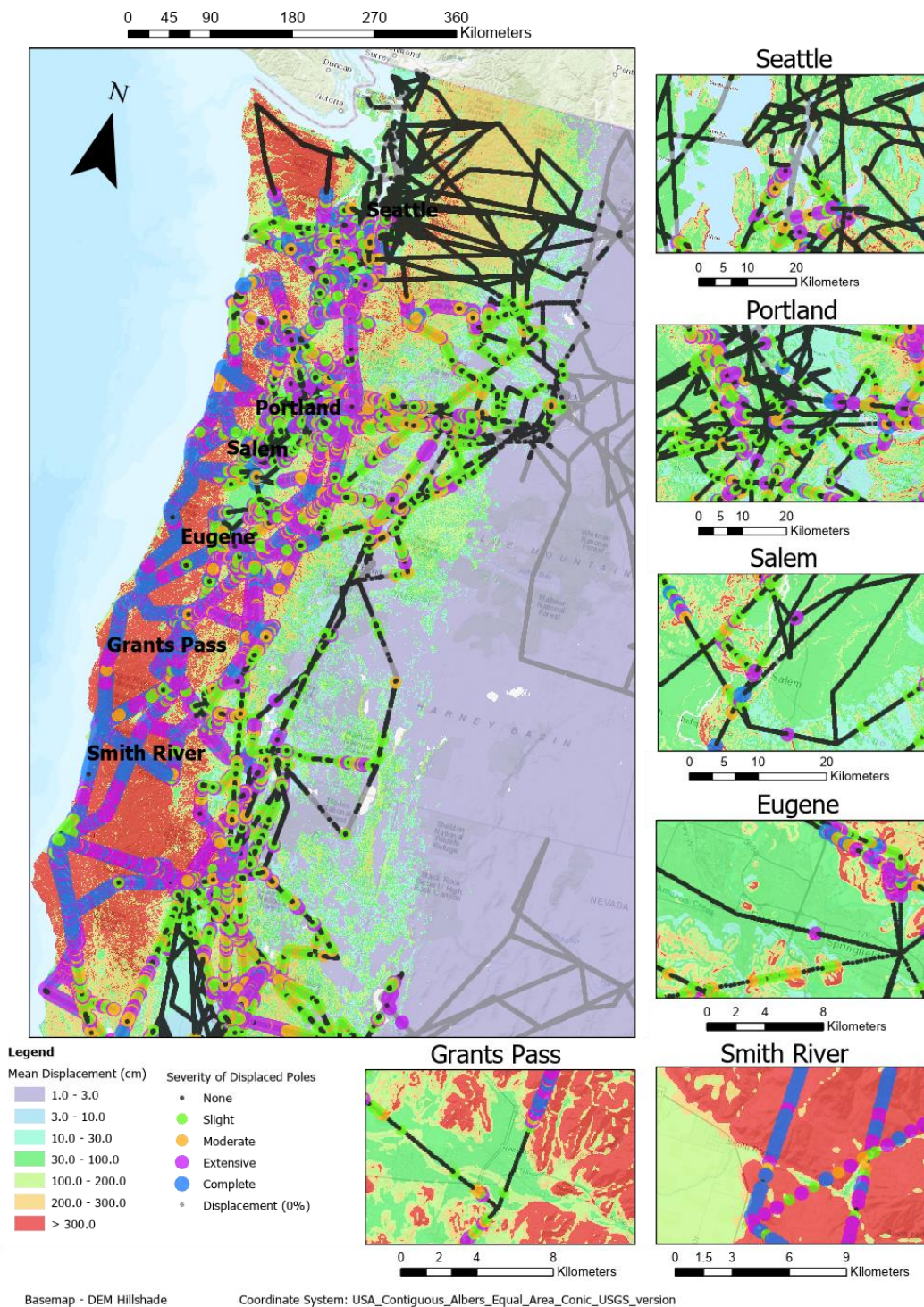


Figure 4 - 10. Dot map showing the distribution of damaged poles for a threshold value of 25% denoted by their reached damages state underlaid with the representative *LOS21* displacement map assuming a 5% probability of exceedance (POE).

4.4 Summary

This portion of the study consisted of analyzing the results of the probabilistic map developed in Chapter 3 through (1) validating the map using past mapped landslides (i.e., SLIDO) and (2) assessing the vulnerability of the power poles using fragility curves. Based on the evaluations performed, the following conclusions can be drawn:

- The maps show reasonable displacement results when compared with landslide inventory databases (i.e., SLIDO) and susceptibility maps (i.e., Burns et al. 2016; Sharifi-Mood et al. 2017).
- An overall trend of high displacement is observed along the west coast on steep slopes (i.e., high seismic region) and in proximity to the Cascadia Subduction Zone. For example, high displacements are limited to west of the Cascadia range due to its proximity to the seismic event.
- The 15% POE produced maximum displacement equal to 3.55 m, while the 50% POE map estimated maximum displacement of 1.10 m and 5% POE map estimated a maximum displacement of 6.07m.
- Based on the *LOS21* predictive displacement regression model, it was found that the electrical infrastructure located west of the Cascades in Washington, Oregon, and Northern California were determined to be subjected to the highest risk of landslide-induced damage.

Chapter 5: Site Response Analysis

5.1 Introduction

Site response analyses are commonly performed to estimate how a site will respond to earthquake-induced ground motions. Of particular interest is the potential for amplification or de-amplification of the bedrock motions when expressed at the ground surface or other interface with supported structures and other civil infrastructure, such as electrical substation components. To assess the broader work of the larger National Science Foundation (NSF) team, a series of site response analyses were completed on an electrical substation evaluation site located in the Portland metro area to compare the fragility curve analyses produced by the regional seismic hazard analysis (i.e., PGA) to the site-specific hazard and corresponding fragility curve assessments (presented in *Section 5.5*) for individual substation components.

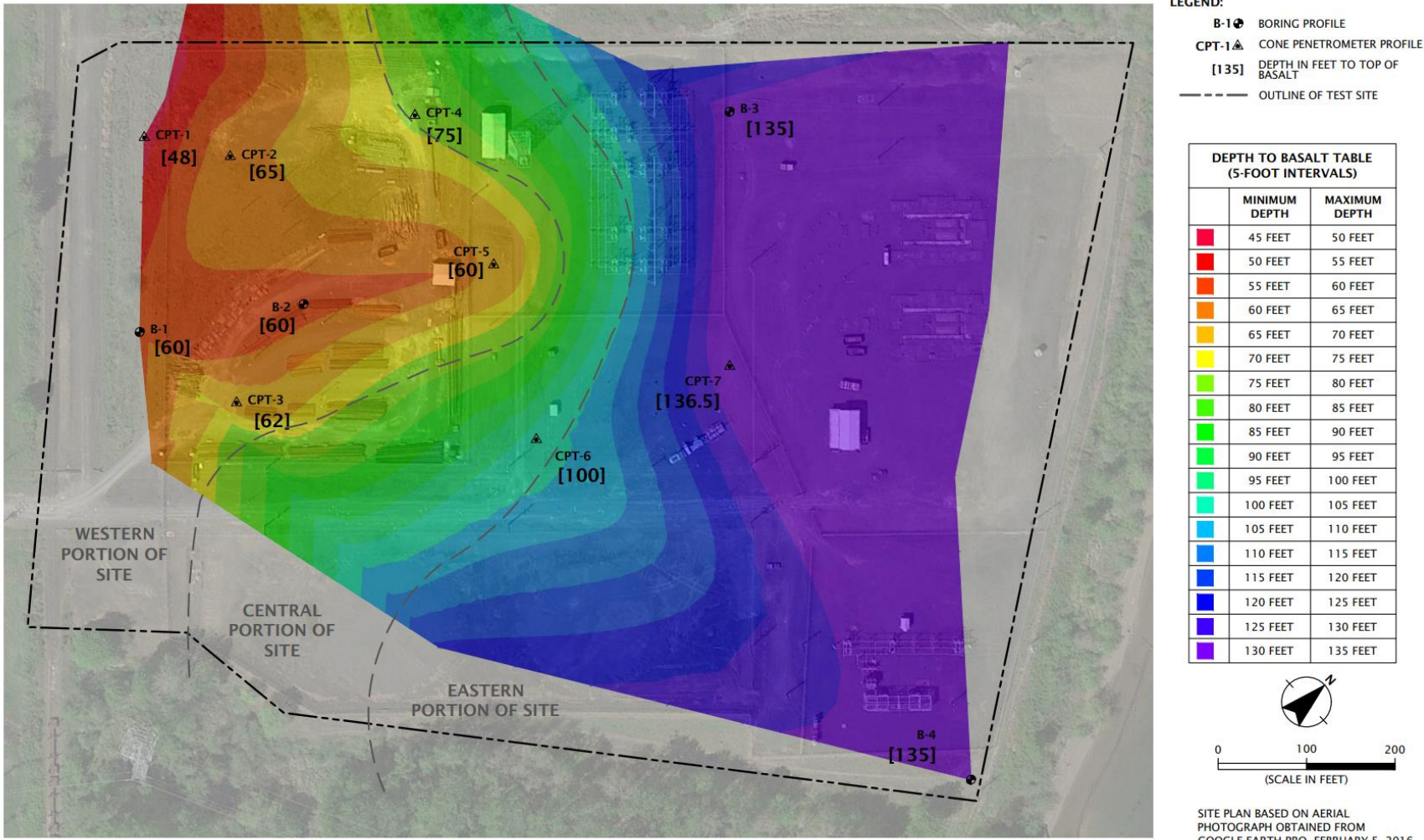
This process entailed: (1) developing the bedrock acceleration response spectrum representative for a scenario CSZ event, (2) selecting and scaling appropriate recorded ground motions to the representative bedrock hazard for the evaluation site, (3) developing representative soil profiles across the site based on available explorations, (4) conducting equivalent linear (EL) and nonlinear (NL) site response analyses (SRAs), and (5) using the results of the SRAs to evaluate the fragility of several typical electrical substation components.

A comparison between the developed peak ground acceleration (PGA) values from the site response analysis (SRA) and the regional seismic landslide hazard map was conducted. The variation of the peak horizontal acceleration (PHA) and shear strain with depth and the spectral acceleration at the ground surface was also generated and analyzed for the evaluation site.

5.2 Evaluation Site

The selection of a suitable evaluation site depended on a several criteria, including location, the availability of subsurface and substation data, and the type of site. The evaluation site selected for analysis is owned and operated by an electrical utility interested in understanding the seismic resilience of its power network. According to the generalized geological map used to develop the seismic landslide map, the subsurface at the evaluation site is classified as *unconsolidated, undifferentiated*; given its geological setting the majority of the soils overlying the basalt bedrock are alluvial and fluvial deposits. It is located along the Willamette River (roughly 0.10 km²), west of Portland on a relatively flat terrain < 10°. The USGS estimates a PGA equal to 0.34g at this site for a M9.3 CSZ scenario earthquake.

The available subsurface explorations for the site (Figure 5-1) includes seven cone penetration tests (CPTs) and four boreholes (mud-rotary) conducted to perform standard penetration tests (SPTs) and retrieve soil samples using 1.5” diameter split-spoon sampler in accordance to ASTM D1586 (ASTM D1586-12 2012). The site map also provides estimates of the depth to basalt bedrock from the exploration. The top of the rock increases in depth towards the east, with implications for the thickness of soil through which bedrock motions can amplify or deamplify. The information presented was adapted from material provided by Portland General Electric (PGE).



*THE MAP IS ADAPTED FROM INFORMATION PROVIDED BY PGE

Figure 5 - 1. Site map and exploration plan of the evaluation site indicating where the CPTs and borings were completed and the corresponding estimated contours indicating the depth of basalt rock.

5.3 Seismic Hazard for the M9.3 CSZ Scenario Earthquake

The target ground motions for the site were determined, in part, using the USGS M9.3 Cascadia Subduction Zone (CSZ) scenario earthquake (e.g., *Section 3.2.4*; USGS 2017) dataset. This dataset provides estimates of the anticipated bedrock acceleration response spectra for the CSZ scenario at periods of zero (i.e., PGA), 0.3, 1.0, and 3.0 s. The approximate distance between the scenario hypocenter and the site is ~141 km.

5.3.1 Interpolation of Mapped Bedrock Scenario Intensities

The grid spacing of the USGS scenario-based dataset was 3.51 km (latitude) by 2.49 km (longitude) rectangles spanning an area of ~12,300 km² and a total of 1,414 grid points for the whole M9.3 earthquake scenario area. Since the evaluation site did not coincide directly a grid point, planar interpolation was used to determine the PGA and PSA at the site using the four surround grid points (i.e., a plane was fit to the 4 points and interpolated). Figure 5-2 presents the PSA at 0.3, 1.0 and 3.0 s, and PGA for the bedrock layer in proximity to the evaluation site, indicating the gridded magnitudes considered in the planar interpolation.

The least squares regression used to develop the bedrock intensity is given by:

$$M = a_i + x * b_i + y * c_i \quad (\text{Eq. 5 - 2})$$

where M is the motion parameter of interest (i.e., PSA at 0.3, 1.0 and 3.0 s, and PGA), a_i , b_i and c_i are the three fitting parameters, and x and y are the latitude and longitude positions of the grid points.

Three fitting parameters (Table 5-1) were determined for each intensity measure (i.e., PSA at 0.3, 1.0 and 3.0 sec, and PGA) using ordinary least squares (OLS) regression to minimize the sum of squared errors (SSE) in the regression. Table 5-2 summarizes the target bedrock intensities resulting from the planar interpolation; note that the PSA at 0 s is equal to the PGA.

Table 5 - 1. Identified “fitting parameters” for the evaluation site to determine PSA at 0.3, 1.0 and 3.0 s, and PGA.

Fitting Parameters	PGA (<i>g</i>)	PSA 0.3 s	PSA 1.0 s	PSA 3.0 s
<i>a</i>	-3608.23	-5409.63	-3607.64	-3617.62
<i>b</i>	-29.72	-44.60	-29.72	-29.64
<i>c</i>	-0.23	-0.23	-0.23	-0.23

Table 5 - 2. Target peak spectral acceleration (PSA) and PGA representing the bedrock motion for the M9.3 CSZ scenario earthquake determined for the evaluation site.

Period (<i>s</i>)	PSA (<i>g</i>)
0.0	0.305
0.3	0.563
1.0	0.317
3.0	0.115

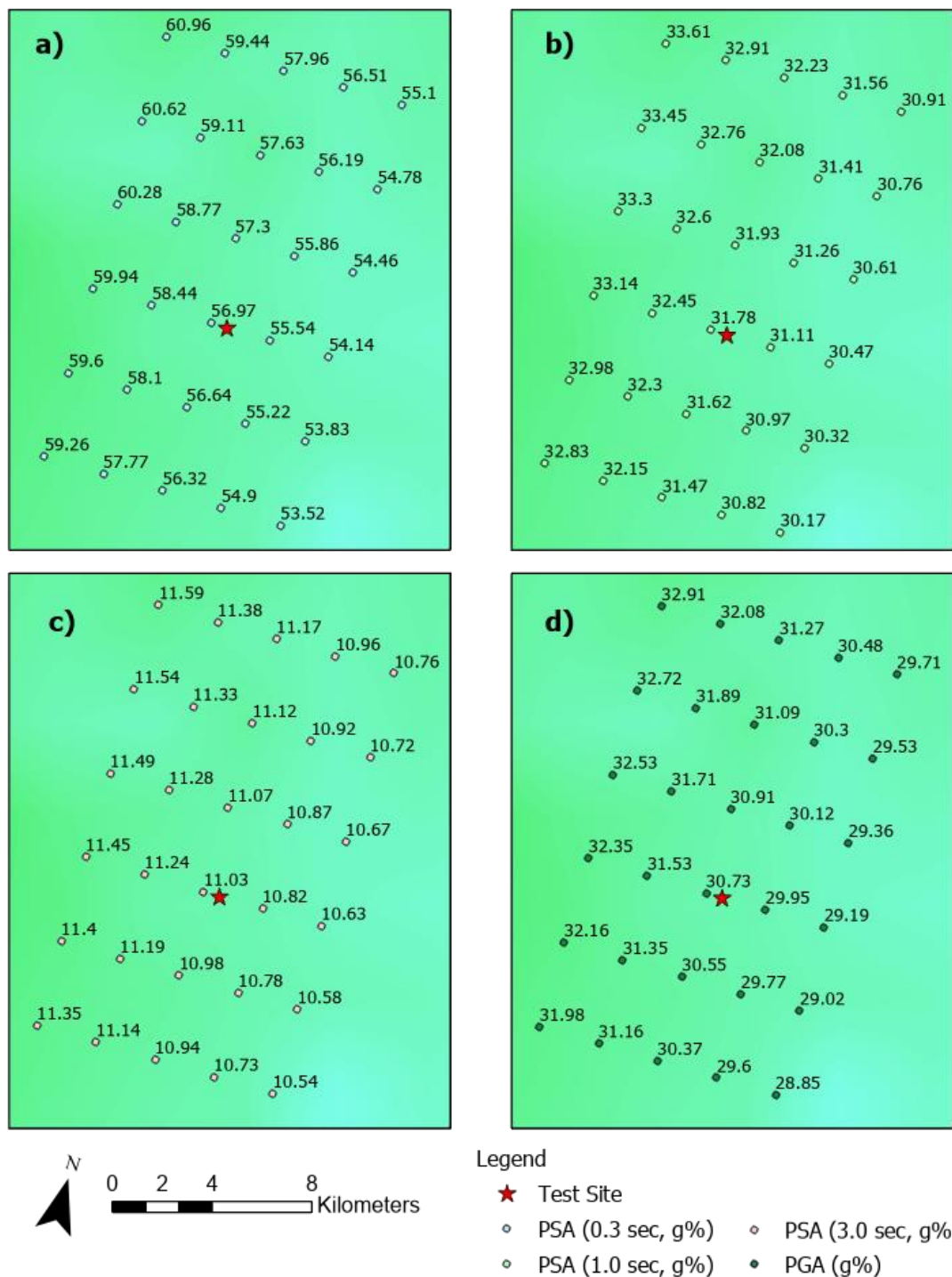


Figure 5 - 2. The intensity/ground motion (PSA and PGA) data for the rock layer near the evaluation site: (a) PSA at 0.3 sec, (b) PSA at 1.0 sec (c) PSA at 3.0 sec, and (d) PGA, in %g. The red star indicates the evaluation site location with respect to the data.

5.3.2 Ground Motion Selection

Ground motions for use in the SRAs were selected based on a variety of criteria stated in the next paragraph. Ten horizontal pairs (i.e., north-south and east-west) of ground motions were selected for evaluation from the Next Generation Attenuation Subduction (NGA-Sub) project (Bozorgnia et al. 2020). The NGA-Sub is one series of Next Generation Attenuation (NGA) projects directed towards database and ground-motion model development for applications in seismic-demand characterization. This database is the first to address subduction zones specifically, which are a dominant source of seismic hazard in many regions globally, including the Pacific Northwest region of the United States and Canada. It contains 70,107 three-component records from 1,880 earthquakes from seven global subduction zone regions: Alaska, Central America and Mexico, Cascadia, Japan, New Zealand, South America, and Taiwan (Bozorgnia et al. 2020). The response spectra provided in the database are equal to the *RotD50* spectra representing the median value of the spectral accelerations of the two motions.

The criteria used to select bedrock (input) ground motions in the SRAs consisted of: (1) the recorded motion should lie within 80 to 200 km from the earthquake epicenter, (2) the magnitude of the earthquake should be larger than M8, (3) the PGA should lie within the range of 0.15 to 0.61g to limit scaling errors, and (4) the shear wave velocity underlying the recording station should be larger than 600 m/s to represent the stiffness anticipated for bedrock. Paired ground motion records meeting three of the four criteria in the NGA-Sub database were identified for consideration of inclusion in the SRAs through spectral matching, described below.

Ten ground motion pairs scaled to the input (i.e., target bedrock) acceleration response spectrum interpolated from the USGS (2017) scenario event were selected based on the goodness of fit to the target spectrum. 48 pairs of ground motions met three of the four criteria described

above, only 10 motions were chosen. The scaling technique consisted of determining a multiplicative scale factor to uniformly increase or decrease the spectral acceleration at the four periods provided by the USGS (2017) dataset in an attempt to best replicate the target response spectrum. The scale factor was chosen through OLS regression to provide an average bias, defined as the ratio of the spectral acceleration of the target motion to that of the scaled ground motion record at a given period, closest to 1.0. Once a motion was scaled, they were evaluated for inclusion in the SRAs based on three goodness-of-fit parameters: (1) smallest root-mean squared error (RMSE) of *RotD50* spectral acceleration at a given period 0, 0.3, 1.0 and 3.0 s, (2) the mean bias in the scaled response spectra equal to 1.0, and (3) the coefficient of variation in the bias (COV) closest to 0. The resulting scale factors ranged from 0.68 to 1.59 with an average scale factor of 1.06 (Table 5-3).

Figure 5-3 displays the scaled *RotD50* response spectra for the ten selected ground motions their average for comparison to the target response spectrum. The average response spectrum matches the target well at 0, 1 and 3 s, however, it is somewhat larger than the target spectrum at 0.3 s. Table 5-3 summarizes the selected ground motion pairs and their associated goodness of fit metrics. Table 5-4 summarizes the ten scaled response spectra and the corresponding average plotted in Figure 5-3.

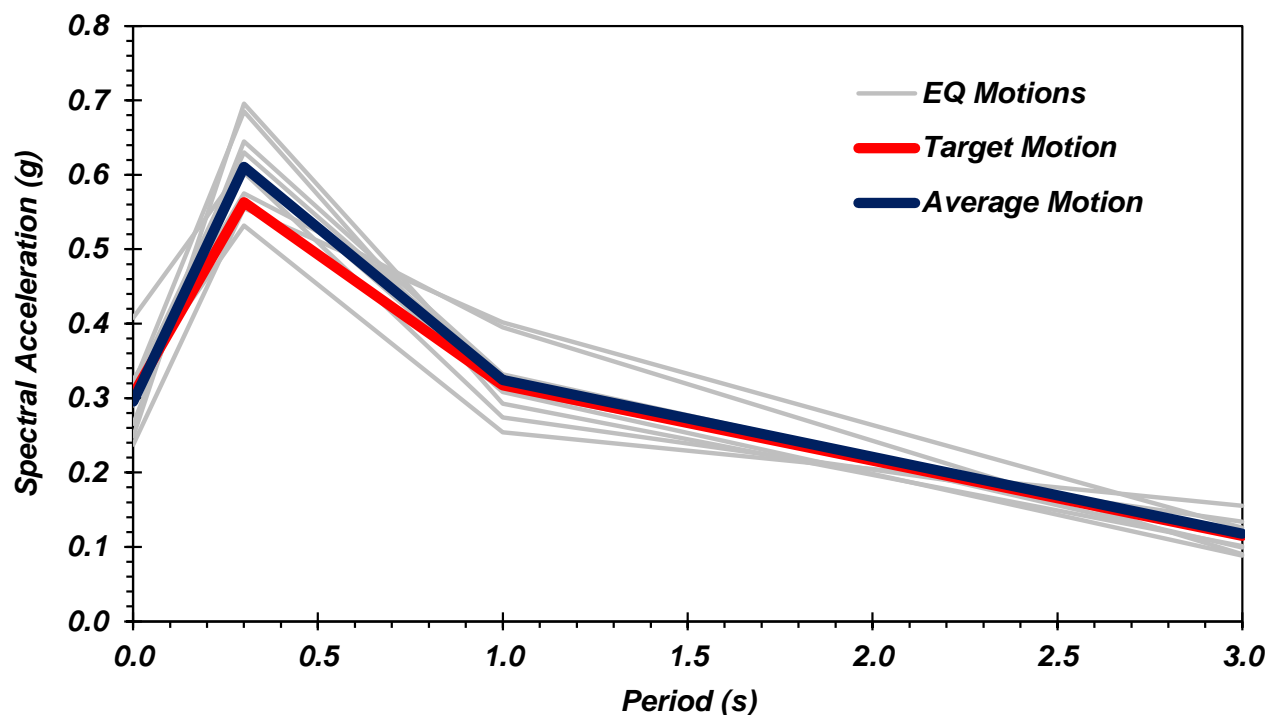


Figure 5 - 3. Comparison of the scaled response spectra and average scaled response spectrum to the target input response spectrum.

Table 5 - 3. Summary of the selected ground motions, scale factor, and goodness of fit metrics.

NGA-Sub Motion #	Scale Factor Producing Mean Bias = 1.0	RMSE	COV(Bias)
4000016	1.06	0.044	23%
4000521	1.19	0.063	14%
4001060	0.68	0.035	11%
4022909	1.06	0.032	13%
4022913	0.58	0.055	21%
4022989	1.90	0.041	21%
4028564	0.69	0.072	18%
4032552	0.69	0.046	12%
4032577	1.14	0.042	20%
6001373	1.59	0.059	23%
Average	1.06	0.049	17%

Table 5 - 4. Scaled and average response spectra for the ten selected ground motions.

Motion	Pseudo-Spectral Acceleration, PSA (s)			
	0 (s)	0.3 (s)	1 (s)	3 (s)
4000016	0.230	0.573	0.346	0.148
4000521	0.318	0.685	0.292	0.101
4001060	0.313	0.630	0.326	0.099
4022909	0.290	0.603	0.274	0.134
4022913	0.238	0.555	0.402	0.126
4022989	0.321	0.532	0.254	0.155
4028564	0.248	0.696	0.311	0.122
4032552	0.265	0.645	0.332	0.113
4032577	0.324	0.575	0.395	0.090
6001373	0.408	0.613	0.308	0.088
Average	0.295	0.611	0.324	0.118

5.4 Development of Representative Soil Profiles at each Exploration Location

The soil profiles produced for the SRAs were developed for each exploration providing 11 representative soil profiles demonstrating the stratigraphic variability across the site footprint, each denoted by its designation (e.g., B# and CPT-#; refer to Figure 5-1 for locations).

Representative soil layers were determined and the corresponding soil properties necessary for conducting SRA estimated using the available data. The boring profiles were developed using correlations to the SPT blow count, and the soil descriptions reported in the borehole logs. The CPT-based soil profiles were estimated using CPT correlations.

The soil layers were characterized into one of two soil types: (1) granular or (2) plastic. Plastic soils are generally fined-grained materials that are cohesive like clayey silt, sandy clay, silty clay, clay and organic clay, while granular soils are non-cohesive materials like gravel, sand or silt. This characterization was done to “calibrate” the layers to the best fit shear modulus (G) and damping curve models for the site response analysis. G is the ratio of shear stress to shear strain and describes the strain-dependent stiffness of the material in response to shear

deformation, while a damping curve describes the strain-dependent energy dissipation in response to shear deformation.

The following soil properties were determined for granular soil layers: moist unit weight (γ_m , kN/m³), vertical effective stress (σ'_{v0} , kPa) at the mid-point of each layer, shear wave velocity (V_s , m/s), drained shear strength (s_d , kPa) and effective friction angle (ϕ'). While these soil properties were determined for plastic soil layers: moist unit weight (γ_m , kN/m³), vertical effective stress (σ'_{v0} , kPa) at the mid-point of each layer, shear wave velocity (V_s , m/s), Over-Consolidation (OCR), Plastic Index (PI), and undrained shear strength (s_u , kPa). The underlying basalt rock layer was simulated uniformly with a shear wave velocity of 760 m/s, unit weight of 25 kN/m³, and a thickness of 10 m. The basalt layer (Figure 5-7) is encountered at a depth of 18.3 m (B1), 41.2 m (B3) and 23.0 m (CPT4) (refer to Figure B-2 and B-4 in Appendix B). The depth to bedrock is of high importance as it controls the spatial distribution of amplification on the site.

5.4.1 SRA Profiles based on Borings

The boring-based soil profile layers and corresponding soil properties were developed consistently using a variety of SPT-based correlations and interpretation of the borehole logs. The results of Atterberg limits tests reported in the borehole logs were used to generalize and correlate to the plasticity index in those layers and the CPT-identified plastic layers where such data was not available. Table 5-5 summarizes the SPT correlations used to develop the soil properties that were necessary, or informed selection of necessary, for conducting the SRAs.

Table 5 - 5. Summary of SPT correlations and assumptions used to develop the boring profiles soil properties.

Property	Equation	Reference or Comment
Moist Unit Weight, γ_m	Reference Table C-1 in the Appendix C	Kulhawy and Mayne (1990)
Correction for overburden Effects. $C_N^{1,3}$	Smaller of 1.6 or $2000/\sigma'_{v0}{}^{0.5}$	Liao and Whitman (1986)
Corrected, Standard Penetration Resistance, N_I^2	$C_N * N_{spt}$	
Shear Wave Velocity, $V_s^{1,3}$	$30 * N_{spt}^{0.215} * \sigma'_{v0}{}^{0.275}$	Wair et al. (2012)
Friction Angle, ϕ (°)	(a) $27.1 + 0.3 * N_I - 0.00054 * N_I^2$ (b) $\tan^{-1} \left(\left(N_{spt} / (12.2 + 20.3 * (\sigma'_{v0} / 2116)) \right)^{0.34} \right) * 57.3$ (c) $(20 * N_I)^{0.5} + 17$	(a) Wolff (1989) (b) Kulhawy and Mayne (1990) (c) Hatanaka and Uchida. (1996) Note that the average of the three methods was used
Overconsolidation ratio, OCR^3	$0.193 * (N_{spt} / (\sigma'_{v0}))^{0.689}$	Mayne and Kemper (1988)
Undrained Shear Strength, s_u^3	$\sigma'_{v0} * 0.3 * OCR^{0.82}$	Jana and Stuedlein (2021)
Drained Shear Strength, s_d^3	$\sigma'_{v0} * \tan(\phi)$	Mohr Failure Criterion
Coefficient of earth pressure, K_0 (at rest, Normally Consolidated)	$1 - \sin(\phi)$	Jaky (1948)

¹ N_{spt} refers to the initial blow count obtained from SPT data

²Assumed 60% energy

³ σ'_{v0} : vertical effective stress

5.4.2 SRA Profiles based on CPTs

The CPT-based profiles were determined using cone tip resistance, q_t , sleeve friction, f_s , and penetration-induced pore pressure, u_2 . Preliminary classification of the soil was determined using the Robertson and Wride (1998) and Robertson (2009) soil behavior index (SBT), I_c and cross-checked against nearby borehole logs. The depth to the groundwater table was determined using the nearby borehole logs and the CPT pore pressure data, where possible. Plasticity indices were estimated for the plastic layers in consideration of the nearby borehole logs that had identified similar soil layers. Table 5-6 summarizes the CPT correlations used to determine the OCR , friction angle, shear wave velocity, and drained or undrained shear strength of the soil layers identified in each sounding. Soil layers were identified using the cone tip resistance and I_c for each CPT-based soil profile, shown in Figure 5-4 CPT-1 for example, where the I_c magnitudes are color-coded by general soil type. For CPT-1, the develop cone tip resistance and I_c with depth graph matches very closely to the CPT-1 soil profile (refer to Figure B-4 in Appendix B).

Table 5 - 6. Summary of CPT correlations and assumptions used to develop the CPT profiles soil properties.

Property	Equation	Reference or Comment
$OCR^{2,5,6}$	$0.33(q_t - \sigma_{v0})/\sigma'_{v0}$	Mayne (2007)
Friction Angle, ϕ' ^{4,5,6}	$17.6+11*\log((q_t/P_{atm})/(\sigma'_{v0}/P_{atm}))$	Mayne (2007)
Undrained Shear Strength, S_u	$(q_t - \sigma'_{v0})/N_k$	Powell and Lunne (2005)
Shear Wave Velocity, V_s (average of both methods) ^{1,5,7}	(a) $2.27*(q_t^{0.412}*I_c^{0.989}*z^{0.033})$ (b) $2.62*(q_t^{0.395}*I_c^{0.912}*z^{0.124})*1.12$	(a) Eq. 5 - Andrus et. al. (2007) (b) Eq. 7 - Andrus et. al. (2007)

¹ z refers to depth at which the data point is collected

²Only if $I_c > 2.6$

³ N_k (cone factor) is assumed to be 18

⁴ P_{atm} atmosphere pressure

⁵ q_t – corrected sleeve resistance

⁶ σ'_{v0} : effective stress and σ_{v0} : total stress

⁷ I_c : soil classification (Robertson and Wride (1998) and Robert (2009))

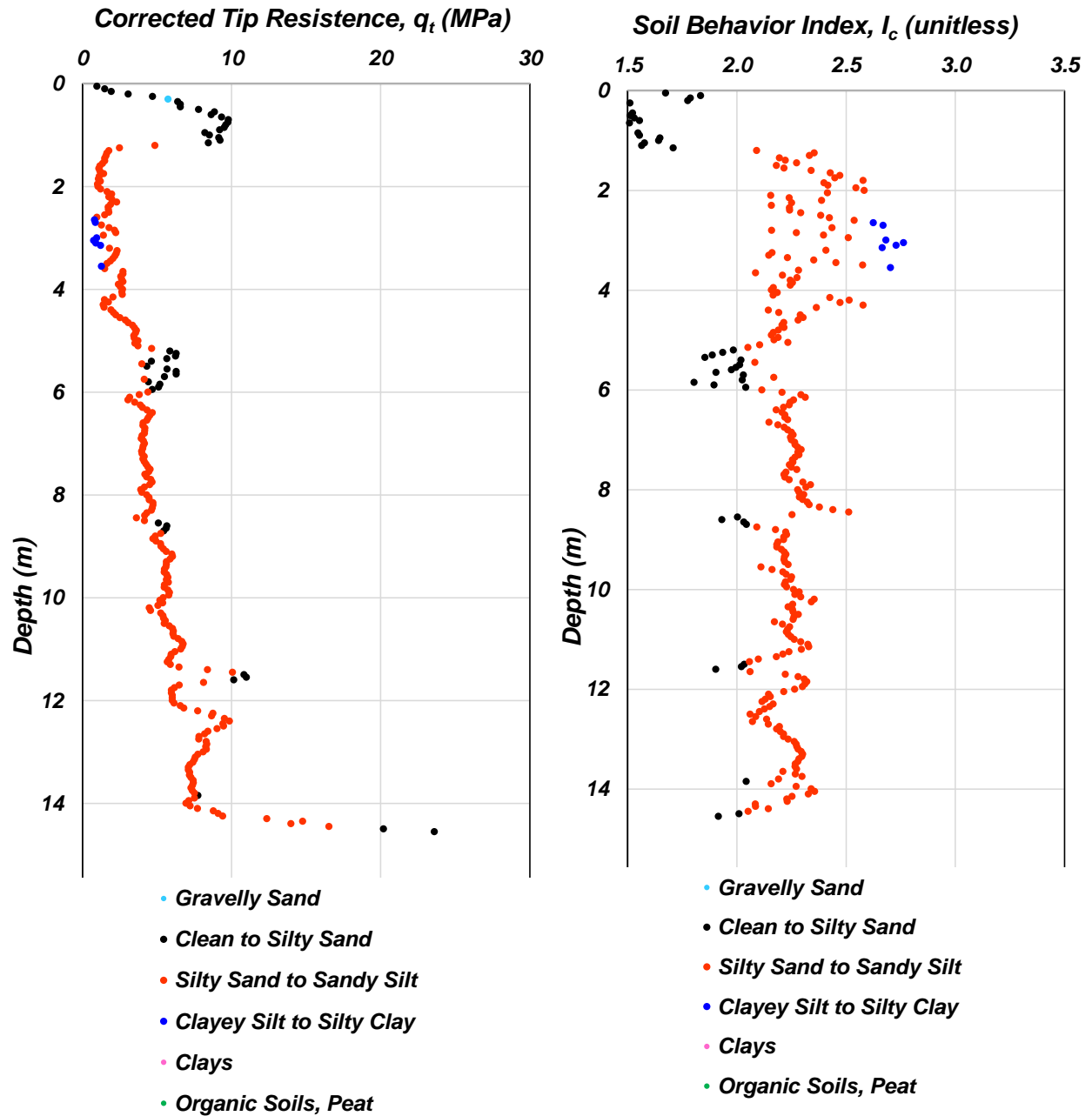


Figure 5 - 4. Variation of corrected cone tip resistance and I_c with depth for CPT-1 (refer to Figure B-5 in Appendix B).

Of the seven CPTs, three (i.e., CPT-2, CPT-5 and CPT-7) were accompanied with downhole shear wave velocity tests measured at ~1 m intervals. These soil profiles were therefore characterized using the V_s obtained directly from the downhole tests, rather than the correlation summarized in Table 5-6. Using the shear wave velocity data for CPT-2, CPT-5 and CPT-7, a shear wave velocity correlation was developed for the site (shown in Table 5-6).

Due to the complexity of the site containing both Holocene and Pleistocene soils, correlations considering the geological age of the soil was used to determine the V_s for CPTs without accompanying V_s measurements. Andrus et. al. (2007) developed correlations for predicting the small-strain V_s of soils of different geologic age from cone penetration resistance data in similar geological regimes as the evaluation site. Andrus et. al. (2007) found that the Holocene soils within their database were generally located within the top 10 m of a given profile, whereas the Pleistocene soils were predominantly located in the top 20 m of the profile (i.e., 51% were < 10 m and 48% were encountered between 10 to 20 m). The soils were characterized using the soil behavior index determined by Robertson (2009), the same method we used herein. Three methods (i.e., Holocene, Holocene combined, and Pleistocene combined) were proposed for this evaluation. The Holocene method assumes the soils are only Holocene-aged and an average scaling factor is determined using only the Holocene-age data to determine V_s . The Holocene combined and Pleistocene combined methods consider both Holocene and Pleistocene-age soils datasets to determine a scaling factor for V_s . Since the V_s was found to vary between Pleistocene and Holocene soils with similar penetration resistances, two scaling values were determined dependent on the soils age. The Holocene combined uses the combined age soil datasets to determine a scaling factor for V_s but assumes a Holocene age soil only, whereas the

Pleistocene combined uses a similar method to determine the scaling factor but assumes a Pleistocene age soil only.

To assess the accuracy of the three methods in estimating V_s at the CPT locations where V_s was not measured, the measured shear wave velocities from CPT-2, CPT-5 and CPT-7 were compared against the Andrus et al. (2007) correlations. The reported shear wave velocities corresponding to the seismic CPTs were corrected to account for the appropriate vertical travel time based on the proximity of the hammer to the rod string (reported herein as “measured”). Figure 5-5 compares the measured (i.e., corrected) shear wave velocity to the shear wave velocity correlated using the CPT-based models in Table 5-7 for CPT-2. The Holocene and Holocene combined methods produced consistently smaller shear wave velocities than that measured, whereas the Pleistocene combined method produced consistently greater shear wave velocities that appear to increase steadily with depth. Figure 5-6 presents the average of the Holocene and Pleistocene combined methods, which appears to represent the measured V_s well, and therefore the average of these two methods were used to estimate V_s for CPTs where V_s was not measured.

Table 5 - 7. Shear wave velocity correlations proposed by Andrus et. al. (2007).

V_s Model Type	Equation
Holocene Dataset	$2.27*(q_t^{0.412}*I_c^{0.989}*z^{0.033})$
Combined Dataset, but Holocene Only	$2.62*(q_t^{0.395}*I_c^{0.912}*z^{0.124})*0.92$
Combined Dataset, but Pleistocene Only	$2.62*(q_t^{0.395}*I_c^{0.912}*z^{0.124})*1.12$

* z refers to depth at which the data point is collected

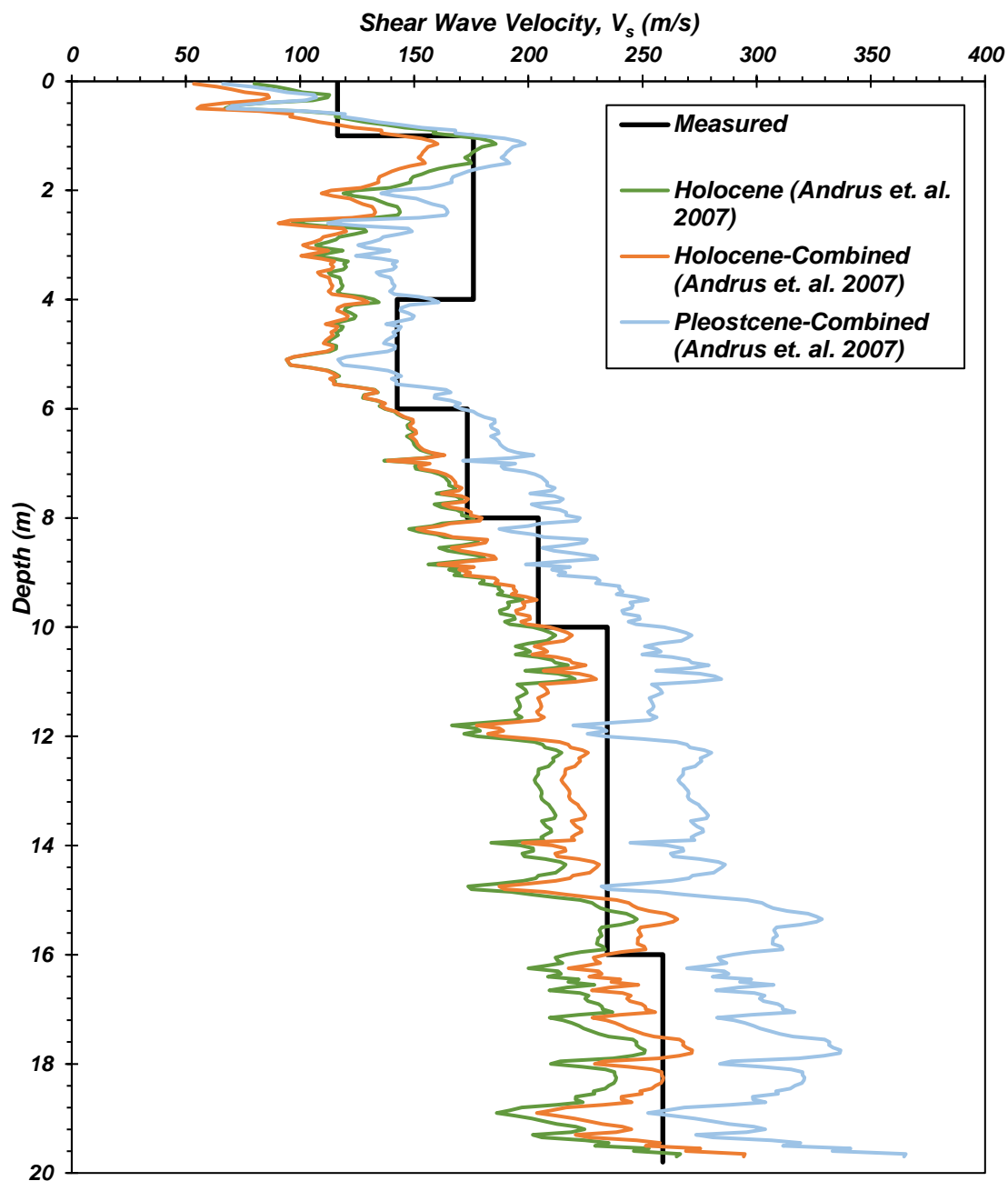


Figure 5 - 5. A comparison of the measured shear wave velocity and the three considered shear wave velocity correlations develop by Andrus et. al. (2007) for CPT-2.

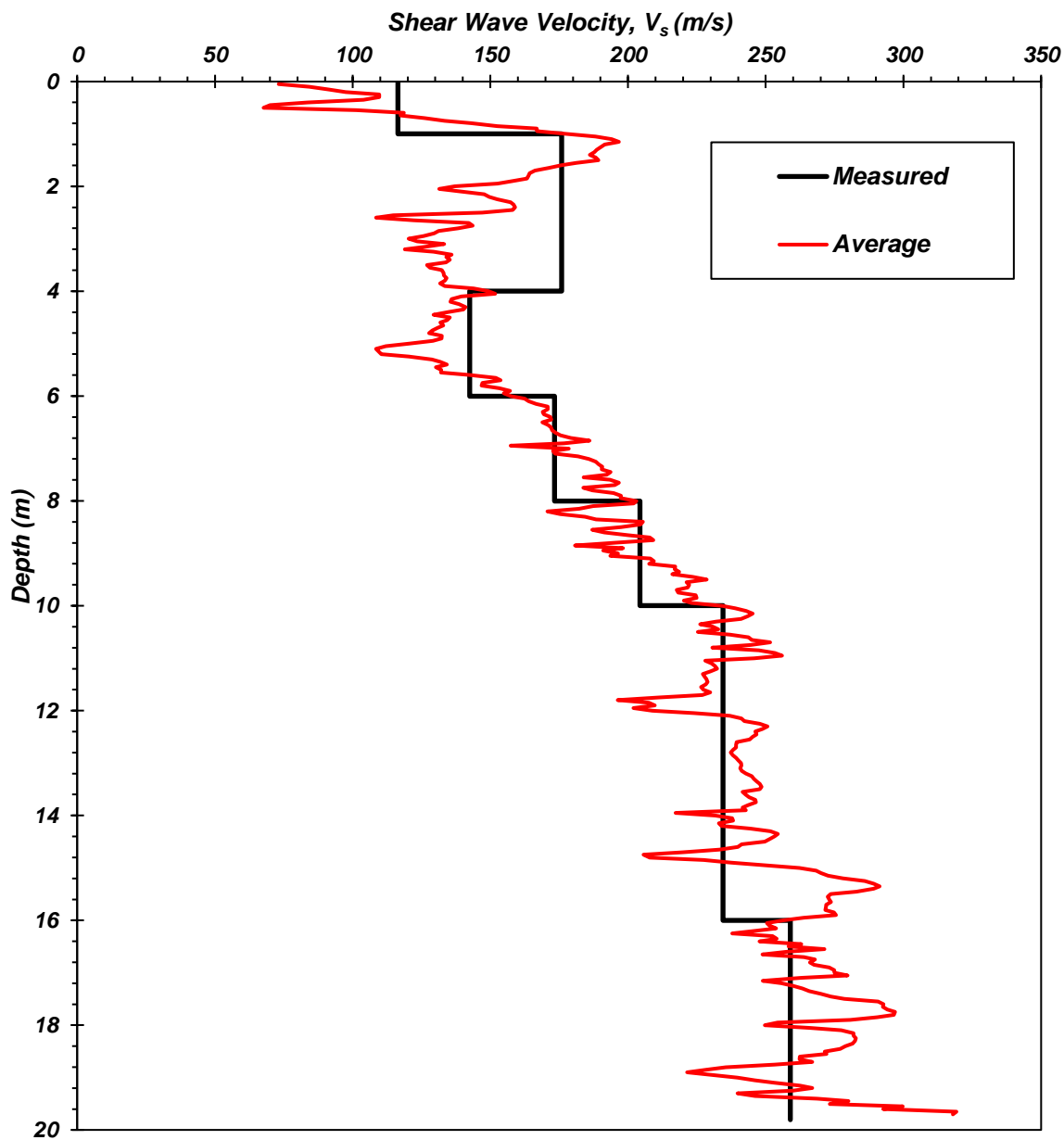


Figure 5 - 6. A comparison of the measured shear wave velocity and the combined Holocene and Pleistocene combined methods (average) correlation used for site applied to CPT-2.

5.4.3 Soil Profiles used for Site Response Analysis

Figure 5-7 presents the interpreted soil profile and corresponding soil properties for Boring 1 (B1) for use in the site response analysis, typical of each of the eleven profiles developed. Layers 1 and 2 consist of a fill comprised of medium to dense brown sand. Layer 3 is also fill but comprised of a lighter medium to dense gray sand. Layers 4, 5 and 6 are a plastic sandy silt that alternates from soft to medium to soft soil texture by layer, respectively, Layers 7, 8, 9 and 10 are granular silty sands that alternates from a loose to medium dense soil composition, respectively. Layer 11 at 18.3 m is where the basalt rock layer starts and extends for 10 m. For the purposes of site response modeling a new layer was created at the depth corresponding to the groundwater table to capture the correct effective stresses below the groundwater table. Figures B-1 through B10 in Appendix B presents the remaining ten soil profiles used in the SRA.

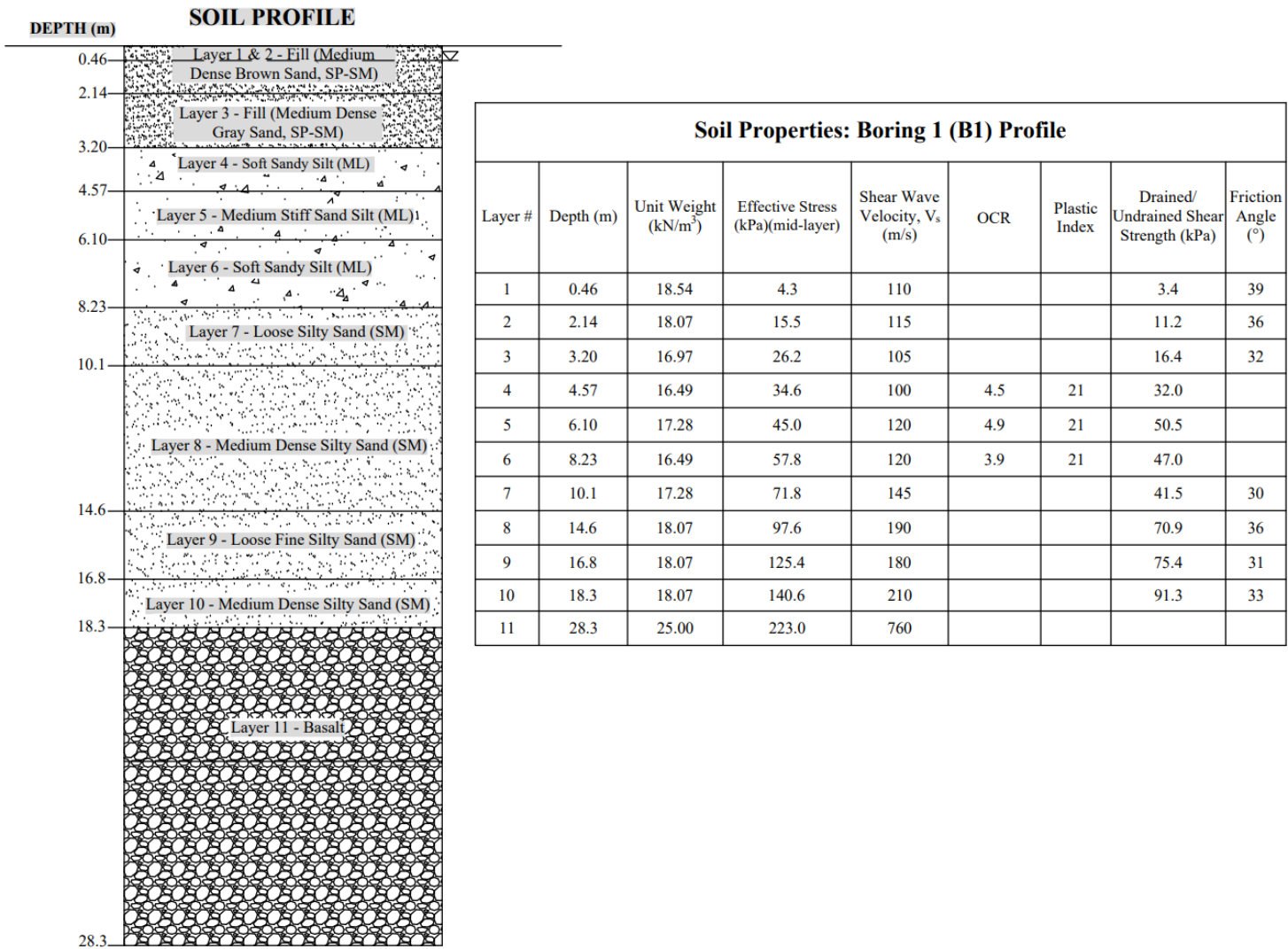


Figure 5 - 7. Diagram of the soil profile for use in site response analysis developed for Boring 1 (B1) and the associated soil properties.

5.5 Total Stress Site Response Analysis

The software package DEEPSOIL version 7.0.29 (Hashash et al. 2020a) was used to simulate one-dimensional NL and EL site response at each soil profile. The NL time domain model site response analyses incorporate changes in the nonlinear hysteresis of stress and strain during the ground motion and evaluated for each time step in the earthquake record. This more rigorous approach can better capture soil behavior under large strains such as for soft soil sites subject to strong ground motions. NL analyses require greater care in the development of required input parameters such as model parameters, viscous damping and profile discretization. The EL model employs an iterative procedure in the selection of the soil shear modulus (G) and damping ratio. They are defined by discrete points or by defining the soil parameters that define the backbone curve of one of the nonlinear models. When defining the soil curves using discrete points, the shear modulus and damping ratio are defined as functions of shear strain. The variation in shear modulus over the course of the simulation is captured using shear modulus reduction curves which are defined by the ratio of G and G_{max} , which is the small-strain, linear-elastic, maximum shear modulus that a soil can exhibit (Hashash et al. 2020b). The variable G_{max} is a fundamental and essential soil property for determining the deformation characteristics and dynamic response of a material. A common method used to determine G_{max} is shown in equation 5-2.

$$G_{max} = \rho * V_s^2$$

(Eq. 5 - 3)

where, ρ is the density of the material.

The damping curve represents the rate at which energy is dissipated by the soil based on the strain magnitude. Mechanisms that contribute to material damping include friction between

soil particles, strain rate effects, and nonlinear soil behavior. The hysteretic damping ratio can be calculated using Eq. 5-3:

$$D = \frac{W_D}{4\pi W_S} \quad (\text{Eq. 5 - 4})$$

where, W_D is the energy dissipated in one cycle of loading (area inside the loop), and W_S is the maximum strain energy stored during the cycle (area of the triangle) shown in Figure 5-8.

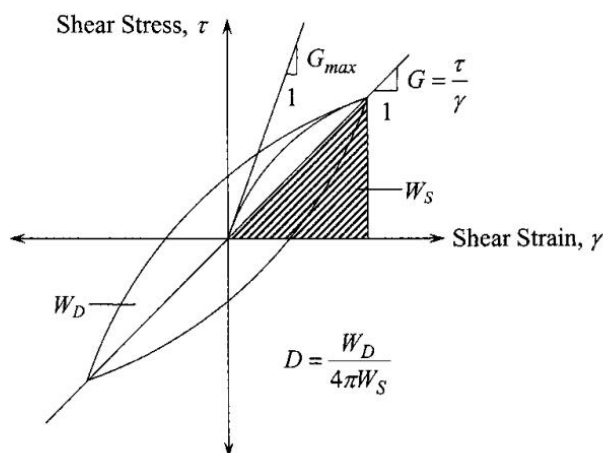


Figure 5 - 8. Hysteretic loop for one cycle of loading showing the G_{max} , G and D (From Zhang et al. 2005).

Refer to *Section 2.2.3* for information regarding the differences and similarities in NL and EL approach. A total stress site response analysis was conducted rather than an effective stress analysis; thus, excess pore pressures that may be anticipated to develop during shaking were not modeled.

5.4.1 Soil Models and Model Parameters

Use of DEEPSOIL requires specification of the G/G_{max} and damping curves. There are two main hyperbolic models used to develop these curves for soil: the General Quadratic/Hyperbolic Model (GQ/H), and the Pressure-Dependent Modified Kondner-Zelasko

(MKZ) Model (Hashash et al. 2020b). The GQ/H model has a curve fitting scheme that automatically corrects the reference curves (such as Darendeli (2001)) to achieve the specified shear strength at large strains. The curve fitting parameters θ_1 through θ_5 are used to preserve the modulus reduction curves obtained from reference studies (Phillips and Hashash 2009; Darendeli 2001). The parameters can be obtained from Groholski et al. (2016) based on maximum shear strength of the material or the values can be generated through the program. The MKZ model is pressure dependent and requires two additional parameters to estimate the stress-strain curve to produce the backbone curve. The GQ/H model was used for the site response analyses conducted herein.

There are multiple fitting procedures (i.e., Masing Rules (MR) , extended Masing rule (MRD) and damping curve (DC)) that are used to fit soil curves to model the hysteretic, unloading-reloading behavior of the soil. The MR procedure finds the parameters that provide the best fit for the modulus reduction curve with potentially significant mismatch of the damping curve, while the MRD procedure finds the parameters that provide the best fit for both the modulus reduction and damping curve and the DC procedure find the parameters that provide the best fit for the damping curve with potentially significant mismatch of the shear modulus backbone curve. A non-Masing model was used in this analysis because Masing's rules provide a poor match to the damping behavior of soil at large strain and do not provide the correct hysteretic damping at small strains (Brandenberg and Yniesta 2015).

The Darendeli (2001) and Vucetic and Dobry (1991) shear modulus and damping curve models were selected for the references curves for granular and plastic soil, respectively, because these models require the least amount of data, and because limited data were available. The Darendeli (2001) model depends on the following parameters: PI , OCR , K_0 , σ'_{v0} and loading

frequency, f . The G/G_{max} curve is developed using Eq. 5-4, where γ_r is the reference strain, γ_c is the cyclic shear strain and σ'_m is the mean effective confining pressure (atm).

$$\frac{G}{G_{max}} = \frac{1}{1 + \left(\frac{\gamma_c}{\gamma_r}\right)^{0.919}}$$

(Eq. 5 - 5)

where $\gamma_r = (0.0352 + 0.0010 * PI * OCR^{0.3246})\sigma'_m{}^{0.3483}$ and $\sigma'_m = \frac{\sigma'_{v0}(1+2k_0)}{3}$. To apply the Darendeli (2001) model on granular materials, it was assumed that $PI = 0$, $OCR=1$, and $f = 1$, while the K_0 value is layer dependent.

The damping curves were estimated using Eq. 5-3 but applied to the G/G_{max} developed using Eq. 5-4 to determine the energy dissipated in one cycle of loading and the maximum strain energy stored during the cycle. Figure 5-9 displays the Darendeli (2001) G/G_{max} and damping curves.

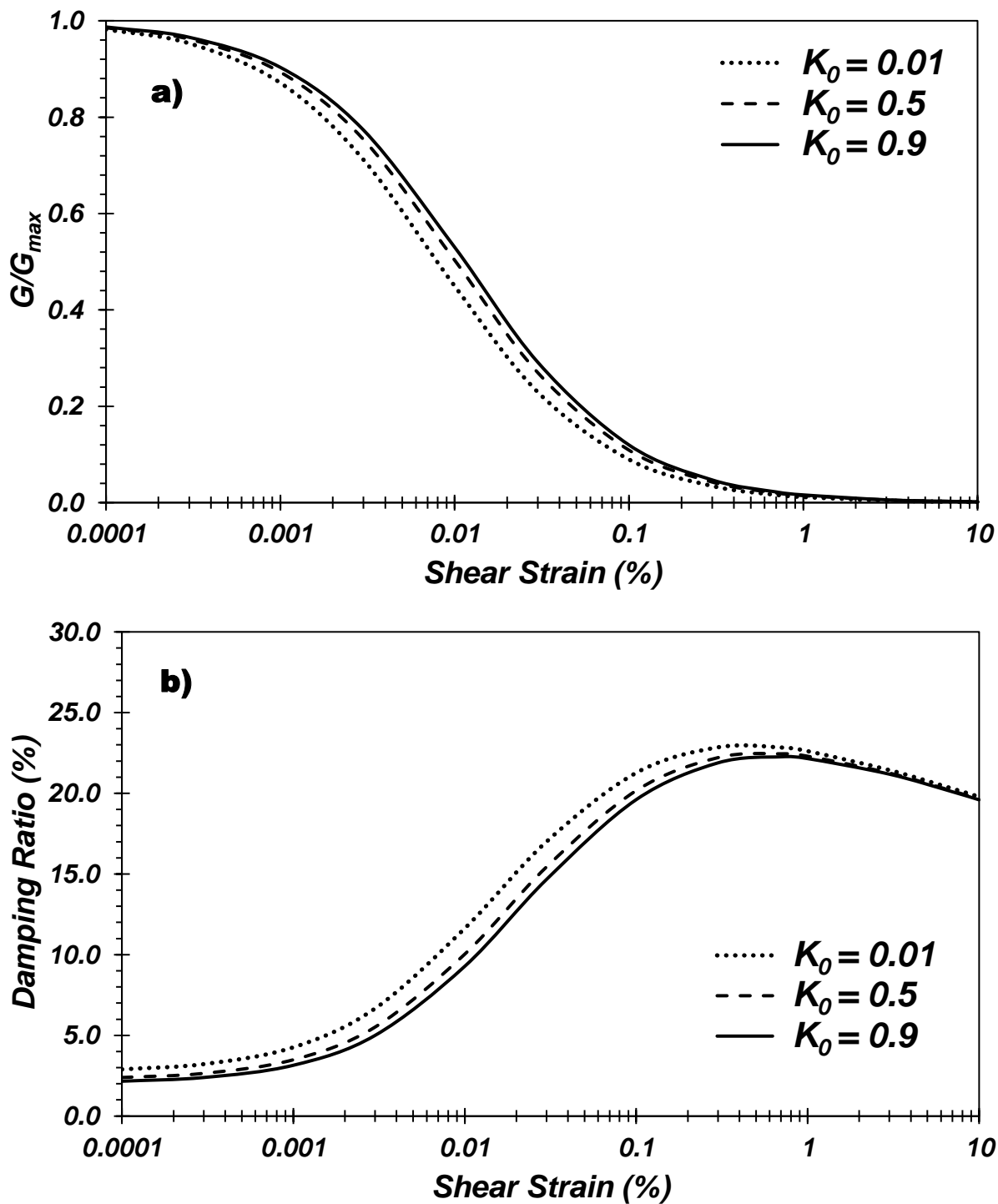


Figure 5 - 9. The Darendeli (2001) (a) G/G_{max} and (2) damping curves assuming $PI = 0$, $OCR = 1$, and $f = 1$.

The Vucetic and Dobry (1991) model G/G_{max} and damping curves were developed for a wide range of saturated clays. They concluded that the plasticity index (PI) is the main factor controlling the G/G_{max} and damping curves, with little apparent role of the OCR . These models are presented graphically, so the modeler needs to digitize and interpolate these curves depending on the considered PI and cyclic shear strain. Figure 5-10 displays the (a) G/G_{max} and (b) damping curves for the Vucetic and Dobry (1991) model.

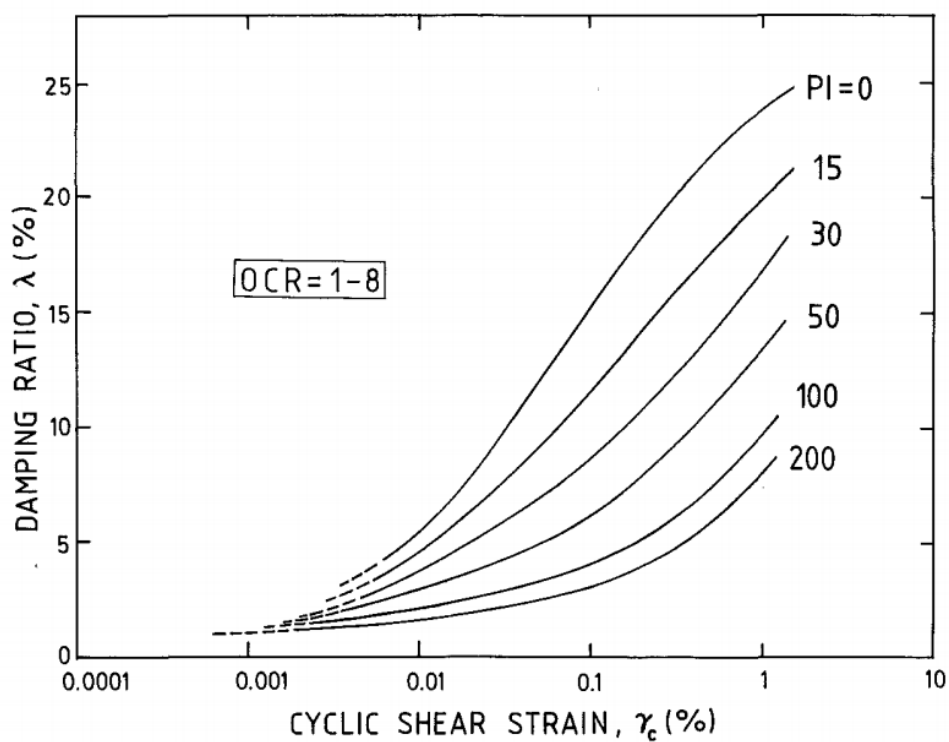
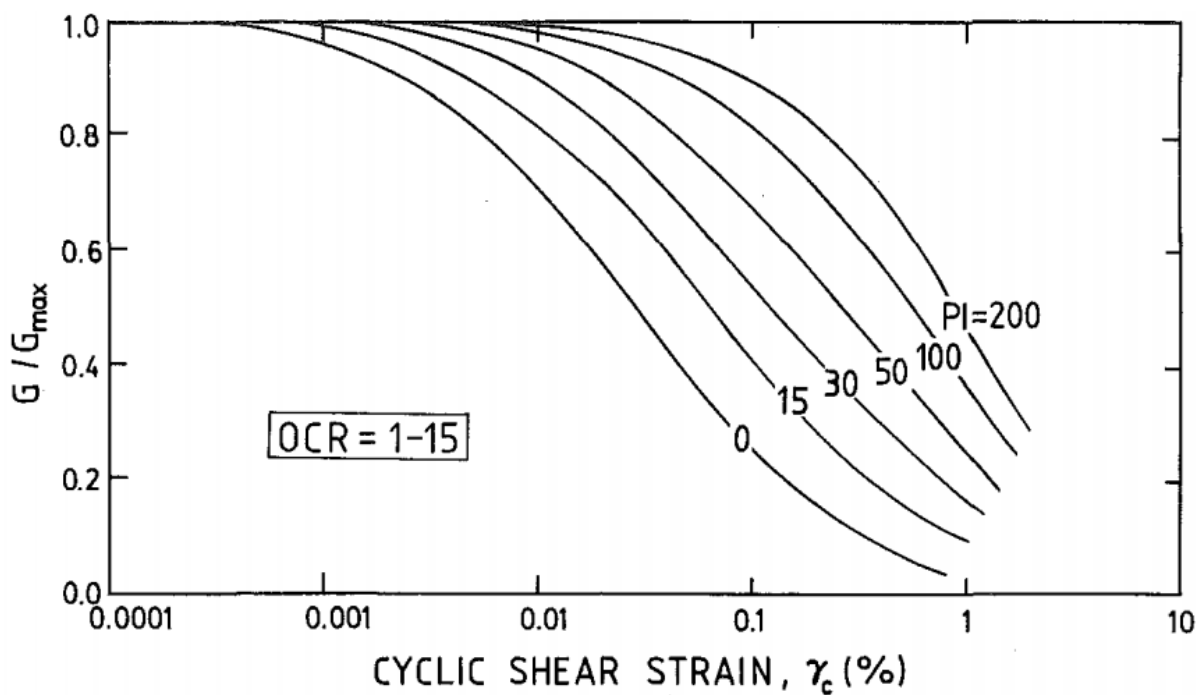


Figure 5 - 10. The developed (a) G/G_{max} and (b) damping curves for the Vucetic and Dobry (1991) model.

Table 5-8 summarizes the program workflow and modeling parameters, including the details regarding the modeling stages and the reference curves used to model plastic and non-plastic soils. In Step 1, the analysis method and basic soil modeling parameters are set. By selecting NL as the analysis method, one can perform an EL analysis at the same time. The *Automatic profile generation tool* generates a more detailed profile by subdividing the input profile layers into sublayers and sets the curve fitting parameters θ_1 through θ_5 for the *GQ/H* model. The default parameters were set for the Soil Models and the Hysteretic Re/Unloading Formulation.

The soil profile and properties are input into the program in Step 2 including the Darendeli (2001) and Vucetic and Dobry (1991) shear modulus reduction and damping curves. After the profile has been input, the program will subdivide the layer thicknesses within the profile. No corrections were made to the selected reference curves because the *GQ/H* model has a curve fitting scheme that automatically corrects the reference curves. The shear wave velocity and shear strength were held constant within each layer due to limitations in the software. The basalt layer is input as an elastic halfspace.

Selection of the motions that are to be used in the analysis is performed in Step 3. In Step 4, the viscous damping formulation and the optimum modes/frequencies are set for the analysis, with the default settings enabled, and is used for the time domain NL analysis only. In Step 5, the appropriate frequency or time domain analyses are set depending on whether an EL or NL analysis is to be performed. The EL frequency domain analysis requires specification of the number of iterations (set to 15), effective shear strain (0.63), and the frequency-independence of the shear modulus formulation. In contrast, the NL time domain analysis requires specification of the step control, the maximum strain increment size, and the number of sub-increments. In the

analyses conducted in the current study, the step control was set to the default setting of “flexible”, in which a time increment is subdivided only if the computed strains in the soil exceed a specified maximum strain increment of 0.005%.

Table 5 - 8. Summary of the step-by-step work flow and modeling parameters for DEEPSOIL used in this evaluation.

Step 1				
<i>Analysis Method</i>	NL			
<i>Pore Pressure Option</i>	Default			
<i>Solution type</i>	Time Domain			
<i>Automatic Profile Generation</i>	ON			
<i>Complementary Analyses</i>	EL-Frequency Domain			
<i>Maximum Layer Thickness</i>	50 Hz			
<i>Randomization</i>	OFF			
<i>Soil Models</i>	Default Settings (General Quadratic/ Hyperbolic)			
<i>Hysteretic Re/Unloading Form.</i>	Default Settings (Non-Masing Re/Unloading)			
Step 2				
<i>Input profile:</i>	<i>Input per layer:</i> Thickness (m), unit weight (kN/m ³), Shear Strength Velocity (m/s), and shear strength (kPa)			
<i>Per layer</i>	<u>Reference Curve</u>			
	<table border="1" style="width: 100%; border-collapse: collapse;"> <tr> <td style="text-align: center;"><i>Plastic</i></td> <td>Vucetic and Dobry (1991)- Input: PI</td> </tr> <tr> <td style="text-align: center;"><i>Non-plastic</i></td> <td>Darendeli (2001) - Input: K_0 value, assumed: $OCR=1$, $N=10$, $PI=0$, Frequency = 1</td> </tr> </table>	<i>Plastic</i>	Vucetic and Dobry (1991)- Input: PI	<i>Non-plastic</i>
<i>Plastic</i>	Vucetic and Dobry (1991)- Input: PI			
<i>Non-plastic</i>	Darendeli (2001) - Input: K_0 value, assumed: $OCR=1$, $N=10$, $PI=0$, Frequency = 1			
<i>Bedrock (Basalt)</i>	Shear wave velocity: 760 m/s, unit weight: 25.0 kN/m ³ , Damping Ratio: 2%.			
<i>Auto-generated Profile</i>	Verify information			
Step 3				
<i>Select Input motions: (PEER NGA earthquake database)</i>	(1) Motion 4000016, (2) Motion 4000521, (3) Motion 4001060, (4) Motion 4022909, (5) Motion 4022989, (6) Motion 4022913, (7) Motion 4032577, (8) Motion 6001373, (9) Motion 4028564, (10) Motion 4032552			
Step 4				
<i>Viscous/Small-Strain Damping Definition</i>	Default Settings			
Step 5				
<i>Analysis Control Definition</i>	Default Settings (SSR=0.65), Output Setting (surface only, layer 1)			

5.4.2 Results of the Site Response Analyses and Discussion

The potential impact of the M9.3 Cascadia Subduction Zone Scenario earthquake on the evaluation site is discussed below using the results of the SRAs described in terms of soil (i.e., within the profile) and ground surface responses and is aided by graphical and spatial representations.

5.4.2.1 Computed Peak Horizontal and Ground Accelerations

Figure 5-11 displays the peak horizontal acceleration (PHA) with depth for the EL and NL site response analyses for the Boring 1 soil profile for each of the selected and scaled ten ground motion pairs. The variation of the PHA with depth for the remaining ten profiles are presented in Figures B11 through B21 in Appendix B.

The significant difference in computed PHA and PGA between the NL and EL approach can be attributed to the many soft (deformable) layers in the soil profiles. The largest difference between the PHA determined using the EL and NL methods occurs in the top 5 to 6 m where the soil profile transitions from a soft or loose sandy silt/silty sand material to a dense silty sand or gravel fill layer. The EL approach amplifies the acceleration more than the NL approach as shown in Figure 5-11 for all the CPT and Boring profiles. As described further below, this is due to the large dynamically-induced shear strains within these layers. This is consistent with the findings of Aimar and Foti (2021) that the NL approach underestimates site amplifications with respect to the EL approach for deep and deformable deposits.

The EL- and NL-based PHAs agree when all the profiles transition from a fill layer to a stiff soil deposit. It also occurs for Boring 1 at 8.2 m when the profile transitions from a soft plastic material to a loose silty sand (Refer to Figure 5-11(a)). For Boring 2, the two analyses agree somewhat at 4 m but are slightly off when it transitions from fill to a loose silty sand. The

two sets of results diverge again at the transition to a soft clay at 7 m and does not converge again until 12.2 m with the transition to a non-plastic loose silty sand (Refer to Figure 5-11(b)). This is also noticeable at Boring 3; the PHA diverges slightly at 16.2 m at the transition from a non-plastic very soft silt with sand layer to a very soft clay that has weaker strength parameters and a lower shear wave velocity. But the biggest variation between the EL and NL results occurs at 9.9 m at the interface of the soft plastic silt with sand layer and the non-plastic, medium stiff silt layer, with higher strength parameters leading to de-amplification of the PHA (refer to Figure 5-11(c)). Another notable difference is evident in Boring 4 where the NL-based PHAs do not agree with the EL results throughout the profile until 28.4 m at the transition from a medium dense silty sand to plastic clays (refer to Figure 5-11(d)).

The NL approach captured the transitions in layer thickness and stiffness better than the EL approach between deeper, stronger granular soils transitioning to softer and weaker plastic layers. For example, at 7 m depth for profile B2 in Figure 5-11(b), where the profile transitions from a loose silty sand to a soft clayey deposit, the NL curve produces a smooth transition in PHA in the soft material due to improved representation of soil nonlinearity whereas the EL PHA curve does not. These differences between the EL and NL responses are also evident in Figure 5-11(k) at depths of 19 and 30 to 35 m for CPT-7, Figure 5-11(b) at 10 m for profile B1, and Figure 5-11(d) at 23 m for Profile B4. These results are consistent with findings reported by Hartzell et al. (2004) that a NL analysis is more suitable for capturing the response of soft-soil deposits.

It is also noticeable that there are certain differences and similarities in a given profile given differences in the ground motions. For Boring 1, the PHA for motions 4001060, 4022913, 6001373, 402564 converge at roughly ~7.5 m, the rough transition point between plastic soft

silty silt to a loose silty sand, whereas motions 403277 and 4000016 diverge as shown in Figure 5-11. It is also evident in Boring 3 (Figure B-13 in Appendix B), the computed PHA converges at ~25 m for motions 4028564 and 2022913, whereas the PHA diverges for motions 6001373, 4001060, 4000016.

Occasional, large differences in the computed site responses may be attributed to directional effects from a given recorded strong ground motion. Multiple studies (Bonamassa and Vidale, 1991; Vidale et al., 1991; Spudich et al., 1996; Xu et al., 1996; Martino et al., 2006) have reported cases of notable directional variations of seismic site response under different geological and topographical conditions. Unfortunately, due to the limited amount of observations, the understanding of factors controlling directional amplification and the definition of practical recognition criteria has not been developed (Gaudio et al. 2008). However, the variability within the selected ground motions is anticipated to capture expected seismic loading variability during the scenario CSZ event.

Figure 5-12 displays the average PHA and +/- 1 standard deviation (σ) with depth for EL and NL site response analyses for the eleven soil profiles evaluated. The average PGA resulting from each EL and NL site response analysis is reported in Table 5-9, which indicates that the EL approach estimated PGA values 1.37 times the size of the NL approach on average. The COV was approximately the same for the EL and NL approaches, equal to 23.4% and 22.3%, respectively. The COV for the ratio of EL to NL is very low (5%) showing that the EL method consistently produced high PHA values.

Table 5 - 9. Summary of the PGA computed using the EL and NL site response analyses at the evaluation site.

Profile	PGA (g) determined from Equivalent Linear (EL) Analysis	PGA (g) determined from Non-Linear (NL) Analysis	Ratio of PGA from EL to NL Analyses
B1	0.40	0.27	1.48
B2	0.30	0.22	1.36
B3	0.20	0.14	1.43
B4	0.22	0.16	1.38
C1	0.43	0.29	1.48
C2	0.38	0.28	1.36
C3	0.39	0.29	1.34
C4	0.33	0.24	1.38
C5	0.30	0.24	1.25
C6	0.26	0.19	1.37
C7	0.28	0.22	1.27
Site Average	0.32	0.23	1.37
Site COV (%)	23.4	22.3	5

The maximum and minimum PGA computed using the SRAs corresponded to profiles B1 and B3 for both EL and NL analyses, respectively. Boring 1 developed the greater PGA value which is not a surprised since the subsurface layers of the profile consists of moderately soft for 10m which can amplify motions. For the EL analysis, the average PGA of 0.32g was determined for the whole site, which is slightly smaller than the PGA developed from the regional seismic hazard estimate of 0.34g (refer to Chapter 3). The NL analysis estimated an average PGA equal to 2/3 of that corresponding to the mapped PGA. In general, the profiles with depth to the bedrock >30 m (i.e., B3, B4, CPT6 and CPT7) produced the lowest PGAs because they had more material through which the ground motion could amplify.

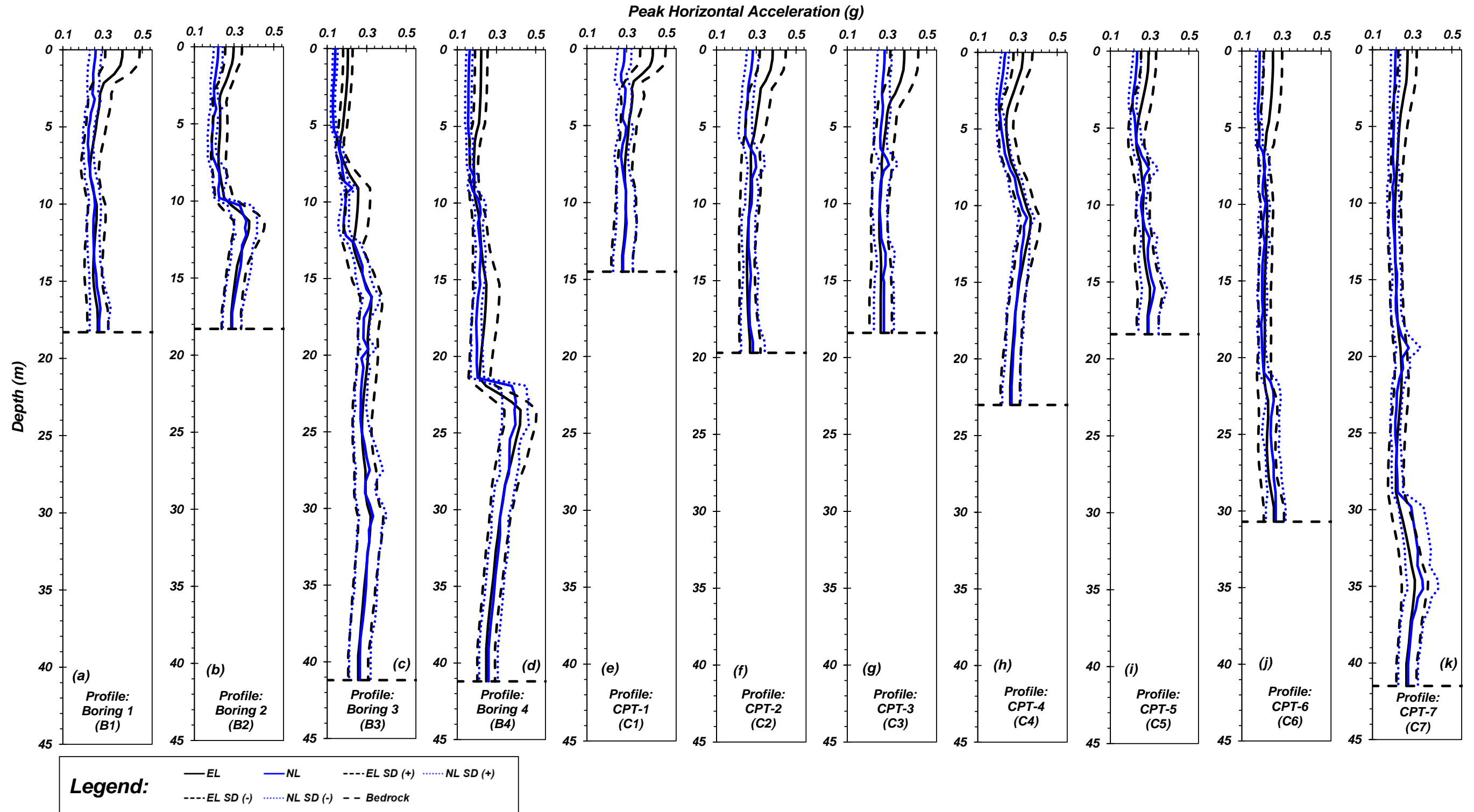


Figure 5 - 12. Comparison of average peak horizontal acceleration (PHA) with depth for equivalent linear (EL) and nonlinear (NL) site response analyses conducted for all the profiles developed for the evaluation site. Profile: (a) Boring 1 (B1), (b) Boring 2 (B2), (c) Boring 3 (B3), (d) Boring 4 (B4), (e) CPT-1 (C1), (f) CPT-2 (C2), (g) CPT-3 (C3), (h) CPT-4 (C4), (i) CPT-5 (C5), (j) CPT-6 (C6) and (k) CPT-7 (C7).

5.4.2.2 Computed Maximum Soil Shear Strain

The variation in shear strain with depth of the soil was evaluated to determine which soil layers could be responsible for significant deformation. Figure 5-13 presents the maximum shear strain, γ_{max} , with depth for the EL and NL site response analyses for the Boring 1 (B1) soil profile. The variation of the shear strain with depth for the remaining ten profiles are presented in Figures B-21 through B-30 in Appendix B. It is noticeable that for most of the motions, the EL and NL methods produce similar estimates of shear strain with variations that depend on the soil characteristics. For example, in Boring 1, the shear strain developed from the NL approach is greater than that for the EL approach at a depth of ~8 m (refer to Figure 5-13) when the soil transitions from a soft plastic sandy silt to a loose silty sand.

There is also a notable variability in shear strain in a given layer between the selected motions. For Boring 2 (refer to Figure B-21), the difference in shear strain at ~ 9 to 11.5 m is extremely small between the two approaches for motions 4000521, 6001373, 4028564 and 4001060, while for motions 4000016, 4022989 and 4032552 the difference in shear strain magnitude is at least 2 to 3%. This variability is even more evident in Boring 3 when the profile transitions from plastic to granular layers at depths of 5 to 8 m, 12 to 16 m, and 16 to 20 m (refer to Figure B-22). Motions 4022909, 4022989 and 4022913 produce large variability in shear strain between the two approaches at those depths; whereas motions 4028564, 4001060 and 4032552 produce little to no variation.

The differences between the maximum shear strain computed using the EL and NL methods vary slightly and are only appear evident when $\gamma_{max} > 0.4\%$, which generally occurs in the softer silty/clayey materials. For example, the EL and NL analyses agree within the soft soil deposits when $\gamma_{max} < 0.4\%$ as shown at depths of 5 to 7 m and at 11 to 15m for Profile B4 in

Figure 5-13(d) and Figure 5-13(h) at 2-5m for Profile C5. When $\gamma_{\max} > 0.4\%$ the NL approach estimates greater maximum shear strain in the soft layers as shown in in Figure 5-11(a) at 7 m depth for Profile B1, Figure 5-11(d) for depths of 21 to 24 m for Profile B4, Figure 5-11(h) for depths ranging from 7 to 10 m for Profile C5, and Figure 5-11(i) for depths of 24 to 30 m Profile C6. These findings are consistent with the results of an informal survey that showed that EL analyses provide reasonable results for shear strains less than 1% to 2% reported by Kramer and Paulsen (2004). Matasovic and Hashash (2012) also showed that NL analyses is preferred when computed shear strains exceed 1%, although they noted that this threshold is likely too high. Kaklamanos et al. (2015) and Kim et al. (2016) conclude that the EL approach should be used only in the case of $\gamma_{\max} < 0.05\%$, when the change in shear modulus and damping is relatively small.

Note that since a total stress analysis was completed, the effects of liquefaction were not considered. The generation of pore water pressure was not evaluated to determine which layers could potentially liquefy. When a soil layer liquefies, the soil strength varies substantially throughout the motion, causing alternating amplification and deamplification during the remainder of the ground motion to alter the site response. Figure 5-14 displays the average maximum shear strain and $\pm 1\sigma$ with depth for EL and NL site response analyses for all of the profiles (11 profiles).

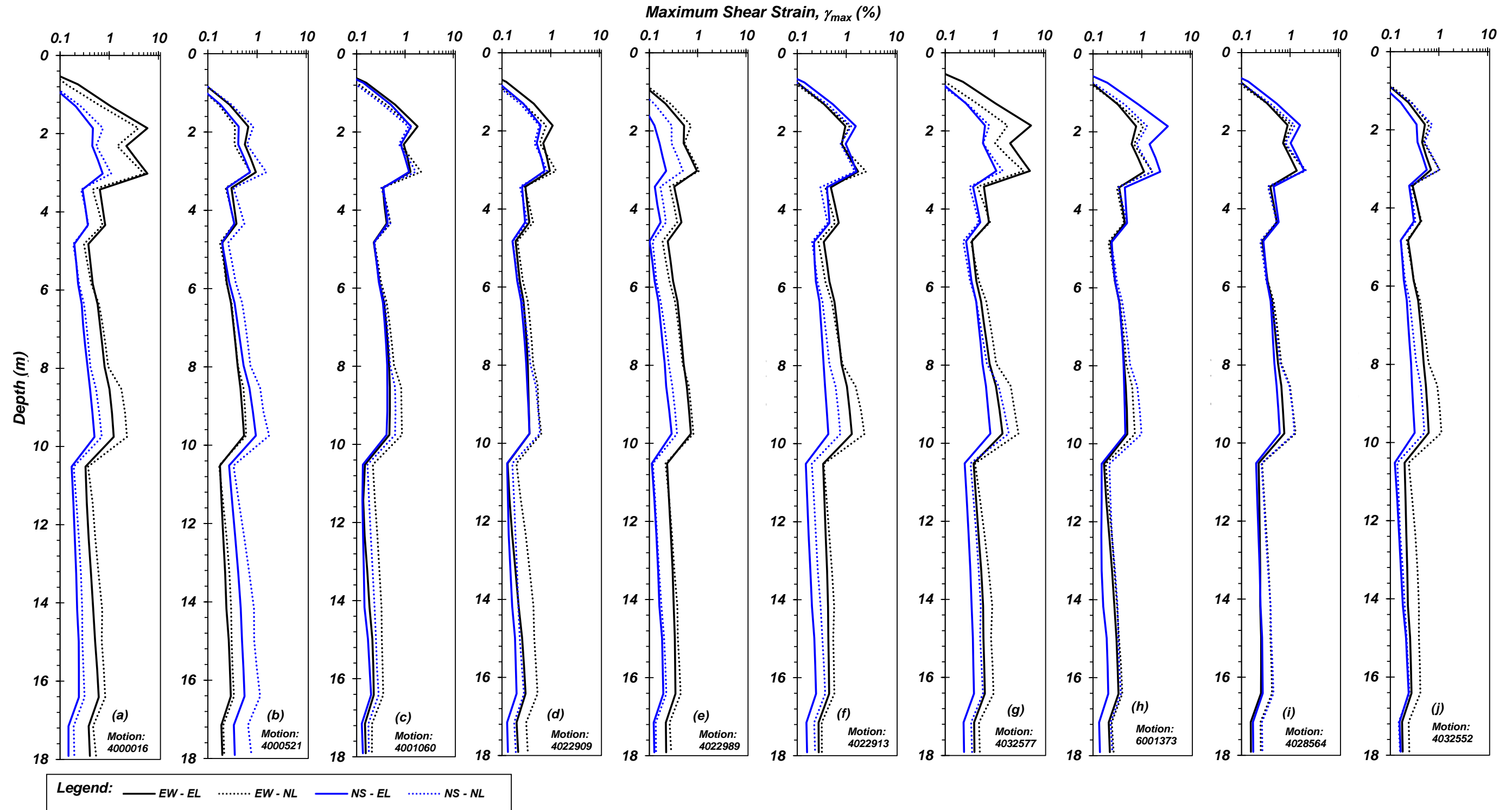


Figure 5 - 13. Comparison of maximum shear strain, γ_{max} (%) with depth for equivalent linear (EL) and nonlinear (NL) site response analyses conducted for the Boring 1 (B1) soil profile. 10 Motions (both NS and EW direction, total 20 motions) were evaluated obtained from the PEER NGA earthquake database: (a) Motion 4000016, (b) Motion 4000521, (c) Motion 4001060, (d) Motion 4022909, (e) Motion 4022989, (f) Motion 4022913, (g) Motion 4032577, (h) Motion 6001373, (i) Motion 4028564, (j) Motion 4032552.

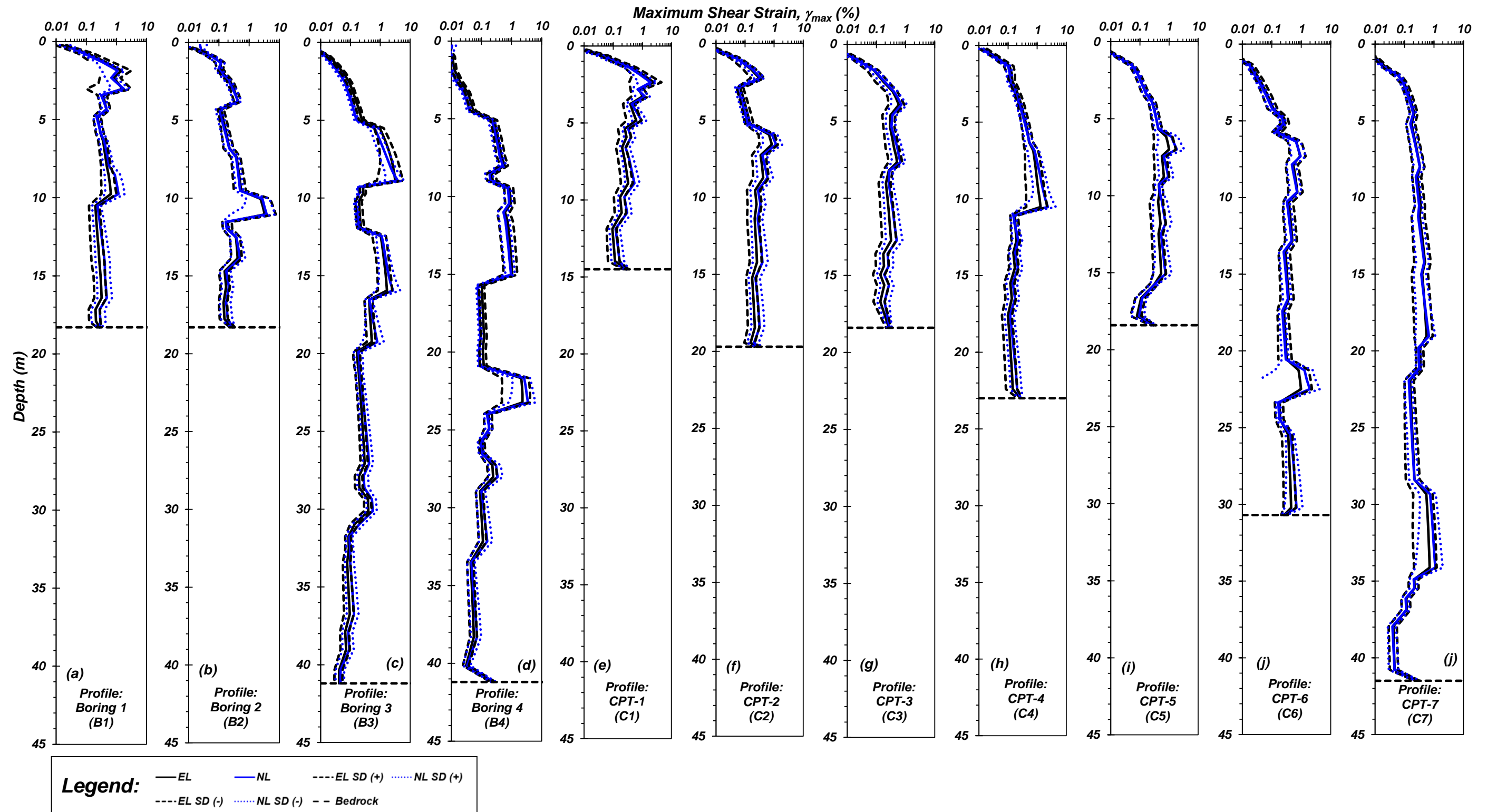


Figure 5 - 14. Comparison of average maximum shear strain, γ_{max} (%) with depth for equivalent linear (EL) and nonlinear (NL) site response analyses conducted for all the profiles developed for the evaluation site. Profile: (a) Boring 1 (B1), (b) Boring 2 (B2), (c) Boring 3 (B3), (d) Boring 4 (B4), (e) CPT-1 (C1), (f) CPT-2 (C2), (g) CPT-3 (C3), (h) CPT-4 (C4), (i) CPT-5 (C5), (j) CPT-6 (C6) and (k) CPT-7 (C7).

5.4.2.3 Acceleration Response Spectra

Acceleration response spectra are an important result of SRAs because they can be used to analyze the performance of structures and equipment during earthquakes. Structures and equipment are frequently modeled as a single-degree-of-freedom (SDOF) system that captures its potential resonance to certain periods or frequencies of motion. The response of a structure will therefore depend on the natural frequency of the soil profile below it. The natural period for each profile is shown in Table 5-7, which describes the period at which resonance occurs therefore resulting in significant amplification of the motion at specific periods. Depending on the natural frequency of the profile, some will amplify short period motions while other periods amplify longer period motions. The ground surface acceleration response spectrum was computed for each profile and ground motion in an effort to quantify the expected response and the motion-dependent variability.

Table 5 - 10. Summary of the estimated natural periods for each soil profile.

Profile	Natural Period (sec)
B1	0.515
B2	0.531
B3	1.05
B4	0.884
C1	0.329
C2	0.391
C3	0.387
C4	0.56
C5	0.515
C6	0.737
C7	0.898

Figure 5-15 displays response spectra for the profiles for the EL and NL site response analyses for the Boring 1 (B1) soil profile. The EL and NL approach show that the peak spectral acceleration occurs at approximately the same period (and roughly the natural period of the

profile); however, the magnitude of acceleration is slightly larger for the EL approach which could be due to the differences in how the constitutive models were implemented by the two approaches. The NL approach uses the backbone curves directly to model hysteretic soil behavior whereas the EL approach uses strain iteration to get to obtain the appropriate G/G_{max} for each time step. The response spectra for the remaining ten profiles are presented in Figures B-31 through B-40 in Appendix B. Figure 5-16 compares the average spectral acceleration (SA) for the equivalent linear (EL) and nonlinear (NL) site response analyses conducted for all the profiles on the evaluation site.

Notable difference between the response spectra produced using the EL and NL approaches are observed at lower periods ($< \sim 0.2$ sec): the EL approach is less sensitive to these periods and therefore exhibits less fluctuations in the spectral acceleration in this range than the NL approach. For example, at ~ 0.02 s, Figures 5-12(a), (b), (e), (h) and (i) show slight variations in spectral acceleration whereas those of the EL analysis flat. This trend of the NL model producing spectra at lower periods is also evident in most of the profiles in Figure 5-15. Campbell and Bozorgnia (2008) and Kaklamani et al. (2013) note that a realistic spectral shape is produced by the NL approach at short periods, suggesting that the results of EL analyses at short periods are unrealistic. Some analysis do not apply strength corrections to the strength curves which can cause the EL approach to over dampen the response. However, that is not likely the issue since corrections were applied in Step 2 in the DEEPSOIL analysis (reference *Section 5.4.1*).

The response spectra vary significantly for the motions considered. For boring 1 (shown in Figure 5-15) motion 4000016 produced a maximum spectral acceleration of $2.7g$ at 1 s, greater than any other motion. Motion 4000016 also generated the largest peak spectral

acceleration for profiles B2 (Figure B-31(a)), C2(Figure B-35(a)), C4 (Figure B-37(a)) and C5 (Figure B-38(a)) at a period of about ~1 s and ranging from 1.4 to 2.0g. Motion 4028564 generated the largest peak spectral acceleration for profile C1 (Figure B-34(i)), C3 (Figure B-36(i)) and C7 (Figure B-40(i)), which occurred at ~0.5 s and which ranged from 1.8 to 2.7g. It is notable that the two motions dominated the peak spectral acceleration responses for the profiles. Motion 4000016 had a relatively high COV in bias (23%) when compared to the target ground motion and was scaled by a factor of 1.06 (refer to *Section 5.3.2*).

The average spectra for profiles B1, C1 and C3 exhibit a single peak spectral acceleration magnitude as shown in Figure 5-16 (a), (e) and (g), at ~0.5 secs at ~1.2g, 1.3g and 1.4g, respectively. However, profiles B2, B3, B4, C4, C6 and C7 also exhibit peaks at higher modes. The natural period for the profiles tends to fall in between the periods corresponding to the peak spectral acceleration for these analyses. Structures can exhibit multiple modes in response to a seismic motion which depend upon its flexibility. Based on the estimated response spectra, structures with lower flexibility would be subjected to intense shaking at this site depending on the specific frequency content of the ground motion generated by the CSZ event.

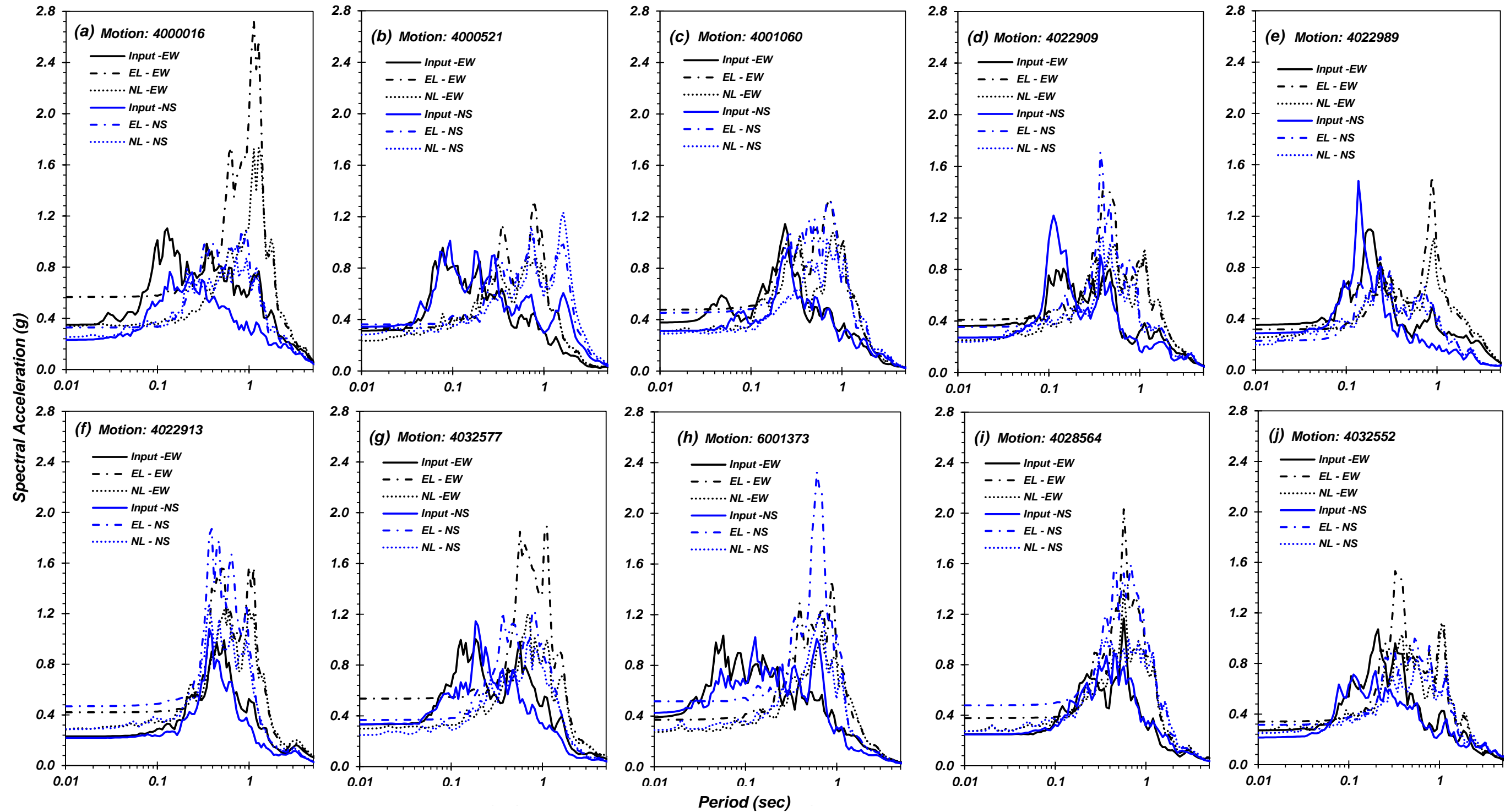


Figure 5 - 15. Comparison of spectral acceleration (SA) with depth for equivalent linear (EL) and nonlinear (NL) site response analyses conducted for the Boring 1 (B1) soil profile. 10 Motions (both NS and EW direction, total 20 motions) were evaluated obtained from the PEER NGA earthquake database: (a) Motion 4000016, (b) Motion 4000521, (c) Motion 4001060, (d) Motion 4022909, (e) Motion 4022989, (f) Motion 4022913, (g) Motion 4032577, (h) Motion 6001373, (i) Motion 4028564, (j) Motion 4032552.

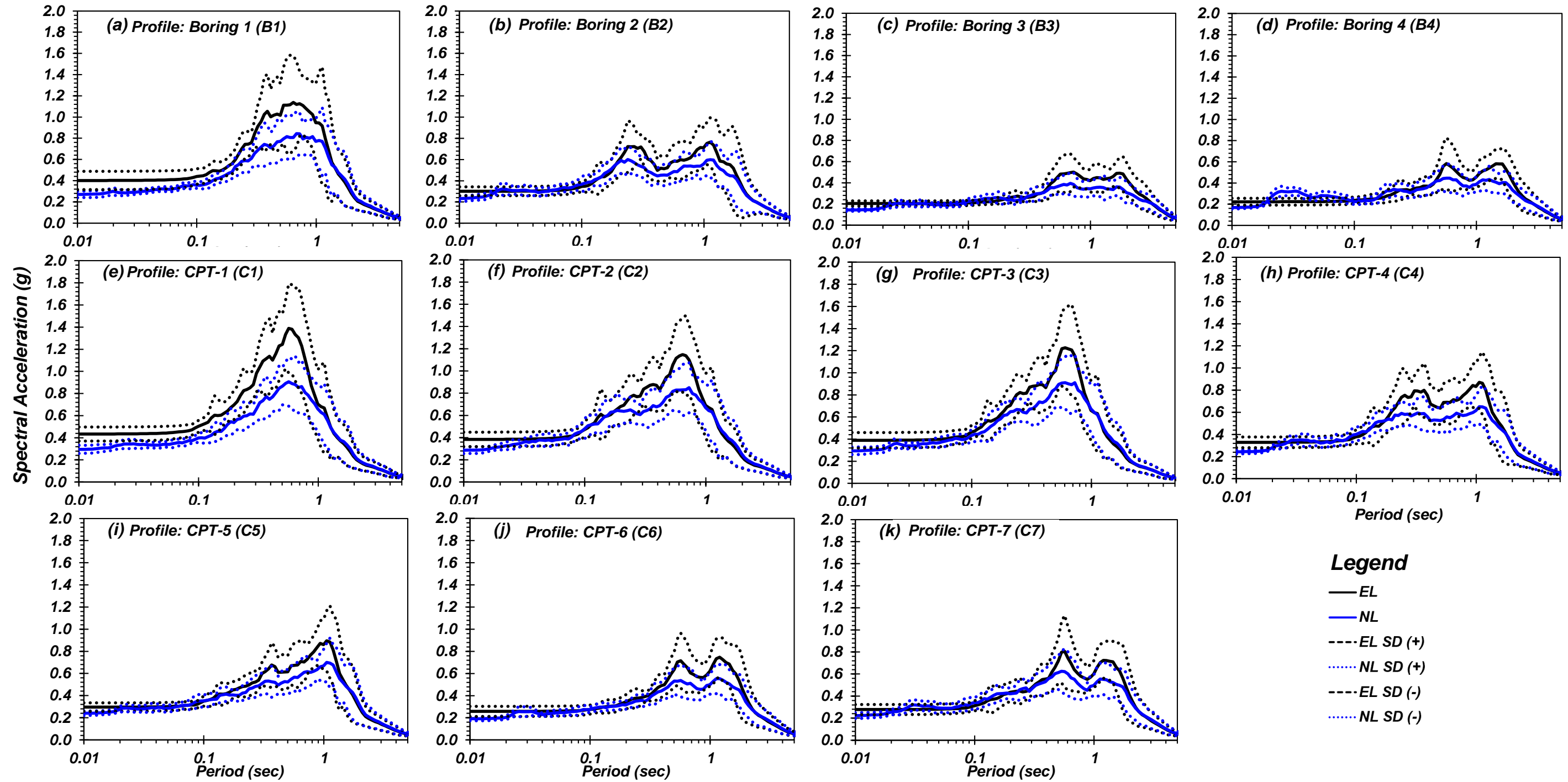
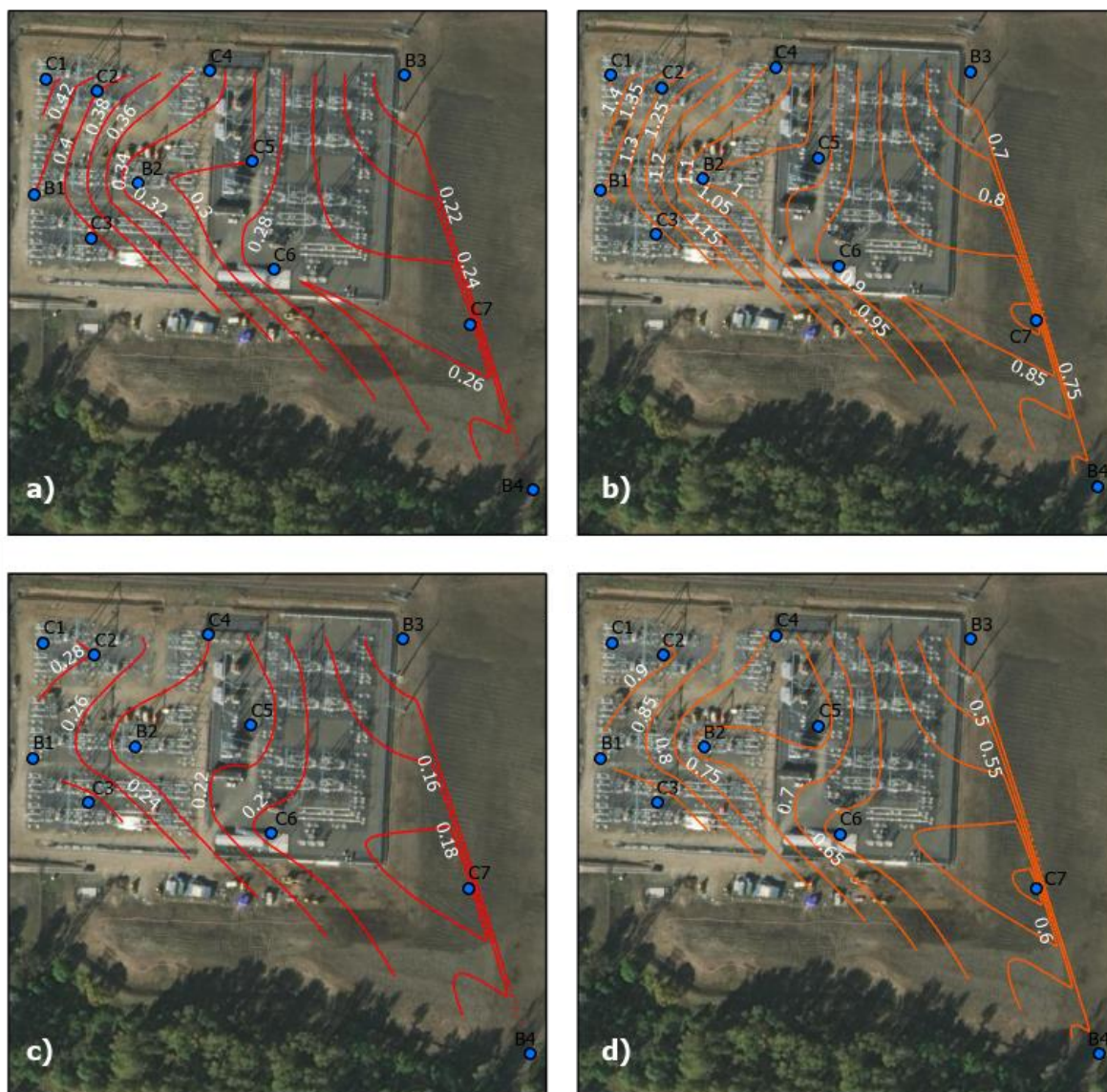


Figure 5 - 16. Comparison of average spectral acceleration (SA) with depth for equivalent linear (EL) and nonlinear (NL) site response analyses conducted for all the profiles developed for the evaluation site. Profile: (a) Boring 1 (B1), (b) Boring 2 (B2), (c) Boring 3 (B3), (d) Boring 4 (B4), (e) CPT-1 (C1), (f) CPT-2 (C2), (g) CPT-3 (C3), (h) CPT-4 (C4), (i) CPT-5 (C5), (j) CPT-6 (C6) and (k) CPT-7 (C7).

5.4.3 Spatial Distribution of PGA at the Evaluation Site

The PGA computed using the EL and NL methods varied greatly across the site. To evaluate the distribution of the PGA across the site visually, a PGA and amplification contour map was developed. The natural neighbor spatial analyst tool in ArcGIS was used to develop a PGA raster surface for the evaluation site. The natural neighbor method applies an “area stealing” interpolation which uses only the subset of samples surrounding the point to interpolate the surface (Sibson 1981). Contours were derived from the surface to develop PGA and amplification ratio contour maps to aid visualization of the spatial distribution of amplification across the footprint of the site determined using the EL and NL approaches and presented in Figure 5-17. The amplification ratio is defined as the ratio of PGA at the ground surface to the PGA of the scaled ground motion. Note that because only 11 profiles were analyzed in the SRA, the accuracy of the map is limited and should be interpreted with caution. The maps highlight how the EL method amplifies the ground motions more than the NL approach, which is consistent with the findings reported by Aimar and Foti (2021) based on the site conditions. Amplification is the greatest on the west side of the site, where the shallow profiles are predominately composed of medium to soft sandy silts that amplify the motion, and decrease in PGA eastward across the site. The two sets of contours generated using both SRA methods are similar to one another; the main difference between them is that the EL approach creates steeper contours than the NL approach. Such an observation is not interpreted to be significant given the number of profiles used to generate the contour maps.



Legend

● Exploration Location

— PGA Contour

— PGA Amplification Ratio Contour



0 25 50 100 150
Meters

Basemap - ESRI

Coordinate Projection: USA_Contiguous_Albers_Equal_Area_Conic_USGS_version

Figure 5 - 17. PGA and amplification contour map using EL and NL approach developed values: (a) EL-PGA contour, (b) EL-PGA amplification ratio, (c) NL-PGA contour, and (d) NL-PGA amplification ratio.

5.5 Impact to Electrical Utility Equipment

An analysis of the probability of failure of electrical equipment using the SRA PGA values as input into fragility curves (Figure 5-18) developed by SEFT (2018) to characterize the probability of failure (POF) of a given asset/structure combination for varying levels of earthquake-induced PGA. To generate these curves, SEFT (2018) assumed the seismic demand and structural capacity followed a lognormal distribution. They developed three sets of response spectra for each substation (assuming 5% damping), where each spectrum corresponds to a potential rupture scenario for a M6.8 Portland Hills Fault earthquake (northern, middle, and southern). To reduce the number of structural analysis cases, SEFT (2018) arranged these response spectra for all the sites into three groups (i.e., A, B, and C) with similar normalized spectral shapes. They assumed that spectral shape is primarily influenced by the “average” soil profile beneath the substation (SEFT 2018).

Based on its normalized spectral shape, the evaluation site is assumed to be represented by response spectrum group B per SEFT criteria. The electrical components summarized in Table 5-11 correspond to the equipment present at the substation and were evaluated for their respective failure modes for two voltage levels (115 kV and 230 kV). Note that the transformer non-LTC power was only evaluated at 115 kV, since it was not designed for a 230 kV load. The non-LTC power is relatively rigid with a very narrow failure window; therefore, it is anticipated to fail even with minimal shaking. The fragility curve for the control house and transformer instrument varies between the two voltage levels: they are narrow for the 115kV level, but fairly broad for 230 kV level. Therefore, their performance is anticipated to vary significantly with PGA. The transformer LTC power equipment is represented by similar curves for both voltage levels.

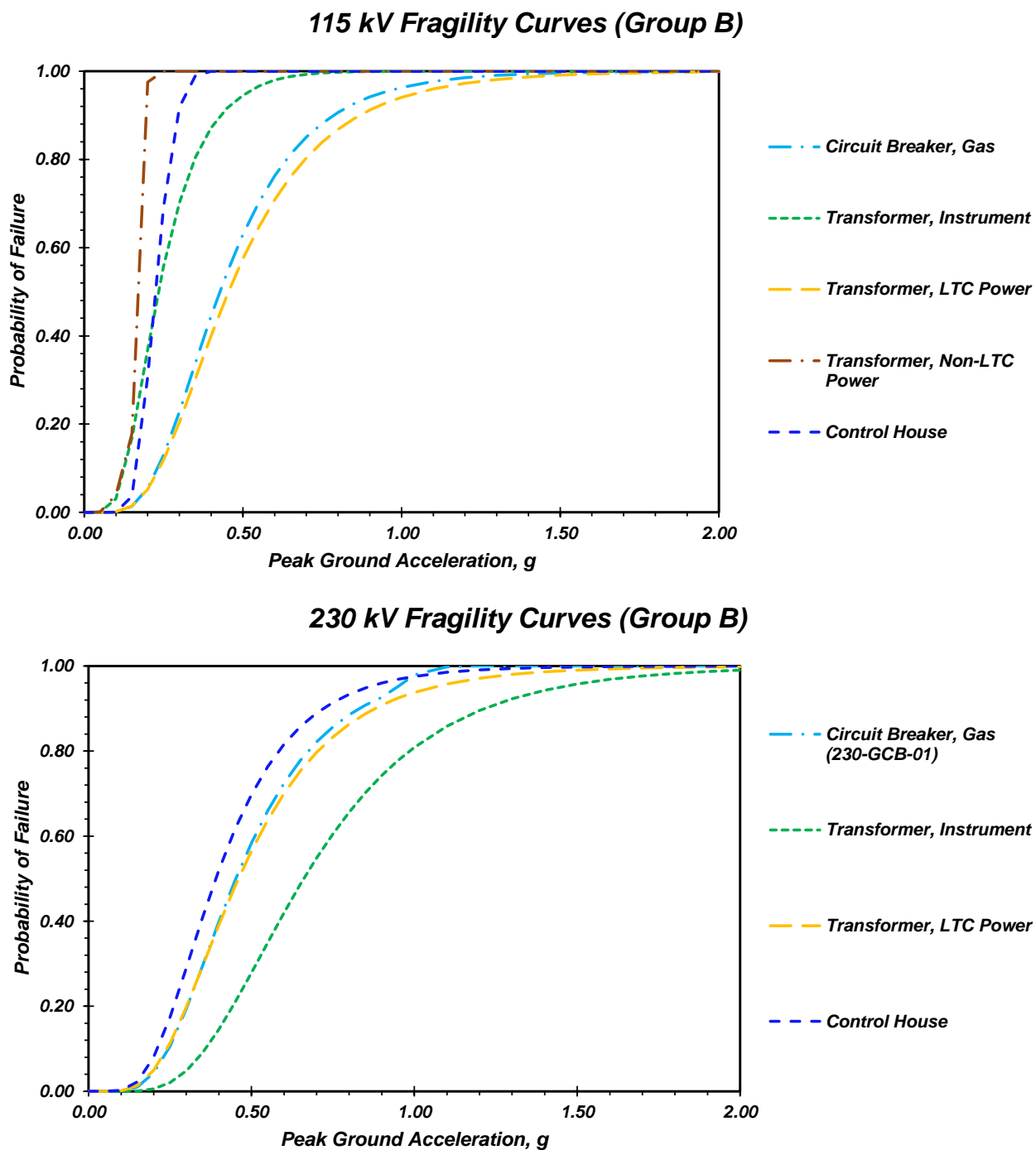


Figure 5 - 18. Response spectra Group B fragility curves at two voltage levels: (a) 115kV and (b) 270 kV, for the various electrical components with their corresponding failure mode.

Table 5 - 11. Electrical equipment and associated failure methods evaluated for the site

Electrical Equipment	Failure Mode
Transformer, Instrument	Anchorage Failure (115 kV), Rocking (230 kV)
Transformer, LTC Power	Sliding
Transformer, Non-LTC Power (115 kV only)	Anchorage Failure
Circuit breaker, gas	Rocking
Control House	Anchorage Failure

Tables 5-12 and 5-13 summarize the POF for the electrical equipment at two voltage levels when exposed to the PGAs determined using the NL and EL approaches and the landslide hazard map and the associated standard deviation (STD) in the POF. For electrical equipment at 115 kV, the non-LTC power transformer would not be suitable for any location on the site with a ~100% POF based on the EL-based PGA estimates. However, the PGAs computed using the NL approach appear to suggest that the POF = 15% if it was positioned near boring B3. Based on the EL analysis, the most suitable location to place the control house is near B3 (POF = 31%) and B4 (POF = 46% POF) since all other locations would result in a high POF (>70%). The POF corresponding to the LTC power transformer and gas circuit breaker computed using the PGAs derived from both approaches is relatively low across the site, equal to 5 and 1%, respectively, when placed near profile B3 and 8 and 2%, respectively when placed near profile B4. The PGAs derived using the EL approach suggest that moderate to high POFs (59 to 90%) would be expected for the transformer instrument considering the site-wide estimates (i.e., considering all soil profiles), whereas those PGAs developed using the NL approach provide low to moderate POFs (14% to 67%), with similar standard deviations in the POFs as those suggested from EL-based PGAs.

Similar trends in the spatial distribution of POFs for the electrical equipment were noted for the 230 kV level; however, the fragility curve for each piece of equipment returned a lower POF. For example, the 230 kV transformer instrument produced lower POFs for both PGA-

estimation methods, ranging from 1 to 20% and 0 to 5% for the EL and NL approaches, respectively. The POFs computed using the EL and NL approach were smaller than the USGS mapped estimated POFs for most areas on the site. On the west side of the site, the EL approach estimated the following B1, C1, C2 and C3 produced POFs greater than the USGS map estimate.

The estimated POF for all pieces of equipment increased towards the northeastern portion of the site similar to the increases in PGA. The EL approach provides a more conservative estimate on the probability of failure for the electrical equipment on the site. All equipment located near B3 exhibited the lowest POF, since the PGA is estimated to be the lowest at this location, regardless of the type of SRA considered.

These results demonstrate the potential sensitivity of electrical component performance during a M9.3 CSZ scenario earthquake to the spatially-distributed amplification of strong ground motion. Significant differences in equipment survivability are observed between the northeastern and southwestern portions of the site. However, it should be noted that these observations stem from purely inertial demands on the equipment; no effort was made to evaluate the kinematic demands that are possible due to lateral spreading hazards present at the site (anticipated to be greatest towards the northeast due to the open river channel face adjacent to the Columbia River), or liquefaction-induced settlement.

Table 5 - 12. Probability of failure of electrical equipment at 115 kV based on PGA values developed from the EL and NL approach and the hazard map.

Location	PGA (EL / NL)	Transformer, Instrument (Anchorage Failure) (EL / NL)	Circuit Breaker, Gas (Rocking) (EL / NL)	Transformer, LTC Power (Sliding) (EL / NL)	Transformer, Non-LTC Power (Anchorage Failure) (EL / NL)	Control House (Anchorage Failure) (EL / NL)
B1	0.40 / 0.27	0.87 / 0.62	0.44 / 0.17	0.40 / 0.15	1.00 / 1.00	1.00 / 0.78
B2	0.30 / 0.22	0.70 / 0.44	0.23 / 0.08	0.20 / 0.08	1.00 / 0.99	0.92 / 0.46
B3	0.20 / 0.14	0.37 / 0.14	0.05 / 0.01	0.05 / 0.01	0.98 / 0.15	0.31 / 0.03
B4	0.22 / 0.16	0.44 / 0.21	0.08 / 0.02	0.08 / 0.02	0.99 / 0.34	0.46 / 0.09
C1	0.43 / 0.29	0.90 / 0.67	0.50 / 0.21	0.45 / 0.19	1.00 / 1.00	1.00 / 0.87
C2	0.38 / 0.28	0.84 / 0.64	0.40 / 0.19	0.36 / 0.17	1.00 / 1.00	1.00 / 0.83
C3	0.39 / 0.29	0.86 / 0.67	0.42 / 0.21	0.38 / 0.19	1.00 / 1.00	1.00 / 0.87
C4	0.33 / 0.24	0.76 / 0.52	0.29 / 0.11	0.26 / 0.10	1.00 / 1.00	0.96 / 0.61
C5	0.30 / 0.24	0.70 / 0.52	0.23 / 0.11	0.20 / 0.10	1.00 / 1.00	0.92 / 0.61
C6	0.26 / 0.19	0.59 / 0.33	0.15 / 0.05	0.14 / 0.04	1.00 / 0.82	0.74 / 0.25
C7	0.28 / 0.22	0.64 / 0.44	0.19 / 0.08	0.17 / 0.08	1.00 / 0.99	0.83 / 0.46
STD	0.08 / 0.05	0.18 / 0.18	0.15 / 0.07	0.14 / 0.07	0.01 / 0.30	0.24 / 0.30
USGS Estimate	0.34	0.78	0.32	0.28	1.00	0.97

Table 5 - 13. Probability of failure of electrical equipment at 230 kV based on PGA values developed from the EL and NL approach and the hazard map.

Location	PGA (EL / NL)	Transformer, Instrument (Anchorage Failure) (EL / NL)	Circuit Breaker, Gas (Rocking) (EL / NL)	Transformer, LTC Power (Sliding) (EL / NL)	Control House (Anchorage Failure) (EL / NL)
B1	0.40 / 0.27	0.16 / 0.04	0.42 / 0.16	0.41 / 0.16	0.54 / 0.24
B2	0.30 / 0.22	0.06 / 0.01	0.21 / 0.08	0.22 / 0.09	0.31 / 0.14
B3	0.20 / 0.14	0.01 / 0.00	0.06 / 0.01	0.06 / 0.01	0.10 / 0.02
B4	0.22 / 0.16	0.01 / 0.00	0.08 / 0.02	0.09 / 0.03	0.14 / 0.05
C1	0.43 / 0.29	0.20 / 0.05	0.48 / 0.19	0.46 / 0.20	0.60 / 0.29
C2	0.38 / 0.28	0.13 / 0.04	0.38 / 0.18	0.37 / 0.18	0.50 / 0.27
C3	0.39 / 0.29	0.15 / 0.05	0.40 / 0.19	0.39 / 0.20	0.52 / 0.29
C4	0.33 / 0.24	0.08 / 0.02	0.27 / 0.11	0.27 / 0.11	0.39 / 0.17
C5	0.30 / 0.24	0.06 / 0.02	0.21 / 0.11	0.22 / 0.11	0.31 / 0.17
C6	0.26 / 0.19	0.03 / 0.01	0.14 / 0.04	0.15 / 0.05	0.22 / 0.08
C7	0.28 / 0.22	0.04 / 0.01	0.18 / 0.08	0.18 / 0.09	0.27 / 0.14
STD	0.08 / 0.05	0.06 / 0.02	0.14 / 0.07	0.14 / 0.07	0.17 / 0.10
USGS Estimate	0.34	0.09	0.29	0.29	0.41

5.6 Summary

This chapter describes a site response analysis through (1) selecting and scaling representative ground motions for the M9.3 Cascadia Subduction Zone scenario earthquake, (2) developing representative soil profiles for various locations at an evaluation site, (3) conducting and comparing the results of equivalent linear (EL) and nonlinear (NL) site response analyses, and (4) assessing the probability of failure of specific electrical equipment for a substation located at the evaluation site. Based on the evaluations performed, the following conclusions can be drawn:

- Amplification can vary dramatically across a given site, in general, and the evaluation site, in particular. Depending on the approach, the PGA values from the southwestern to the northeastern side of the site varied up to 50%, decreasing eastward across the site. The EL approach estimated PGA values ranging from 0.20g to 0.43g, compared with a significantly smaller range of 0.14g to 0.27g for the NL analysis.
- The average PGA value estimated for the site using the NL approach is lower than the USGS estimate by 32% for this scenario event, whereas the difference computed using the EL approach was lower by 0.02g (6%).
- The peak horizontal accelerations computed using the EL and NL approaches were similar for those soil layers with a maximum shear strain, γ_{\max} , less than 0.4%.
- The NL approach is more suitable to capture the presence of soft-soil deposits and capturing the nonlinear behavior of the soil layers, particularly for $\gamma_{\max} > 0.4\%$.
- The NL approach also appears to capture short period amplification more effectively.
- The EL approach provides higher probability of failure estimates for the electrical equipment on the site.

- The lowest POF for all electrical components considered was computed for location B3, since the PGA is estimated to be the lowest at this location, regardless of the site response analysis approach.
- The POF for all pieces of equipment increased as one moves eastward across the site.
- The transformer, non-LTC power is characterized with the highest POF and is the limiting piece of electrical equipment for the site based on the equipment analyzed.

Chapter 6: Summary

6.1 Summary

The main objective of this thesis was to quantify the likelihood and magnitude of seismically-induced landslide occurrence at a regional scale to determine the associated vulnerabilities of the western power grid from a M9.3 Megathrust CSZ scenario earthquake. This thesis was part of a broader study evaluating the seismic resilience of the western power grid. This goal was accomplished by developing a probabilistic method for a regional seismic landslide hazard analysis and map for the Western United States based on the M9.3 Megathrust CSZ scenario earthquake (Chapter 3). Using the results of the developed seismic landslide hazard map, an assessment of the vulnerability of transmission poles and towers was completed for three probabilities of exceedance: 5%, 15% and 50% (Chapter 4). The map was validated qualitatively using previously-mapped landslides (Chapter 4). To provide context to the broader study focusing on non-landslide-induced impacts to the western power grid (e.g., ground shaking and inertial equipment loading), an evaluation site was characterized through a detailed site-specific site response analyses to evaluate the differences in amplification between equivalent linear and nonlinear, total stress analyses using ten ground motions pairs scaled and matched to the USGS seismic scenario hazard (Chapter 5). The results of the site-specific site response analysis were then used to evaluate the potential impact to the electrical components for the substation at the evaluation site for comparison to the seismic hazard developed using the regional map (Chapter 5).

6.2 Conclusion

The following summarizes the findings and contributions of the thesis regarding the developed probabilistic landslide hazard map and the potential impacts to the power grid as well as the site response analysis:

- The soil strength (i.e., friction angle) for each lithological unit was estimated by determining the slope failure angle of past landslides to develop cumulative distribution functions (CDF). The CDFs (i.e., Distribution of Mobilized Strength (DOMS) curves) are used as a proxy for the friction angle of the lithological units and display the probability of failure for a lithological unit given a specific angled slope face.
- To calculate the aggregated probability of a landslide, conditional properties (i.e., $PGA > 0.05g$) were used for a set of random variables (e.g., slope angle, lithological unit, PGA and PGV), Newmark's Method downhill equation was used to calculate the yield acceleration of the slope (*section 3.3.1*). When the peak ground acceleration exceeds the yield acceleration given the condition that a pixel located at x,y with a slope angle of θ , and estimated friction angle of ϕ'_j sampled from the statistical distribution of the corresponding lithological unit (i.e., DOMS curves).
- A logic tree approach was used to develop the *LOS2I* model that is dependent on a minimum threshold of shaking (i.e., $PGA = 0.05g$). The following landslide regression models were used: *AM88*, *JS07*, *BT07*, *SRS08* and *S16* (Reference *Table 3-6* for the regression model), with the following weights stated in *Table 3-7*. When the ratio of $\frac{a_y}{PGA} < 0.05$, method 1 is used, otherwise method 2 is applied.
- Probabilities of exceeding displacement thresholds, δ , of 0.03, 0.05, 0.07, 0.1, 0.13, 0.15, 0.2, 0.4, 0.6, 1.0, 1.5, 2.0, 3.0, 5.0, 10, and 100 m were determined for the following

models: *AM88*, *JS07*, *BT07*, *SRS08* and *SI6*. The representative displacement model *LOS21*, was applied to probabilities to calculate the final probability of exceedance for each displacement threshold.

- The proposed seismic landslide hazard maps provide reasonable consistency with detailed landslide inventory databases (i.e., SLIDO; (Burns and Watzig 2020) and susceptibility maps (i.e., (Burns et al. 2016; Sharifi-Mood et al. 2017).
- An overall trend of large displacements is observed along the west coast on steep slopes (i.e., a region of intense seismic shaking) and in proximity to the Cascadia Subduction Zone. Large displacements are generally limited to west of the Cascades range due to sufficient decay in PGA with distance from the fault zone that landsliding is unlikely.
- The 15% POE produced maximum displacement equal to 3.55 m, while the 50% POE map estimated maximum displacement of 1.10 m and 5% POE map estimated a maximum displacement of 6.07m.
- Based on the *LOS21* predictive displacement model, it is anticipated that electrical infrastructure located west of the Cascades in Washington, Oregon, and Northern California will be subjected to the highest risk of landslide-induced damage.
- Amplification can vary dramatically across a given site, in general, and the selected evaluation site, in particular. Depending on the approach, the peak ground accelerations (PGAs) from the southwestern to the northeastern side of the site can vary up to 50%. The PGAs are anticipated to decrease eastward across the site.
- The equivalent linear approach estimated a relatively wide range of PGA values from 0.20g to 0.43g, whereas the non-linear approach produced a significantly smaller range of 0.14g to 0.27g.

- The average PGA developed for the site using the non-linear approach is 32% lower than that developed for the seismic hazard map, whereas the difference computed using the equivalent linear approach was slightly lower by 0.02g (6%).
- The peak horizontal accelerations computed using the equivalent linear and non-linear approaches were similar for those soil layers where the maximum shear strain, γ_{\max} , was less than 0.4%. However, the non-linear approach is more suitable in capturing the presence of soft-soil deposits and capturing the nonlinear behavior of the soil layers, particularly for $\gamma_{\max} > 0.4\%$. The non-linear approach also appears better suited for capturing short period amplification.
- The EL approach provides higher probability of failure estimates for the electrical equipment on the site.
- The lowest POF for all electrical components considered was computed for location B3, since the PGA is estimated to be the lowest at this location, regardless of the site response analysis approach.
- The POF for all pieces of equipment increased as one moves eastward across the site.
- The transformer, non-LTC power is characterized with the highest POF and is the limiting piece of electrical equipment for the site based on the equipment analyzed.
- The variability observed between the expected seismic conditions for the evaluation site determined using the regional seismic landslide map results and the site-specific site response analysis (6% lower for the EL and 36% lower for the NL) can be attributed to the much coarser resolution of the USGS M9.3 earthquake scenario dataset (0.0316° equating to approximately 3.5 km in latitude and 2.5 km in longitude) spanning an area of $\sim 9 \text{ km}^2$, while the evaluation site encompasses only 0.10 km^2 ,

6.3 Suggestions for Future Research

Based on the findings of this study, there are several areas for further study in order to better understand the seismic resilience of the western power grid:

1. Application of the *LOS21* model to a past megathrust ($> M 9.0$) earthquake event (e.g., the 2011 Tōhoku earthquake) and assess the accuracy of the probabilistic model.
2. Perform additional site response analyses for at-risk substations across the study area to compare to the mapped estimates with the analysis results.
3. Develop true fragility curves for power poles and towers and apply it to the probabilistic map to assess which pole and towers are at risk.
4. Improve the understanding of the resilience of the existing transportation network from a $M9.3$ event and use it to estimate the expected road closures or delays in emergency response to develop new emergency routes.
5. For the boarder study, evaluate how they the expected road closures or delays in emergency response might impact the recovery rate of substation equipment and the electrical grid.

References

- Adams, J. (1990). "Paleoseismicity of the Cascadia subduction zone: Evidence from turbidites off the Oregon-Washington margin." *Tectonics*, Wiley Online Library, 9(4), 569–583.
- Aimar, M., and Foti, S. (2021). "Simplified Criteria to Select Ground Response Analysis Methods for Seismic Building Design: Equivalent Linear versus Nonlinear Approaches." *Bulletin of the Seismological Society of America*.
- Alam, M. S., Simpson, B., and Barbosa, A. R. (2020). *Defining Appropriate Fragility Functions for Oregon*. A report for the Cascadia Lifeline Program, Oregon State University.
- Algermissen, S. T., Perkins, D. M., Thenhaus, P. C., Hanson, S. L., and Bender, B. L. (1982). *Probabilistic estimates of maximum acceleration and velocity in rock in the contiguous United States*. US Geological Survey.
- Ambraseys, N. N., and Menu, J. M. (1988). "Earthquake-induced ground displacements." *Earthquake Engineering & Structural Dynamics*, 16(7), 985–1006.
- Anderson, L. R., Keaton, J. R., Aubrey, K., and Ellis, S. J. (1982). "Liquefaction potential map for Davis County, Utah: Logan, Utah State University Department of Civil and Environmental Engineering and Dames & Moore Consulting Engineers." *S. Geological Survey*, 94–7.
- Andrews, D. C., and Martin, G. R. (2000). "Criteria for liquefaction of silty soils." *Proc., 12th World Conf. on Earthquake Engineering*, NZ Soc. for EQ Engrg. Upper Hutt, New Zealand, 1–8.
- Andrus, R. D., Mohanan, N. P., Piratheepan, P., Ellis, B. S., and Holzer, T. L. (2007). "Predicting shear-wave velocity from cone penetration resistance." *Proceedings of the 4th international conference on earthquake geotechnical engineering, Thessaloniki, Greece*.
- Armstrong, R. J., and Malvick, E. J. (2016). "Practical Considerations in the Use of Liquefaction Susceptibility Criteria." *Earthquake Spectra*, SAGE Publications Ltd STM, 32(3), 1941–1950.
- Ashford, S. A., and Sitar, N. (1997). "Analysis of topographic amplification of inclined shear waves in a steep coastal bluff." *Bulletin of the seismological society of America*, The Seismological Society of America, 87(3), 692–700.
- Ashford, S. A., and Sitar, N. (2002). "Simplified Method for Evaluating Seismic Stability of Steep Slopes." *Journal of Geotechnical and Geoenvironmental Engineering*, 128(2), 119–128.
- Ashford, S. A., Sitar, N., Lysmer, J., and Deng, N. (1997). "Topographic effects on the seismic response of steep slopes." *Bulletin of the seismological society of America*, The Seismological Society of America, 87(3), 701–709.
- ASTM D1586-12. (2012). *Standard Test Method for Penetration Test and Split-Barrel Sampling of Soils*. ASTM International, West Conshohocken, PA.
- Baise, L. G., Brankman, C. M., Higgins, R. B., and Dawson, K. M. (2002). *Liquefaction Hazard Mapping in Boston, Massachusetts: Collaborative Research with William Lettis & Associates, Inc., and Tufts University*. Department of Civil and Environmental Engineering, Tufts University.
- Baise, L. G., Higgins, R. B., and Brankman, C. M. (2006). "Liquefaction Hazard Mapping—Statistical and Spatial Characterization of Susceptible Units." *Journal of Geotechnical and Geoenvironmental Engineering*, 132(6), 705–715.

- Bard, P.-Y. (1982). “Diffracted waves and displacement field over two-dimensional elevated topographies.” *Geophysical Journal International*, 71(3), 731–760.
- Bard, P.-Y., and Bouchon, M. (1985). “The two-dimensional resonance of sediment-filled valleys.” *Bulletin of the Seismological Society of America*, The Seismological Society of America, 75(2), 519–541.
- Bartlett, S. F., and Youd, T. L. (1992). “Empirical Analysis of Horizontal Ground Displacement Generated by Liquefaction-Induced Lateral Spreads.”
- Bath, M. (1981). “Earthquake magnitude—recent research and current trends.” *Earth-Science Reviews*, Elsevier, 17(4), 315–398.
- Bazzurro, P., and Cornell, C. A. (2004). “Nonlinear Soil-Site Effects in Probabilistic Seismic-Hazard Analysis.” *Bulletin of the Seismological Society of America*, GeoScienceWorld, 94(6), 2110–2123.
- Birchfield, A. B., Xu, T., Gegner, K. M., Shetye, K. S., and Overbye, T. J. (2017). “Grid Structural Characteristics as Validation Criteria for Synthetic Networks.” *IEEE Transactions on Power Systems*, 32(4), 3258–3265.
- Birchfield, A. B., Xu, T., and Overbye, T. J. (2018). “Power flow convergence and reactive power planning in the creation of large synthetic grids.” *IEEE Transactions on Power Systems*, IEEE, 33(6), 6667–6674.
- Bird, J. F., and Bommer, J. J. (2004). “Earthquake losses due to ground failure.” *Engineering Geology*, 75(2), 147–179.
- Bolton, M. (1986). “Strength and dilatancy of sands.” *Geotechnique*, 36, 65–78.
- Bommer, J. J., and Scherbaum, F. (2008). “The Use and Misuse of Logic Trees in Probabilistic Seismic Hazard Analysis.” *Earthquake Spectra*, SAGE Publications Ltd STM, 24(4), 997–1009.
- Borcherdt, R. D. (1970). “Effects of local geology on ground motion near San Francisco Bay.” *Bulletin of the Seismological Society of America*, The Seismological Society of America, 60(1), 29–61.
- Boulanger, R. W., and Idriss, I. M. (2006). “Liquefaction Susceptibility Criteria for Silts and Clays.” *Journal of Geotechnical and Geoenvironmental Engineering*, American Society of Civil Engineers, 132(11), 1413–1426.
- Boulanger, R. W., and Idriss, I. M. (2014). “CPT and SPT based liquefaction triggering procedures.” *Report No. UCD/CGM.-14*, 1.
- Boulanger, R. W., and Idriss, I. M. (2015). “Magnitude scaling factors in liquefaction triggering procedures.” *Soil Dynamics and Earthquake Engineering*, Soil Liquefaction during Recent Large-Scale Earthquakes, 79, 296–303.
- Boulanger, R. W., and Idriss, I. M. (2016). “CPT-Based Liquefaction Triggering Procedure.” *Journal of Geotechnical and Geoenvironmental Engineering*, 142(2), 04015065.
- Bozorgnia, Y., Stewart, J. P., and Abrahamson, N. A. (2020). “Data resources for NGA-subduction project.” *PEER No. Report 2020*, 2.
- Brandenberg, S. J., and Yniesta, S. (2015). “Unloading-reloading rule for nonlinear site response analysis.”
- Bray, J. D., and Macedo, J. (2019). “Procedure for Estimating Shear-Induced Seismic Slope Displacement for Shallow Crustal Earthquakes.” *Journal of Geotechnical and Geoenvironmental Engineering*, 145(12), 04019106.

- Bray, J. D., Macedo, J., and Travararou, T. (2018). "Simplified Procedure for Estimating Seismic Slope Displacements for Subduction Zone Earthquakes." *Journal of Geotechnical and Geoenvironmental Engineering*, 144(3), 04017124.
- Bray, J. D., and Rathje, E. M. (1998). "Earthquake-Induced Displacements of Solid-Waste Landfills." *Journal of Geotechnical and Geoenvironmental Engineering*, 124(3), 242–253.
- Bray, J. D., and Sancio, R. B. (2006). "Assessment of the Liquefaction Susceptibility of Fine-Grained Soils." *Journal of Geotechnical and Geoenvironmental Engineering*, 132(9), 1165–1177.
- Bray, J. D., and Travararou, T. (2007). "Simplified Procedure for Estimating Earthquake-Induced Deviatoric Slope Displacements." *Journal of Geotechnical and Geoenvironmental Engineering*, 133(4), 381–392.
- Brekken et al. (2021) *Personal Communication*.
- Bunn, M., Leshchinsky, B., and Olsen, M. J. (2020). "Estimates of three-dimensional rupture surface geometry of deep-seated landslides using landslide inventories and high-resolution topographic data." *Geomorphology*, Elsevier, 367, 107332.
- Burns, W. J., and Franczyk, J. J. (2021). "HISTORY OF THE OREGON LANDSLIDE WARNING SYSTEM 1997–2018 AND RECOMMENDATIONS FOR IMPROVEMENTS." *DOGAMI*, 126.
- Burns, W. J., and Madin, I. (2009). "Protocol for inventory mapping of landslide deposits from light detection and ranging (LiDAR) imagery." Portland, OR.
- Burns, W. J., Mickelson, K. A., and Madin, I. (2016). *Landslide susceptibility overview map of Oregon*. Oregon Department of Geology and Mineral Industries.
- Burns, W. J., and Watzig, R. J. (2020). "SLIDO-4.2: Statewide Landslide Information Database for Oregon, release 4.2." 41.
- Campbell, K. W., and Bozorgnia, Y. (2008). "NGA ground motion model for the geometric mean horizontal component of PGA, PGV, PGD and 5% damped linear elastic response spectra for periods ranging from 0.01 to 10 s." *Earthquake spectra*, SAGE Publications Sage UK: London, England, 24(1), 139–171.
- Cho, Y. (2020). "Probabilistic assessment of the seismic performance of earth slopes using computational simulation." PhD Thesis.
- Chu, D. B., Stewart, J. P., Boulanger, R. W., and Lin, P. S. (2008). "Cyclic Softening of Low-Plasticity Clay and Its Effect on Seismic Foundation Performance." *Journal of Geotechnical and Geoenvironmental Engineering*, 134(11), 1595–1608.
- Clough, R. W., and Penzien, J. (1975). "Structural dynamics." *New York: McGrawHill*.
- Cornell, C. A. (1968). "Engineering seismic risk analysis." *Bulletin of the seismological society of America*, The Seismological Society of America, 58(5), 1583–1606.
- Corominas, J., van Westen, C., Frattini, P., Cascini, L., Malet, J.-P., Fotopoulou, S., Catani, F., Van Den Eeckhaut, M., Mavrouli, O., Agliardi, F., Pitilakis, K., Winter, M. G., Pastor, M., Ferlisi, S., Tofani, V., Hervás, J., and Smith, J. T. (2014). "Recommendations for the quantitative analysis of landslide risk." *Bulletin of Engineering Geology and the Environment*, 73(2), 209–263.
- Cramer, C. H., Rix, G. J., and Tucker, K. (2008). "Probabilistic Liquefaction Hazard Maps for Memphis, Tennessee." *Seismological Research Letters*, GeoScienceWorld, 79(3), 416–423.

- Cruden, D. M., and Varnes, D. J. (1996). "LANDSLIDES: INVESTIGATION AND MITIGATION. CHAPTER 3 - LANDSLIDE TYPES AND PROCESSES." *Transportation Research Board Special Report*, (247).
- Darendeli, M. B. (2001). *Development of a new family of normalized modulus reduction and material damping curves*. The university of Texas at Austin.
- Del Gaudio, V., Pierri, P., and Wasowski, J. (2003). "An approach to time-probabilistic evaluation of seismically induced landslide hazard." *Bulletin of the Seismological Society of America*, Seismological Society of America, 93(2), 557–569.
- Delgado, J., Garrido, J., López-Casado, C., Martino, S., and Peláez, J. A. (2011). "On far field occurrence of seismically induced landslides." *Engineering Geology*, 123(3), 204–213.
- Dobry, R., Borcherdt, R. D., Crouse, C. B., Idriss, I. M., Joyner, W. B., Martin, G. R., Power, M. S., Rinne, E. E., and Seed, R. B. (2000). "New site coefficients and site classification system used in recent building seismic code provisions." *Earthquake spectra*, SAGE Publications Sage UK: London, England, 16(1), 41–67.
- Du, W. (2018). "Effects of directionality and vertical component of ground motions on seismic slope displacements in Newmark sliding-block analysis." *Engineering Geology*, 239, 13–21.
- Du, W., and Wang, G. (2014). "Fully probabilistic seismic displacement analysis of spatially distributed slopes using spatially correlated vector intensity measures." *Earthquake Engineering & Structural Dynamics*, 43(5), 661–679.
- Du, W., Wang, G., and Huang, D. (2018). "Evaluation of Seismic Slope Displacements Based on Fully Coupled Sliding Mass Analysis and NGA-West2 Database." *Journal of Geotechnical and Geoenvironmental Engineering*, 144(8), 06018006.
- Dueñas-Osorio, L., Craig, J. I., and Goodno, B. J. (2007). "Seismic response of critical interdependent networks." *Earthquake Engineering & Structural Dynamics*, 36(2), 285–306.
- Erickson, G. L. (2006). "Probabilistic liquefaction potential mapping of the Salt Lake Valley Book Thesis." *University of Utah*.
- ESRI. (2019). *ArcGIS Pro 2.4.0*. ESRI.
- FEMA. (2010). "Earthquake Loss Estimation Methodology: User's Manual." *Federal Emergency Management Agency, Washington, DC*.
- FEMA. (2012). "Hazus®–MH 2.1." <https://www.fema.gov/media-library-data/20130726-1820-25045-6286/hzmh2_1_eq_tm.pdf> (Nov. 5, 2020).
- Fotopoulou, S. D., and Pitilakis, K. D. (2015). "Predictive relationships for seismically induced slope displacements using numerical analysis results." *Bulletin of Earthquake Engineering*, Springer, 13(11), 3207–3238.
- Gardoni, P., van de Lindt, J. W., Ellingwood, B., McAllister, T. P., Lee, J., Cutler, H., and Cox, D. (2018). "The interdependent networked community resilience modeling environment (IN-CORE)." *16th European Conference on Earthquake Engineering*.
- Gaudio, V. D., Coccia, S., Wasowski, J., Gallipoli, M. R., and Mucciarelli, M. (2008). "Detection of directivity in seismic site response from microtremor spectral analysis." *Natural Hazards and Earth System Sciences*, Copernicus GmbH, 8(4), 751–762.
- Ghafghazi, M., DeJong, J. T., Sturm, A. P., and Temple, C. E. (2017). "Instrumented Becker Penetration Test. II: iBPT-SPT Correlation for Characterization and Liquefaction Assessment of Gravelly Soils." *Journal of Geotechnical and Geoenvironmental Engineering*, American Society of Civil Engineers, 143(9), 04017063.

- Gillins, D. T. (2012). *Mapping the probability and uncertainty of liquefaction-induced ground failure*. The University of Utah.
- Gillins, D. T. (2014). "Considering topography when mapping liquefaction hazard with the liquefaction potential index." *Proc. 10th National Conf. on Earthquake Engrg., Anchorage, Alaska, (July 21–25, 12 pp.)*.
- Gillins, D. T., and Bartlett, S. F. (2014). "Multilinear regression equations for predicting lateral spread displacement from soil type and cone penetration test data." *Journal of Geotechnical and Geoenvironmental Engineering*, American Society of Civil Engineers, 140(4), 04013047.
- Goldfinger, C., Nelson, C. H., Johnson, J. E., and Party, S. S. (2003). "Holocene earthquake records from the Cascadia subduction zone and northern San Andreas fault based on precise dating of offshore turbidites." *Annual Review of Earth and Planetary Sciences*, Annual Reviews 4139 El Camino Way, PO Box 10139, Palo Alto, CA 94303-0139, USA, 31(1), 555–577.
- Goldfinger, C., Nelson, C. H., Morey, A. E., Johnson, J. E., Patton, J. R., Karabanov, E. B., Gutierrez-Pastor, J., Eriksson, A. T., Gracia, E., Dunhill, G., Enkin, R. J., Dallimore, A., and Vallier, T. (2012). *Turbidite event history—Methods and implications for Holocene paleoseismicity of the Cascadia subduction zone*. *Turbidite event history—Methods and implications for Holocene paleoseismicity of the Cascadia subduction zone*, Professional Paper, USGS Numbered Series, U.S. Geological Survey, Reston, VA.
- Hartzell, S., Bonilla, L. F., and Williams, R. A. (2004). "Prediction of nonlinear soil effects." *Bulletin of the Seismological Society of America*, Seismological Society of America, 94(5), 1609–1629.
- Hashash, Y. M. A., Musgrove, M. I., Harmon, J. A., Ilhan, O., Xing, G., Numanoglu, O., Groholski, D., Phillips, C. A., and Park, D. (2020a). *DEEPSOIL V7.0*. Board of Trustees of University of Illinois at Urbana-Champaign, Urbana, IL.
- Hashash, Y. M. A., Musgrove, M. I., Harmon, J. A., Xing, G., Numanoglu, O., Groholski, D. R., Phillips, C. A., and Park, D. (2020b). *DEEPSOIL 7.0, User Manual*. Urbana, IL, Board of Trustees of University of Illinois at Urbana-Champaign.
- Hatanaka, M., and Uchida, A. (1996). "Empirical correlation between penetration resistance and internal friction angle of sandy soils." *Soils and foundations*, Elsevier, 36(4), 1–9.
- Heaton, T. H., and Hartzell, S. H. (1987). "Earthquake hazards on the Cascadia subduction zone." *Science*, American Association for the Advancement of Science, 236(4798), 162–168.
- Highland, L., and Bobrowsky, P. T. (2008). *The landslide handbook: a guide to understanding landslides*. US Geological Survey Reston.
- Holzer, T. L. (2008). "Probabilistic liquefaction hazard mapping." *Geotechnical earthquake engineering and soil dynamics IV*, 1–32.
- Holzer, T. L., Bennett, M. J., Noce, T. E., Padovani, A. C., and Tinsley III, J. C. (2006). "Liquefaction hazard mapping with LPI in the greater Oakland, California, area." *Earthquake Spectra*, SAGE Publications Sage UK: London, England, 22(3), 693–708.
- Holzer, T. L., Noce, T. E., and Bennett, M. J. (2007). "LiqueMap: A real-time postearthquake map of liquefaction probability." *AGUFM*, 2007, S51A-0225.
- Holzer, T. L., Toprak, S., and Bennett, M. J. (2003). "The application of the liquefaction potential index to liquefaction hazard mapping." *Eighth US–Japan Workshop on*

- Earthquake Resistant Design of Lifeline Facilities and Countermeasures against Liquefaction*, Tokyo, 171.
- Horton, J. D., San Juan, C. A., and Stoesser, D. B. (2017). *The State Geologic Map Compilation (SGMC) geodatabase of the conterminous United States. The State Geologic Map Compilation (SGMC) geodatabase of the conterminous United States*, Data Series, USGS Numbered Series, U.S. Geological Survey, Reston, VA, 56.
- Hsein, J., ChingJianye, WangLei, KhoshnevisanSara, and KuChih-Sheng. (2013). “Simplified procedure for estimation of liquefaction-induced settlement and site-specific probabilistic settlement exceedance curve using cone penetration test (CPT).” *Canadian Geotechnical Journal*, NRC Research Press.
- Hwang, H. H. M., and Huo, J.-R. (1998). “Seismic fragility analysis of electric substation equipment and structures.” *Probabilistic Engineering Mechanics*, 13(2), 107–116.
- Idriss, I. M. (1999). “An update to the Seed-Idriss simplified procedure for evaluating liquefaction potential.” *Proc., TRB Workshop on New Approaches to Liquefaction*, Publ. n. FHWA-RD-99-165, Federal Highway Administration.
- Idriss, I. M., and Boulanger, R. W. (2008). *Soil liquefaction during earthquakes*. Earthquake Engineering Research Institute.
- Idriss, I. M., and Boulanger, R. W. (2010). “SPT-based liquefaction triggering procedures.” *Rep. UCD/CGM-10*, 2, 4–13.
- Irikura, K. (1986). “Prediction of strong acceleration motion using empirical Green’s function.” *Proc. 7th Japan Earthq. Eng. Symp*, 151–156.
- Iwasaki, T., Tokida, K. I., Tatsuoka, F., Watanabe, S., Yasuda, S., and Sato, H. (1982). “Microzonation for soil liquefaction potential using simplified methods.” *Proceedings of the 3rd international conference on microzonation, Seattle*, 1310–1330.
- Jaimés, M. A., Niño, M., and Reinoso, E. (2015). “Regional map of earthquake-induced liquefaction hazard using the lateral spreading displacement index D_{LL}.” *Natural Hazards*, Springer, 77(3), 1595–1618.
- Jaky, J. (1948). “Pressure in Soils.” *Conference of Soil Mechanis and Foundation Engineering*, 1, 103–107.
- Jana, A., and Stuedlein, A. W. (2021). “Monotonic, Cyclic, and Postcyclic Responses of an Alluvial Plastic Silt Deposit.” *Journal of Geotechnical and Geoenvironmental Engineering*, American Society of Civil Engineers, 147(3), 04020174.
- Jibson, R. W. (1993). “Predicting earthquake-induced landslide displacements using Newmark’s sliding block analysis.” *Transportation research record*, 1411, 9–17.
- Jibson, R. W. (2007). “Regression models for estimating coseismic landslide displacement.” *Engineering Geology*, 91(2), 209–218.
- Jibson, R. W., and Harp, E. L. (2016). “Ground Motions at the Outermost Limits of Seismically Triggered LandslidesGround Motions at the Outermost Limits of Seismically Triggered Landslides.” *Bulletin of the Seismological Society of America*, GeoScienceWorld, 106(2), 708–719.
- Jibson, R. W., Harp, E. L., and Michael, J. A. (2000). “A method for producing digital probabilistic seismic landslide hazard maps.” *Engineering Geology*, 58(3), 271–289.
- Kaklamanos, J., Baise, L. G., Thompson, E. M., and Dorfmann, L. (2015). “Comparison of 1D linear, equivalent-linear, and nonlinear site response models at six KiK-net validation sites.” *Soil Dynamics and Earthquake Engineering*, 69, 207–219.

- Kaklamanos, J., Bradley, B. A., Thompson, E. M., and Baise, L. G. (2013). “Critical parameters affecting bias and variability in site-response analyses using KiK-net downhole array data.” *Bulletin of the Seismological Society of America*, Seismological Society of America, 103(3), 1733–1749.
- Kayen, R., Moss, R. E. S., Thompson, E. M., Seed, R. B., Cetin, K. O., Kiureghian, A. D., Tanaka, Y., and Tokimatsu, K. (2013). “Shear-Wave Velocity–Based Probabilistic and Deterministic Assessment of Seismic Soil Liquefaction Potential.” *Journal of Geotechnical and Geoenvironmental Engineering*, American Society of Civil Engineers, 139(3), 407–419.
- Keefer, D. K. (1984). “Landslides caused by earthquakes.” *Geological Society of America Bulletin*, Geological Society of America, 95(4), 406–421.
- Keefer, D. K. (2002). “Investigating Landslides Caused by Earthquakes – A Historical Review.” *Surveys in Geophysics*, 23(6), 473–510.
- Kempner Jr., L. (n.d.). “IEEE 693-2005 Recommended Practice for Seismic Design of Substations (images).”
- Khazai, B., and Sitar, N. (2000). “Assessment of Seismic Slope Stability Using GIS Modeling.” *Geographic Information Sciences*, Taylor & Francis, 6(2), 121–128.
- Kim, B., Hashash, Y. M. A., Stewart, J. P., Rathje, E. M., Harmon, J. A., Musgrove, M. I., Campbell, K. W., and Silva, W. J. (2016). “Relative Differences between Nonlinear and Equivalent-Linear 1-D Site Response Analyses.” *Earthquake Spectra*, SAGE Publications Ltd STM, 32(3), 1845–1865.
- Kirschbaum, D. B., Adler, R., Hong, Y., Hill, S., and Lerner-Lam, A. (2010). “A global landslide catalog for hazard applications: method, results, and limitations.” *Natural Hazards*, 52(3), 561–575.
- Kirschbaum, D., Stanley, T., and Zhou, Y. (2015). “Spatial and temporal analysis of a global landslide catalog.” *Geomorphology*, *Geohazard Databases: Concepts, Development, Applications*, 249, 4–15.
- Kramer, S. L. (1996). *Geotechnical earthquake engineering*. Prentice-Hall international series in civil engineering and engineering mechanics, Prentice Hall, Upper Saddle River, N.J.
- Kramer, S. L., and Paulsen, S. B. (2004). “Practical use of geotechnical site response models.” *Proc. Int. Workshop on Uncertainties in Nonlinear Soil Properties and their Impact on Modeling Dynamic Soil Response*, Univ. of California Berkeley, 10.
- Kulhawy, F. H., and Mayne, P. W. (1990). *Manual on estimating soil properties for foundation design*. Electric Power Research Inst., Palo Alto, CA (USA); Cornell Univ., Ithaca
- LaHusen, S. R., Duvall, A. R., Booth, A. M., Grant, A., Mishkin, B. A., Montgomery, D. R., Struble, W., Roering, J. J., and Wartman, J. (2020). “Rainfall triggers more deep-seated landslides than Cascadia earthquakes in the Oregon Coast Range, USA.” *Science Advances*, 6(38), eaba6790.
- Lee, C.-T., Huang, C.-C., Lee, J.-F., Pan, K.-L., Lin, M.-L., and Dong, J.-J. (2008). “Statistical approach to earthquake-induced landslide susceptibility.” *Engineering Geology*, 100(1), 43–58.
- Lee, D.-H., Ku, C.-S., and Yuan, H. (2004). “A study of the liquefaction risk potential at Yuanlin, Taiwan.” *Engineering Geology*, *Reconnaissance of the Chi-Chi Earthquakes, Taiwan*, 71(1), 97–117.
- Lee, J., and Green, R. a. (2015). “Empirical predictive relationship for seismic lateral displacement of slopes.” *Géotechnique*, ICE Publishing, 65(5), 374–390.

- Li, H.-H., Lin, C.-H., Zu, W., Chen, C.-C., and Weng, M.-C. (2018). "Dynamic response of a dip slope with multi-slip planes revealed by shaking table tests." *Landslides*, Springer, 15(9), 1731–1743.
- Liao, S. S., and Whitman, R. V. (1986). "Overburden correction factors for SPT in sand." *Journal of geotechnical engineering*, American Society of Civil Engineers, 112(3), 373–377.
- Liu, F., Li, Z., Jiang, M., Frattini, P., and Crosta, G. (2016). "Quantitative liquefaction-induced lateral spread hazard mapping." *Engineering Geology*, 207, 36–47.
- Luna, R., and Frost, J. D. (1998). "Spatial Liquefaction Analysis System." *Journal of Computing in Civil Engineering*, 12(1), 48–56.
- Mabey, M. A., and Madin, I. (1993). *Relative Earthquake Hazard Map: Portland, Oregon 7-1/2 Minute Quadrangle*. Oregon Department of Geology and Mineral Industries.
- Mahalingam, R., Olsen, M. J., and O'Banion, M. S. (2016). "Evaluation of landslide susceptibility mapping techniques using lidar-derived conditioning factors (Oregon case study)." *Geomatics, Natural Hazards and Risk*, Taylor & Francis, 7(6), 1884–1907.
- Makdisi, F. I., and Seed, H. B. (1978). "Simplified procedure for estimating dam and embankment earthquake-induced deformations." *Journal of Geotechnical and Geoenvironmental Engineering*, 104(Proceeding).
- Massey, C. I., Townsend, D., Jones, K., Lukovic, B., Rhoades, D., Morgenstern, R., Rosser, B., Ries, W., Howarth, J., and Hamling, I. (2020). "Volume characteristics of landslides triggered by the MW 7.8 2016 Kaikōura Earthquake, New Zealand, derived from digital surface difference modeling." *Journal of Geophysical Research: Earth Surface*, Wiley Online Library, 125(7), e2019JF005163.
- Matasovic, N., and Hashash, Y. (2012). *Practices and procedures for site-specific evaluations of earthquake ground motions*.
- Maurer, B. W., Green, R. A., Cubrinovski, M., and Bradley, B. A. (2014). "Evaluation of the Liquefaction Potential Index for Assessing Liquefaction Hazard in Christchurch, New Zealand." *Journal of Geotechnical and Geoenvironmental Engineering*, 140(7), 04014032.
- Mayne, P. W. (2007). "Cone penetration testing (Vol. 368)." *Transportation Research Board*.
- Mayne, P. W., and Kemper, J. B. (1988). "Profiling OCR in stiff clays by CPT and SPT." *Geotechnical testing journal*, ASTM International, 11(2), 139–147.
- McCulloch, D. S., and Bonilla, M. G. (1970). *Effects of the earthquake of March 27, 1964, on the Alaska Railroad*. US Government Printing Office Washington, DC.
- Mogami, T., and Kubo, K. (1953). "The behaviour of sand during vibration." *Proceedings of 3rd International Conference on Soil Mechanics and Foundation*.
- Newmark, N. M. (1965). "Effects of Earthquakes on Dams and Embankments." *Géotechnique*, 15(2), 139–160.
- Nowicki, M. A., Wald, D. J., Hamburger, M. W., Hearne, M., and Thompson, E. M. (2014). "Development of a globally applicable model for near real-time prediction of seismically induced landslides." *Engineering Geology*, 173, 54–65.
- O'Banion, M. S., and Olsen, M. J. (2014). "Predictive seismically-induced landslide hazard mapping in Oregon using a maximum entropy model (MaxEnt)." *Proceedings of the 10th national conference in earthquake engineering, Earthquake Engineering Research Institute, Anchorage*.

- Olsen, M. J., Bartlett, S. F., and Solomon, B. J. (2007). “Lateral spread hazard mapping of the Northern Salt Lake Valley, Utah, for a M7.0 scenario earthquake.” *Earthquake Spectra*, SAGE Publications Sage UK: London, England, 23(1), 95–113.
- Omidvar, B., Azizi, R., and Abdollahi, Y. (2017). “Seismic Risk Assessment of Power Substations.” *Environmental Energy and Economic Research*, 1(1).
- Oommen, T., Baise, L. G., and Vogel, R. (2010). “Validation and application of empirical liquefaction models.” *Journal of geotechnical and geoenvironmental engineering*, American Society of Civil Engineers, 136(12), 1618–1633.
- OSSPAC, O. S. S. P. A. C. (2013). “Oregon Resilience Plan.” <https://www.oregongeology.org/tsuclearinghouse/resources/pdfs/Oregon_Resilience_Plan_Final.pdf> (Nov. 8, 2020).
- Panteli, M., Mancarella, P., Trakas, D. N., Kyriakides, E., and Hatzigiorgiou, N. D. (2017). “Metrics and Quantification of Operational and Infrastructure Resilience in Power Systems.” *IEEE Transactions on Power Systems*, 32(6), 4732–4742.
- Phillips, C., and Hashash, Y. M. A. (2009). “Damping formulation for nonlinear 1D site response analyses.” *Soil Dynamics and Earthquake Engineering*, 29(7), 1143–1158.
- Porter, K., Hamburger, R., and Kennedy, R. (2012). “Practical Development and Application of Fragility Functions.” American Society of Civil Engineers, 1–16.
- Powell, J. J., and Lunne, T. (2005). “Use of CPTU data in clays/fine grained soils.” *Studia Geotechnica et Mechanica*, 27.
- Rashidian, V., and Gillins, D. T. (2018). “Modification of the liquefaction potential index to consider the topography in Christchurch, New Zealand.” *Engineering Geology*, Elsevier, 232, 68–81.
- Rathje, E. M., and Saygili, G. (2011). “Estimating Fully Probabilistic Seismic Sliding Displacements of Slopes from a Pseudoprobabilistic Approach.” *Journal of Geotechnical and Geoenvironmental Engineering*, 137(3), 208–217.
- Rathje, E. M., Wang, Y., Stafford, P. J., Antonakos, G., and Saygili, G. (2014). “Probabilistic assessment of the seismic performance of earth slopes.” *Bulletin of Earthquake Engineering*, Springer, 12(3), 1071–1090.
- Rauch, A. (1997). “Liquefaction Lateral Spreading_Chap3.” <<https://vtechworks.lib.vt.edu/bitstream/handle/10919/30346/Chp03.pdf?sequence=8&isAllowed=y>> (Nov. 5, 2020).
- Refice, A., and Capolongo, D. (2002). “Probabilistic modeling of uncertainties in earthquake-induced landslide hazard assessment.” *Computers & Geosciences*, 28(6), 735–749.
- Robertson, P. K. (2009). “Interpretation of cone penetration tests—a unified approach.” *Canadian geotechnical journal*, 46(11), 1337–1355.
- Robertson, P. K. (2015). “Comparing CPT and Vs Liquefaction Triggering Methods.” *Journal of Geotechnical and Geoenvironmental Engineering*, 141(9), 04015037.
- Robertson, P. K., and Wride, C. E. (1998). “Evaluating cyclic liquefaction potential using the cone penetration test.” *Canadian geotechnical journal*, NRC Research Press Ottawa, Canada, 35(3), 442–459.
- Rodriguez-Marek, A., and Song, J. (2016). “Displacement-Based Probabilistic Seismic Demand Analyses of Earth Slopes in the Near-Fault Region.” *Earthquake Spectra*, SAGE Publications Ltd STM, 32(2), 1141–1163.

- Sarkar, S., and Kanungo, D. P. (2004). "An integrated approach for landslide susceptibility mapping using remote sensing and GIS." *Photogrammetric Engineering & Remote Sensing*, American Society for Photogrammetry and Remote Sensing, 70(5), 617–625.
- Saygili, G., and Rathje, E. M. (2008). "Empirical Predictive Models for Earthquake-Induced Sliding Displacements of Slopes." *Journal of Geotechnical and Geoenvironmental Engineering*, 134(6), 790–803.
- Scanlan, R. H., and Sachs, K. (1974). "Earthquake time histories and response spectra." *Journal of the Engineering Mechanics Division*, American Society of Civil Engineers, 100(4), 635–655.
- Schnabel, P. B., Lysmer, J., and Seed, H. B. (1972). *Shake*. University of California, Berkeley.
- Seed, H. B., and Idriss, I. M. (1971). "Simplified Procedure for Evaluating Soil Liquefaction Potential." *Journal of the Soil Mechanics and Foundations Division*, ASCE, 97(9), 1249–1273.
- Seed, H. B., and Idriss, I. M. (1982). "Ground motions and soil liquefaction during earthquakes." *Earthquake engineering research insitutue*.
- Seed, H. B., Tokimatsu, K., Harder, L. F., and Chung, R. M. (1985). "Influence of SPT Procedures in Soil Liquefaction Resistance Evaluations." *Journal of Geotechnical Engineering*, 111(12), 1425–1445.
- Seed, R. B., Cetin, K. O., Moss, R. E., Kammerer, A. M., Wu, J., Pestana, J. M., Riemer, M. F., Sancio, R. B., Bray, J. D., and Kayen, R. E. (2003). "Recent advances in soil liquefaction engineering: a unified and consistent framework." *Proceedings of the 26th Annual ASCE Los Angeles Geotechnical Spring Seminar: Long Beach, CA*.
- SEFT. (2018). *PGE T&D Seismic Vulnerability Assessment: Seismic Fragility Curves for Select 57 kV, 115 kV, and 230 kV Asset/Structure Combinations*. PGE Substations, 308.
- Sharifi-Mood, M., Olsen, M. J., Gillins, D. T., and Mahalingam, R. (2017). "Performance-based, seismically-induced landslide hazard mapping of Western Oregon." *Soil Dynamics and Earthquake Engineering*, 103, 38–54.
- Song, J., Gao, G.-Y., Rodriguez-Marek, A., and Rathje, E. M. (2016). "Seismic assessment of the rigid sliding displacements caused by pulse motions." *Soil Dynamics and Earthquake Engineering*, 82, 1–10.
- Song, J., Gao, Y., and Feng, T. (2018a). "Probabilistic assessment of earthquake-induced landslide hazard including the effects of ground motion directionality." *Soil Dynamics and Earthquake Engineering*, 105, 83–102.
- Song, J., Gao, Y., Feng, T., and Xu, G. (2018b). "Effect of site condition below slip surface on prediction of equivalent seismic loading parameters and sliding displacement." *Engineering Geology*, 242, 169–183.
- Song, J., Gao, Y., Rodriguez-Marek, A., and Feng, T. (2017). "Empirical predictive relationships for rigid sliding displacement based on directionally-dependent ground motion parameters." *Engineering Geology*, 222, 124–139.
- Song, J., and Rodriguez-Marek, A. (2015). "Sliding Displacement of Flexible Earth Slopes Subject to Near-Fault Ground Motions." *Journal of Geotechnical and Geoenvironmental Engineering*, 141(3), 04014110.
- Sonmez, H., and Gokceoglu, C. (2005). "A liquefaction severity index suggested for engineering practice." *Environmental Geology*, Springer, 48(1), 81–91.
- Stewart, J., Afshari, K., and Hashash, Y. (2014). "Guidelines for performing hazard-consistent one-dimensional ground response analysis for ground motion prediction."

- Stewart, J. P. (2008). *Benchmarking of nonlinear geotechnical ground response analysis procedures*. Pacific Earthquake Engineering Research Center.
- Straub, D., and Der Kiureghian, A. (2008). “Improved seismic fragility modeling from empirical data.” *Structural Safety*, 30(4), 320–336.
- Sy, A., and Campanella, R. G. (1994). “Becker and standard penetration tests (BPT–SPT) correlations with consideration of casing friction.” *Canadian geotechnical journal*, NRC Research Press, 31(3), 343–356.
- Tsai, T.-L., and Chen, H.-F. (2010). “Effects of degree of saturation on shallow landslides triggered by rainfall.” *Environmental Earth Sciences*, 59(6), 1285–1295.
- USGS. (2007). “What is Directivity?” <<https://earthquake.usgs.gov/data/rupture/directivity.php>> (Mar. 7, 2021).
- USGS. (2008). “United States National Seismic Hazard Maps.” *USGS*, <<https://www.usgs.gov/natural-hazards/earthquake-hazards/seismic-hazard-maps-and-site-specific-data>> (Mar. 6, 2021).
- USGS. (2016). “USGS Circular 1325: The Landslide Handbook—A Guide to Understanding Landslides.” <<https://pubs.usgs.gov/circ/1325/>> (Nov. 1, 2020).
- USGS. (2017). “M 9.3 Scenario Earthquake - Cascadia Megathrust - whole CSZ Characteristic largest M branch.” <https://earthquake.usgs.gov/scenarios/eventpage/bssc2014cascadia_sub0_m9p34_se/executive> (Nov. 22, 2020).
- USGS. (2018). “Disperate Landslide Inventory.” <<https://usgs.maps.arcgis.com/home/item.html?id=b55cb063e4f240089986d6d437c1e926>> (Mar. 12, 2021).
- USGS. (2020). “TNM Dataset.” *TNM Download (v2.0)*, <<https://viewer.nationalmap.gov/basic/#/>> (Jan. 20, 2021).
- Van Westen, C. J., Van Asch, T. W., and Soeters, R. (2006). “Landslide hazard and risk zonation—why is it still so difficult?” *Bulletin of Engineering geology and the Environment*, Springer, 65(2), 167–184.
- Vanmarcke, E. H. (1976). “Structural response to earthquakes.” *Developments in geotechnical engineering*, Elsevier, 287–337.
- Vanzi, I. (1996). “Seismic reliability of electric power networks: methodology and application.” *Structural Safety*, 18(4), 311–327.
- Vanzi, I. (2000). “Structural upgrading strategy for electric power networks under seismic action.” *Earthquake Engineering & Structural Dynamics*, 29(7), 1053–1073.
- Varnes, D. J. (1958). “Landslide Types and Processes.” 28.
- Vucetic, M., and Dobry, R. (1991). “Effect of soil plasticity on cyclic response.” *Journal of geotechnical engineering*, American Society of Civil Engineers, 117(1), 89–107.
- Wair, B. R., DeJong, J. T., and Shantz, T. (2012). “Guidelines for Estimation of Shear Wave Velocity Profiles.” *Pacific Earthquake Engineering Research Center*, 1.
- Wang, W. (1979). *Some findings in soil liquefaction*. Earthquake Engineering Department, Water Conservancy and Hydroelectric Power
- Wang, Y., and Rathje, E. M. (2015). “Probabilistic seismic landslide hazard maps including epistemic uncertainty.” *Engineering Geology*, 196, 313–324.
- WECC. (2019). “The Western Interconnection.” <<https://www.wecc.org/epubs/StateOfTheInterconnection/Pages/The-Western-Interconnection.aspx>> (Mar. 25, 2021).

- Whitman, R. V. (1971). "Resistance of soil to liquefaction and settlement." *Soils and Foundations*, Elsevier, 11(4), 59–68.
- Wilson, J. T. (1942). "Surface waves in a heterogeneous medium." *Bulletin of the Seismological Society of America*, The Seismological Society of America, 32(4), 297–304.
- Wilson, R. (1985). "Predicting areal limit of earthquake-induced landsliding, evaluating earthquake hazards in the Los Angeles region-an earth-science perspective." *US Geological Survey Professional Paper 1360*, 317–345.
- Wolff, T. F. (1989). "Pile capacity prediction using parameter functions." *Predicted and observed axial behavior of piles: results of a pile prediction symposium*, ASCE, 96–106.
- Worden, B., Thompson, E. M., Hearne, M., and Wald, D. (2020). "3.3. ShakeMap Archives." *ShakeMap Documentation*, <http://usgs.github.io/shakemap/manual3_5/shakemap_archives.html#generating-earthquake-scenarios> (Feb. 17, 2021).
- Wyllie, D. C., and Norrish, N. I. (1996). *LANDSLIDES: INVESTIGATION AND MITIGATION. CHAPTER 14-ROCK STRENGTH PROPERTIES AND THEIR MEASUREMENT*.
- Yang, C. Y. (1986). "Random vibration of structures." John Wiley.
- Yegian, M. K., Marciano, E. A., and Ghahraman, V. G. (1991). "Earthquake-induced permanent deformations: probabilistic approach." *Journal of Geotechnical Engineering*, American Society of Civil Engineers, 117(1), 35–50.
- Youd, T. L. (1984). "Recurrence of liquefaction at the same site." *Proc. 8th World Conf. Earthq. Engng*, Prentice-Hall Inc, 231–238.
- Youd, T. L. (1991). "Mapping of earthquake-induced liquefaction for seismic zonation." *PROCEEDING OF THE INTERNATIONAL CONFERENCE ON SEISMIC ZONATION*.
- Youd, T. L. (1993). *Liquefaction-induced lateral spread displacement*. NAVAL CIVIL ENGINEERING LAB PORT HUENEME CA.
- Youd, T. L., Hansen, C. M., and Bartlett, S. F. (1999). "Revised MLR equations for predicting lateral spread displacement." *Proc. 7th US–Japan Workshop on Earthquake Resistant Design of Lifeline Facilities and Countermeasures Against Liquefaction, Seattle, Tech. Rep. No. MCEER-99*, 99–114.
- Youd, T. L., Hansen, C. M., and Bartlett, S. F. (2002). "Revised multilinear regression equations for prediction of lateral spread displacement." *Journal of Geotechnical and Geoenvironmental Engineering*, American Society of Civil Engineers, 128(12), 1007–1017.
- Youd, T. L., and Hoose, S. N. (1977). "Liquefaction susceptibility and geologic setting." *Proc., 6th World Conf. on Earthquake Engineering*, Indian Society of Earthquake Technology Roorkee, India, 37–42.
- Youd, T. L., and Idriss, I. M. (2001). "Liquefaction resistance of soils: summary report from the 1996 NCEER and 1998 NCEER/NSF workshops on evaluation of liquefaction resistance of soils." *Journal of geotechnical and geoenvironmental engineering*, American Society of Civil Engineers, 127(4), 297–313.
- Youd, T. L., Idriss, I. M., Andrus, R. D., Arango, I., Castro, G., Christian, J. T., Dobry, R., Finn, W. D. L., Harder, L. F., Hynes, M. E., Ishihara, K., Koester, J. P., Liao, S. S. C., Marcuson, W. F., Martin, G. R., Mitchell, J. K., Moriwaki, Y., Power, M. S., Robertson, P. K., Seed, R. B., and Stokoe, K. H. (2001). "Liquefaction Resistance of Soils: Summary Report from the 1996 NCEER and 1998 NCEER/NSF Workshops on Evaluation of

- Liquefaction Resistance of Soils.” *Journal of Geotechnical and Geoenvironmental Engineering*, American Society of Civil Engineers, 127(10), 817–833.
- Youd, T. L., and Perkins, D. M. (1987). “Mapping of Liquefaction Severity Index.” *Journal of Geotechnical Engineering*, American Society of Civil Engineers, 113(11), 1374–1392.
- Zhang, J., Andrus, R. D., and Juang, C. H. (2005). “Normalized shear modulus and material damping ratio relationships.” *Journal of Geotechnical and Geoenvironmental Engineering*, American Society of Civil Engineers, 131(4), 453–464.
- Zhu, J., Baise, L. G., and Koch, M. (2016). “Mapping earthquake induced liquefaction surface effects from the 2011 Tohoku earthquake using satellite imagery.” *2016 IEEE International Geoscience and Remote Sensing Symposium (IGARSS)*, IEEE, 2328–2331.

Appendix A

Table A - 1. Site information for the twenty-four sites used in developing the regression model, *LOS21*.

Low PGA (0.0 - 0.2 g)								
Soil Number	19	5	16	9	6	5	8	1
PGA (g)	0.132	0.121	0.014	0.027	0.188	0.062	0.103	0.011
Slope (°)	2.75	7.53	9.64	15.96	16.12	18.83	31.42	48.18
PGV (cm/s²)	16.31	12.76	1.82	3.16	22.47	7.00	11.08	1.29
Medium PGA (0.2 - 0.4 g)								
Soil Number	1	5	3	5	16	5	19	1
PGA (g)	0.27	0.39	0.33	0.22	0.35	0.32	0.33	0.01
Slope (°)	10.48	11.78	17.55	22.04	1.57	34.45	24.83	48.18
PGV (cm/s²)	29.33	38.36	36.76	24.96	32.07	29.00	32.09	1.29
High PGA (≥ 0.4 g)								
Soil Number	16	19	14	16	2	6	3	12
PGA (g)	0.56	0.50	0.44	0.57	0.50	0.56	0.47	0.49
Slope (°)	5.04	8.14	25.55	30.12	36.88	40.05	18.49	50.58
PGV (cm/s²)	57.47	45.86	42.80	52.54	42.38	45.34	48.01	40.81

¹ Reference Table 3-5 for which soil distribution that was applied based on the soil number

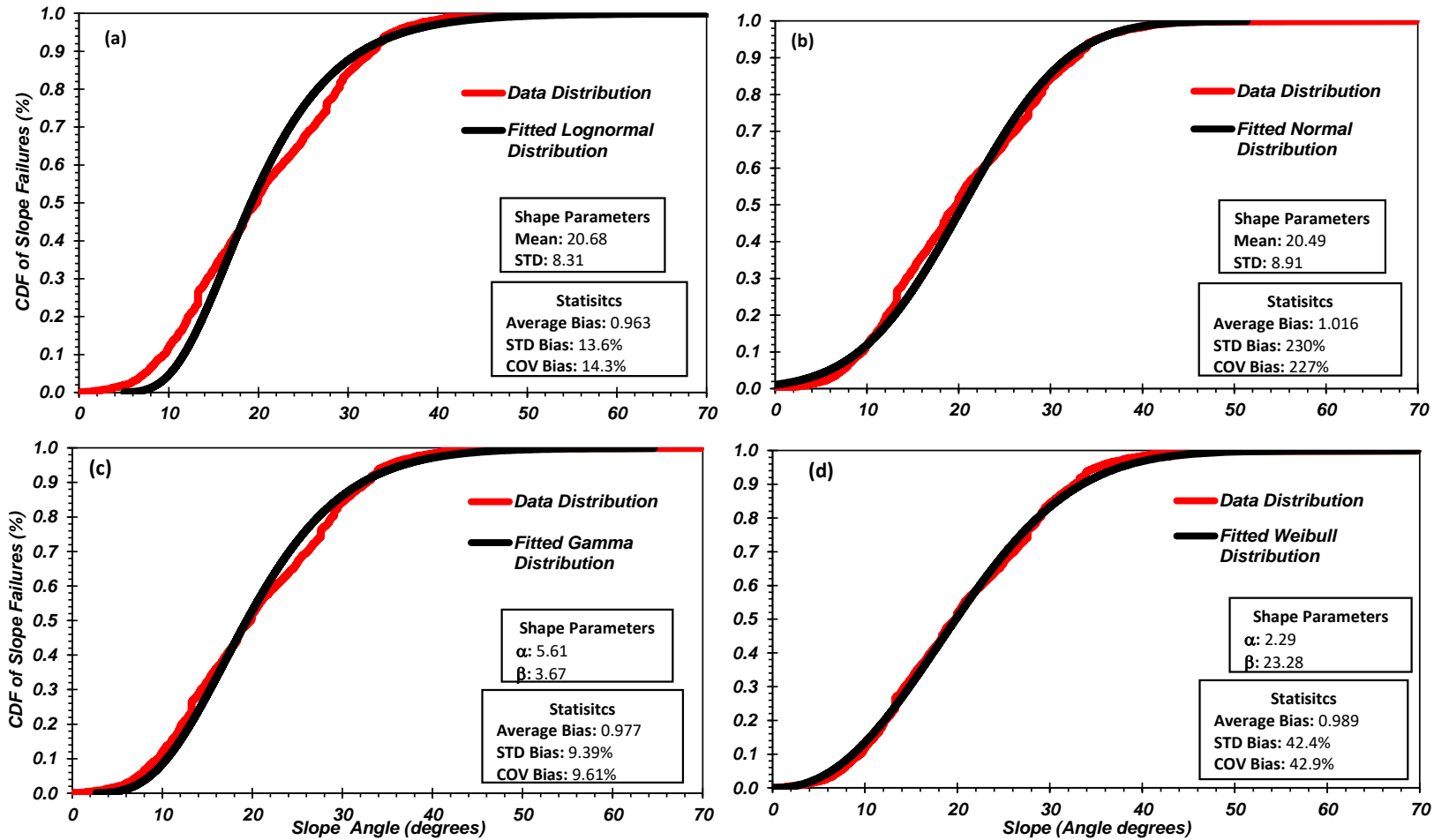


Figure A - 1. Cumulative Distribution Functions (CDF) for Metamorphic and Sedimentary, undifferentiated lithology type with shape parameters and statistic information regarding the determined bias values: (a) Lognormal, (b) Normal, (c) Gamma, (d) Weibull. The Gamma distribution (c) provided was selected as the best fit for this Metamorphic and Sedimentary, undifferentiated lithology type.

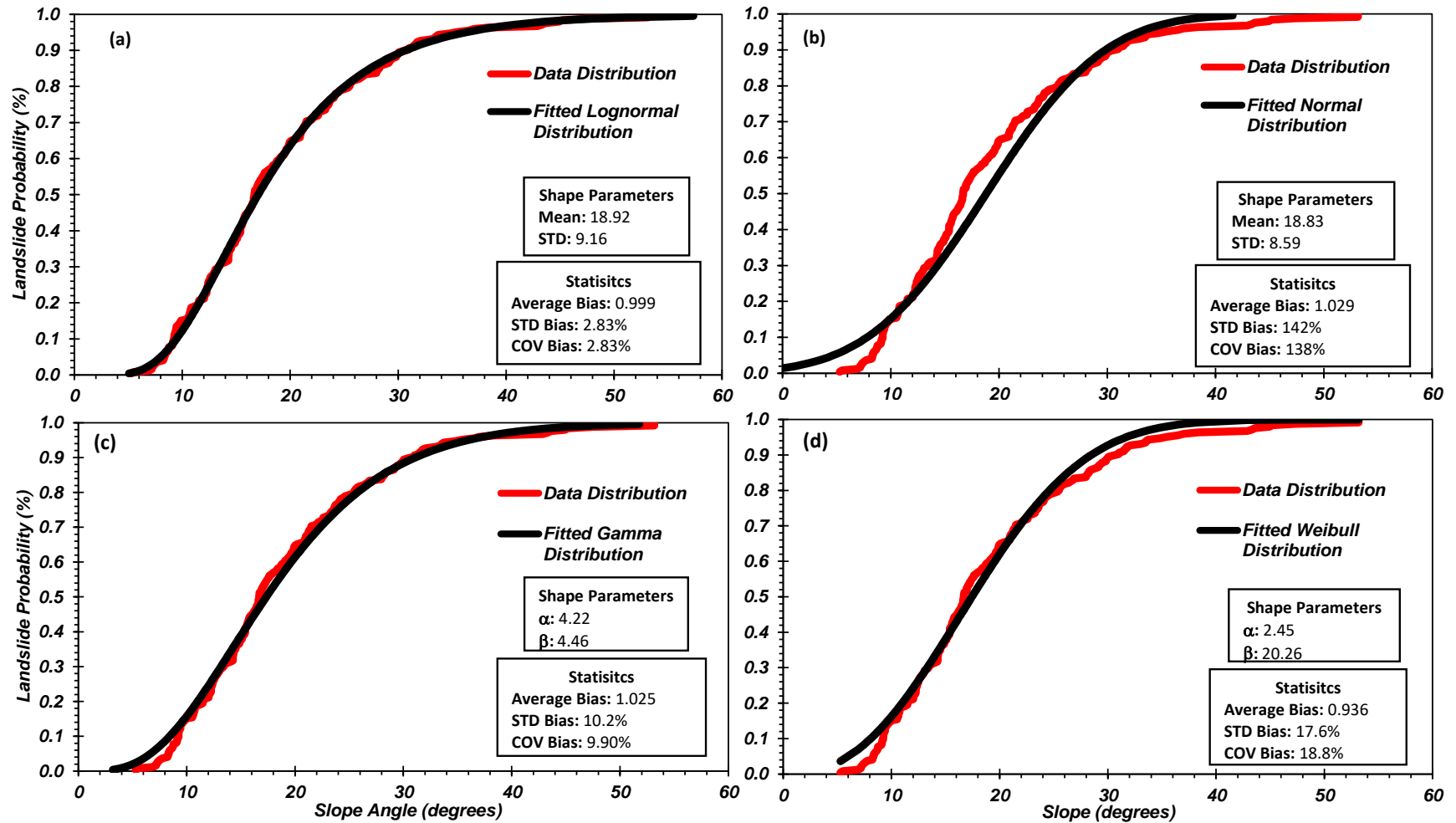


Figure A - 2. Cumulative Distribution Functions (CDF) for Metamorphic, gneiss lithology type with shape parameters and statistic information regarding the determined bias values: (a) Lognormal, (b) Normal, (c) Gamma, (d) Weibull. The Gamma distribution (c) provided was selected as the best fit for this Metamorphic, gneiss lithology type.

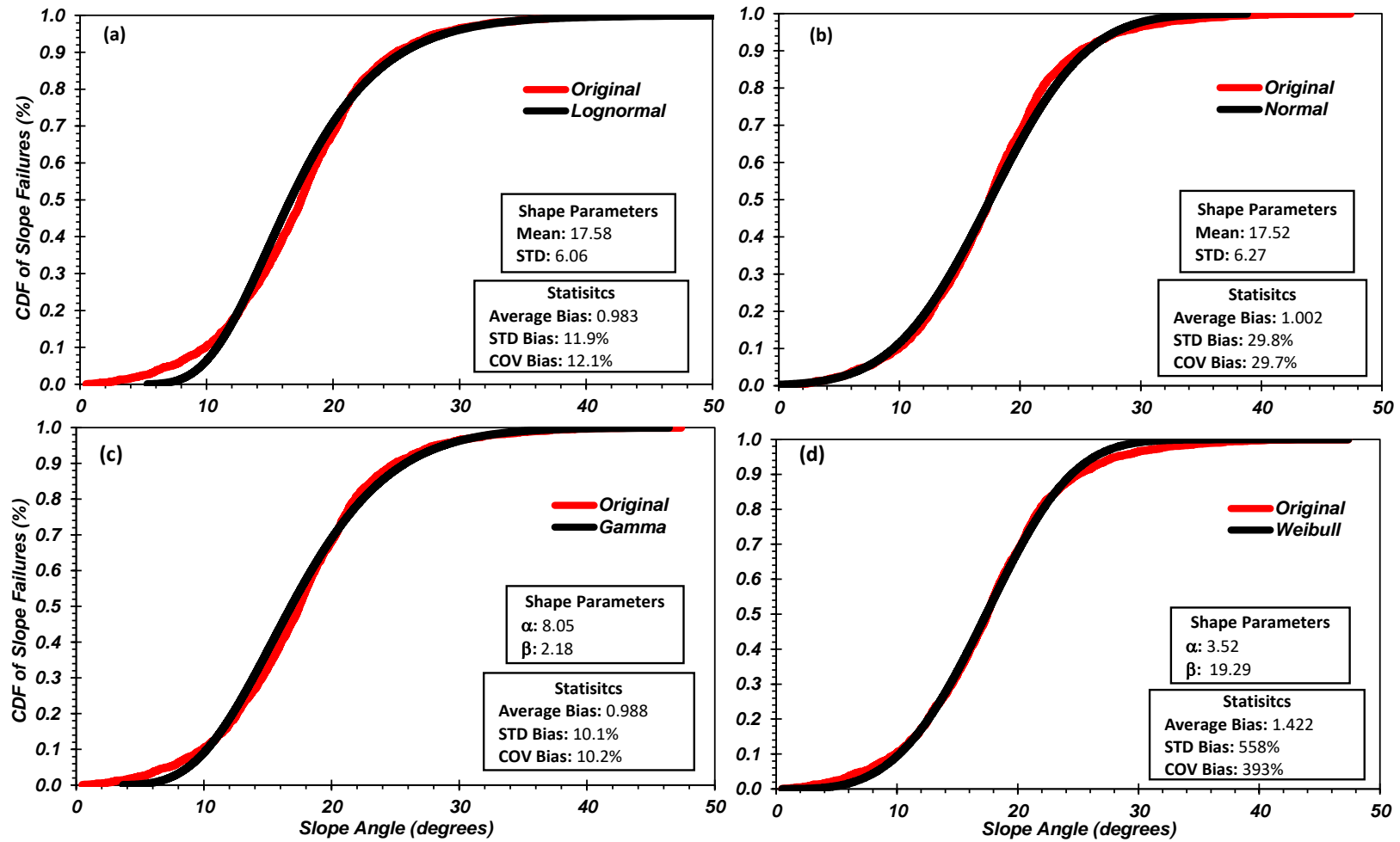


Figure A - 3. Cumulative Distribution Functions (CDF) for Metamorphic, schist lithology type with shape parameters and statistic information regarding the determined bias values: (a) Lognormal, (b) Normal, (c) Gamma, (d) Weibull. The Gamma distribution (c) provided was selected as the best fit for this Metamorphic, schist lithology type.

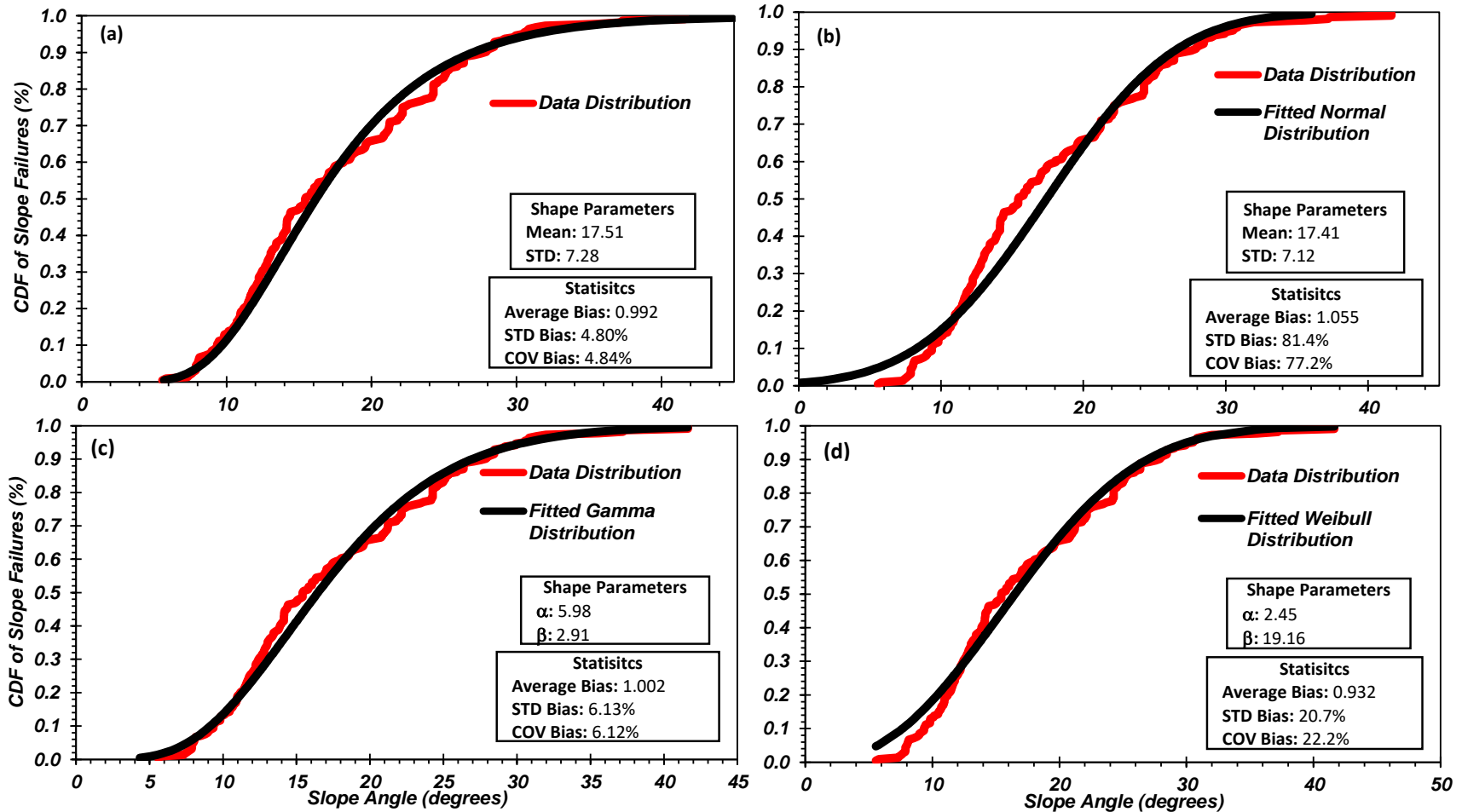


Figure A - 4. Cumulative Distribution Functions (CDF) for Metamorphic, sedimentary lithology type with shape parameters and statistic information regarding the determined bias values: (a) Lognormal, (b) Normal, (c) Gamma, (d) Weibull. The Gamma distribution (c) provided was selected as the best fit for this Metamorphic, sedimentary lithology type.

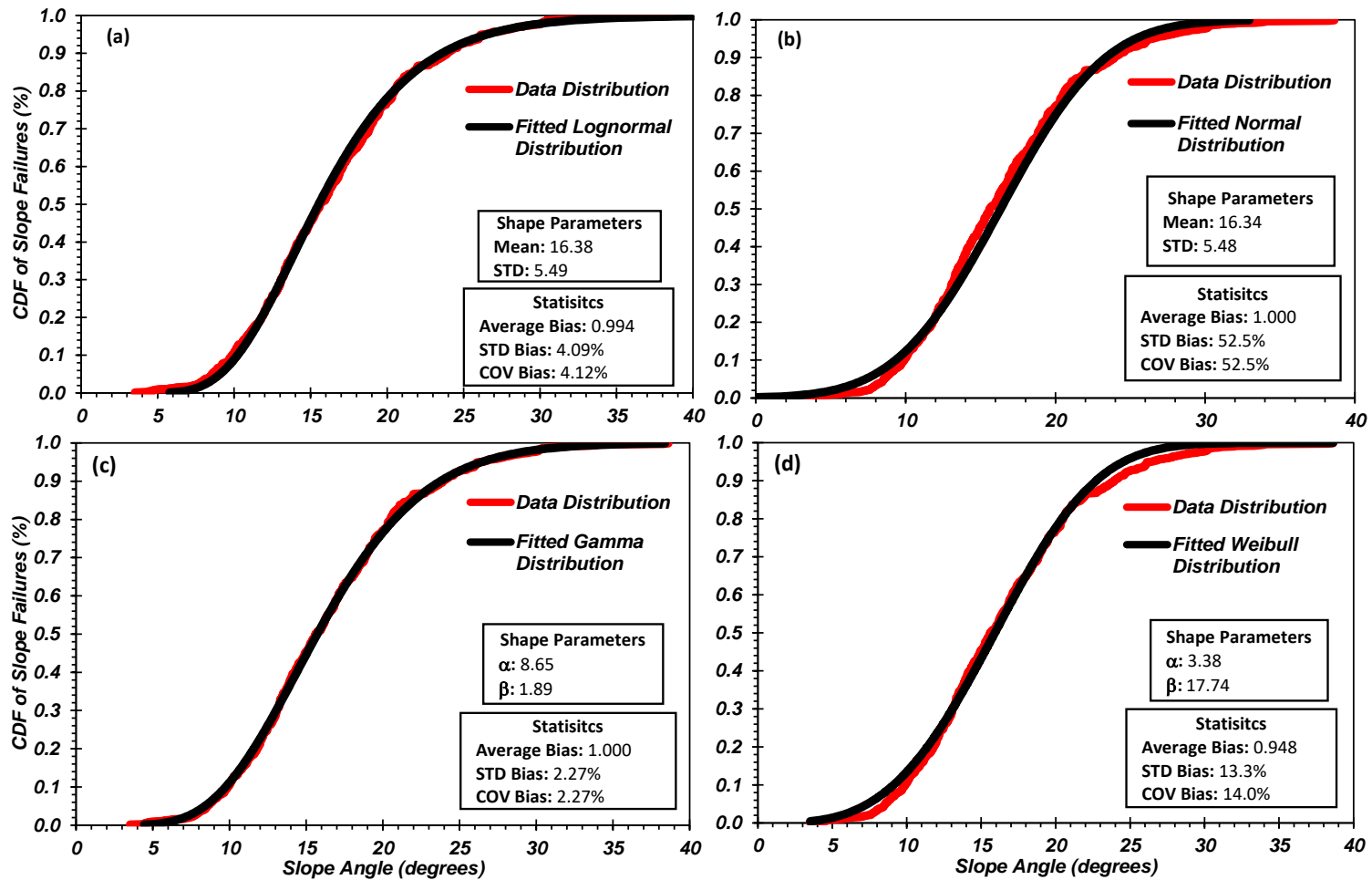


Figure A - 5. Cumulative Distribution Functions (CDF) for Metamorphic, serpentinite lithology type with shape parameters and statistic information regarding the determined bias values: (a) Lognormal, (b) Normal, (c) Gamma, (d) Weibull. The Gamma distribution (c) provided was selected as the best fit for this Metamorphic, serpentinite lithology type.

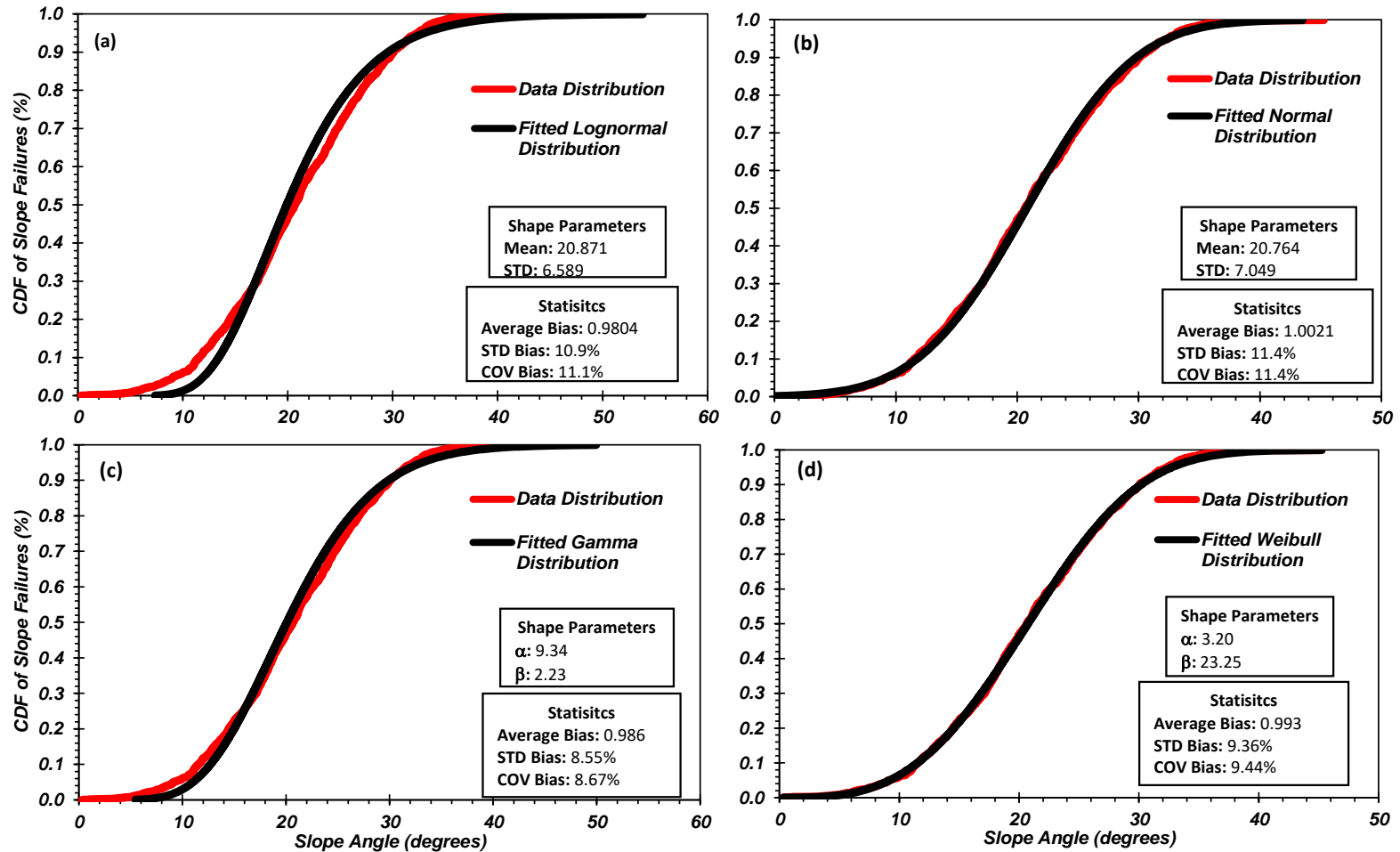


Figure A - 6. Cumulative Distribution Functions (CDF) for Metamorphic, undifferentiated lithology type with shape parameters and statistic information regarding the determined bias values: (a) Lognormal, (b) Normal, (c) Gamma, (d) Weibull. The Weibull distribution (d) provided was selected as the best fit for this Metamorphic, undifferentiated lithology type.

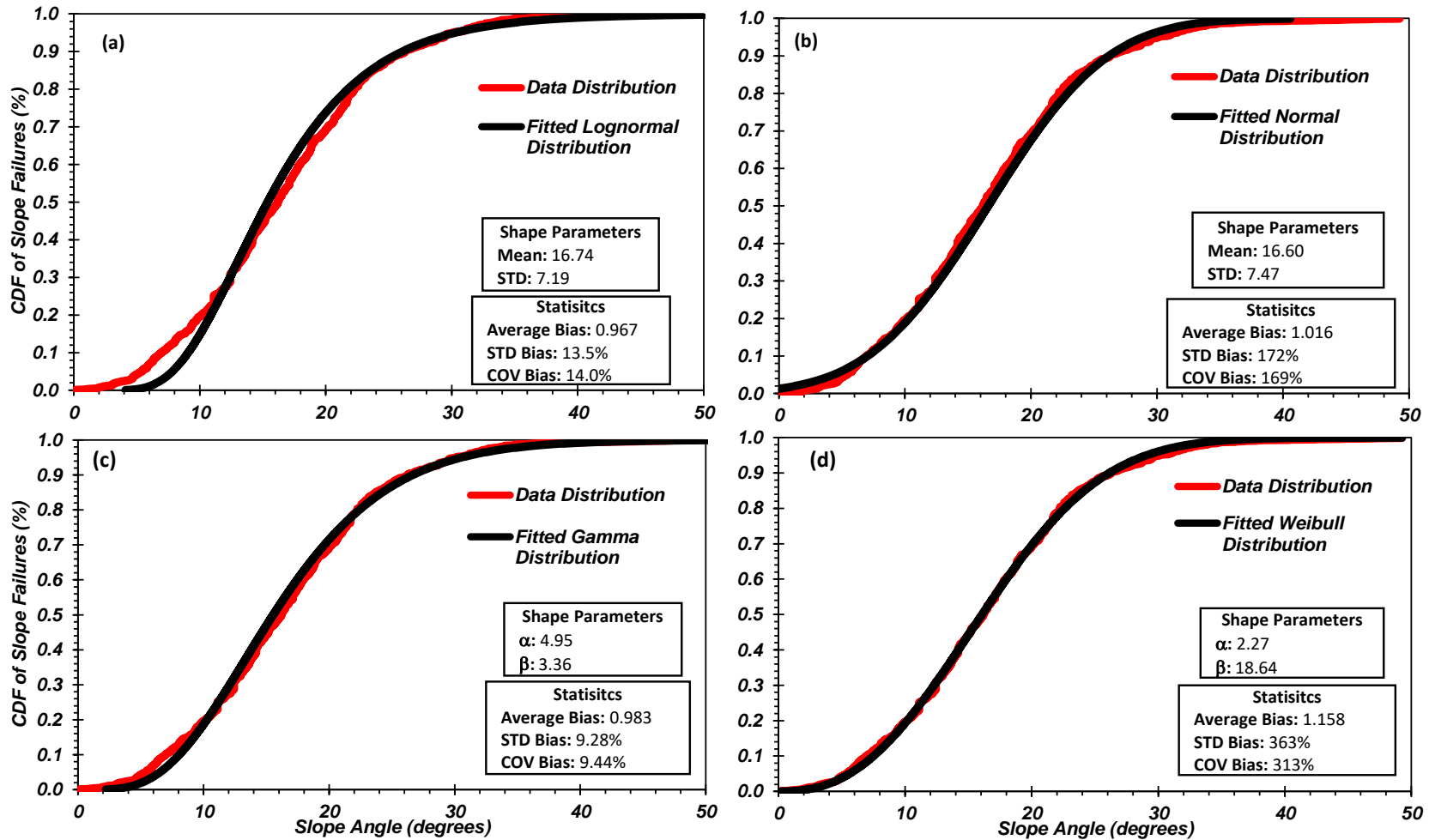


Figure A - 7. Cumulative Distribution Functions (CDF) for Metamorphic, volcanic lithology type with shape parameters and statistic information regarding the determined bias values: (a) Lognormal, (b) Normal, (c) Gamma, (d) Weibull. The Weibull distribution (d) provided was selected as the best fit for this Metamorphic, volcanic lithology type.

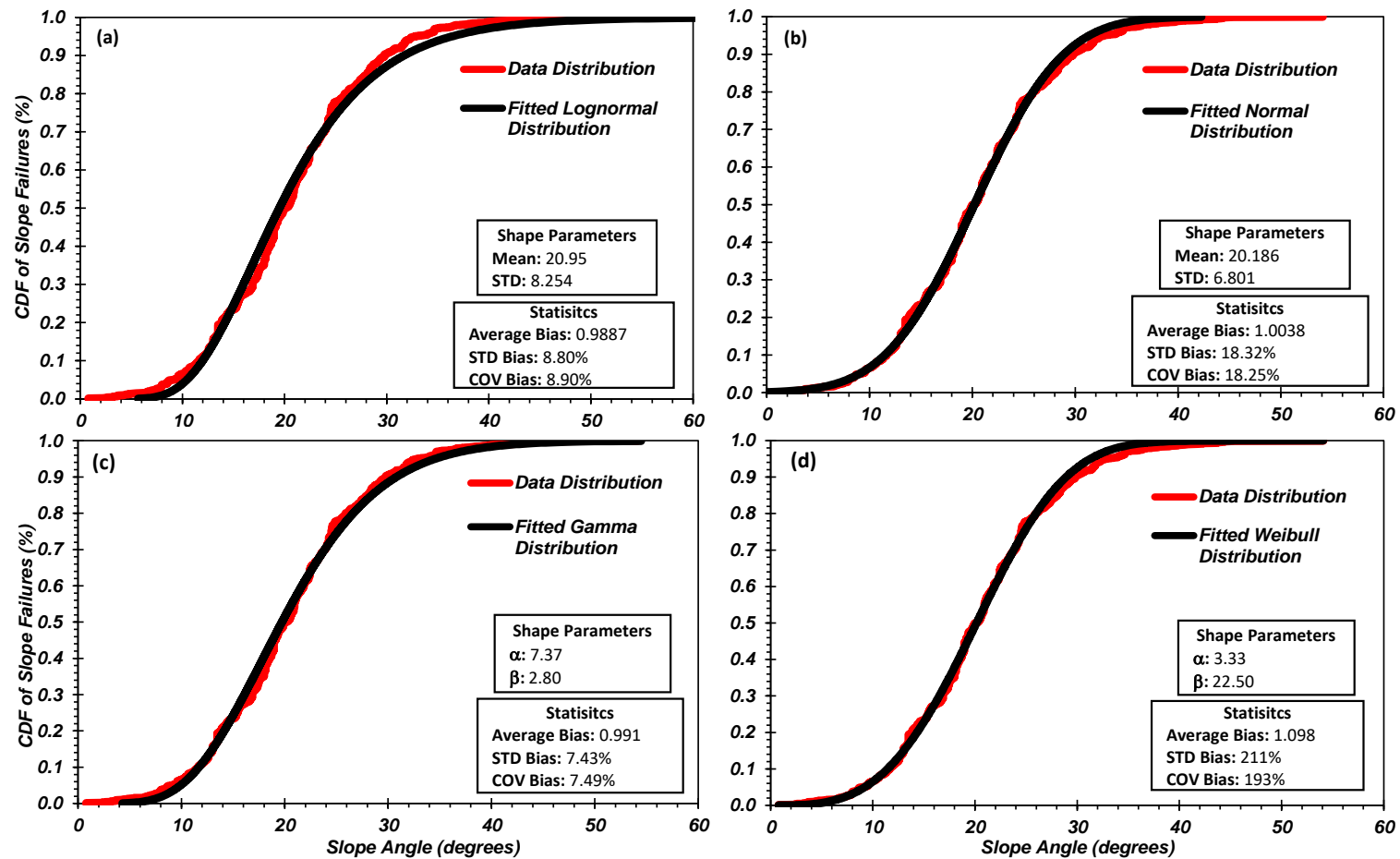


Figure A - 8. Cumulative Distribution Functions (CDF) for Metamorphic, sedimentary clastic lithology type with shape parameters and statistic information regarding the determined bias values: (a) Lognormal, (b) Normal, (c) Gamma, (d) Weibull. The Gamma distribution (c) provided was selected as the best fit for this Metamorphic, sedimentary clastic lithology type.

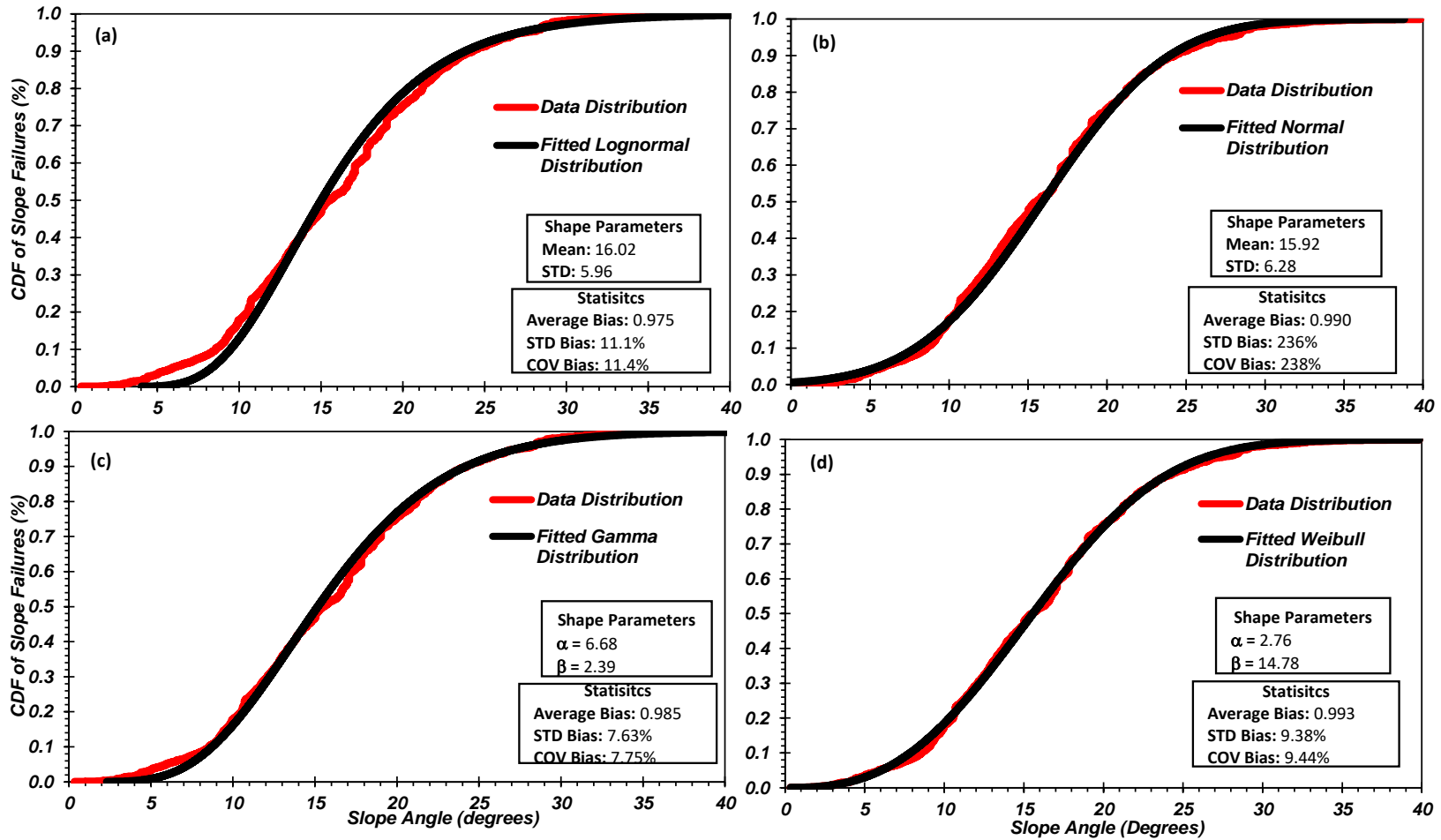


Figure A - 9. Cumulative Distribution Functions (CDF) for Igneous and Sedimentary, undifferentiated lithology type with shape parameters and statistic information regarding the determined bias values: (a) Lognormal, (b) Normal, (c) Gamma, (d) Weibull. The Weibull distribution (d) provided was selected as the best fit for this Igneous and Sedimentary, undifferentiated lithology type.

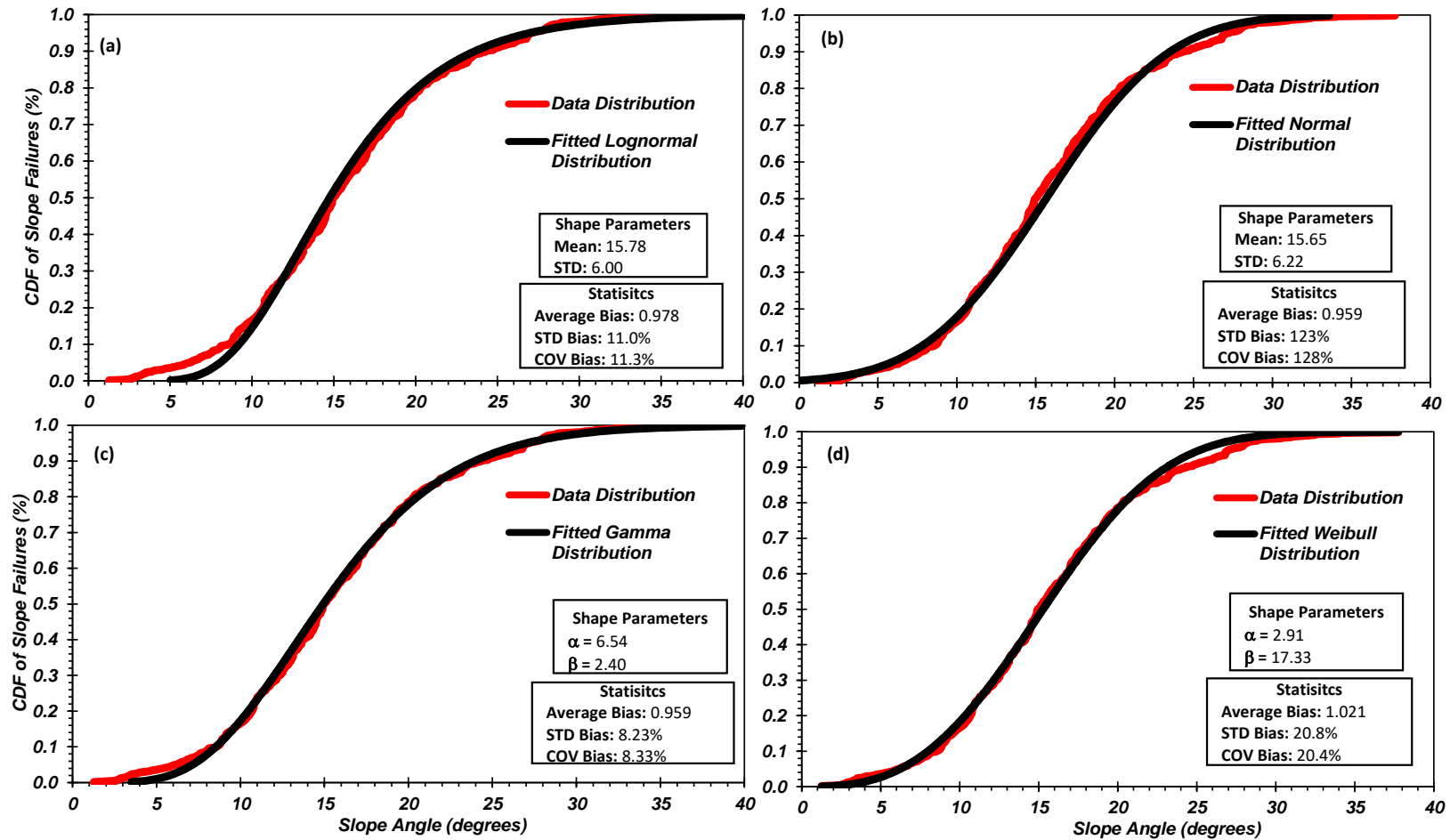


Figure A - 10. Cumulative Distribution Functions (CDF) for Igneous Metamorphic, undifferentiated lithology type with shape parameters and statistic information regarding the determined bias values: (a) Lognormal, (b) Normal, (c) Gamma, (d) Weibull. The Weibull distribution (d) provided was selected as the best fit for this Igneous Metamorphic, undifferentiated lithology type.

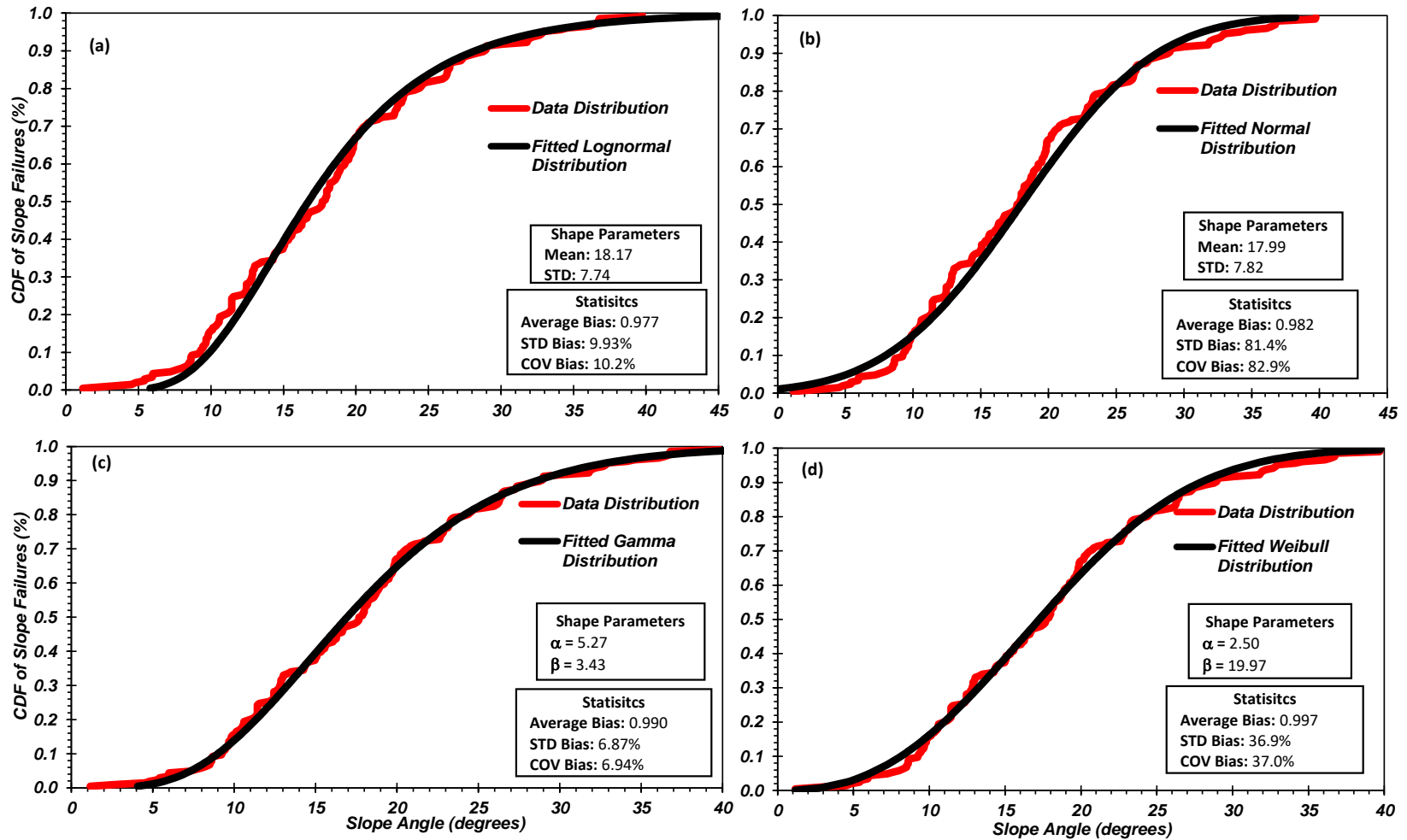


Figure A - 11. Cumulative Distribution Functions (CDF) for Igneous, undifferentiated lithology type with shape parameters and statistic information regarding the determined bias values: (a) Lognormal, (b) Normal, (c) Gamma, (d) Weibull. The Gamma distribution (c) provided was selected as the best fit for this Igneous, undifferentiated lithology type.

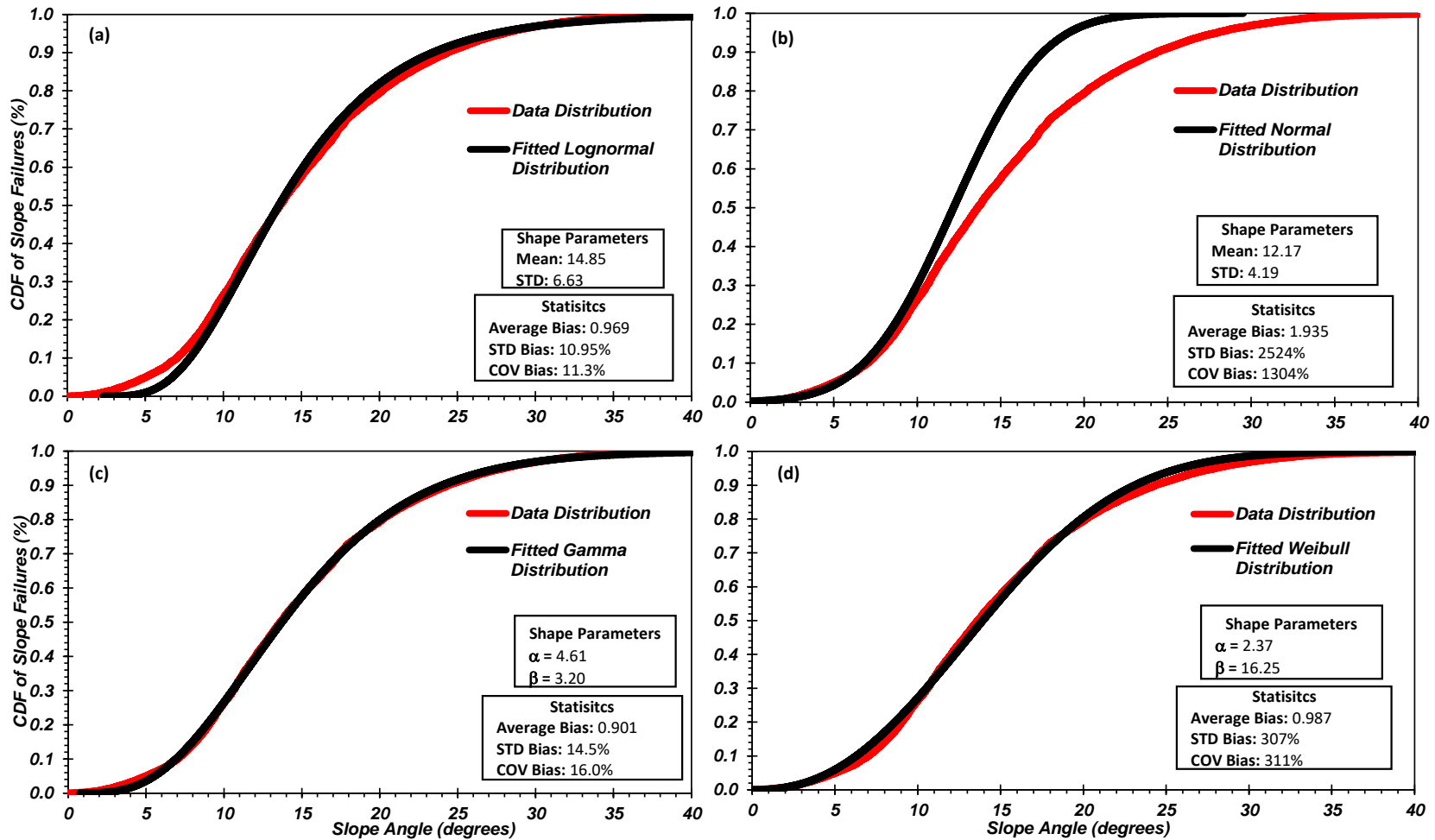


Figure A - 12. Cumulative Distribution Functions (CDF) for Igneous, volcanic lithology type with shape parameters and statistic information regarding the determined bias values: (a) Lognormal, (b) Normal, (c) Gamma, (d) Weibull. The Gamma distribution (c) provided was selected as the best fit for this Igneous, volcanic lithology type.

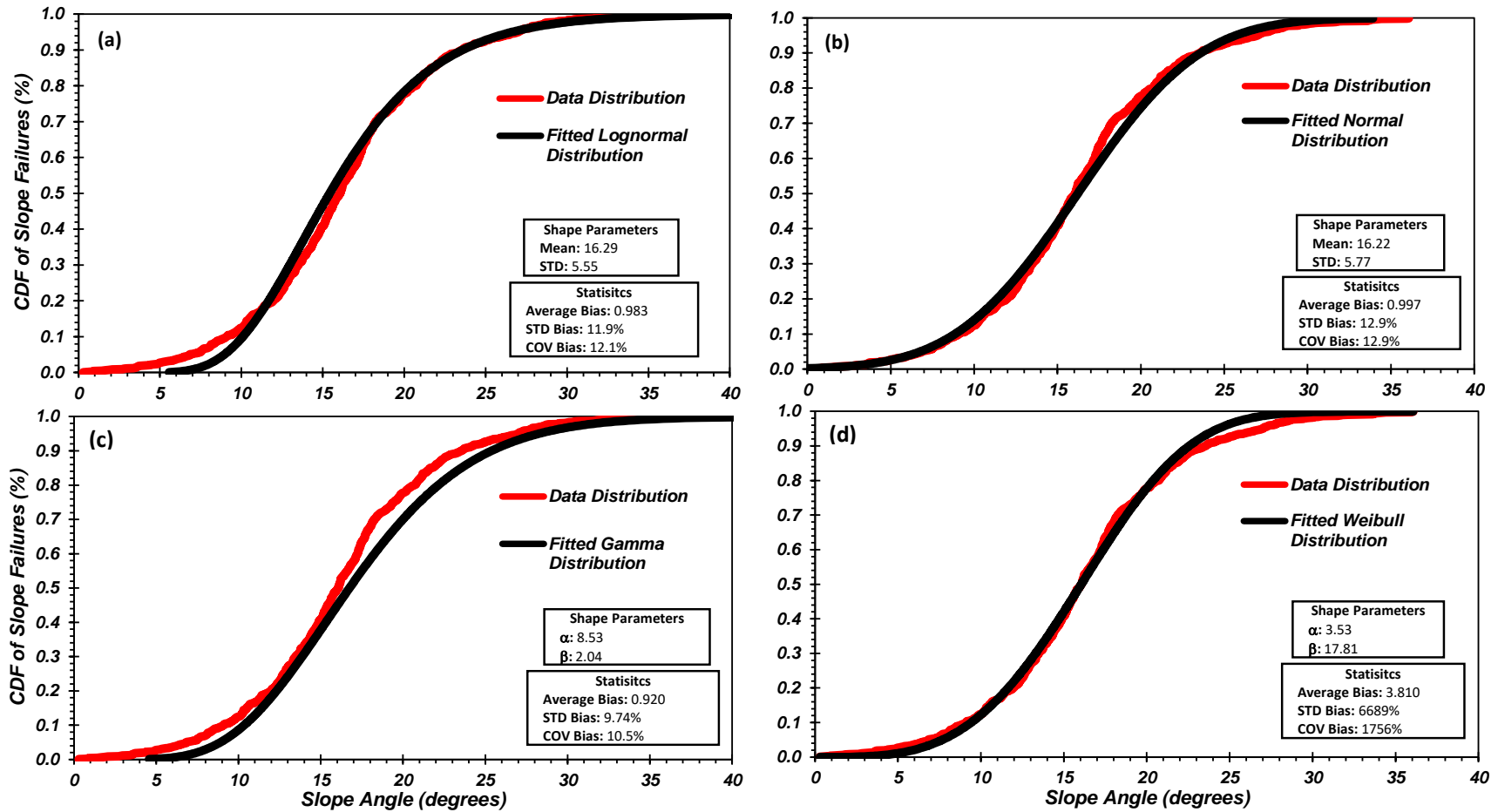


Figure A - 13. Cumulative Distribution Functions (CDF) for Melange lithology type with shape parameters and statistic information regarding the determined bias values: (a) Lognormal, (b) Normal, (c) Gamma, (d) Weibull. The Normal distribution (b) provided was selected as the best fit for this Melange lithology type.

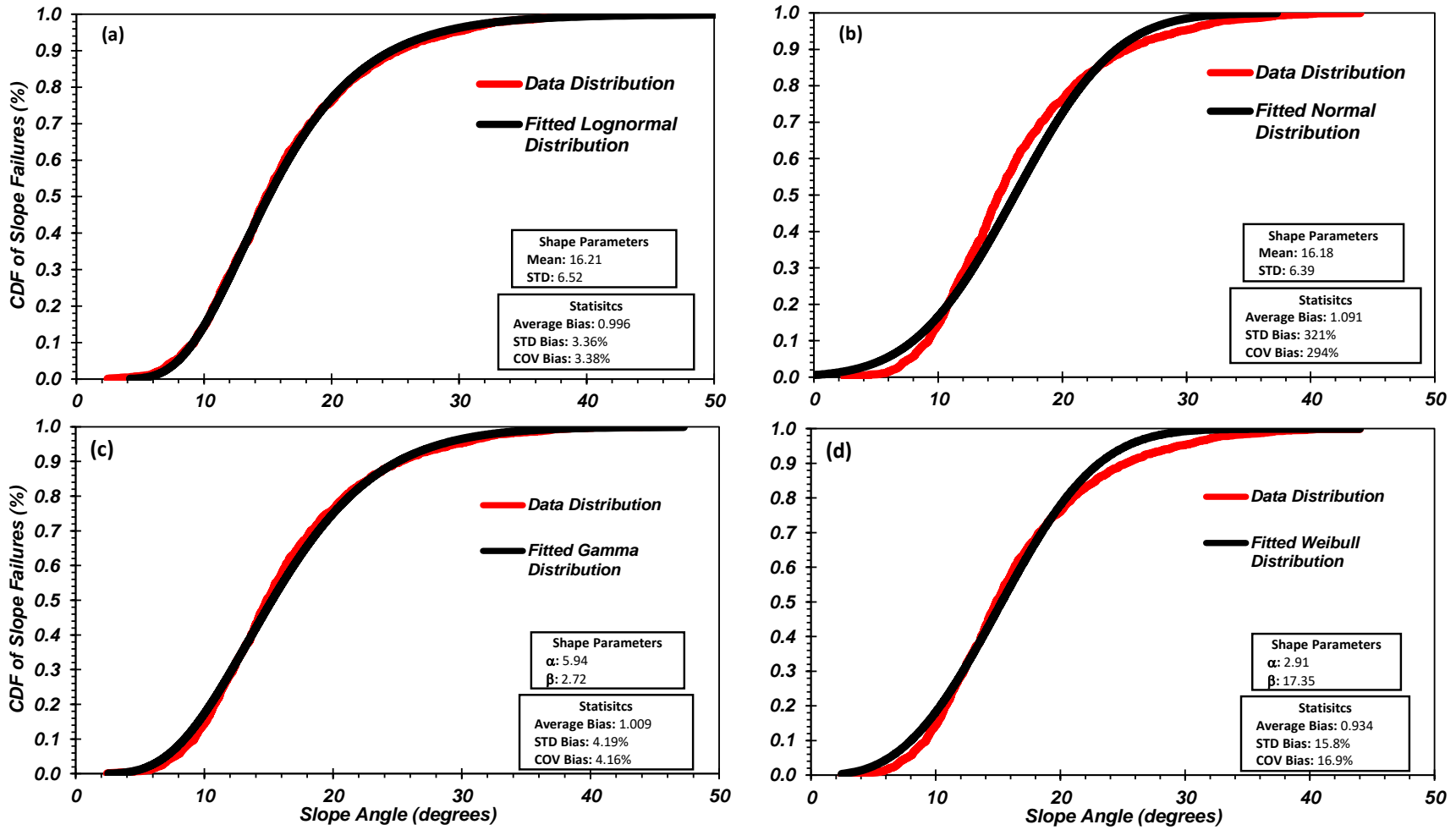


Figure A - 14. Cumulative Distribution Functions (CDF) for Sedimentary, carbonate lithology type with shape parameters and statistic information regarding the determined bias values: (a) Lognormal, (b) Normal, (c) Gamma, (d) Weibull. The Gamma distribution (c) provided was selected as the best fit for this Sedimentary, carbonate lithology type.

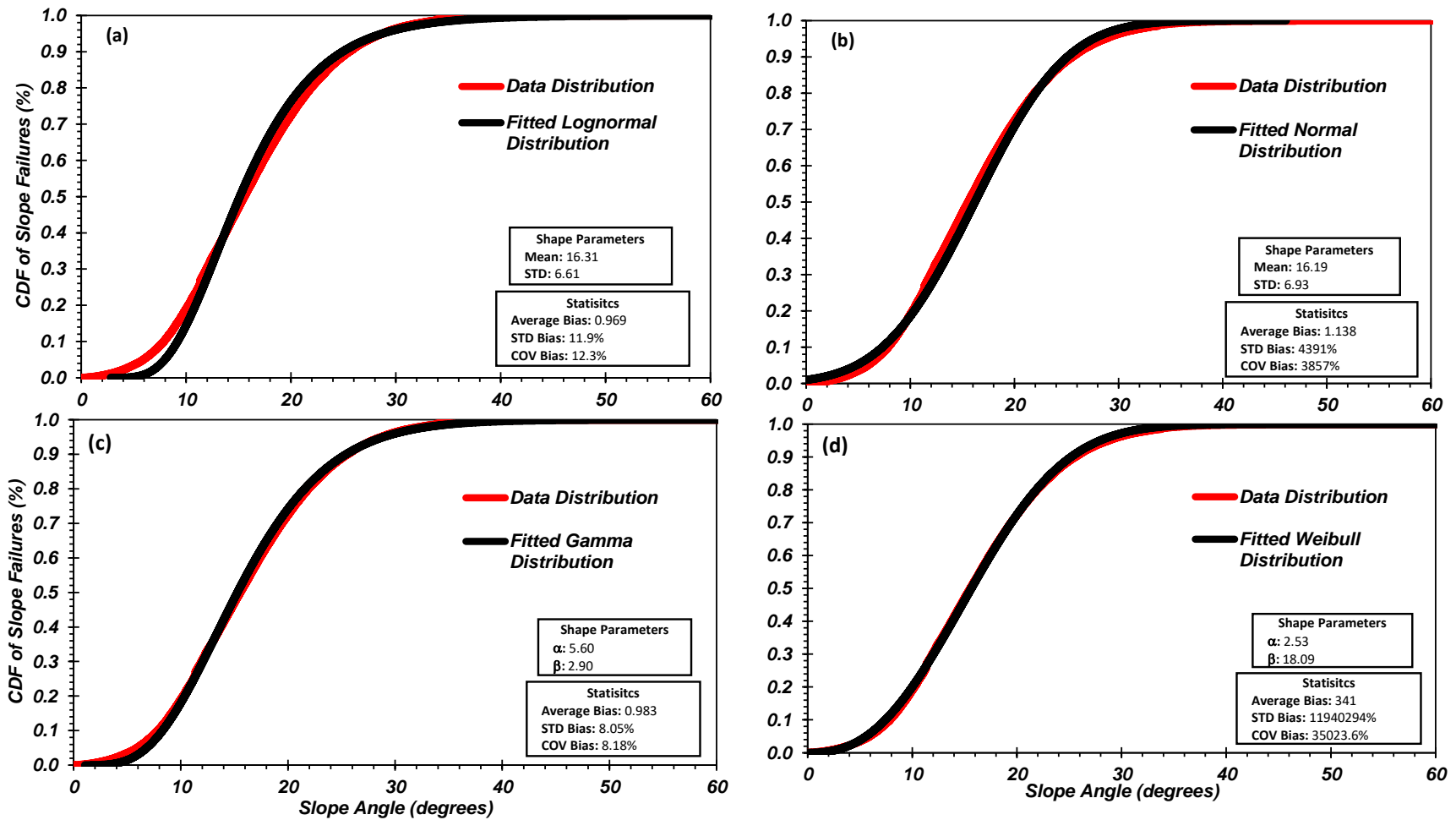


Figure A - 15. Cumulative Distribution Functions (CDF) for Sedimentary, clastic lithology type with shape parameters and statistic information regarding the determined bias values: (a) Lognormal, (b) Normal, (c) Gamma, (d)Weibull. The Weibull distribution (d) provided was selected as the best fit for this Sedimentary, clastic lithology type.

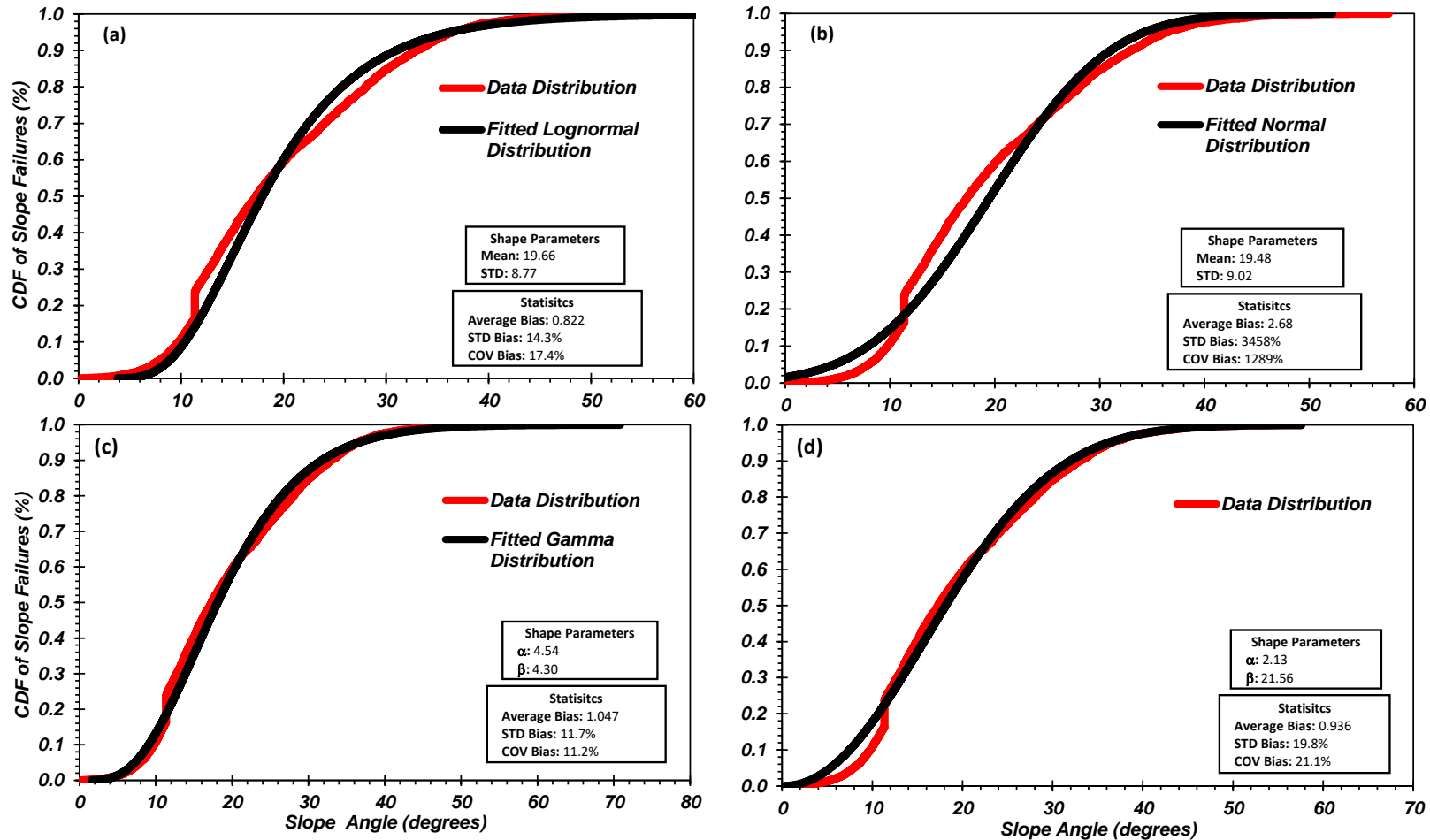


Figure A - 16. Cumulative Distribution Functions (CDF) for Sedimentary, undifferentiated lithology type with shape parameters and statistic information regarding the determined bias values: (a) Lognormal, (b) Normal, (c) Gamma, (d) Weibull. The Weibull distribution (c) provided was selected as the best fit for this Sedimentary, undifferentiated lithology type.

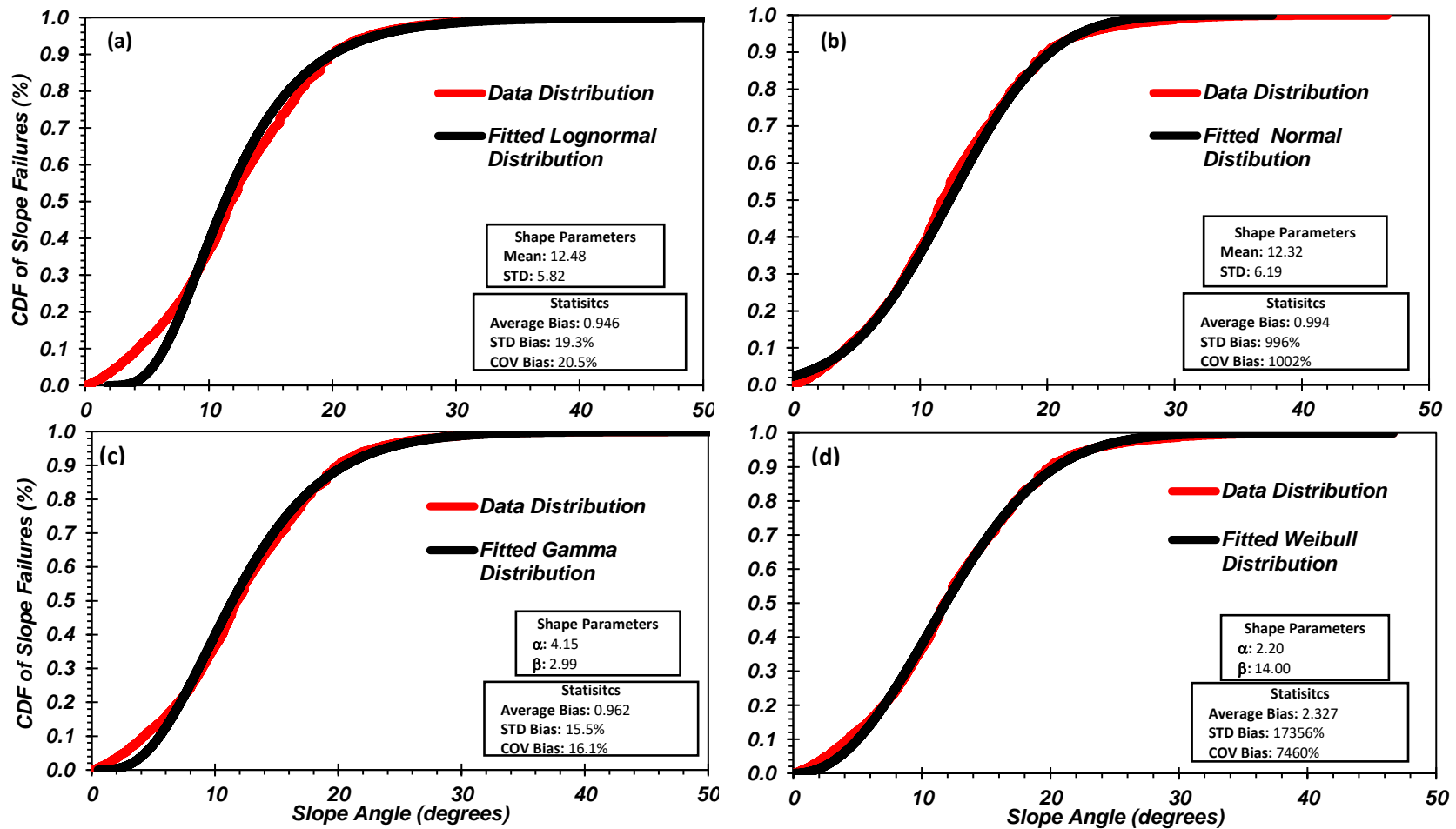


Figure A - 17. Cumulative Distribution Functions (CDF) for Unconsolidated, undifferentiated lithology type with shape parameters and statistic information regarding the determined bias values: (a) Lognormal, (b) Normal, (c) Gamma, (d) Weibull. The Weibull distribution (d) provided was selected as the best fit for this Unconsolidated, undifferentiated lithology type.

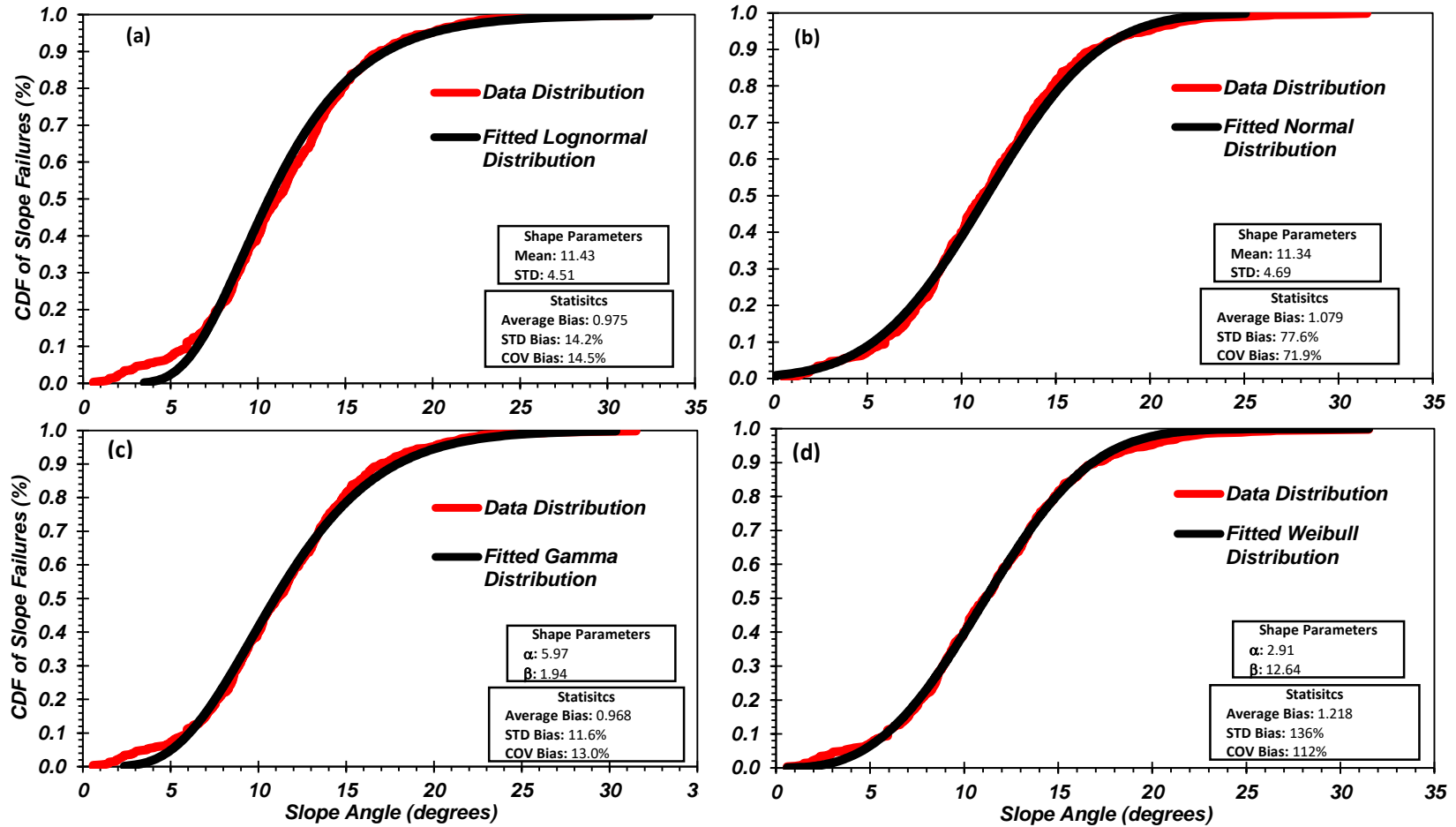


Figure A - 18. Cumulative Distribution Functions (CDF) for Unconsolidated and Sedimentary, undifferentiated lithology type with shape parameters and statistic information regarding the determined bias values: (a) Lognormal, (b) Normal, (c) Gamma, (d) Weibull. The Normal distribution (b) provided was selected as the best fit for this Unconsolidated and Sedimentary, undifferentiated lithology type.

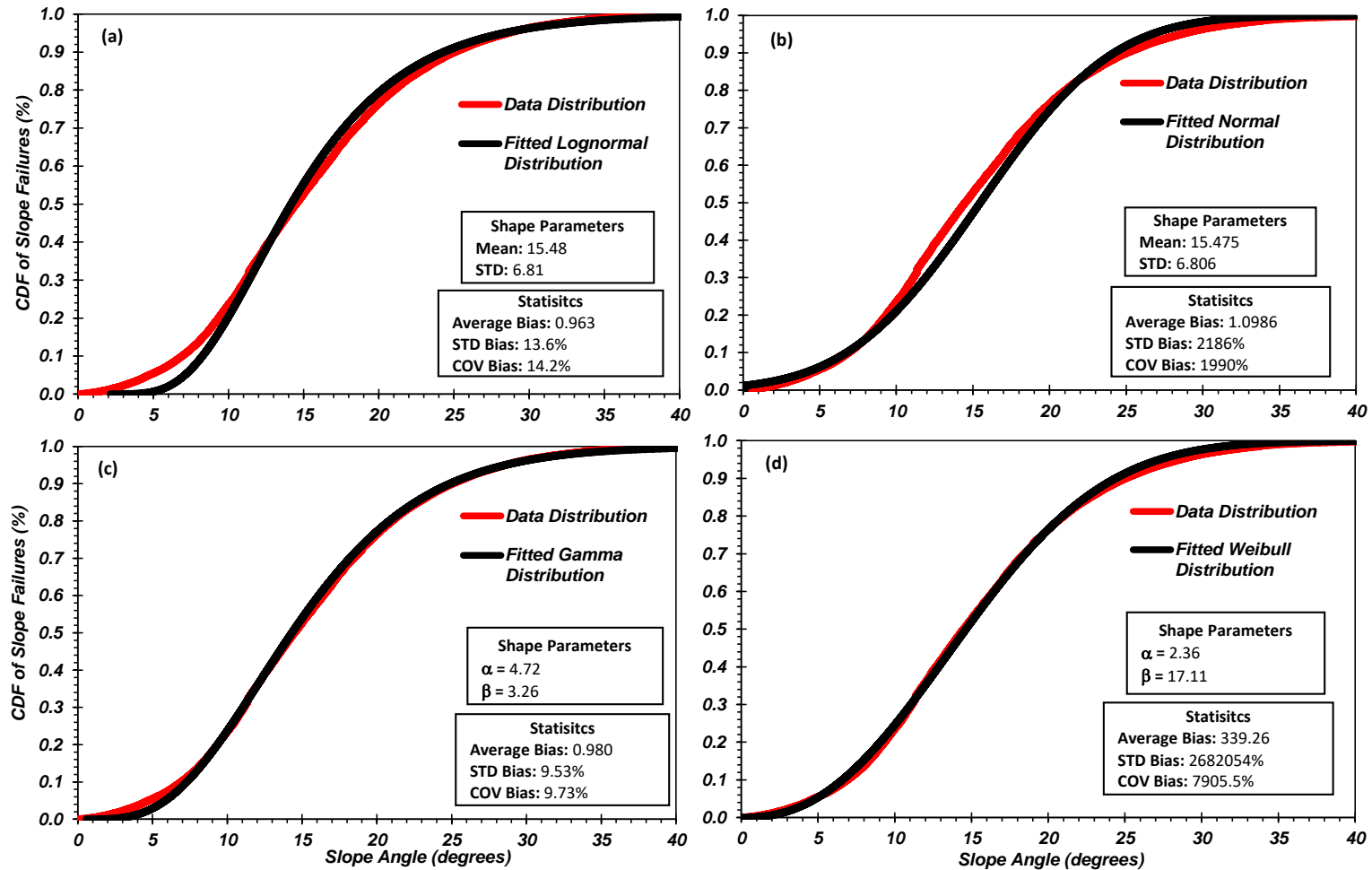


Figure A - 19. Cumulative Distribution Functions (CDF) for General lithology type with shape parameters and statistic information regarding the determined bias values: (a) Lognormal, (b) Normal, (c) Gamma, (d) Weibull. The Normal distribution (b) provided was selected as the best fit for this General lithology type.

Appendix B

Site Profiles

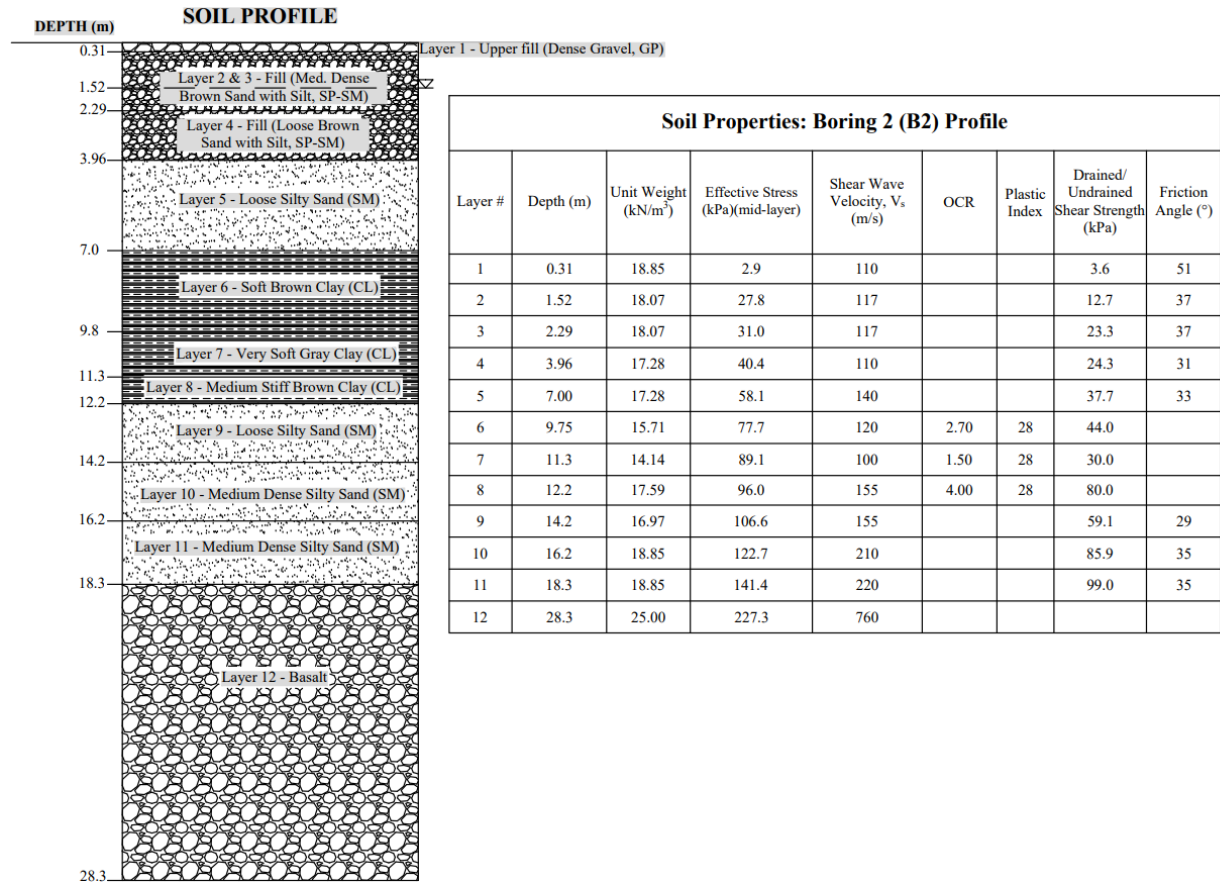


Figure B - 1. Diagram of the soil profile for use in site response analysis developed for Boring 2 (B2) and the associated soil properties.

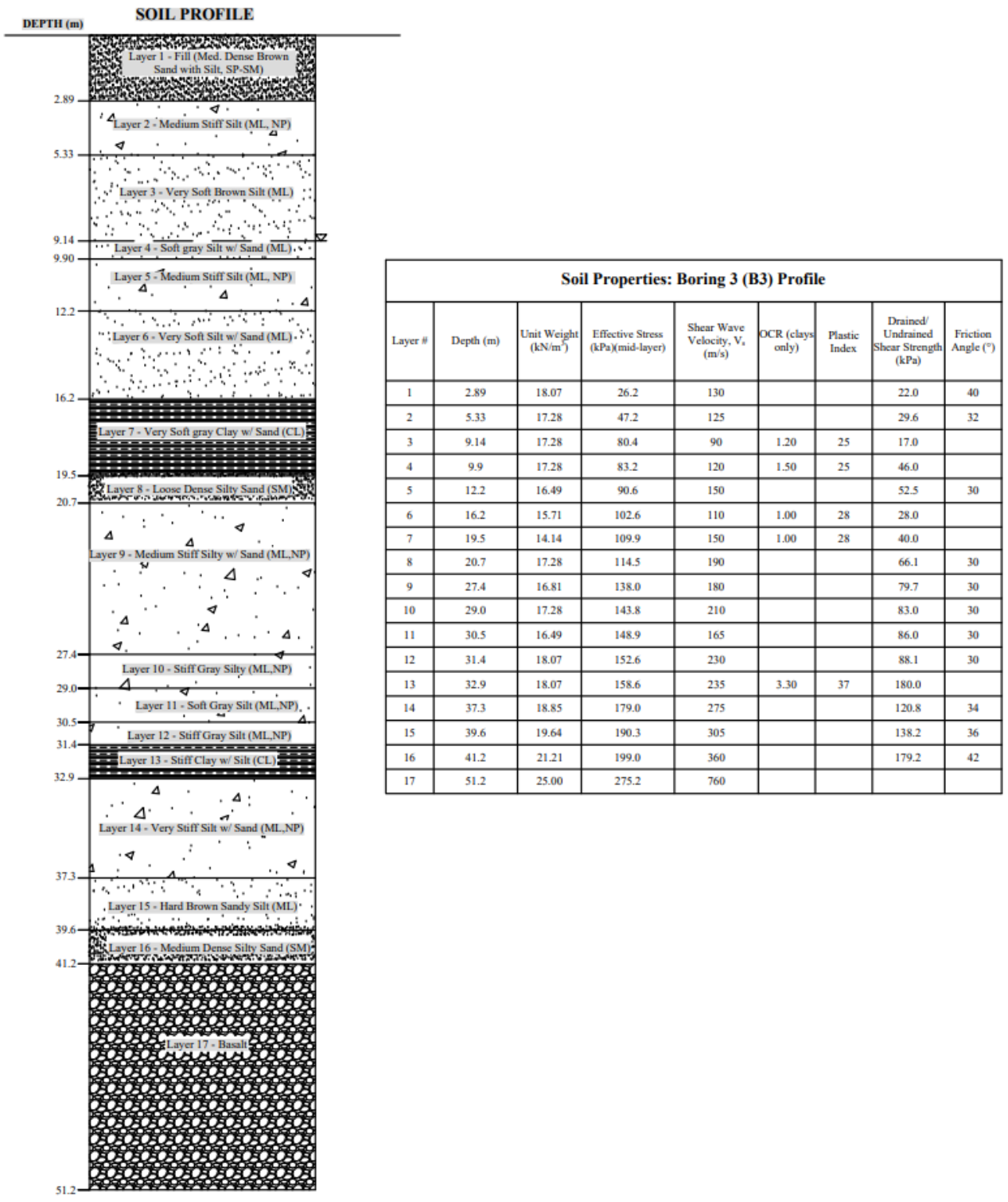
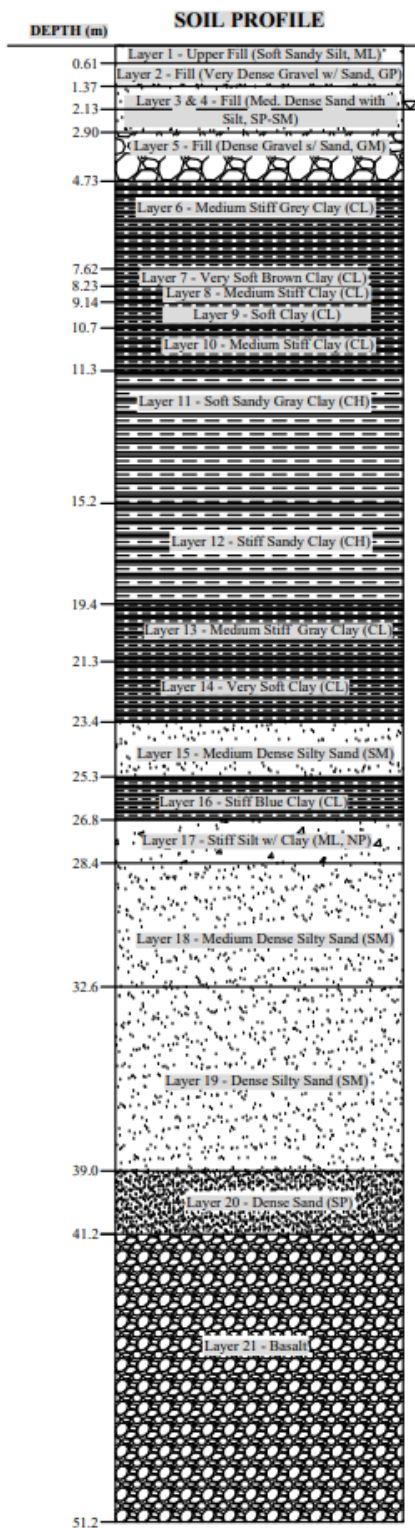


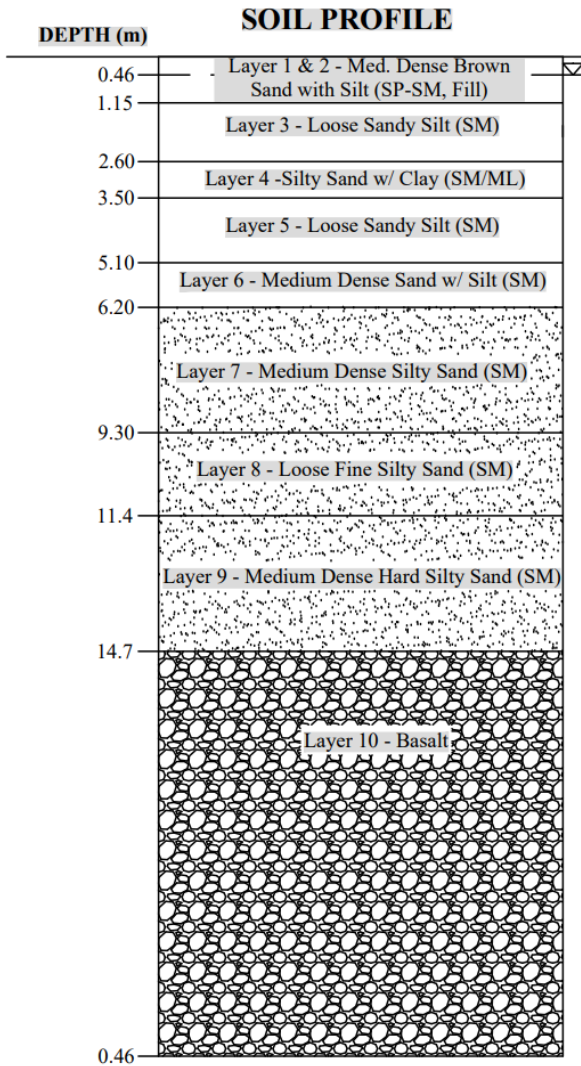
Figure B - 2. Diagram of the soil profile for use in site response analysis developed for Boring 3 (B3) and the associated soil properties.



Soil Properties: Boring 4 (B4) Profile

Layer #	Depth (m)	Unit Weight (kN/m ³)	Effective Stress (kPa)(mid-layer)	Shear Wave Velocity, V _s (m/s)	OCR (clays only)	Plastic Index	Drained/Undrained Shear Strength (kPa)	Friction Angle (°)
1	0.61	17.28	5.3	120			3.1	30
2	1.37	21.99	13.7	160			11.5	40
3	2.13	21.21	21.7	208			18.2	40
4	2.90	20.42	25.8	215			21.7	40
5	4.73	20.42	35.6	170			29.9	40
6	7.62	16.81	45.7	120	2.00	29	40.0	
7	8.23	14.14	47.1	120	2.00	29	40.0	
8	9.14	18.07	50.8	150	2.00	29	40.0	
9	10.7	14.14	54.2	110	2.00	29	40.0	
10	11.3	16.49	56.2	136	2.00	29	40.0	
11	15.2	17.28	71.0	115	2.00	37	40.0	
12	19.4	18.38	88.7	185	3.50	37	125.0	
13	21.3	17.28	96.2	205	2.40	32	95.0	
14	23.4	14.14	100.7	140	2.00	32	40.0	
15	25.3	18.07	108.5	235			73.2	34
16	26.8	18.85	115.4	230	2.80	27	170.0	
17	28.4	18.07	121.7	230			82.1	34
18	32.6	19.64	142.8	285			103.7	36
19	39.0	20.42	176.8	375			148.3	40
20	41.2	21.99	189.8	450			189.8	45
21	51.2	25.00	266.0	760				

Figure B - 3. Diagram of the soil profile for use in site response analysis developed for Boring 4 (B4) and the associated soil properties.



Soil Properties: CPT-1 (C1) Profile

Layer #	Depth (m)	Unit Weight (kN/m ³)	Effective Stress (kPa)(mid-layer)	Shear Wave Velocity, V _s (m/s)	OCR	Plastic Index	Drained/Undrained Shear Strength (kPa)	Friction Angle (°)
1	0.46	18.07	4.2	130			3.9	43
2	1.15	18.07	11.2	130			10.4	43
3	2.60	16.49	18.9	118			12.7	34
4	3.50	17.28	27.1	125			17.6	33
5	5.10	16.49	35.9	150			25.1	35
6	6.20	17.28	45.3	180			35.4	38
7	9.30	17.28	61.1	195			46.0	37
8	11.4	18.07	81.2	220			61.2	37
9	14.7	18.85	104.0	260			81.2	38
10	25.0	25.00	194.4	760				

Figure B - 4. Diagram of the soil profile for use in site response analysis developed for CPT-1 (C1) and the associated soil properties.

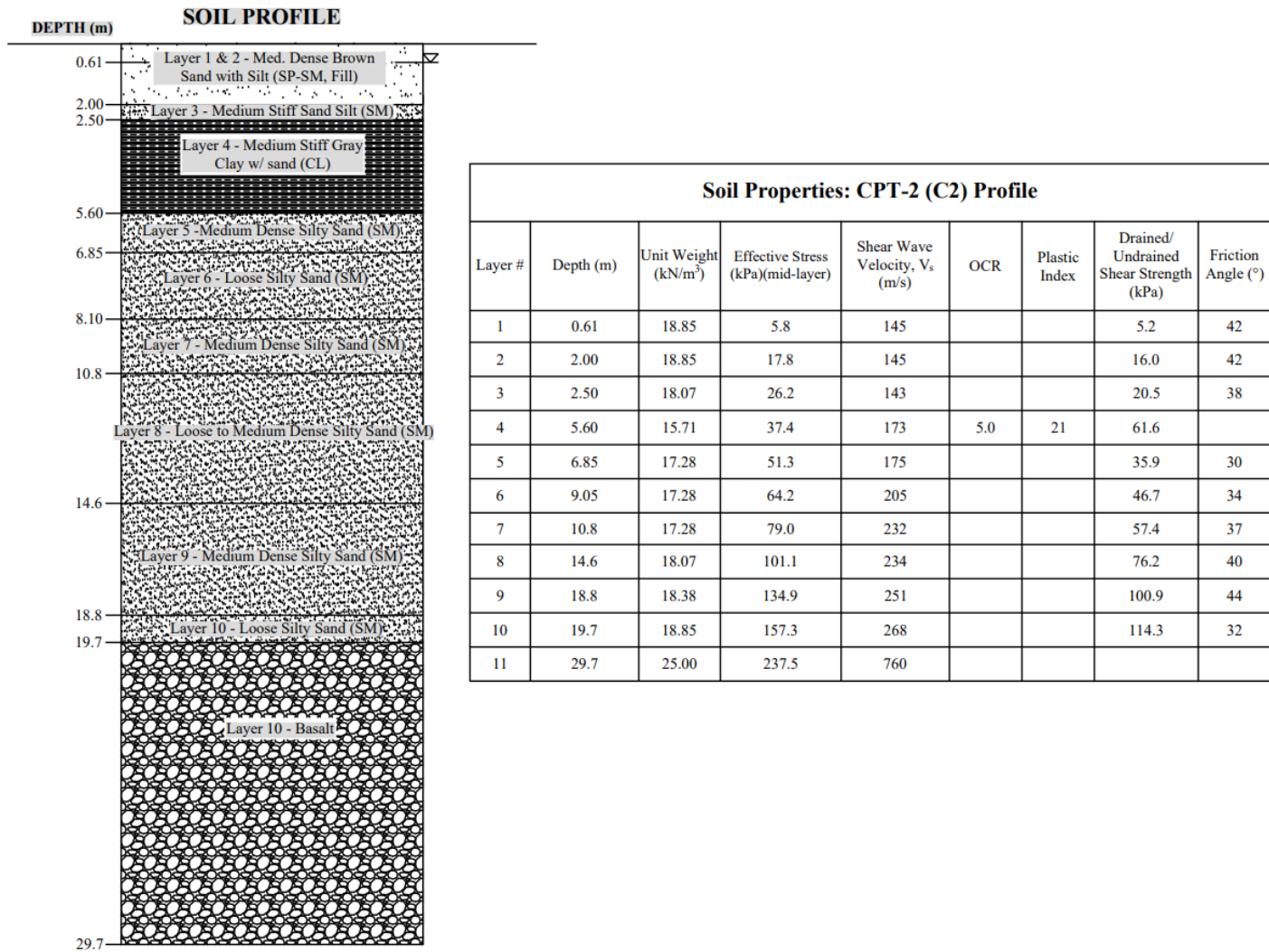


Figure B - 5. Diagram of the soil profile for use in site response analysis developed for CPT-2 (C2) and the associated soil properties.

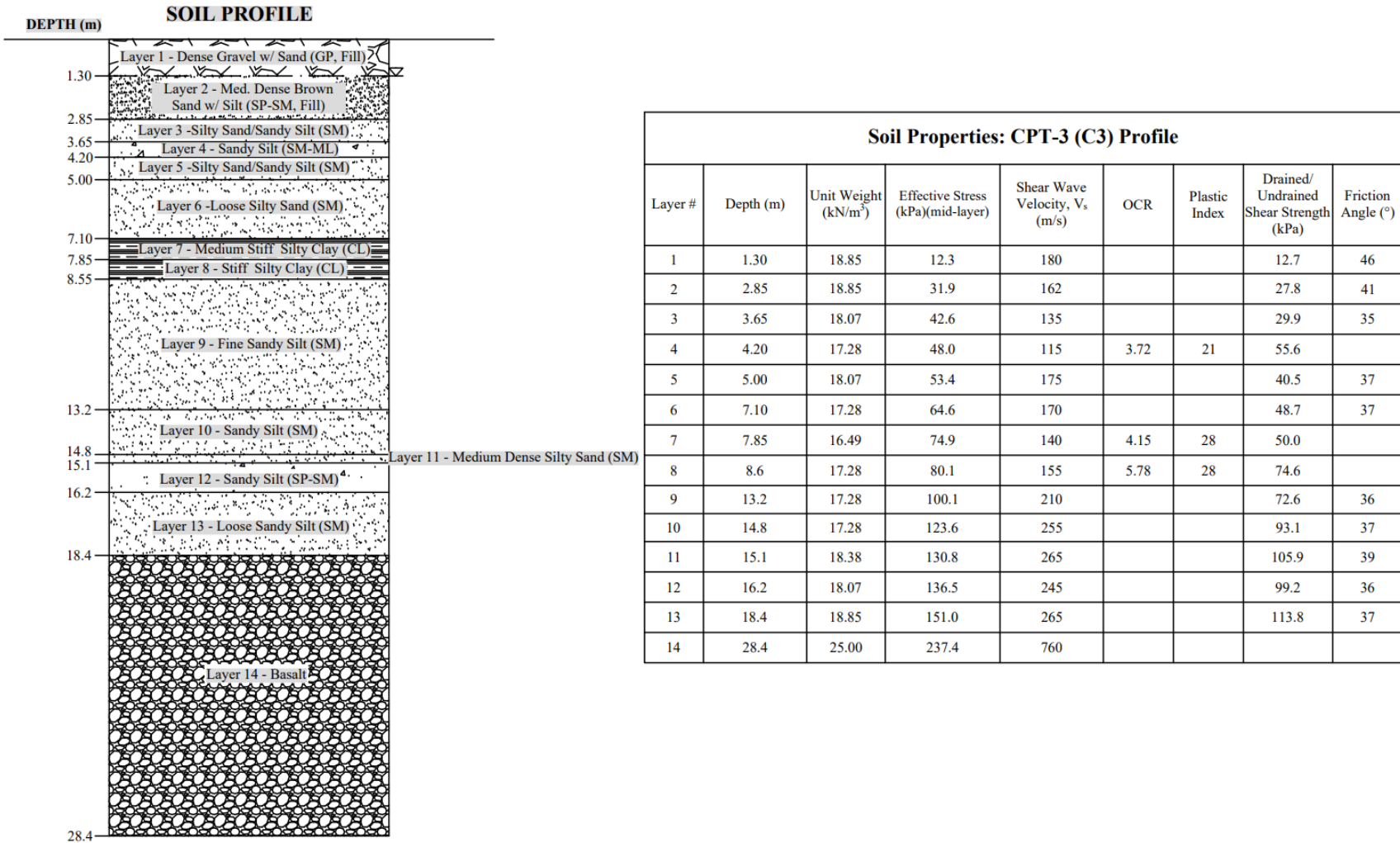


Figure B - 6. Diagram of the soil profile for use in site response analysis developed for CPT-3 (C3) and the associated soil properties.

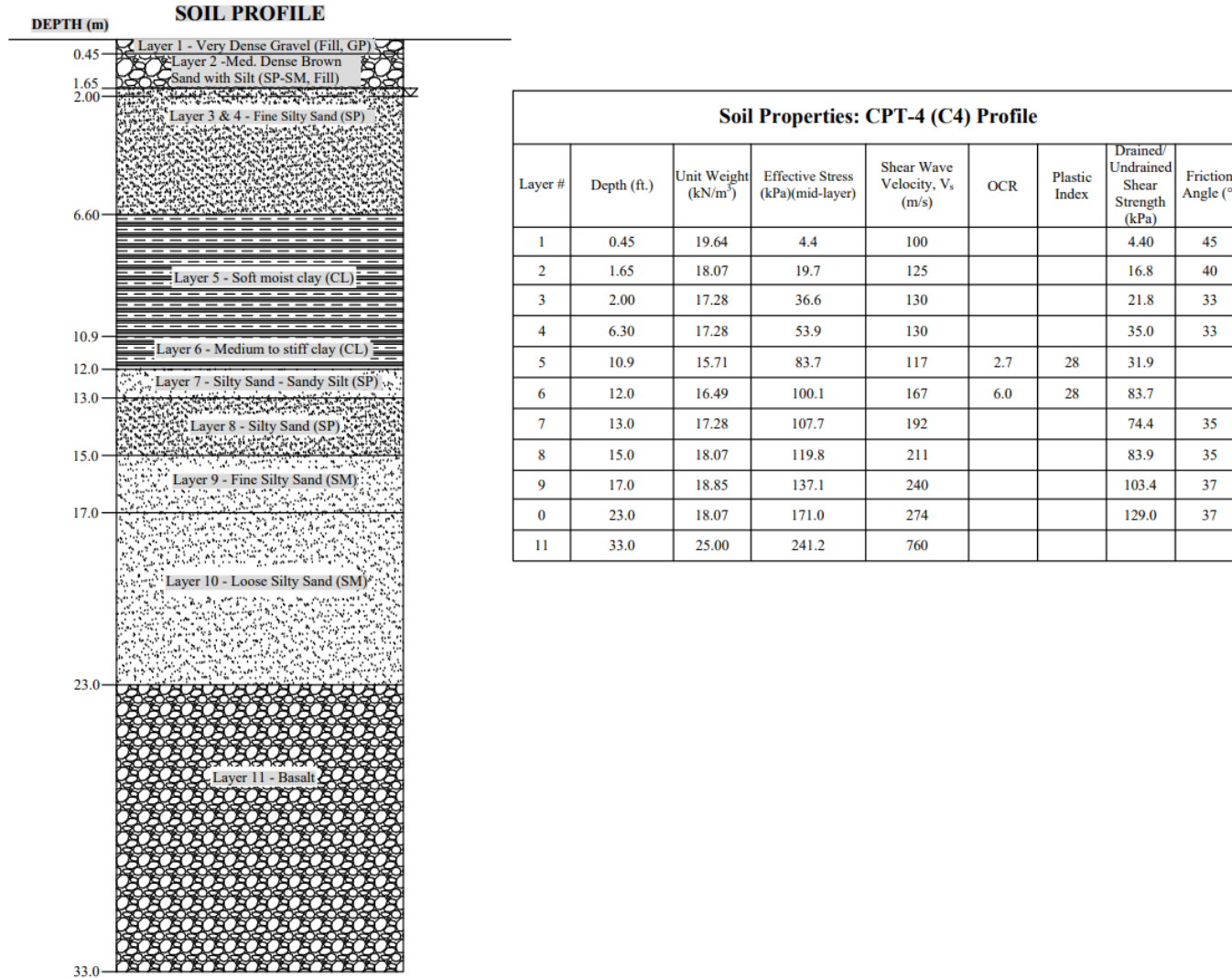


Figure B - 7. Diagram of the soil profile for use in site response analysis developed for CPT-4 (C4) and the associated soil properties.

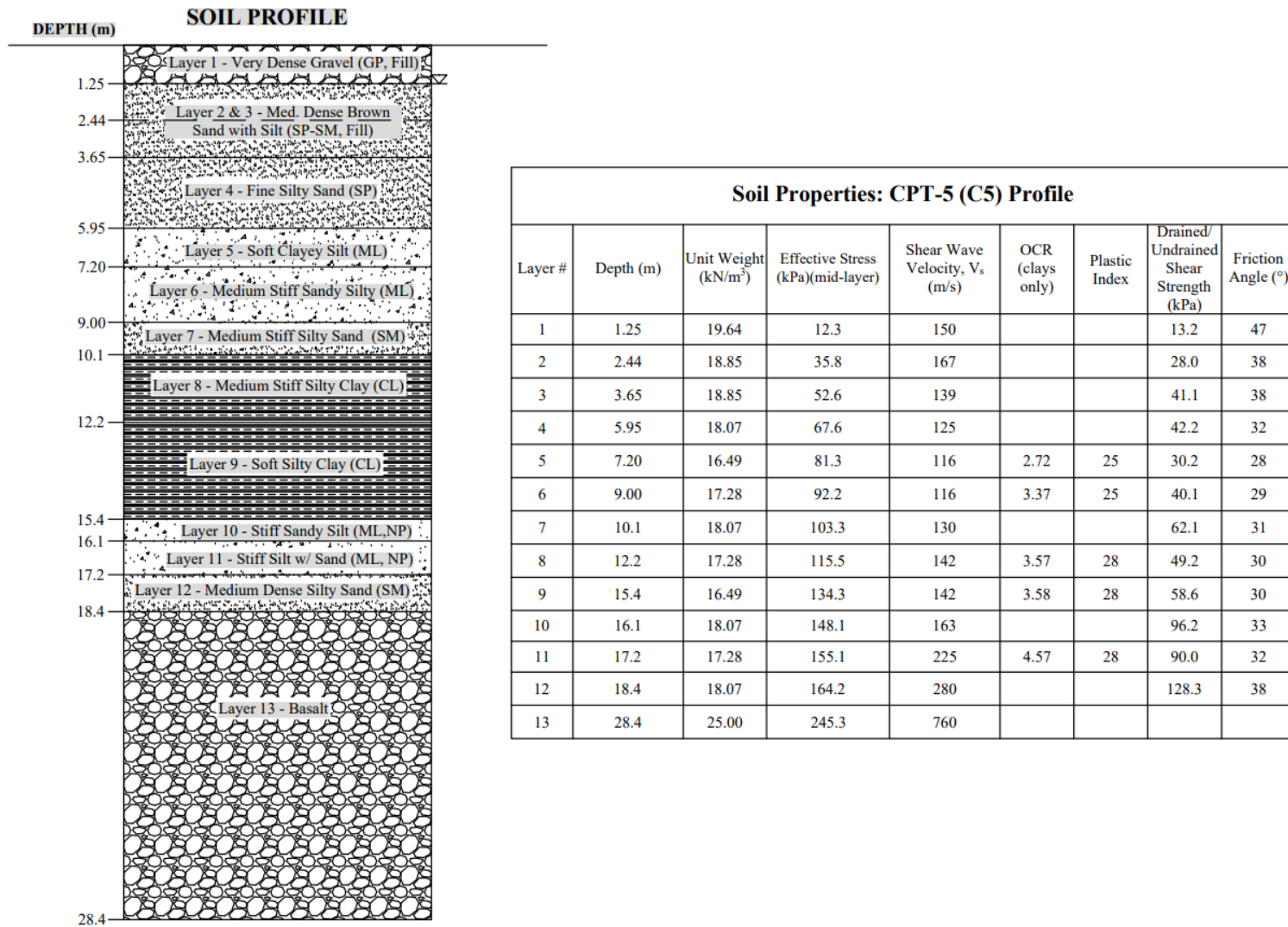


Figure B - 8. Diagram of the soil profile for use in site response analysis developed for CPT-5 (C5) and the associated soil properties.

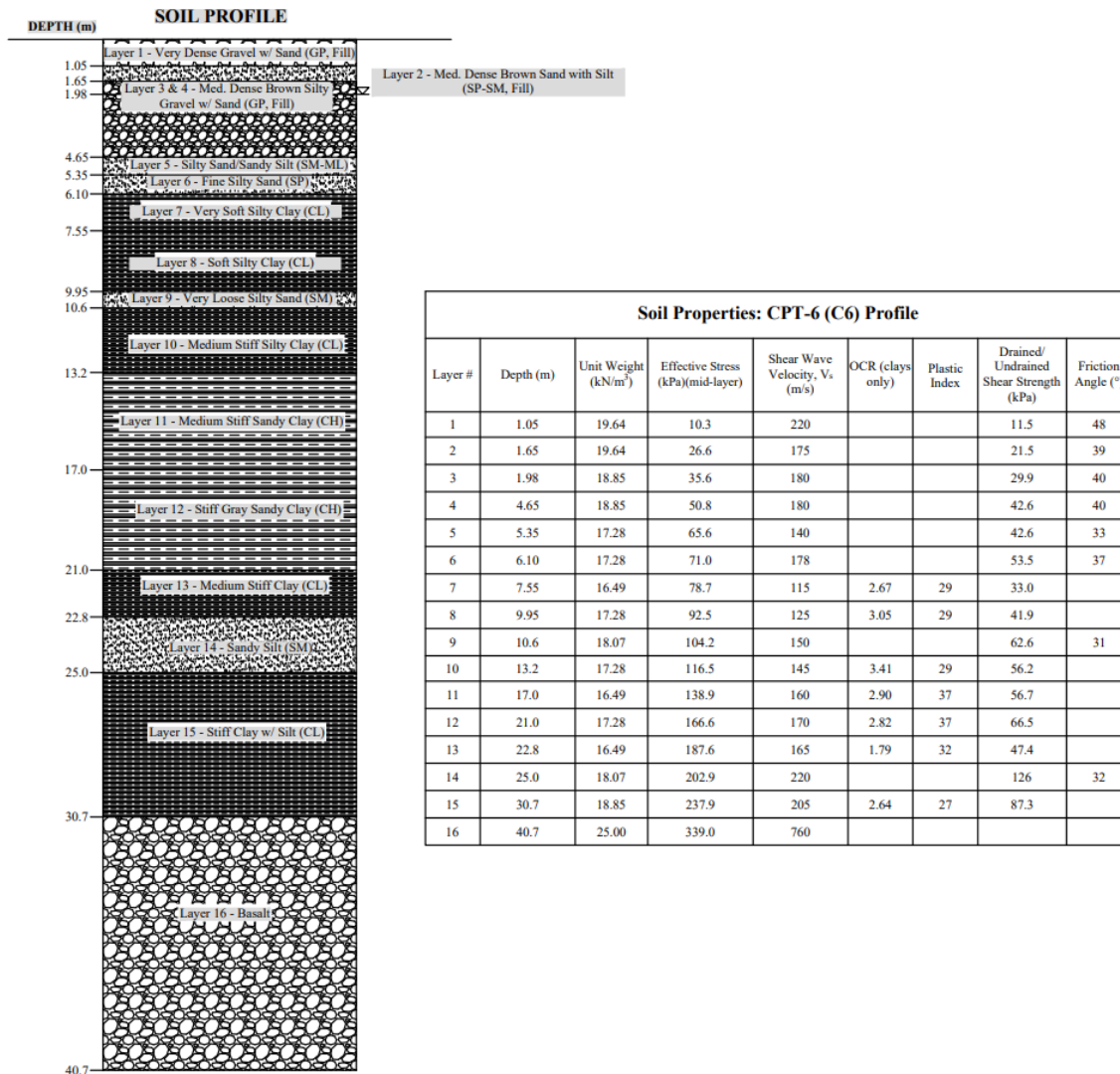


Figure B - 9. Diagram of the soil profile for use in site response analysis developed for CPT-6 (C6) and the associated soil properties.

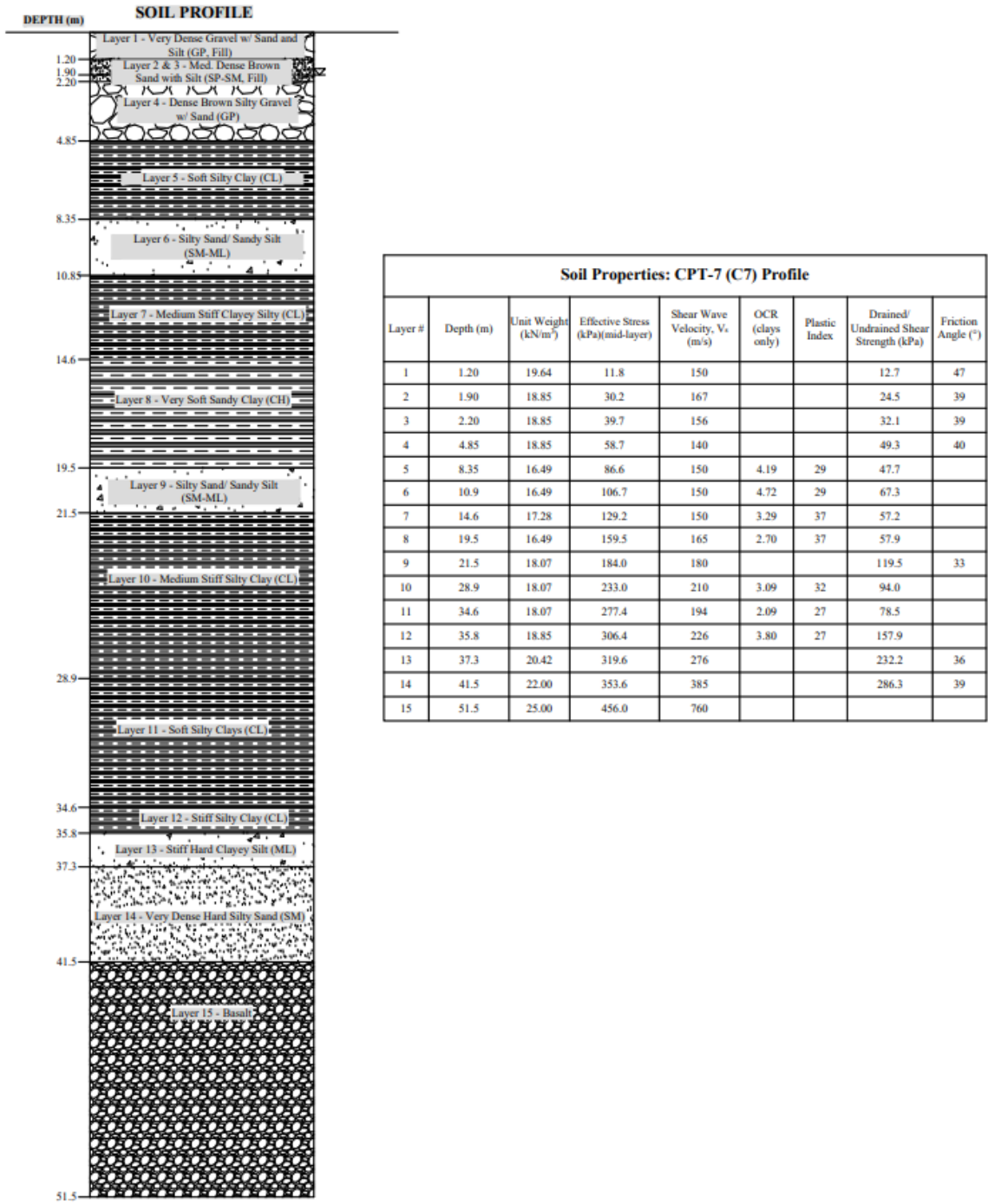


Figure B - 10. Diagram of the soil profile for use in site response analysis developed for CPT-7 (C7) and the associated soil properties.

Peak Horizontal Acceleration Plots

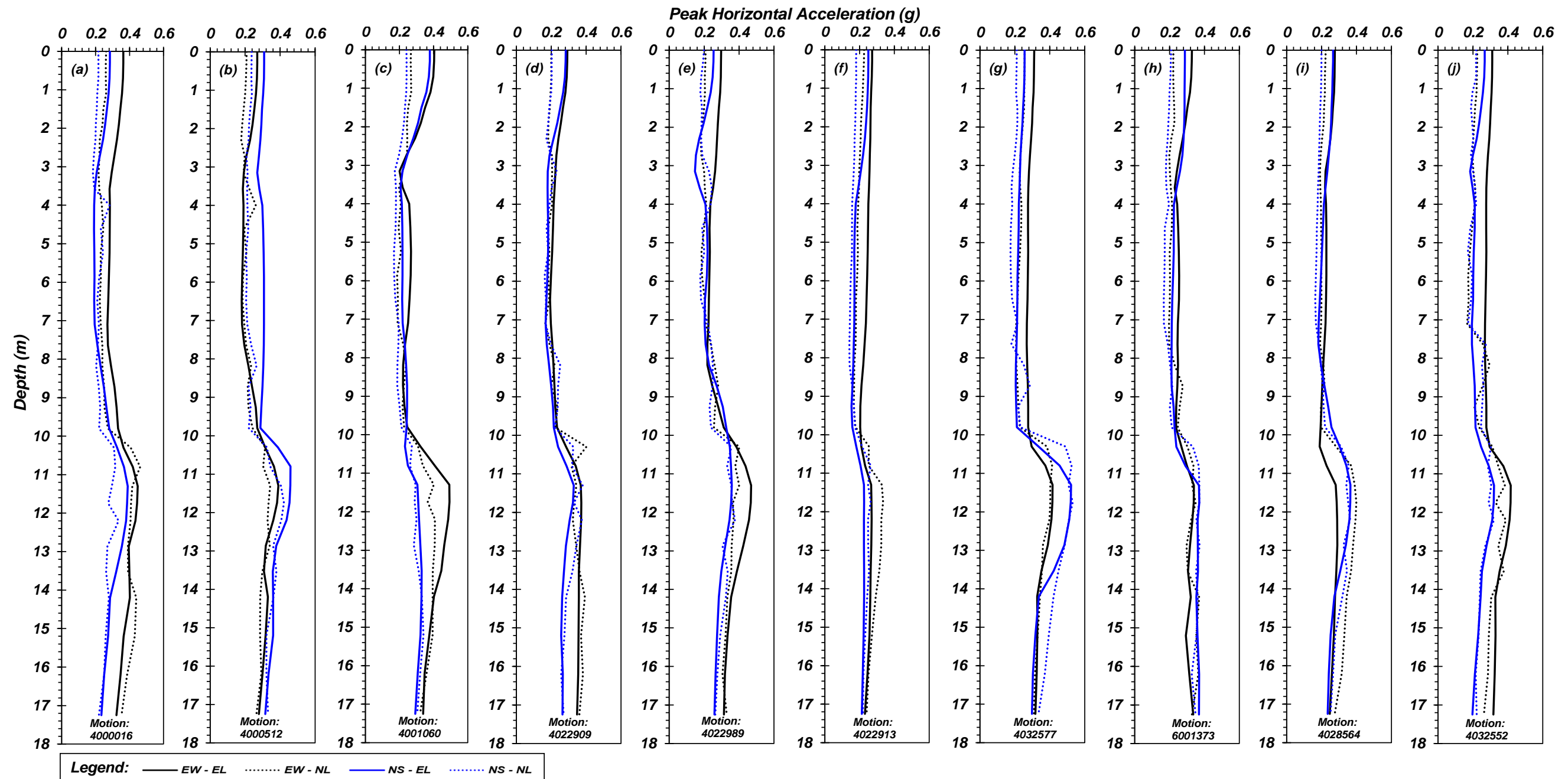


Figure B - 11. Comparison of peak horizontal acceleration (PHA) with depth for equivalent linear (EL) and nonlinear (NL) site response analyses conducted for the Boring 2 (B2) soil profile. 10 Motions (both NS and EW direction, total 20 motions) were evaluated obtained from the PEER NGA earthquake database: (a) Motion 4000016, (b) Motion 4000521, (c) Motion 4001060, (d) Motion 4022909, (e) Motion 4022989, (f) Motion 4022913, (g) Motion 4032577, (h) Motion 6001373, (i) Motion 4028564, (j) Motion 4032552.

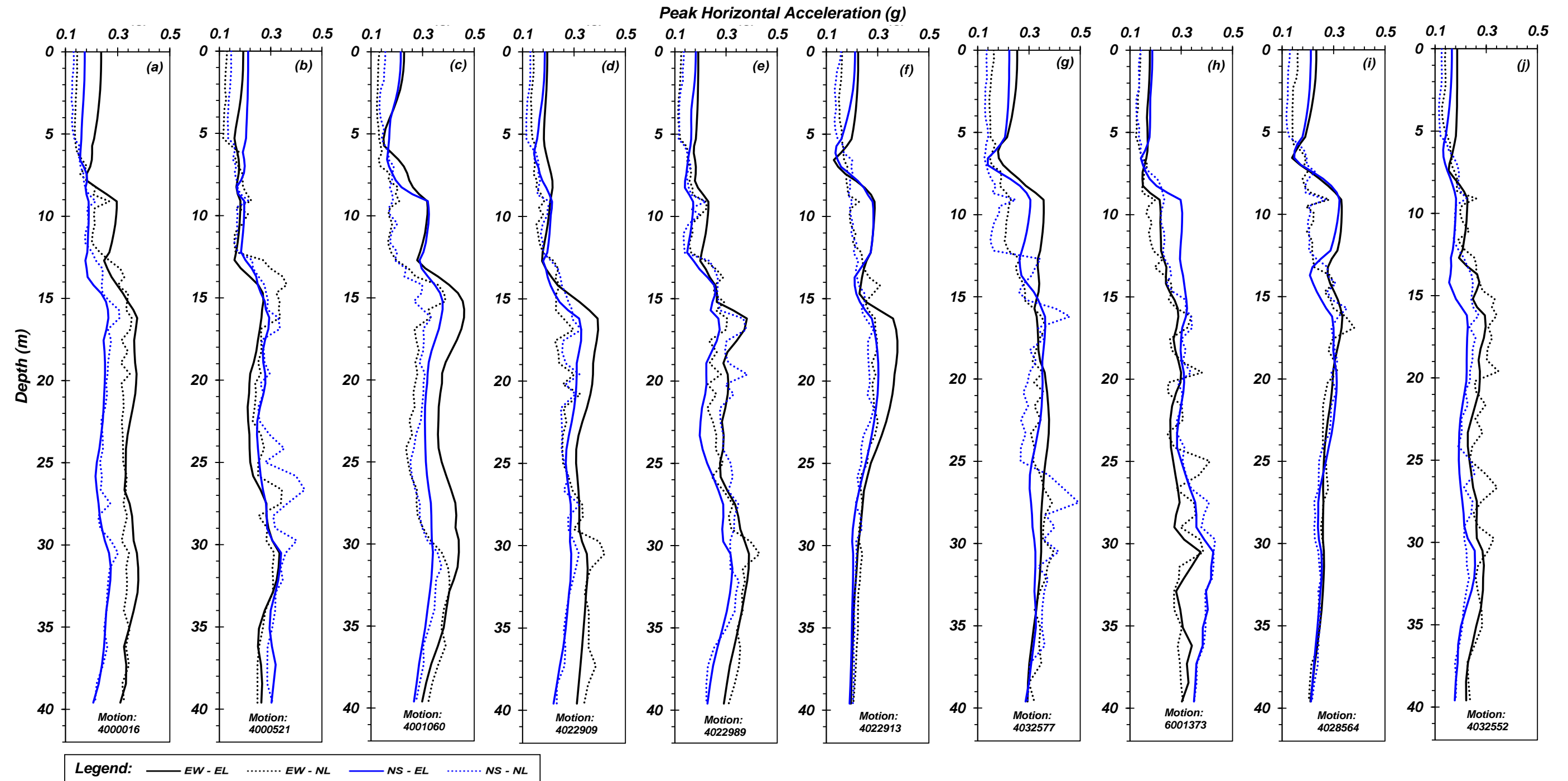


Figure B - 12. Comparison of peak horizontal acceleration (PHA) with depth for equivalent linear (EL) and nonlinear (NL) site response analyses conducted for the Boring 3 (B3) soil profile. 10 Motions (both NS and EW direction, total 20 motions) were evaluated obtained from the PEER NGA earthquake database: (a) Motion 4000016, (b) Motion 4000521, (c) Motion 4001060, (d) Motion 4022909, (e) Motion 4022989, (f) Motion 4022913, (g) Motion 4032577, (h) Motion 6001373, (i) Motion 4028564, (j) Motion 4032552.

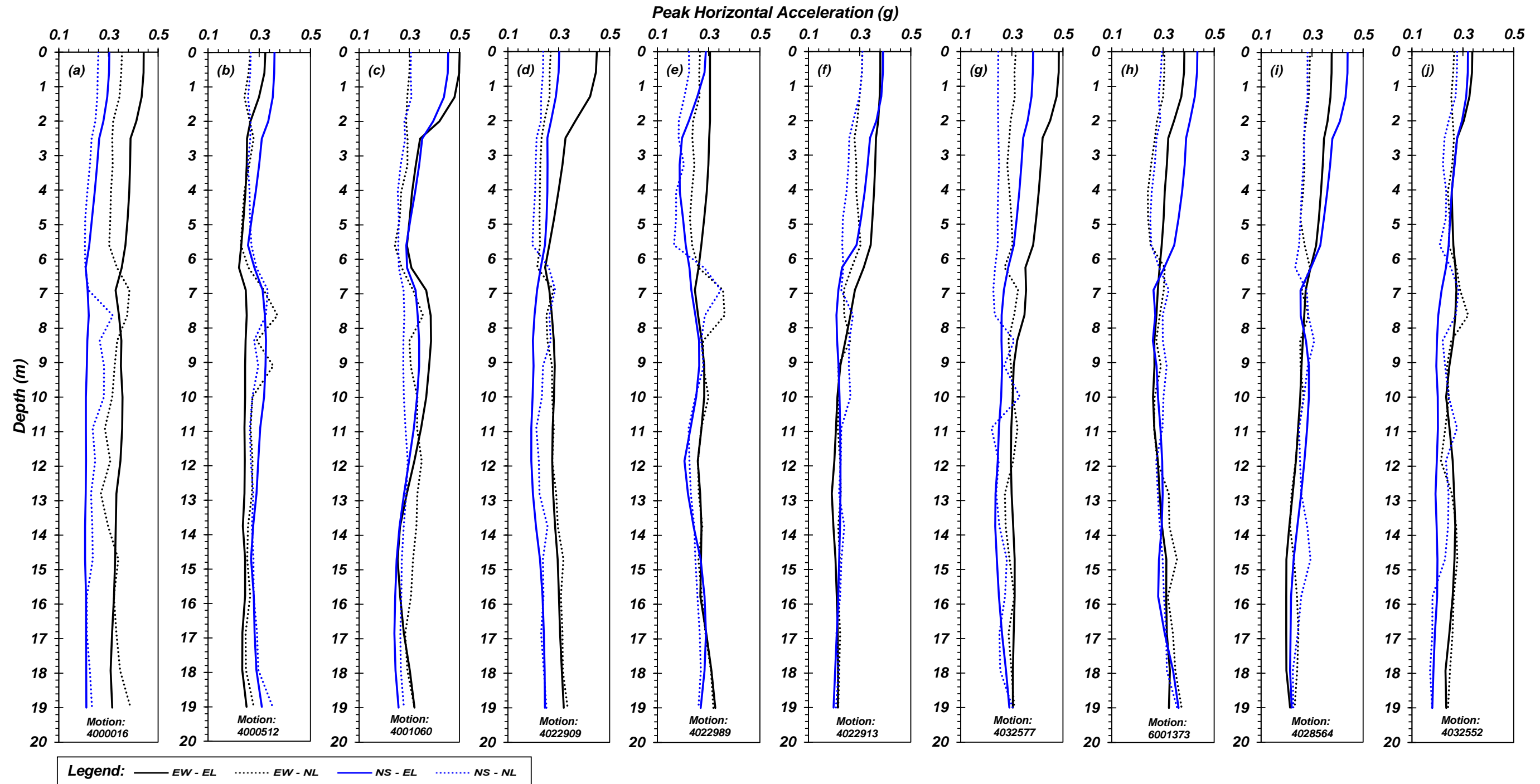


Figure B - 15. Comparison of peak horizontal acceleration (PHA) with depth for equivalent linear (EL) and nonlinear (NL) site response analyses conducted for the CPT-2 (C2) soil profile. 10 Motions (both NS and EW direction, total 20 motions) were evaluated obtained from the PEER NGA earthquake database: (a) Motion 4000016, (b) Motion 4000521, (c) Motion 4001060, (d) Motion 4022909, (e) Motion 4022989, (f) Motion 4022913, (g) Motion 4032577, (h) Motion 6001373, (i) Motion 4028564, (j) Motion 4032552.

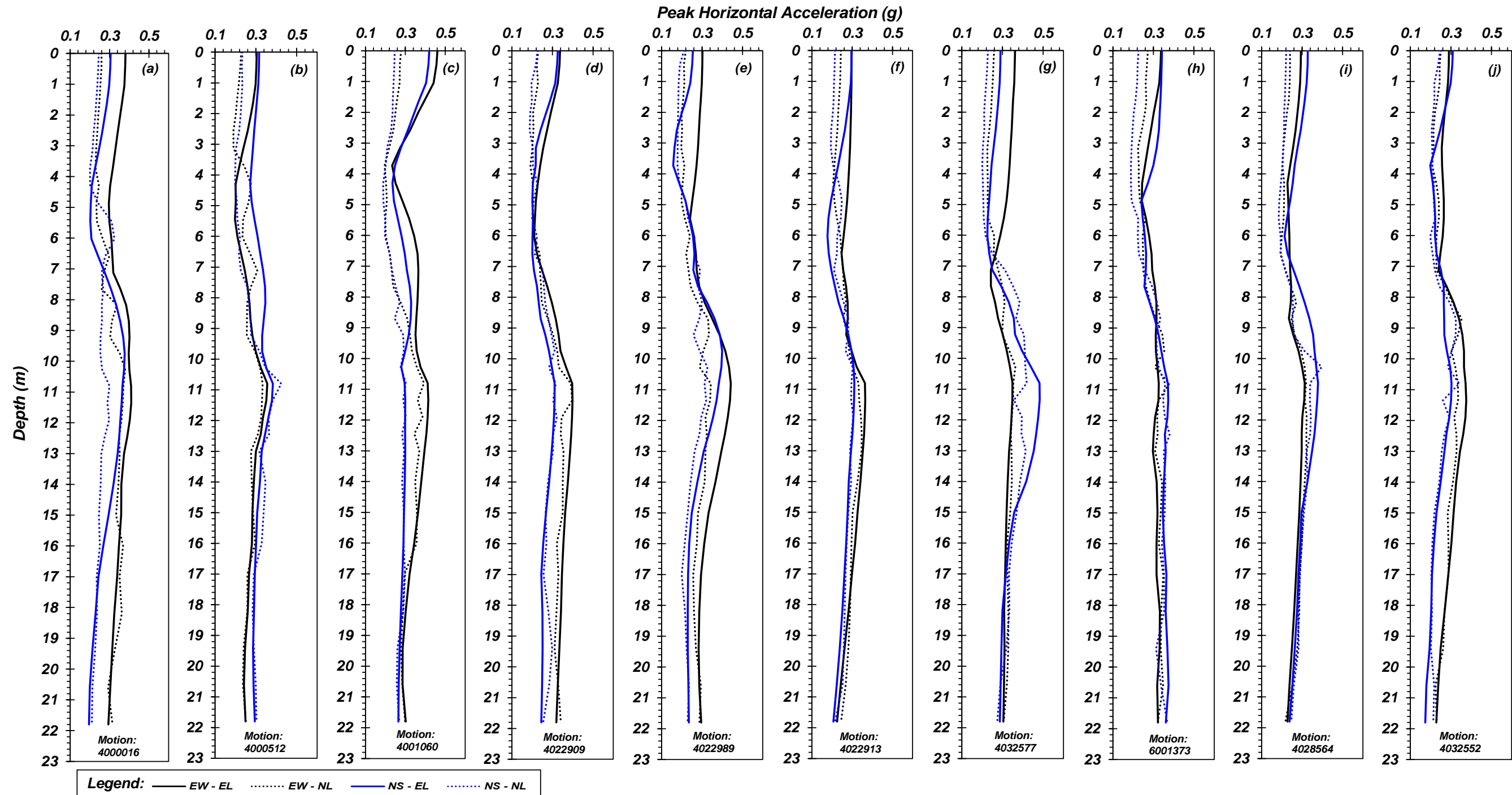


Figure B - 17. Comparison of peak horizontal acceleration (PHA) with depth for equivalent linear (EL) and nonlinear (NL) site response analyses conducted for the CPT-4 (C4) soil profile. 10 Motions (both NS and EW direction, total 20 motions) were evaluated obtained from the PEER NGA earthquake database: (a) Motion 4000016, (b) Motion 4000521, (c) Motion 4001060, (d) Motion 4022909, (e) Motion 4022989, (f) Motion 4022913, (g) Motion 4032577, (h) Motion 6001373, (i) Motion 4028564, (j) Motion 4032552.

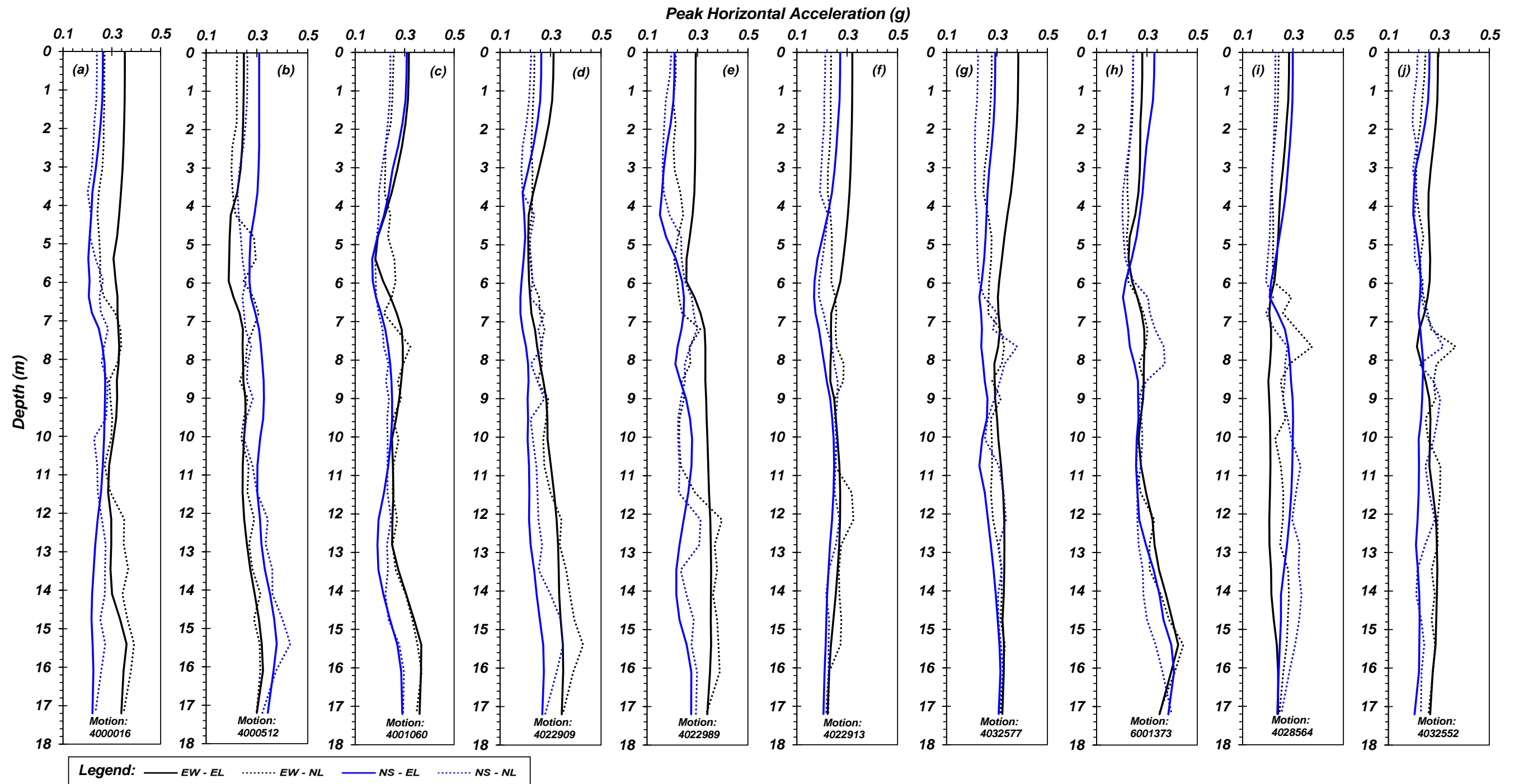


Figure B - 18. Comparison of peak horizontal acceleration (PHA) with depth for equivalent linear (EL) and nonlinear (NL) site response analyses conducted for the CPT-5 (C5) soil profile. 10 Motions (both NS and EW direction, total 20 motions) were evaluated obtained from the PEER NGA earthquake database: (a) Motion 4000016, (b) Motion 4000521, (c) Motion 4001060, (d) Motion 4022909, (e) Motion 4022989, (f) Motion 4022913, (g) Motion 4032577, (h) Motion 6001373, (i) Motion 4028564, (j) Motion 4032552.

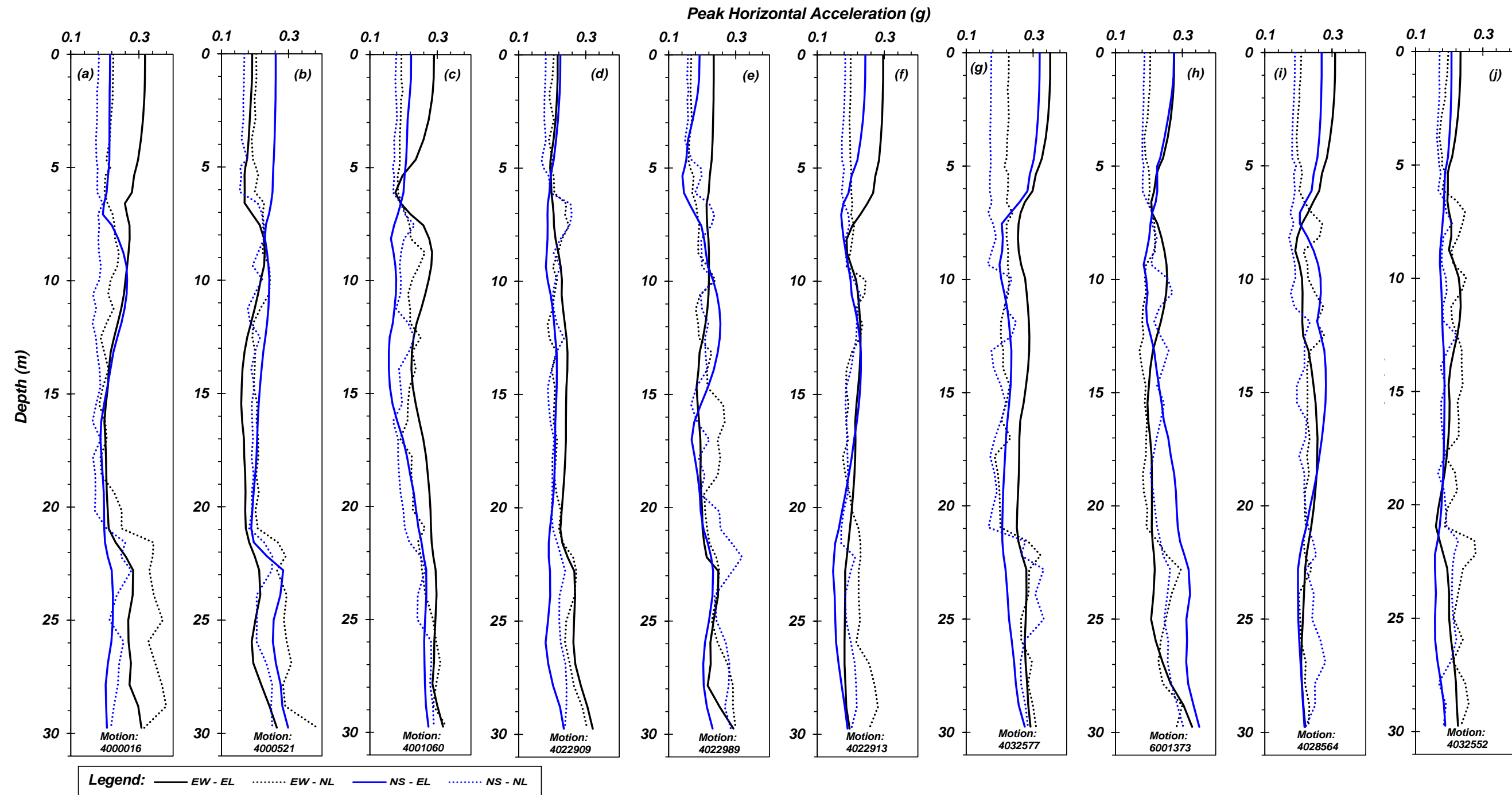


Figure B - 19. Comparison of peak horizontal acceleration (PHA) with depth for equivalent linear (EL) and nonlinear (NL) site response analyses conducted for the CPT-6 (C6) soil profile. 10 Motions (both NS and EW direction, total 20 motions) were evaluated obtained from the PEER NGA earthquake database: (a) Motion 4000016, (b) Motion 4000521, (c) Motion 4001060, (d) Motion 4022909, (e) Motion 4022989, (f) Motion 4022913, (g) Motion 4032577, (h) Motion 6001373, (i) Motion 4028564, (j) Motion 4032552.

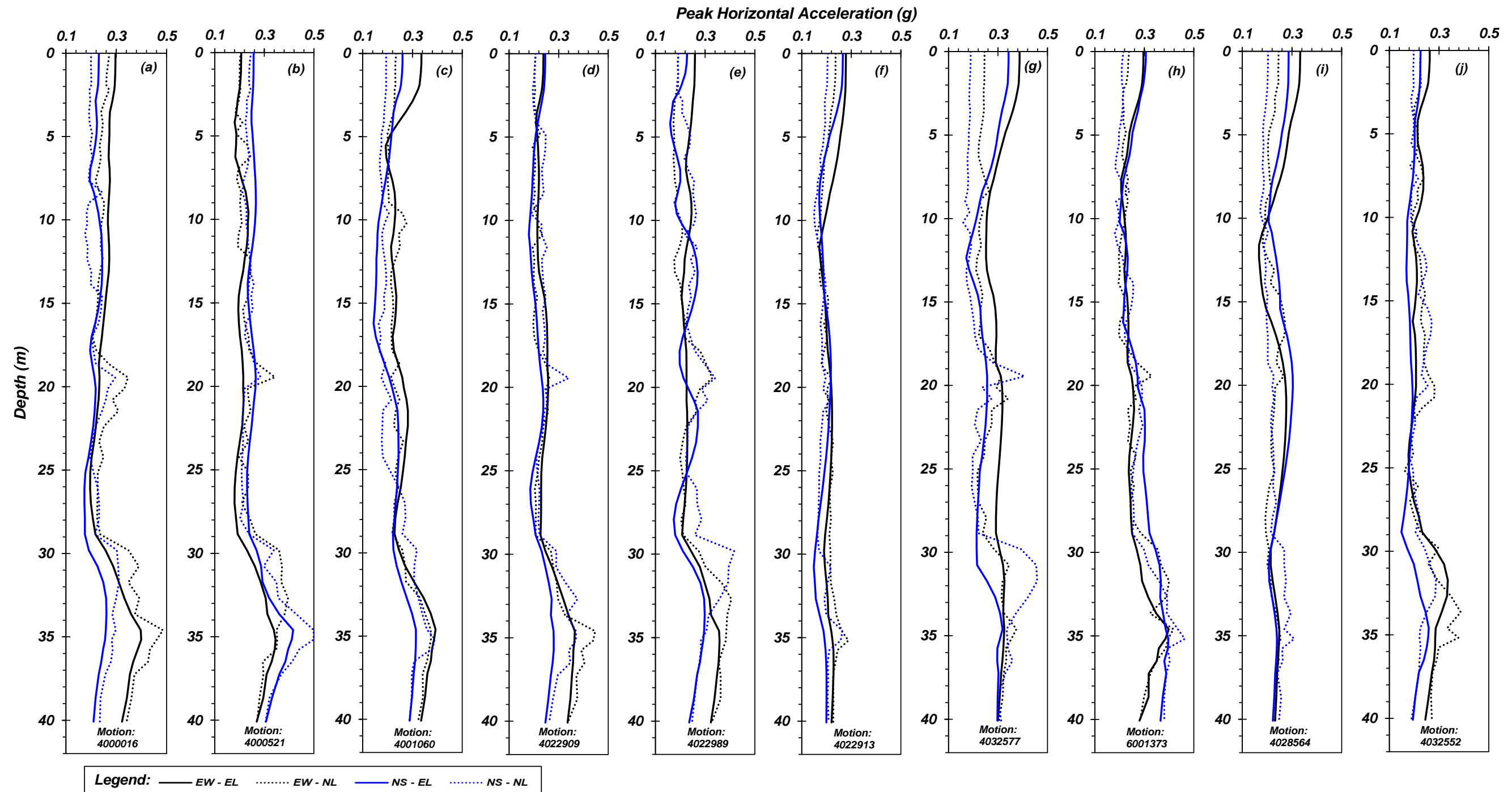


Figure B - 20. Comparison of peak horizontal acceleration (PHA) with depth for equivalent linear (EL) and nonlinear (NL) site response analyses conducted for the CPT-7 (C7) soil profile. 10 Motions (both NS and EW direction, total 20 motions) were evaluated obtained from the PEER NGA earthquake database: (a) Motion 4000016, (b) Motion 4000521, (c) Motion 4001060, (d) Motion 4022909, (e) Motion 4022989, (f) Motion 4022913, (g) Motion 4032577, (h) Motion 6001373, (i) Motion 4028564, (j) Motion 4032552.

Maximum Shear Strain Plots

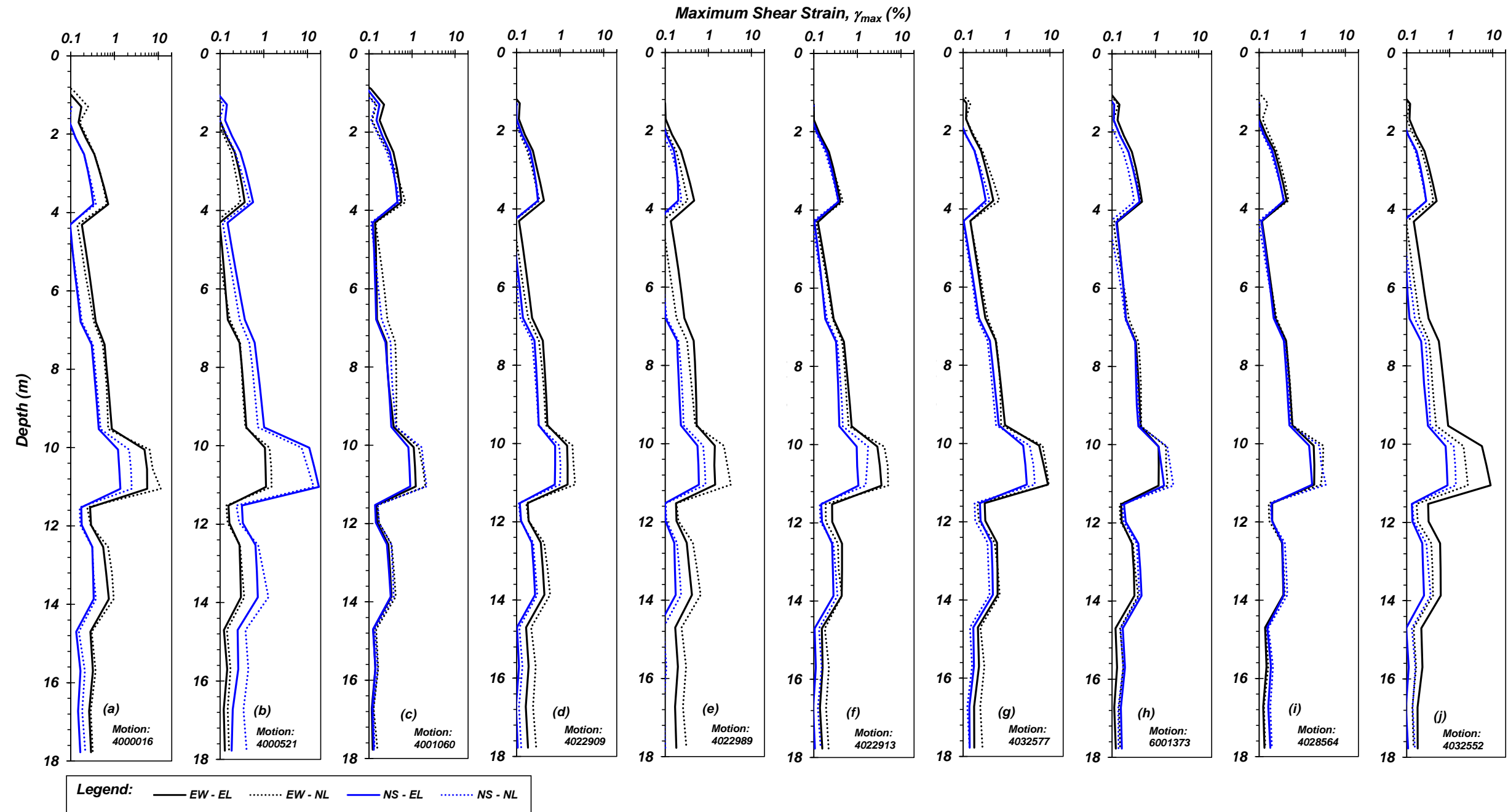


Figure B - 21. Comparison of maximum shear strain, γ_{max} (%) with depth for equivalent linear (EL) and nonlinear (NL) site response analyses conducted for the Boring 2 (B2) soil profile. 10 Motions (both NS and EW direction, total 20 motions) were evaluated obtained from the PEER NGA earthquake database: (a) Motion 4000016, (b) Motion 4000521, (c) Motion 4001060, (d) Motion 4022909, (e) Motion 4022989, (f) Motion 4022913, (g) Motion 4032577, (h) Motion 6001373, (i) Motion 4028564, (j) Motion 4032552.

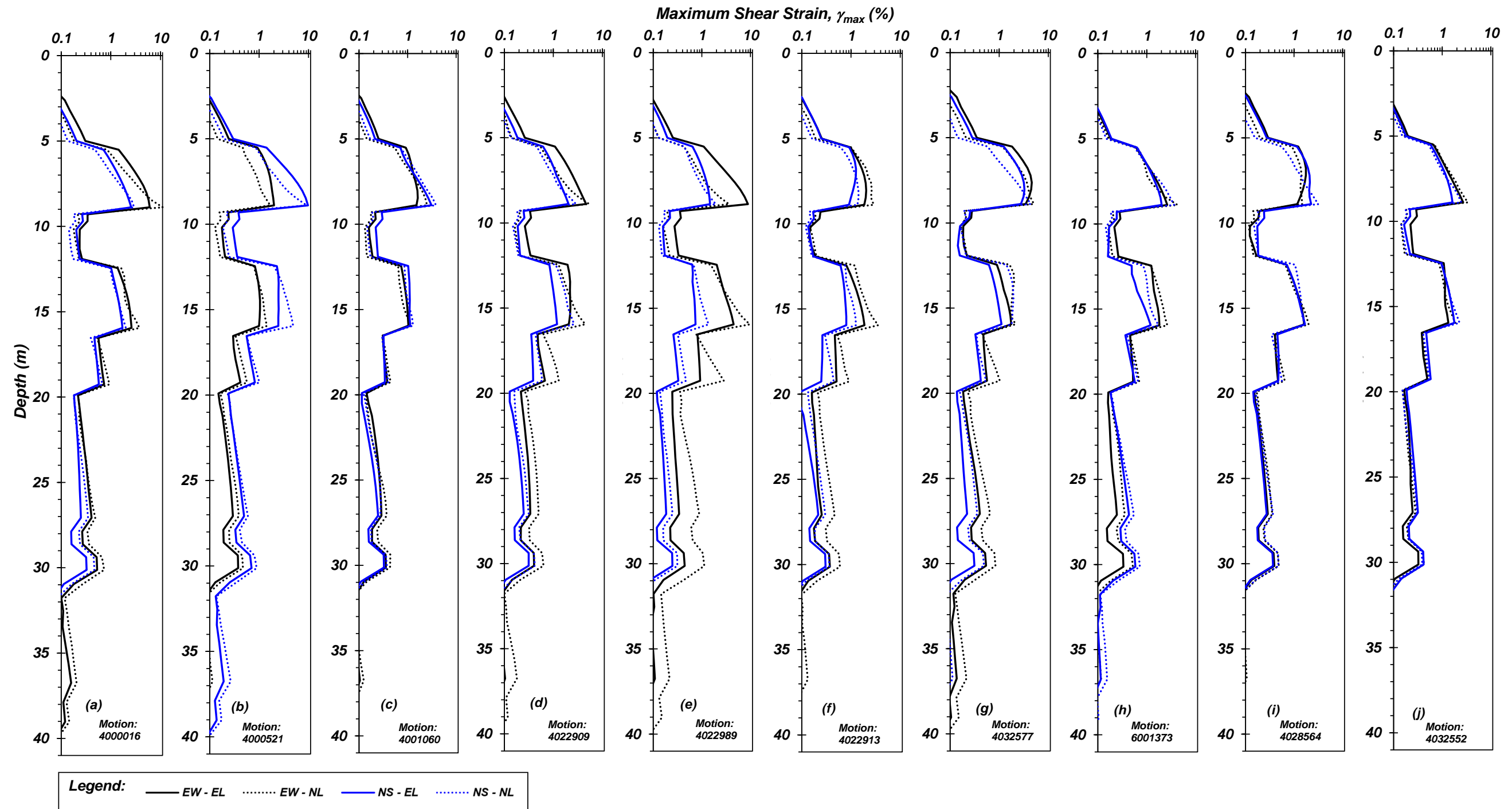


Figure B - 22. Comparison of maximum shear strain, γ_{max} (%) with depth for equivalent linear (EL) and nonlinear (NL) site response analyses conducted for the Boring 3 (B3) soil profile. 10 Motions (both NS and EW direction, total 20 motions) were evaluated obtained from the PEER NGA earthquake database: (a) Motion 4000016, (b) Motion 4000521, (c) Motion 4001060, (d) Motion 4022909, (e) Motion 4022989, (f) Motion 4022913, (g) Motion 4032577, (h) Motion 6001373, (i) Motion 4028564, (j) Motion 4032552.

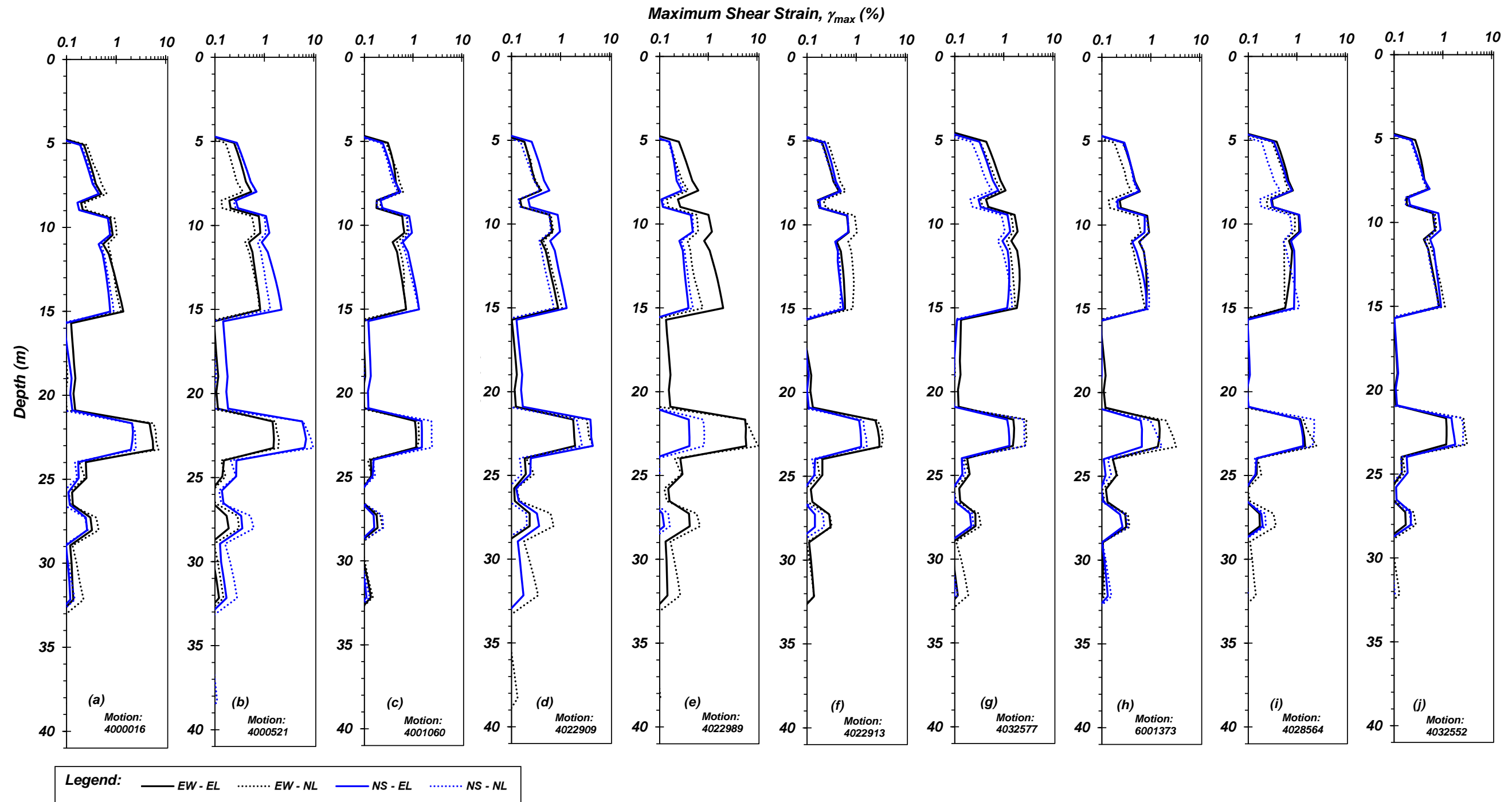


Figure B - 23. Comparison of maximum shear strain, γ_{max} (%) with depth for equivalent linear (EL) and nonlinear (NL) site response analyses conducted for the Boring 4 (B4) soil profile. 10 Motions (both NS and EW direction, total 20 motions) were evaluated obtained from the PEER NGA earthquake database: (a) Motion 4000016, (b) Motion 4000521, (c) Motion 4001060, (d) Motion 4022909, (e) Motion 4022989, (f) Motion 4022913, (g) Motion 4032577, (h) Motion 6001373, (i) Motion 4028564, (j) Motion 4032552.

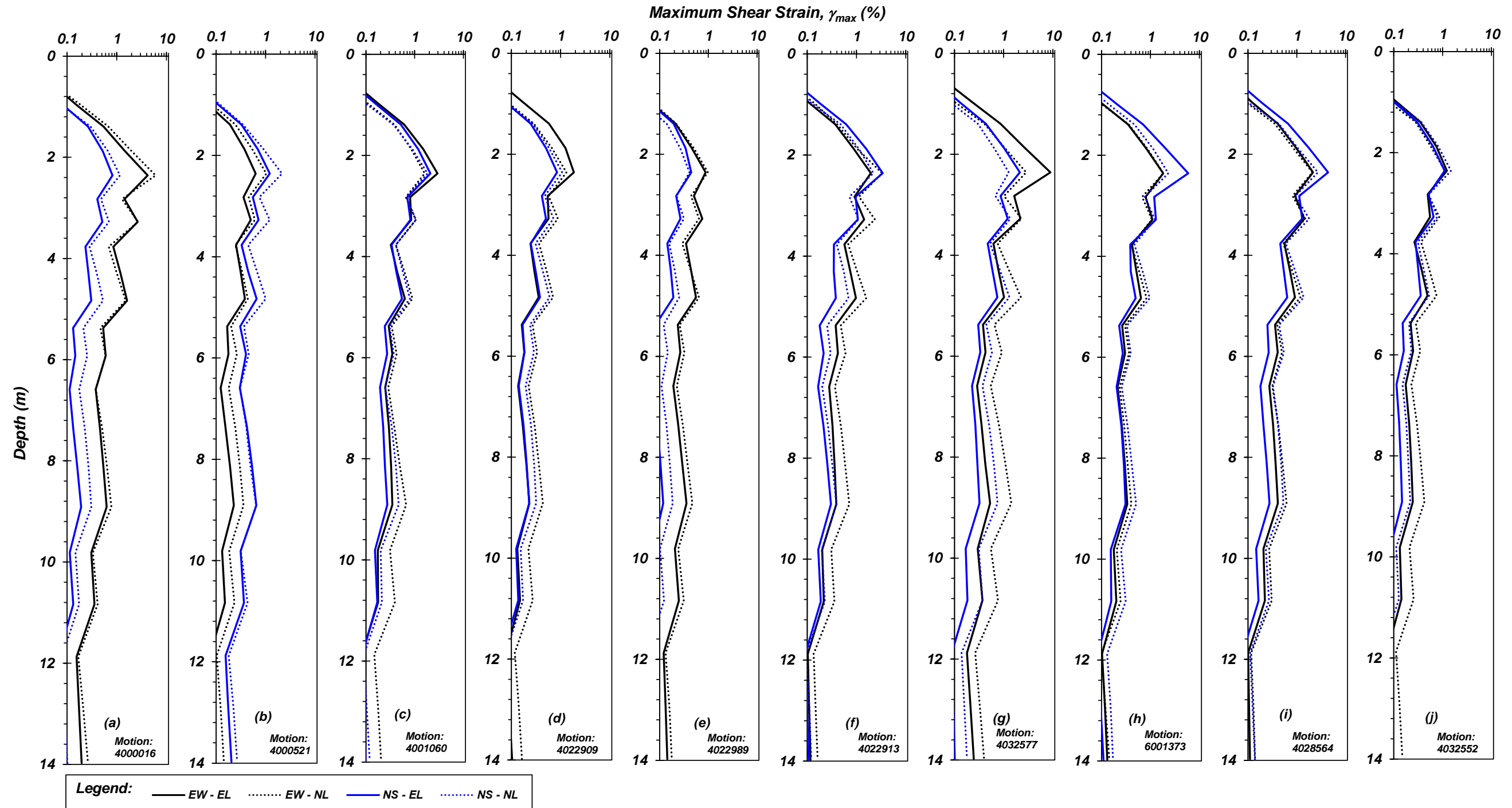


Figure B - 24. Comparison of maximum shear strain, γ_{max} (%) with depth for equivalent linear (EL) and nonlinear (NL) site response analyses conducted for the CPT-1 (C1) soil profile. 10 Motions (both NS and EW direction, total 20 motions) were evaluated obtained from the PEER NGA earthquake database: (a) Motion 4000016, (b) Motion 4000521, (c) Motion 4001060, (d) Motion 4022909, (e) Motion 4022989, (f) Motion 4022913, (g) Motion 4032577, (h) Motion 6001373, (i) Motion 4028564, (j) Motion 4032552.

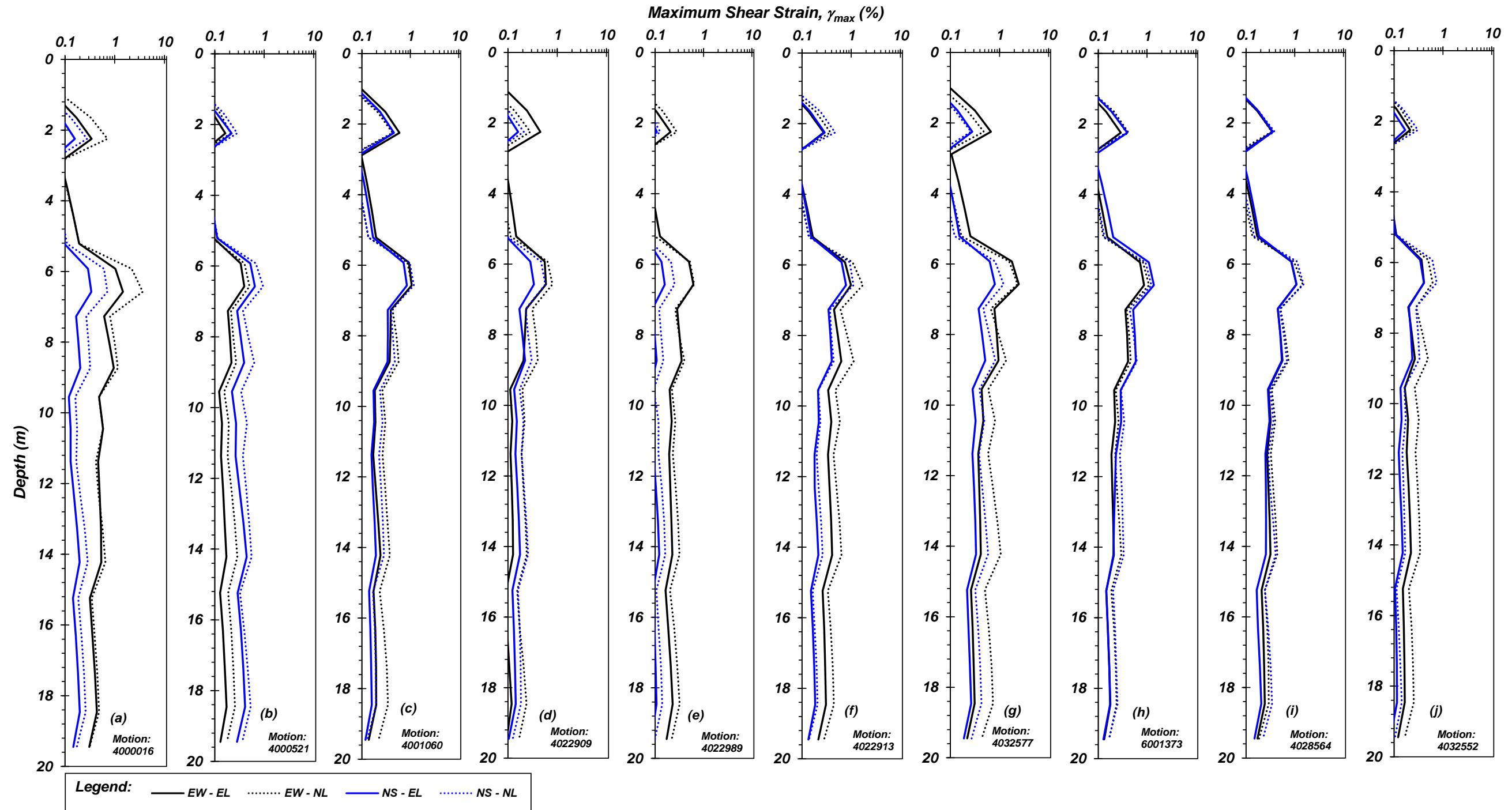


Figure B - 25. Comparison of maximum shear strain, γ_{max} (%) with depth for equivalent linear (EL) and nonlinear (NL) site response analyses conducted for the CPT-2 (C2) soil profile. 10 Motions (both NS and EW direction, total 20 motions) were evaluated obtained from the PEER NGA earthquake database: (a) Motion 4000016, (b) Motion 4000521, (c) Motion 4001060, (d) Motion 4022909, (e) Motion 4022989, (f) Motion 4022913, (g) Motion 4032577, (h) Motion 6001373, (i) Motion 4028564, (j) Motion 4032552.

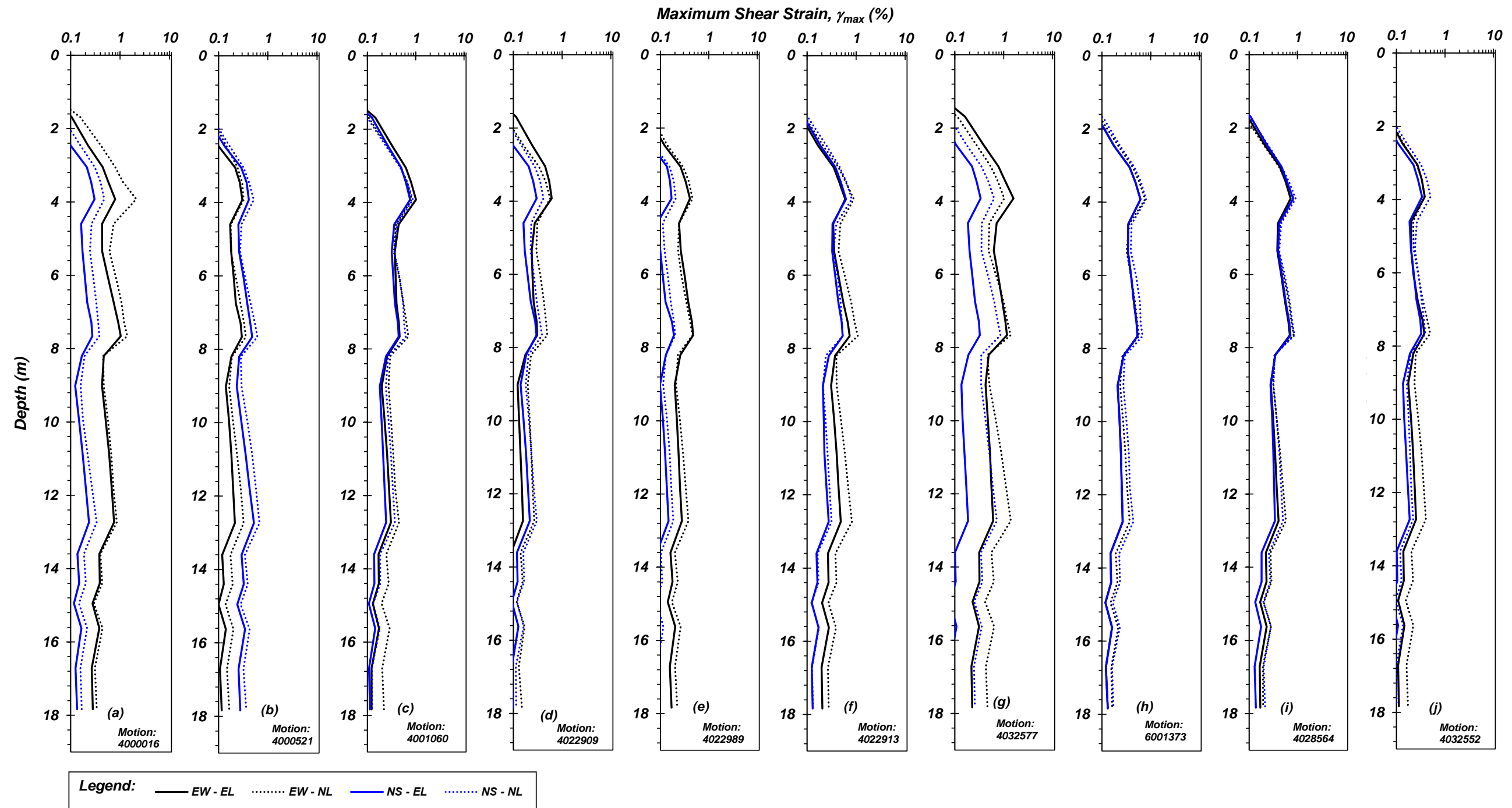


Figure B - 26. Comparison of maximum shear strain, γ_{max} (%) with depth for equivalent linear (EL) and nonlinear (NL) site response analyses conducted for the CPT-3 (C3) soil profile. 10 Motions (both NS and EW direction, total 20 motions) were evaluated obtained from the PEER NGA earthquake database: (a) Motion 4000016, (b) Motion 4000521, (c) Motion 4001060, (d) Motion 4022909, (e) Motion 4022989, (f) Motion 4022913, (g) Motion 4032577, (h) Motion 6001373, (i) Motion 4028564, (j) Motion 4032552.

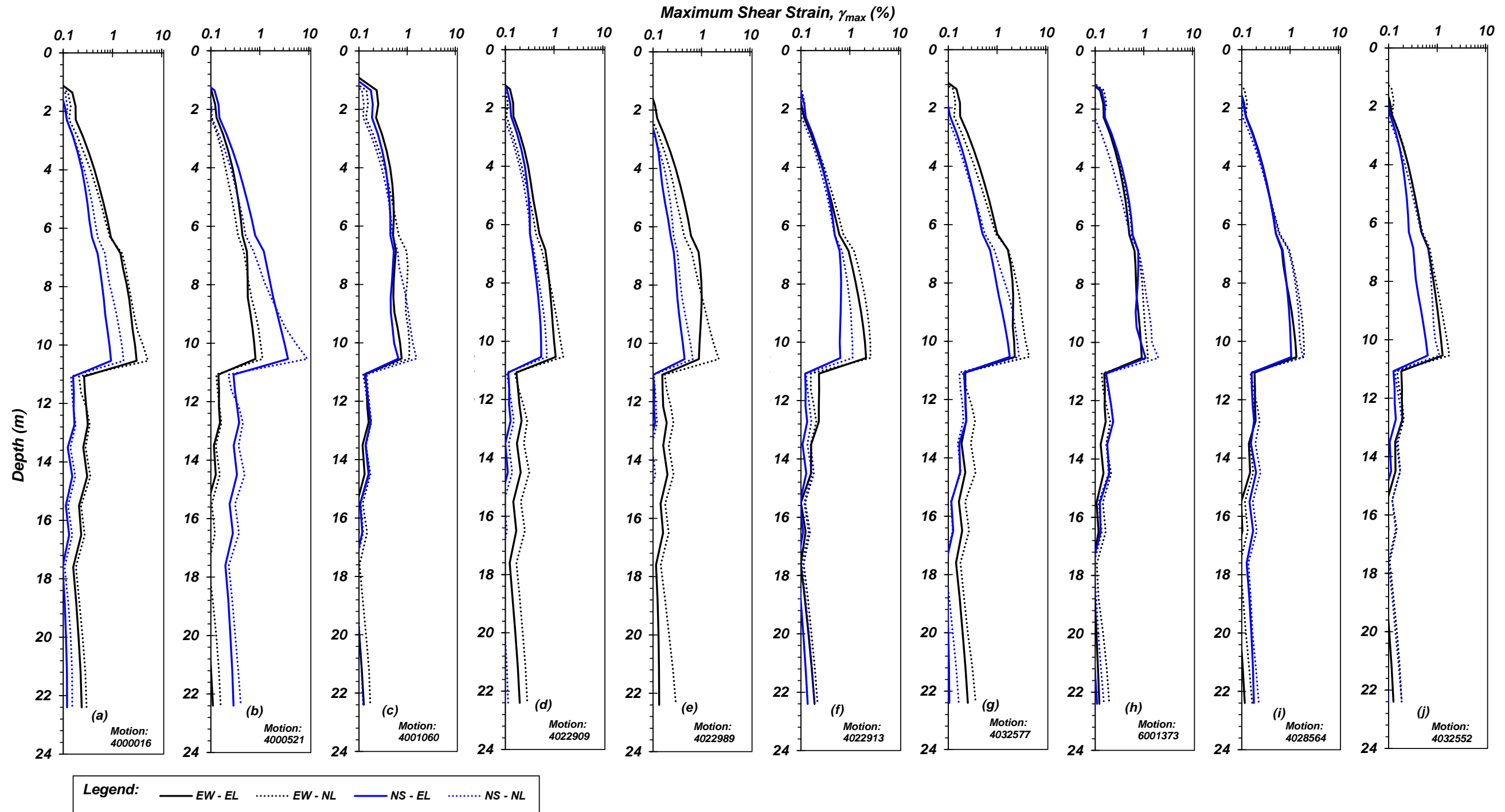


Figure B - 27. Comparison of maximum shear strain, γ_{max} (%) with depth for equivalent linear (EL) and nonlinear (NL) site response analyses conducted for the CPT-4 (C4) soil profile. 10 Motions (both NS and EW direction, total 20 motions) were evaluated obtained from the PEER NGA earthquake database: (a) Motion 4000016, (b) Motion 4000521, (c) Motion 4001060, (d) Motion 4022909, (e) Motion 4022989, (f) Motion 4022913, (g) Motion 4032577, (h) Motion 6001373, (i) Motion 4028564, (j) Motion 4032552.

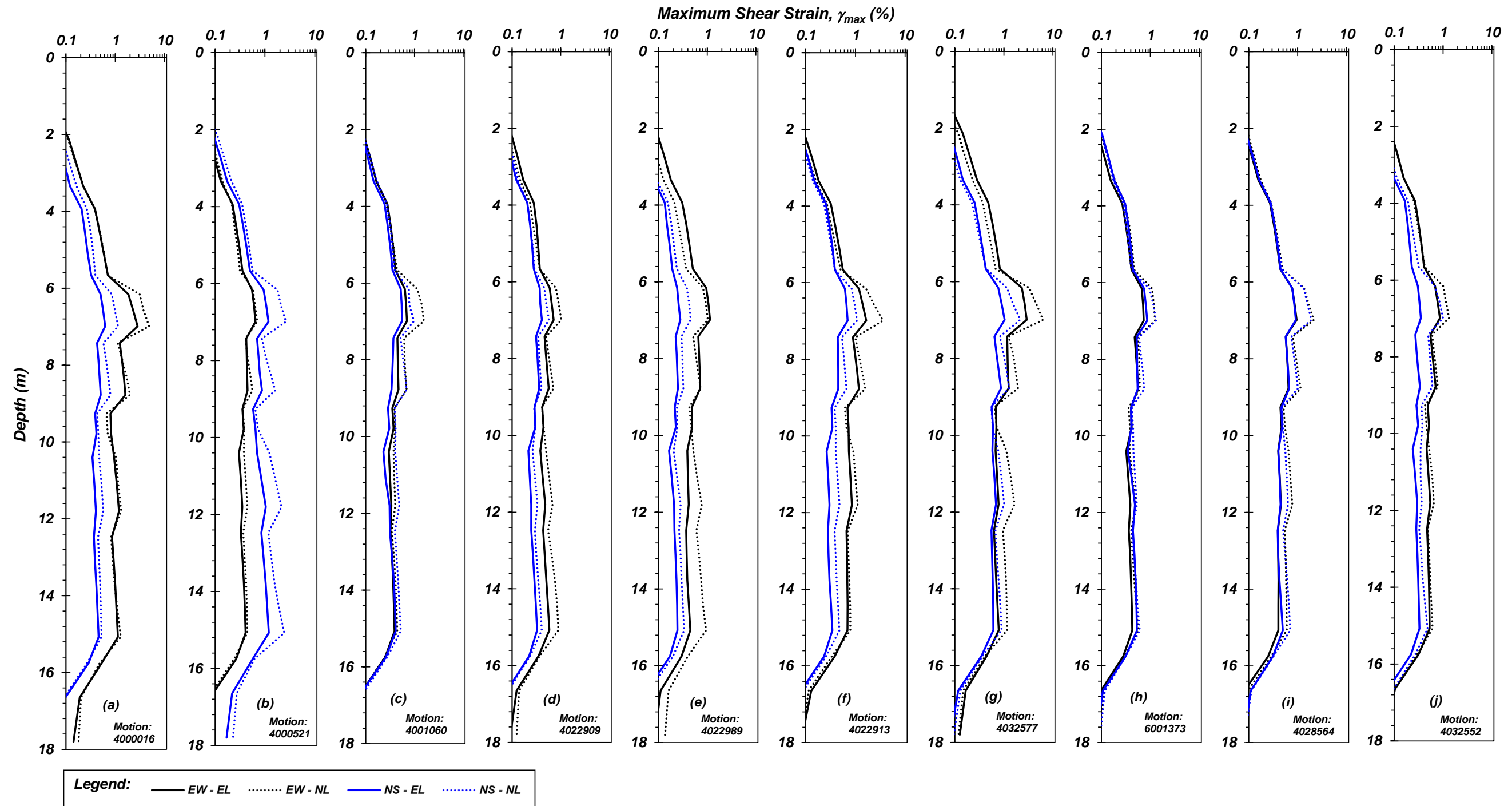


Figure B - 28. Comparison of maximum shear strain, γ_{max} (%) with depth for equivalent linear (EL) and nonlinear (NL) site response analyses conducted for the CPT-5 (C5) soil profile. 10 Motions (both NS and EW direction, total 20 motions) were evaluated obtained from the PEER NGA earthquake database: (a) Motion 4000016, (b) Motion 4000521, (c) Motion 4001060, (d) Motion 4022909, (e) Motion 4022989, (f) Motion 4022913, (g) Motion 4032577, (h) Motion 6001373, (i) Motion 4028564, (j) Motion 4032552.

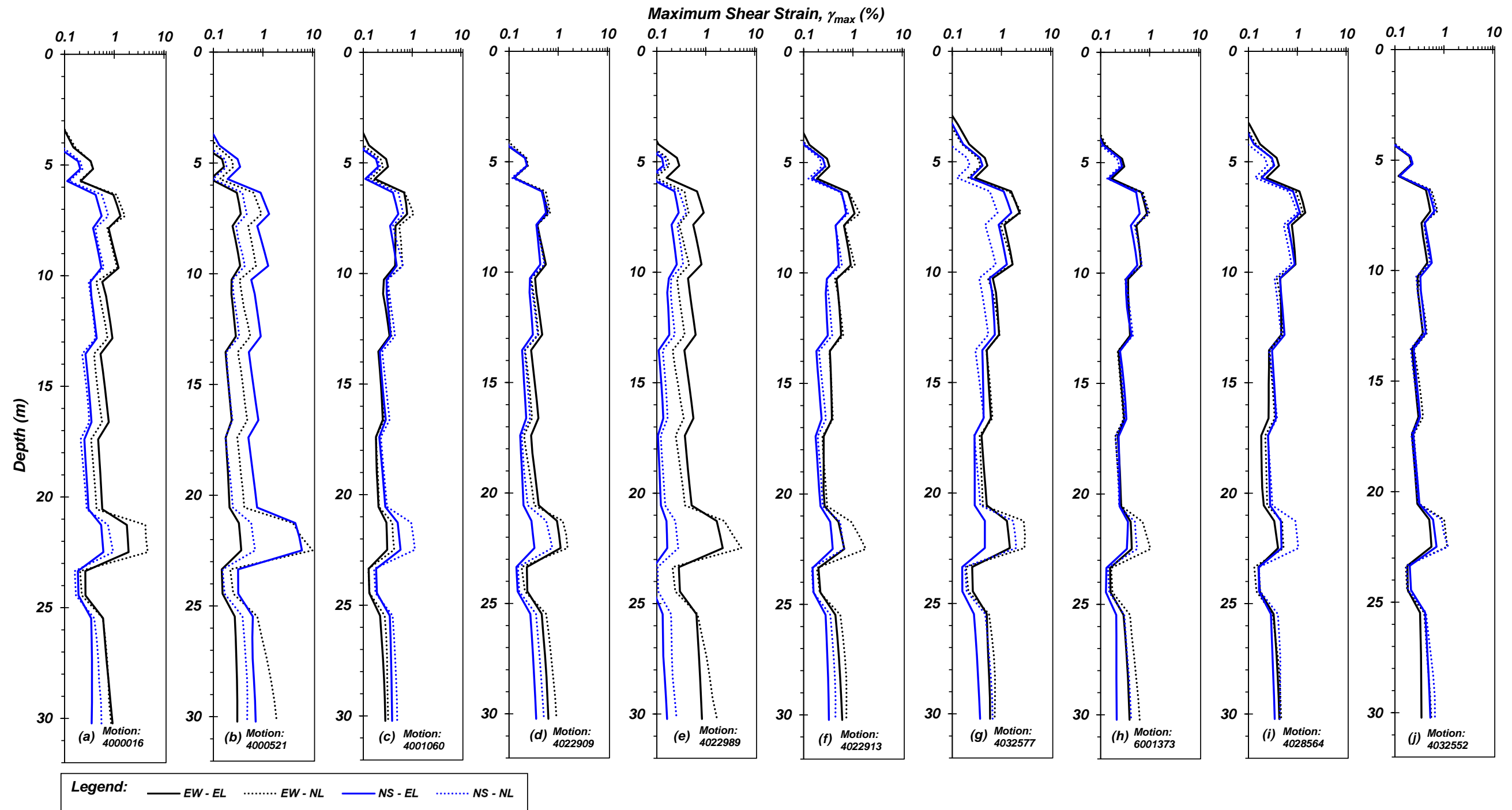


Figure B - 29. Comparison of maximum shear strain, γ_{max} (%) with depth for equivalent linear (EL) and nonlinear (NL) site response analyses conducted for the CPT-6 (C6) soil profile. 10 Motions (both NS and EW direction, total 20 motions) were evaluated obtained from the PEER NGA earthquake database: (a) Motion 4000016, (b) Motion 4000521, (c) Motion 4001060, (d) Motion 4022909, (e) Motion 4022989, (f) Motion 4022913, (g) Motion 4032577, (h) Motion 6001373, (i) Motion 4028564, (j) Motion 4032552.

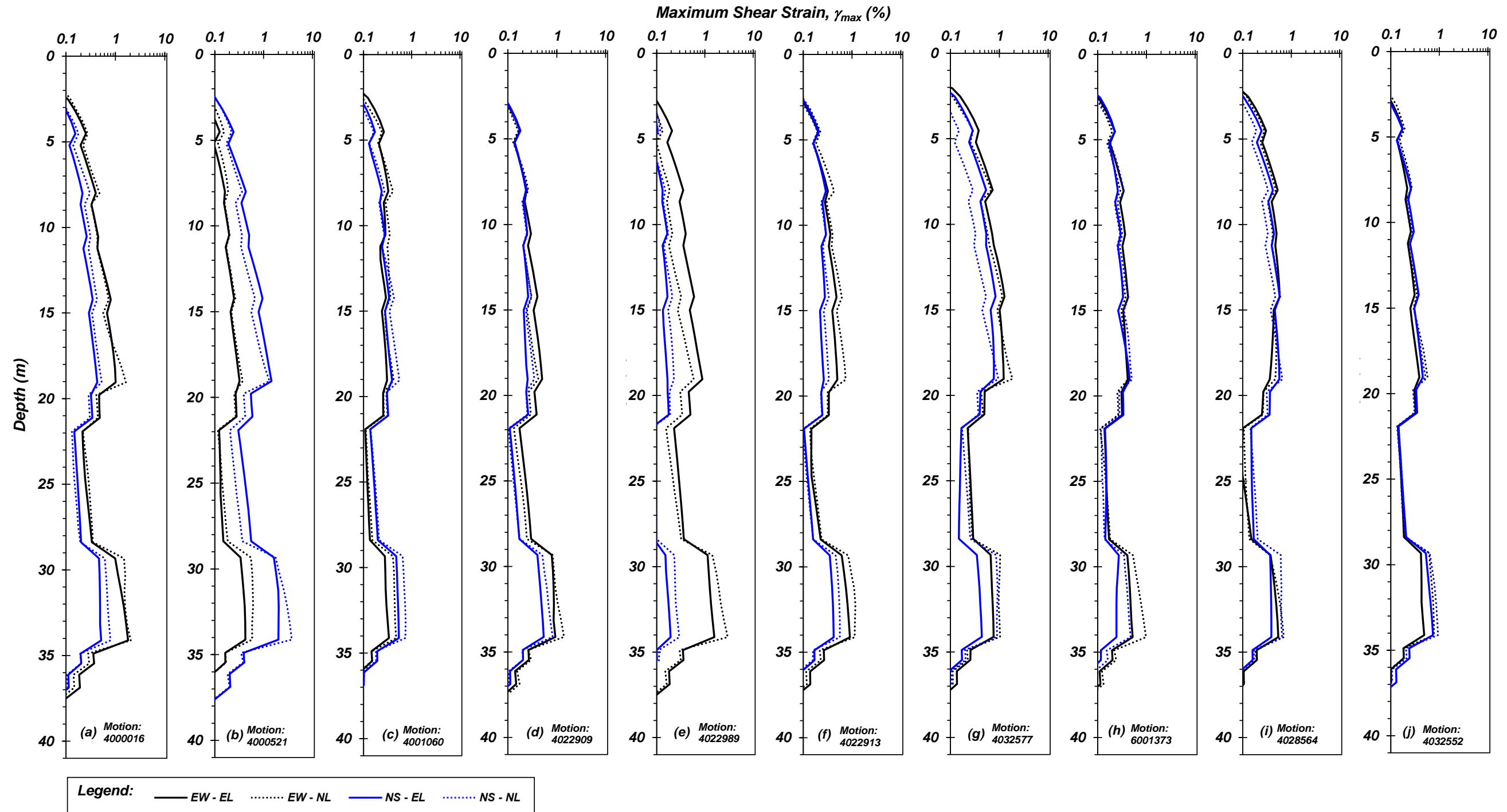


Figure B - 30. Comparison of maximum shear strain, γ_{max} (%) with depth for equivalent linear (EL) and nonlinear (NL) site response analyses conducted for the CPT-7 (C7) soil profile. 10 Motions (both NS and EW direction, total 20 motions) were evaluated obtained from the PEER NGA earthquake database: (a) Motion 4000016, (b) Motion 4000521, (c) Motion 4001060, (d) Motion 4022909, (e) Motion 4022989, (f) Motion 4022913, (g) Motion 4032577, (h) Motion 6001373, (i) Motion 4028564, (j) Motion 4032552.

Spectra Acceleration Plots

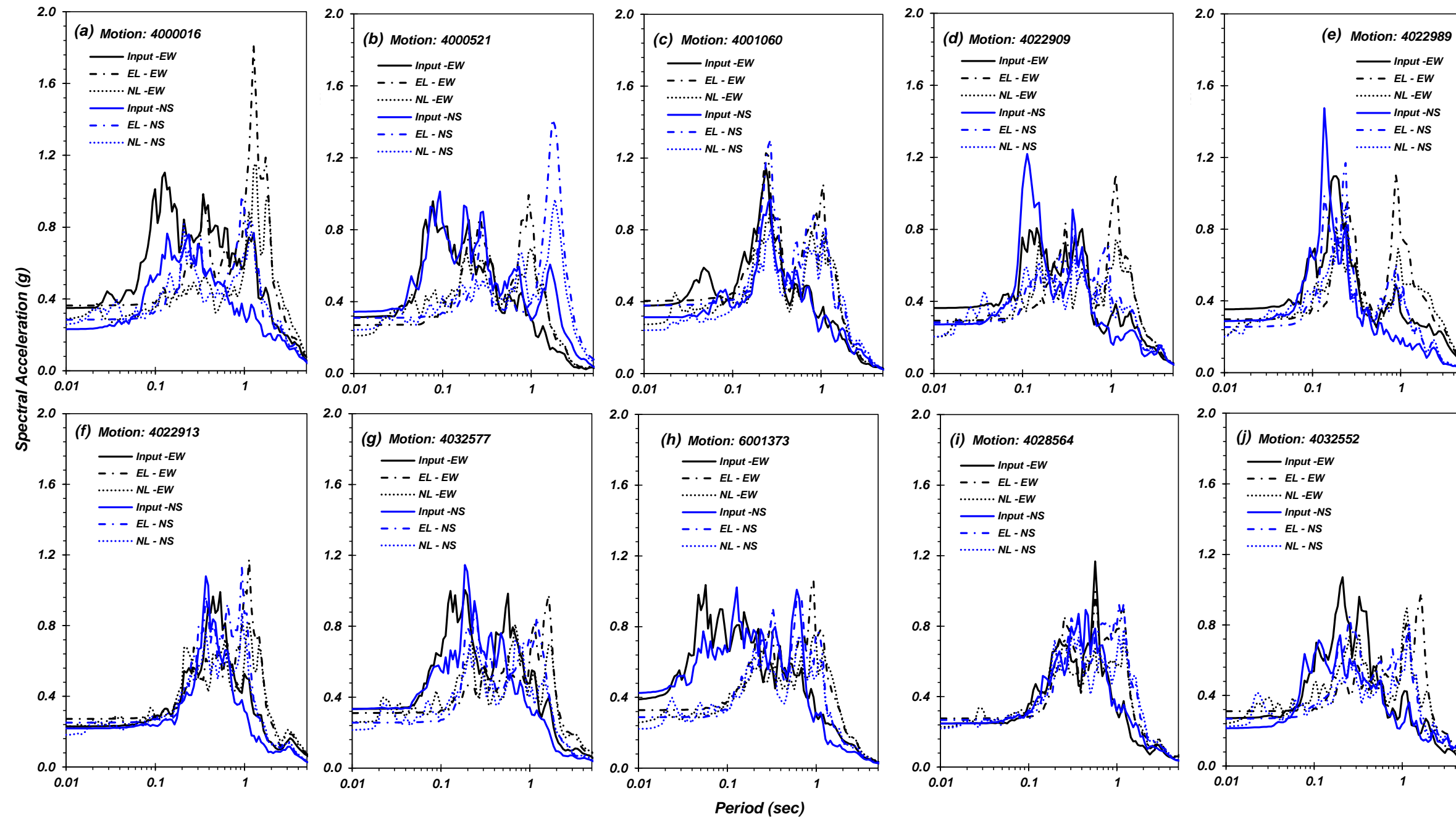


Figure B - 31. Comparison of spectral acceleration (SA) with depth for equivalent linear (EL) and nonlinear (NL) site response analyses conducted for the Boring 2 (B2) soil profile. 10 Motions (both NS and EW direction, total 20 motions) were evaluated obtained from the PEER NGA earthquake database: (a) Motion 4000016, (b) Motion 4000521, (c) Motion 4001060, (d) Motion 4022909, (e) Motion 4022989, (f) Motion 4022913, (g) Motion 4032577, (h) Motion 6001373, (i) Motion 4028564, (j) Motion 4032552.

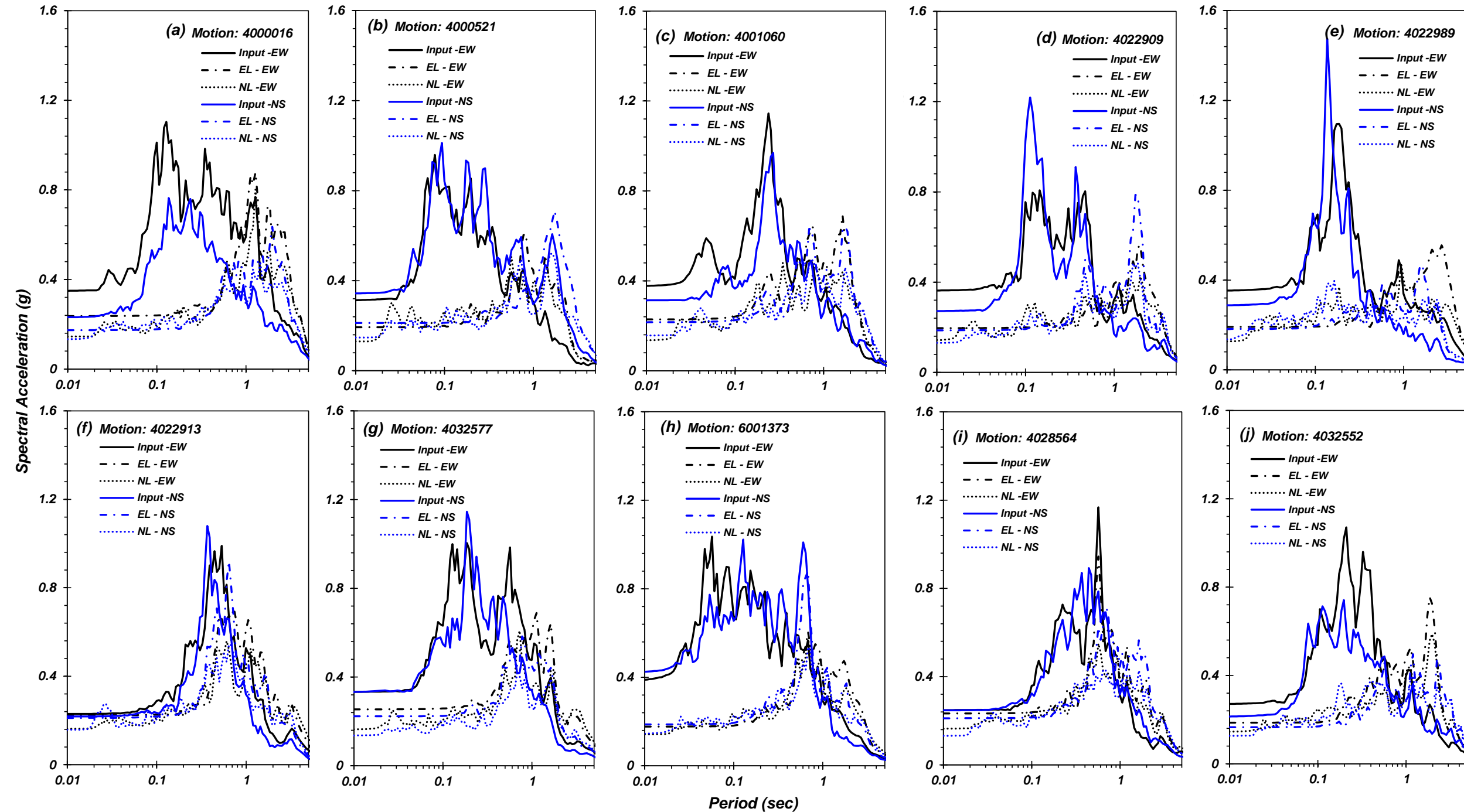


Figure B - 32. Comparison of spectral acceleration (SA) with depth for equivalent linear (EL) and nonlinear (NL) site response analyses conducted for the Boring 3 (B3) soil profile. 10 Motions (both NS and EW direction, total 20 motions) were evaluated obtained from the PEER NGA earthquake database: (a) Motion 4000016, (b) Motion 4000521, (c) Motion 4001060, (d) Motion 4022909, (e) Motion 4022989, (f) Motion 4022913, (g) Motion 4032577, (h) Motion 6001373, (i) Motion 4028564, (j) Motion 4032552.

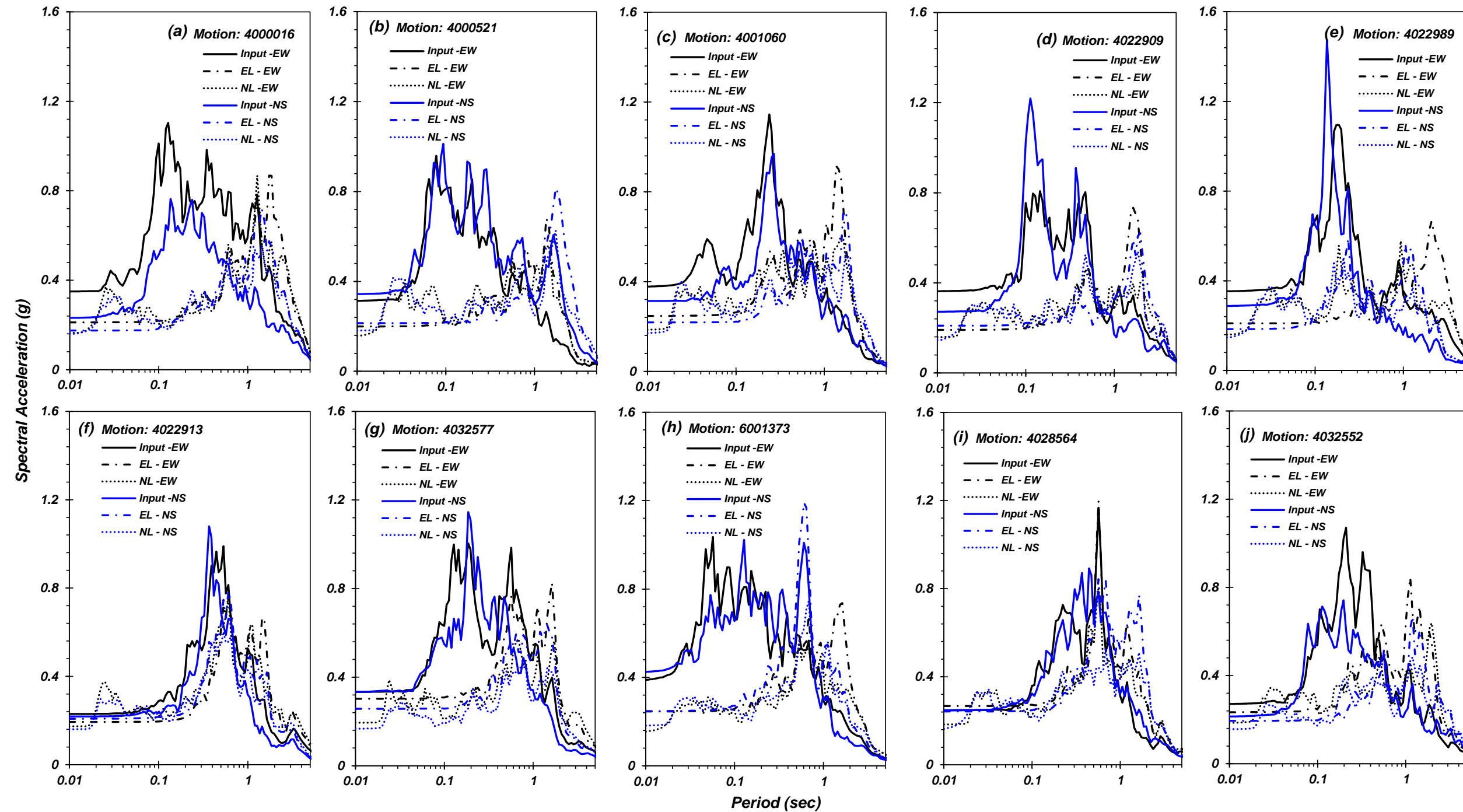


Figure B - 33. Comparison of spectral acceleration (SA) with depth for equivalent linear (EL) and nonlinear (NL) site response analyses conducted for the Boring 4 (B4) soil profile. 10 Motions (both NS and EW direction, total 20 motions) were evaluated obtained from the PEER NGA earthquake database: (a) Motion 4000016, (b) Motion 4000521, (c) Motion 4001060, (d) Motion 4022909, (e) Motion 4022989, (f) Motion 4022913, (g) Motion 4032577, (h) Motion 6001373, (i) Motion 4028564, (j) Motion 4032552.

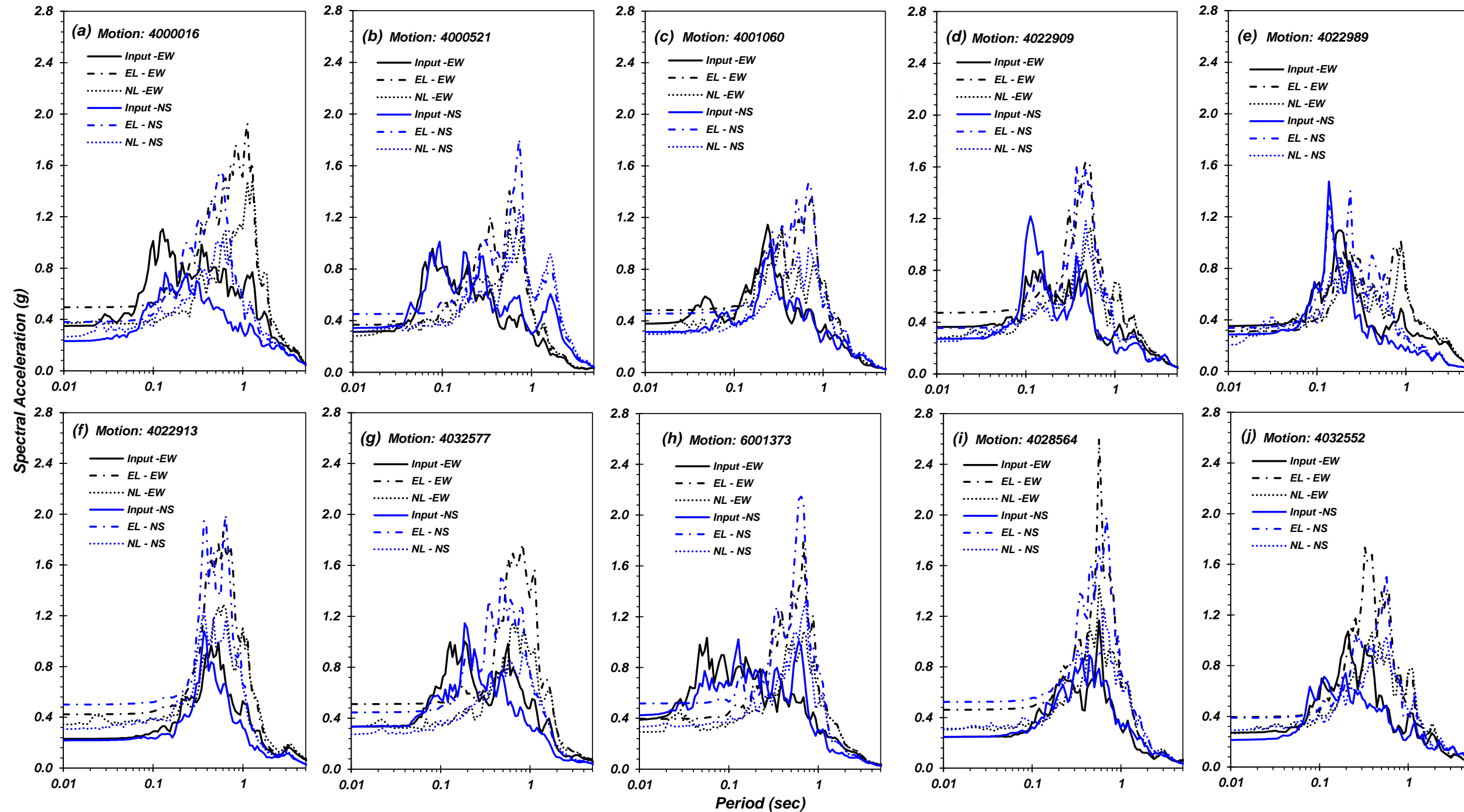


Figure B - 34. Comparison of spectral acceleration (SA) with depth for equivalent linear (EL) and nonlinear (NL) site response analyses conducted for the CPT-1 (C1) soil profile. 10 Motions (both NS and EW direction, total 20 motions) were evaluated obtained from the PEER NGA earthquake database: (a) Motion 4000016, (b) Motion 4000521, (c) Motion 4001060, (d) Motion 4022909, (e) Motion 4022989, (f) Motion 4022913, (g) Motion 4032577, (h) Motion 6001373, (i) Motion 4028564, (j) Motion 4032552.

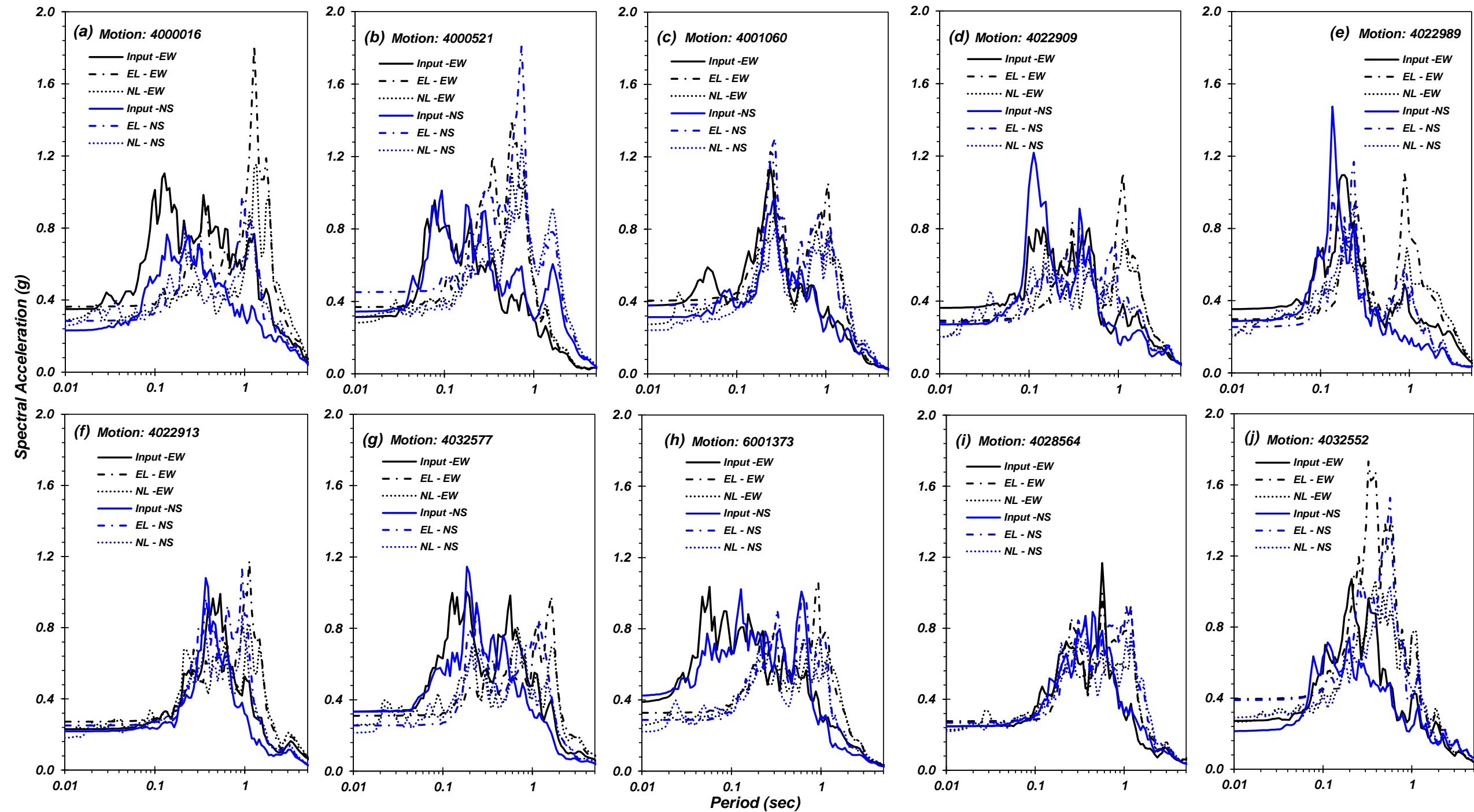


Figure B - 35. Comparison of spectral acceleration (SA) with depth for equivalent linear (EL) and nonlinear (NL) site response analyses conducted for the CPT-2 (C2) soil profile. 10 Motions (both NS and EW direction, total 20 motions) were evaluated obtained from the PEER NGA earthquake database: (a) Motion 4000016, (b) Motion 4000521, (c) Motion 4001060, (d) Motion 4022909, (e) Motion 4022989, (f) Motion 4022913, (g) Motion 4032577, (h) Motion 6001373, (i) Motion 4028564, (j) Motion 4032552.

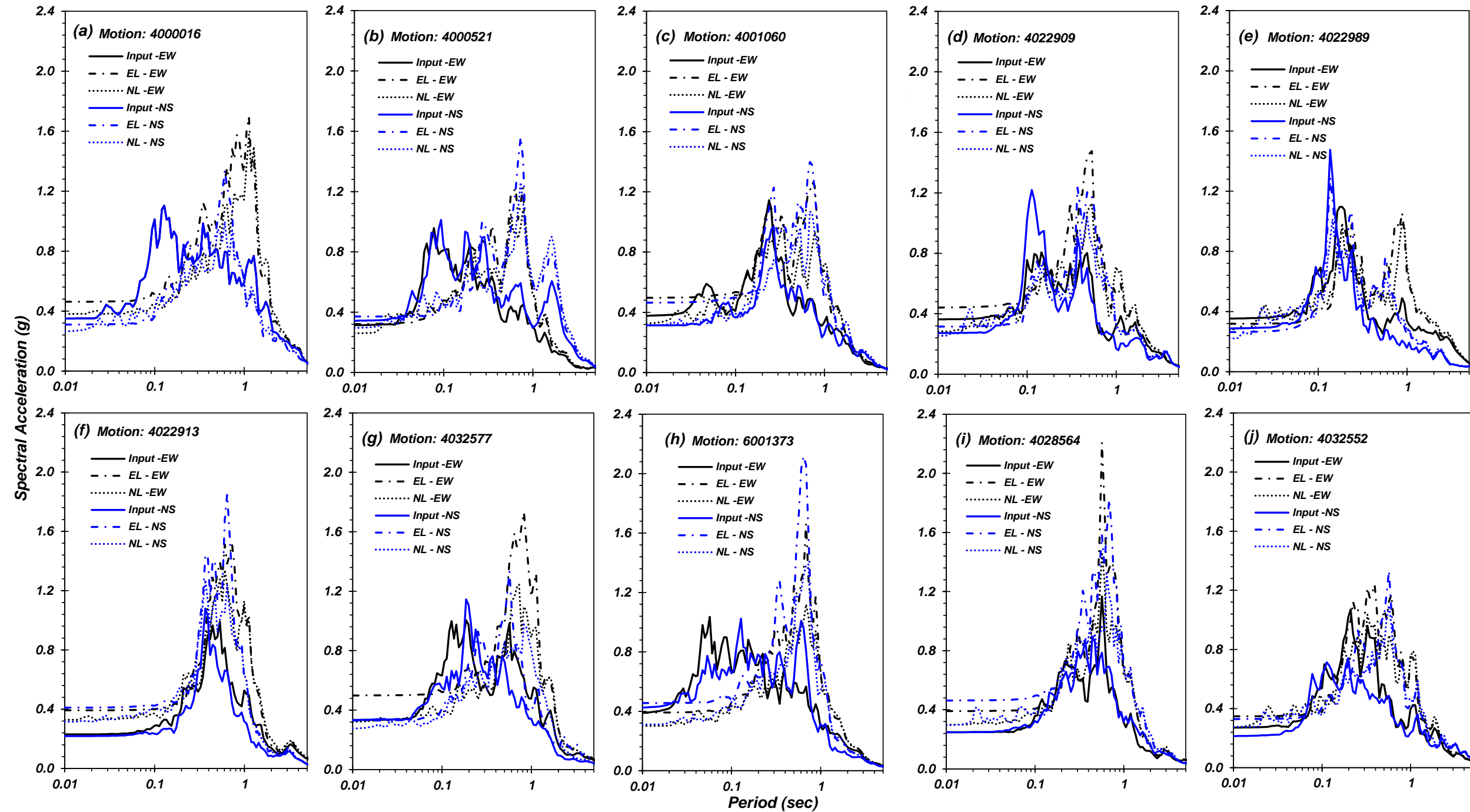


Figure B - 36. Comparison of spectral acceleration (SA) with depth for equivalent linear (EL) and nonlinear (NL) site response analyses conducted for the CPT-3 (C3) soil profile. 10 Motions (both NS and EW direction, total 20 motions) were evaluated obtained from the PEER NGA earthquake database: (a) Motion 4000016, (b) Motion 4000521, (c) Motion 4001060, (d) Motion 4022909, (e) Motion 4022989, (f) Motion 4022913, (g) Motion 4032577, (h) Motion 6001373, (i) Motion 4028564, (j) Motion 4032552.

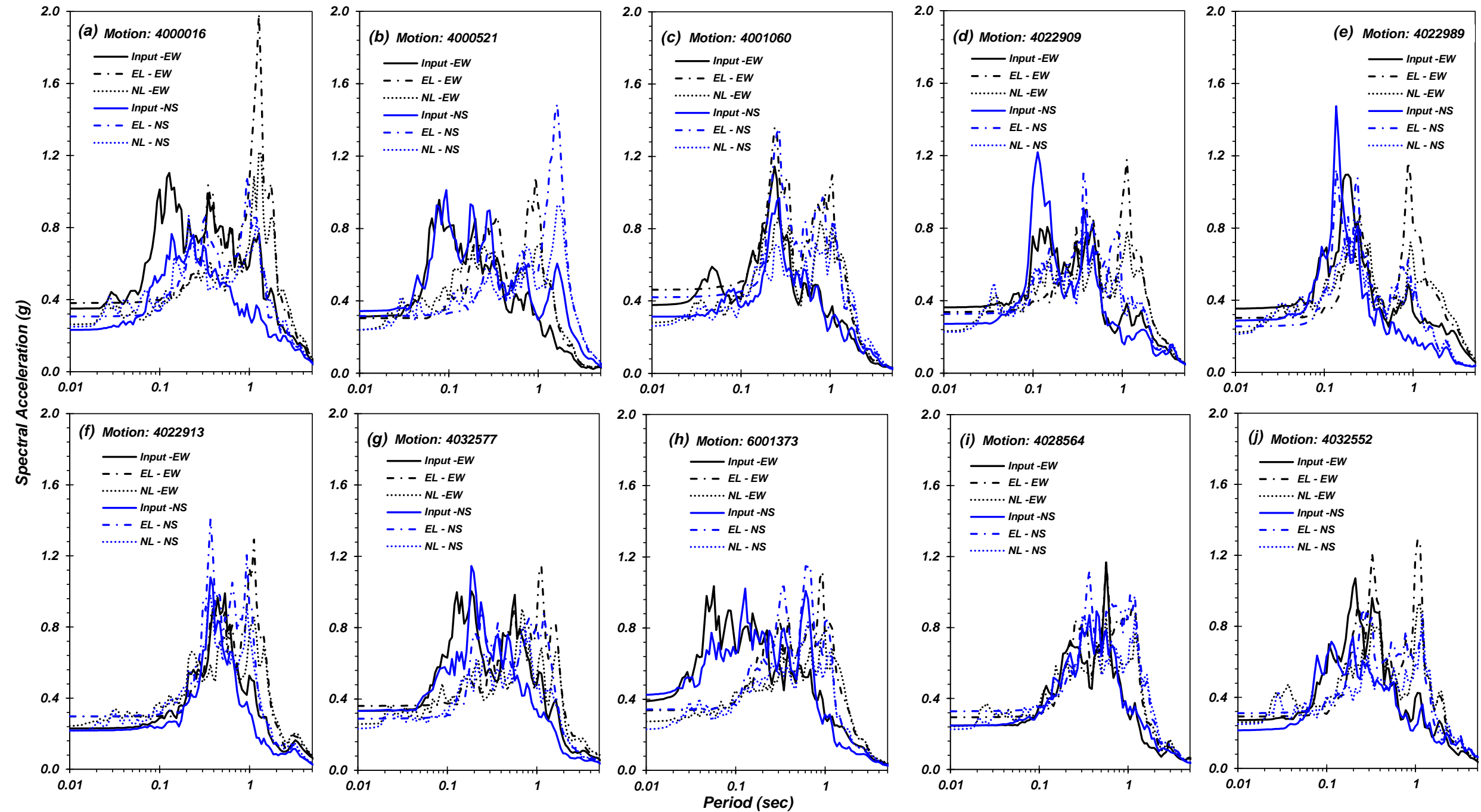


Figure B - 37. Comparison of spectral acceleration (SA) with depth for equivalent linear (EL) and nonlinear (NL) site response analyses conducted for the CPT-4 (C4) soil profile. 10 Motions (both NS and EW direction, total 20 motions) were evaluated obtained from the PEER NGA earthquake database: (a) Motion 4000016, (b) Motion 4000521, (c) Motion 4001060, (d) Motion 4022909, (e) Motion 4022989, (f) Motion 4022913, (g) Motion 4032577, (h) Motion 6001373, (i) Motion 4028564, (j) Motion 4032552.

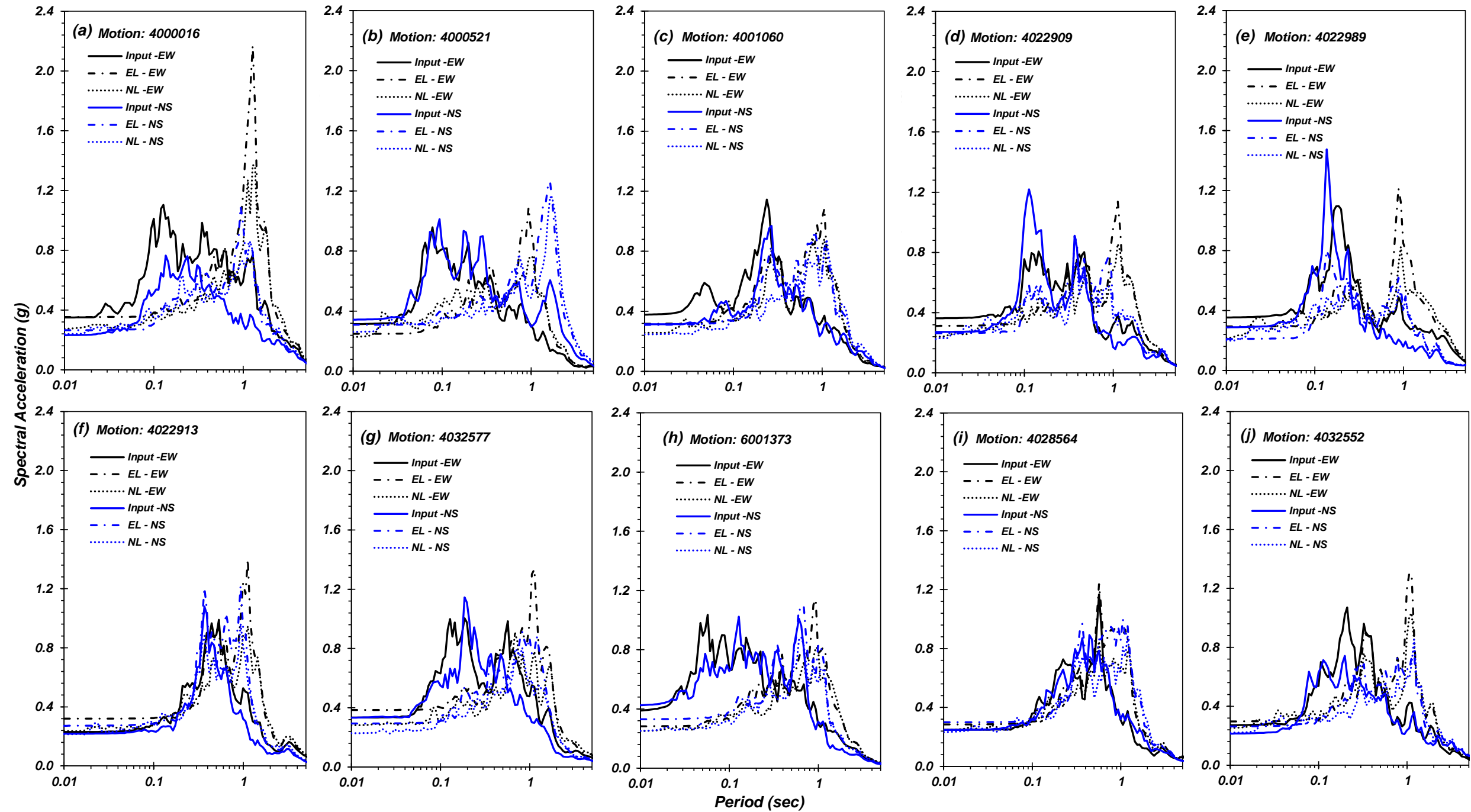


Figure B - 38. Comparison of spectral acceleration (SA) with depth for equivalent linear (EL) and nonlinear (NL) site response analyses conducted for the CPT-5 (C5) soil profile. 10 Motions (both NS and EW direction, total 20 motions) were evaluated obtained from the PEER NGA earthquake database: (a) Motion 4000016, (b) Motion 4000521, (c) Motion 4001060, (d) Motion 4022909, (e) Motion 4022989, (f) Motion 4022913, (g) Motion 4032577, (h) Motion 6001373, (i) Motion 4028564, (j) Motion 4032552.

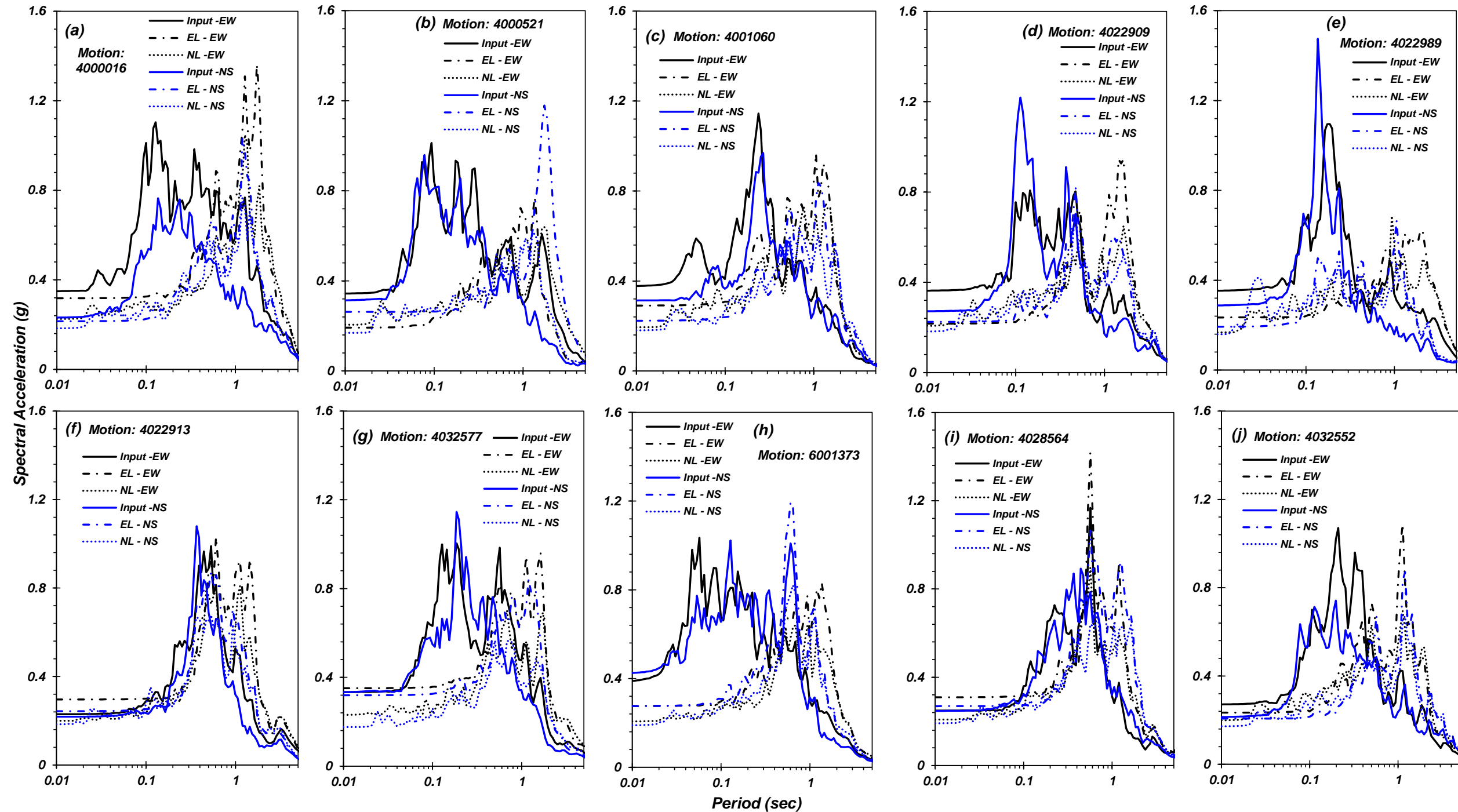


Figure B - 39. Comparison of spectral acceleration (SA) with depth for equivalent linear (EL) and nonlinear (NL) site response analyses conducted for the CPT-6 (C6) soil profile. 10 Motions (both NS and EW direction, total 20 motions) were evaluated obtained from the PEER NGA earthquake database: (a) Motion 4000016, (b) Motion 4000521, (c) Motion 4001060, (d) Motion 4022909, (e) Motion 4022989, (f) Motion 4022913, (g) Motion 4032577, (h) Motion 6001373, (i) Motion 4028564, (j) Motion 4032552.

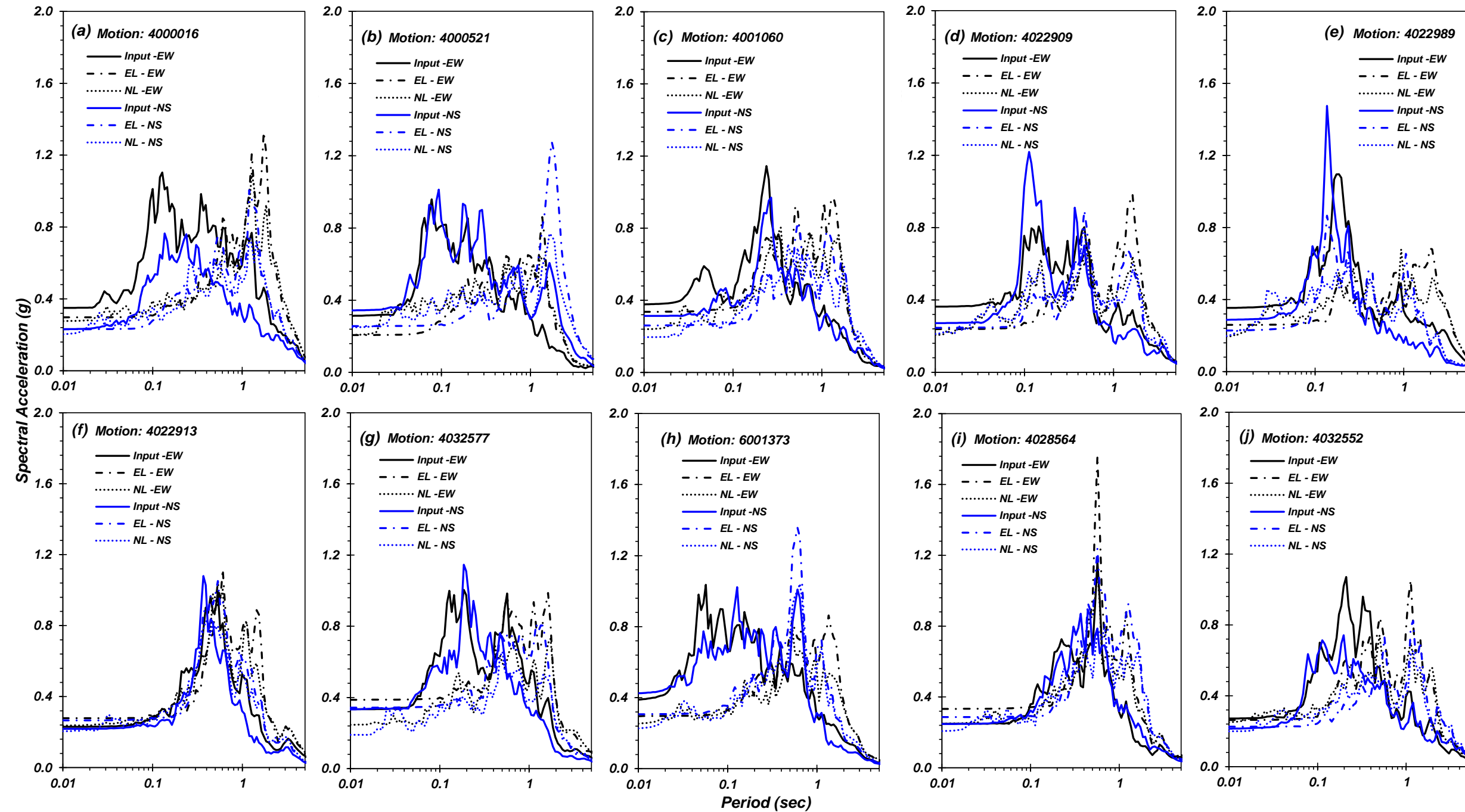


Figure B - 40. Comparison of spectral acceleration (SA) with depth for equivalent linear (EL) and nonlinear (NL) site response analyses conducted for the CPT-7 (C7) soil profile. 10 Motions (both NS and EW direction, total 20 motions) were evaluated obtained from the PEER NGA earthquake database: (a) Motion 4000016, (b) Motion 4000521, (c) Motion 4001060, (d) Motion 4022909, (e) Motion 4022989, (f) Motion 4022913, (g) Motion 4032577, (h) Motion 6001373, (i) Motion 4028564, (j) Motion 4032552.